Doctoral dissertation

Investigation of the anisotropic optical and electronic properties of group IV-VI van der Waals crystals

Agata Karolina Tołłoczko

Supervisor: Prof. dr hab. inż. Robert Kudrawiec
Assistant supervisor: Dr inż. Szymon J. Zelewski

Wrocław 2024

Acknowledgements

First and foremost, I would like to express my deepest appreciation to my supervisors, Prof. Robert Kudrawiec and Dr Szymon Zelewski. Thank you for your faith, dedicated time and invaluable support, both at the optical table during experiments and at the coffee table discussing the results and ideas.

I also thank my colleagues, especially Ewelina Zdanowicz, who guided me at the beginning and became my friend as time passed by. I thank Kamil Misztal and Maciej Peter, who followed my path as PhD students, and Artur Herman, who only follows a path of his own. I thank Jakub Ziembicki, Miłosz Rybak, and the whole team of theoreticians for their ab initio magic. At the end of the list, I thank my three infrared rays of sunshine for brightening the darkness of the laboratory.

Eventually, with all my heart I thank my fiancé Marcin, for his patience and support outside the university walls, and for all the nautical miles we sailed together.

A.K.T., 29.09.2024

Abstract

This doctoral thesis presents a comprehensive investigation of group IV mono- and dichalcogenides (MX and MX_2, respectively), a family of van der Waals (vdW) crystals with significant potential in optoelectronic applications. The study focuses on the experimental characterization of the fundamental optical and electronic properties of the materials, employing various methods of optical and photoemission spectroscopy. Furthermore, potential applications of the investigated materials are explored. One of the key findings of the research is the strong linear dichroism of the optical response of MXs, which can be exploited in polarization-sensitive photodetection. For MX_2 crystals the measurements revealed a strong influence of native defects on the optical properties, indicating the possibilities of tuning them by adjusting the defect concentration.

The work is a series of five scientific publications (Chapters 2 – 6), preceded by an introduction (Chapter 1), including general information about the investigated materials and a description of the utilized experimental techniques.

In the first three reports GeSe (Chapter 2), GeS (Chapter 3), SnS, and SnSe (Chapter 4) crystals are characterized using complementary methods of optical spectroscopy, with emphasis on the in-plane anisotropy of the fundamental properties.

The fourth work (Chapter 5) is an experimental study of the electronic band structure of GeS, SnS, and SnSe by means of angle-resolved photoemission spectroscopy (ARPES), revealing characteristic features potentially responsible for high thermoelectric conversion efficiency.

The fifth work (Chapter 6) regards SnS_2 and $SnSe_2$ crystals. Alongside the investigation of the optical activity, the influence of high intrinsic concentration of native donor defects on the optical and electronic properties is discussed.

The study contributes to the general understanding of the fundamental properties of MX and MX_2, as well as phenomena related to interaction with light. The obtained results point toward the most promising future applications.

Streszczenie

Niniejsza praca doktorska przedstawia kompleksowe badanie mono- oraz dichalkogenków grupy IV (odpowiednio MX i MX_2), należących do rodziny kryształów van der Waalsa (vdW), o dużym potencjale w zastosowaniach optoelektronicznych. Badania koncentrują się na eksperymentalnej charakteryzacji podstawowych właściwości optycznych i elektronowych tych materiałów, przy użyciu różnych metod spektroskopii optycznej i fotoemisyjnej. Ponadto analizowane są potencjalne zastosowania badanych kryształów. Jednym z kluczowych wyników jest potwierdzenie silnej anizotropii odpowiedzi optycznej MX – zjawiska, które może być wykorzystane w detekcji światła czułej na polaryzację. W przypadku kryształów MX_2 pomiary ujawniły znaczący wpływ natywnych defektów na właściwości optyczne, co stwarza możliwość ich dostosowania poprzez kontrolowaną zmianę koncentracji defektów.

Praca składa się z serii pięciu publikacji naukowych (Rozdziały 2–6), poprzedzonych wstępem (Rozdział 1), który zawiera ogólne informacje o badanych materiałach oraz opis wykorzystanych technik eksperymentalnych.

W pierwszych trzech artykułach kryształy GeSe (Rozdział 2), GeS (Rozdział 3), SnS i SnSe (Rozdział 4) zostały zbadane przy użyciu komplementarnych metod spektroskopii optycznej, z naciskiem na anizotropię właściwości optycznych.

Czwarta praca (Rozdział 5) przedstawia eksperymentalne badanie struktury pasmowej materiałów GeS, SnS i SnSe za pomocą kątowo rozdzielczej spektroskopii fotoemisyjnej (ARPES), ujawniające charakterystyczne cechy potencjalnie odpowiedzialne za wysoką efektywność konwersji termoelektrycznej.

Piąta praca (Rozdział 6) dotyczy kryształów SnS_2 i $SnSe_2$. Oprócz analizy aktywności optycznej, omawiany jest wpływ natywnych defektów donorowych na właściwości optyczne i elektroniczne.

Przeprowadzone badana przyczyniają się do ogólnego zrozumienia podstawowych właściwości MX i MX_2 oraz zjawisk związanych z odziaływaniem ze światłem. Uzyskane wyniki wskazują najbardziej obiecujące przyszłe zastosowania.

Contents

List of acronyms 7

1 Introduction 8

1.1 Motivation and overview 8

1.2 Investigated materials 9

1.2.1 Van der Waals crystals – an overview 9

1.2.2 Group IV monochalcogenides 15

1.2.3 Group IV dichalcogenides 18

1.3 Experimental techniques 20

1.3.1 Optical spectroscopy 20

1.3.2 Photoemission spectroscopy 27

2 Optical properties of orthorhombic germanium selenide: an anisotropic layered semiconductor promising for optoelectronic applications 29

3 Valley polarization investigation of GeS under high pressure 44

4 Linear dichroism of the optical properties of SnS and SnSe van der Waals crystals 59

5 Photoemission Study of the Thermoelectric Group IV-VI van der Waals Crystals (GeS, SnS, and SnSe) 78

6 Influence of Native Defects on the Optical Properties of SnX_2 (X = S, Se) van der Waals Crystals 97

7 Conclusions 119

Bibliography 121

List of Acronyms

ARPES	Angle-Resolved Photoemission Spectroscopy
BP	black phosphorus
BZ	Brillouin zone
CB	conduction band
CBM	conduction band minimum
CVD	chemical vapor deposition
DFT	Density Functional Theory
MXs	group IV monochalcogenides (M = Ge, Sn; X = S, Se)
MX_2	group IV dichalcogenides (M = Ge, Sn; X = S, Se)
PBE	Perdew-Burke-Ernzerhof
PES	Photoemission Spectroscopy
PL	photoluminescence
PR	photoreflectance
SO	spin-orbit
TMDs	transition metal dichalcogenides
UPS	Ultraviolet Photoemission Spectroscopy
VB	valence band
VBM	valence band maximum
vdW	van der Waals
XPS	X-ray Photoemission Spectroscopy

CHAPTER 1

INTRODUCTION

1.1 Motivation and overview

It has been exactly 20 years since the groundbreaking work of Novoselov and Geim *et al.*[1] was published in October 2004, reporting the first fully functional field effect transistor (FET) based on atomically thin carbon films, commonly known as graphene. The achievement revealed entirely new opportunities across various fields of technology, particularly those aiming for device miniaturization. In electronics, reducing the size of a single transistor allows more units to fit within the same chip area, thereby increasing computational power. In the technology of light emitters and detectors, the smaller size of light emitting diodes (LEDs) and light-sensitive elements lead to higher resolution of displays and cameras. Additionally, thinner films offer improved transparency, which can be utilized in applications like transparent displays or photovoltaic systems. The silicon-based technology appears to be inevitably approaching its physical limits, as deviation from Moore's law,[2] predicting doubling of the transistor density, and hence computational power, every two years, can already be observed.[3] The demand for novel solutions has led researchers to explore alternatives, where materials such as graphene, naturally occurring in the thinnest possible form of single atomic layers, hold great promise. This emerging class of materials is known as van der Waals (vdW) crystals, after the character of interaction binding together individual layers.[4] Despite multiple superior properties, graphene's semimetallic nature severely limits its potential as an active material in semiconductor-based applications. As a result, in the past two decades, other vdW crystals have garnered significant attention, offering a broad range of electronic properties, from insulating to metallic.[4,5] What is more, vdW monolayers often display unique behavior, distinct from their bulk counterparts, sometimes revealing entirely novel phenomena. While the versatility of vdW crystals offers vast potential, many of these promising materials are still not well understood. Comprehensive research is necessary to characterize their fundamental properties and identify the most suitable applications for future commercialization.

This thesis focuses on the investigation of group IV chalcogenides (MX and MX_2, where M = Ge, Sn, and X = S, Se), belonging to the family of vdW crystals. The primary objectives of the study are the experimental characterization of the fundamental optical and electronic properties of MX and MX_2 crystals, followed by an exploration of their potential applications. A significant portion of the work is dedicated to strong anisotropy of the optical response, a feature that could enable their application in polarization-sensitive optoelectronics.[6–8] Such technology can be exploited for the detection of light polarization changes after traveling through a birefringent medium, including various solids and liquid crystals, but also biological systems such as protein solutions.[9] The state-of-the-art polarization detectors are complex devices composed of multiple optical elements, therefore materials with intrinsic polarization sensitivity are extremely desired. Alongside experimental

evidence of linear dichroism, the thesis provides an in-depth discussion of its fundamental origins, rooted in the crystal structure and symmetry of the materials. The investigation employs complementary methods of optical spectroscopy and photoemission spectroscopy. The experimental results acquired by the author are supported by theoretical calculations performed by Miłosz Rybak, Jakub Ziembicki, Tomasz Woźniak, and Michał Błaszczak, under the supervision of Prof. Paweł Scharoch.

1.2 Investigated materials

1.2.1 Van der Waals crystals

Van der Waals crystals are materials with a specific layered structure, often referred to as two-dimensional (2D), schematically illustrated in Fig. 1.1a. Within each layer, atoms form strong covalent bonds, while individual layers are held together only by weak van der Waals interactions. The distances between atoms depend on the type of bonding, so the lattice parameters within the layer plane are much smaller than in the perpendicular direction. Such a structure leads to quasi-two-dimensional behavior of the electrons, to some degree confined within the layer plane, and strong anisotropy of the fundamental properties. One of the most straightforward examples is the electrical conductivity, usually significantly better in the layer plane compared to the out-of-plane direction, as charge carriers can move more easily within the layer than between them. The structure also allows relatively easy isolation of single layers (or few-layer flakes), for which the confinement-related effects are even more apparent, and often some novel properties emerge, dependent on the number of layers. The first to obtain an atomically thin graphite flake, graphene, were Novoselov and Geim, supported by their research team,[1] for which they were awarded a Nobel Prize in physics in 2010. The discovery boosted the interest in van der Waals crystals, pointing toward entirely new possibilities of applications. To date, various techniques allowing to obtain van der Waals monolayers have been developed, and a wide range of materials besides graphene were investigated,[4,5,10,11] in many cases rediscovered after years of being studied in their bulk form. The versatility of materials with a broad range of properties makes van der Waals crystals suitable for many different areas of technology, beginning with electronics and optoelectronics (transistors, light emitters and detectors, photovoltaics),[12–17] through nonlinear optics,[18–21] thermoelectric conversion,[22–26] photocatalysis,[27–29] piezotronics,[30] and energy storage,[31–33] ending with advanced experimental-stage applications based on phenomena such as superconductivity,[34–36] and quantum Hall or other topological effects.[37,38]

In the following sections, the growth techniques and examples of van der Waals materials will be discussed, with an emphasis on the crystals investigated in this work. Often, analogies to *traditional* semiconductors (such as Si, GaAs etc.) will be used, which will be referred to as *covalent* crystals.

Examples of van der Waals crystals

The most common and well-studied van der Waals crystal is graphite, found both in bulk form and as two-dimensional graphene.[1] Graphite is an allotrope of carbon, where sp^2 hybridization causes each carbon atom to form covalent bonds with three neighboring atoms, creating a large planar molecule with a hexagonal honeycomb arrangement, shown in Fig. 1.1a. Since a carbon atom has

four valence electrons, one of them remains delocalized, forming a structure similar to a benzene molecule. This delocalization makes graphite and graphene excellent electricity and heat conductors.[39] The theoretical phonon-limited carrier mobility of graphene within the layer plane can reach up to 200000 cm^2/Vs,[40,41] which exceeds the electron mobility in silicon by three orders of magnitude.[42] Possessing also other desired properties, such as transparency, flexibility, and mechanical strength, which can be further tuned by doping, surface functionalization or integration with other materials, graphene is promising for numerous applications. The extraordinary conductive performance of graphene is the consequence of its semimetallic character, determined by the electronic band structure with zero band gap and linear (Dirac-like) dispersion, illustrated in Fig. 1.1b.[43] In some aspects, the feature can be considered the greatest disadvantage of graphene, limiting its use in technologies where semiconductors are required, especially light emitters and detectors or photovoltaics. Therefore, more and more researchers focus on the investigation of other materials, fulfilling the open band gap condition and, as a consequence, more suitable for applications in optoelectronics.

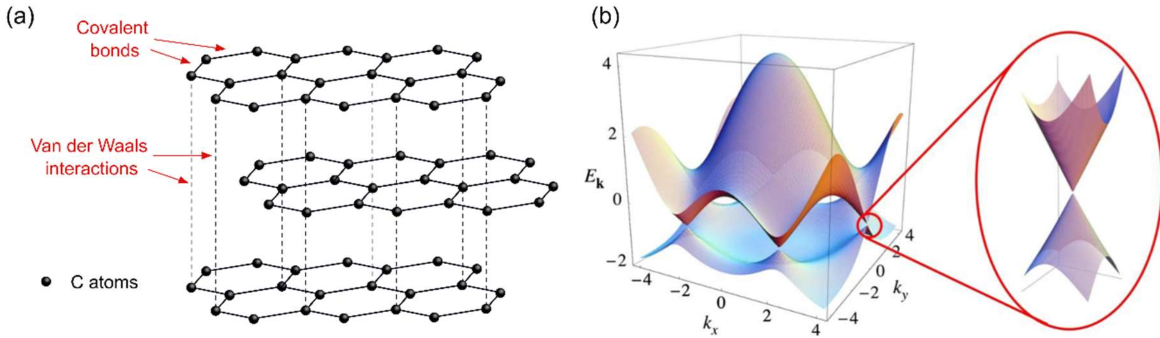

Fig. 1.1 (a) Crystal structure of graphene and (b) electronic band dispersion of graphene, visualizing linear dispersion and zero band gap in the Dirac point. Reprinted with permission from Ref. [43]. Copyright 2009 American Physical Society.

A family of van der Waals crystals attracting increasing attention are transition metal dichalcogenides (TMDs) - compounds of d-block elements (Ti, Hf, Zr, Mo, W, V, Nb, Ta) and chalcogens (S, Se, Te).[5,44] Depending on the occupation of the *d* bands of the electronic structure, they exhibit different behavior, from insulating, through semiconducting, to metallic. TMDs crystallize in a hexagonal structure, with a single van der Waals layer consisting of three atomic layers bind covalently, as shown in Fig. 1.2a.[44] Two main polytypes can be distinguished, in which metal atoms are either in octahedral or trigonal prismatic coordination, labeled 1T and 2H, respectively. In Fig. 1.2b the reciprocal unit cell (first Brillouin zone, BZ) is presented, with labeled high symmetry points. The most widely studied TMDs are compounds of Mo and W with S, Se, or Te, which are semiconductors with energy gaps in the visible or near-infrared spectral range. Plenty of interesting physical phenomena were observed, such as transition from indirect to direct band gap in the monolayer limit (see the electronic band structure in Fig. 1.2c),[45,46] extremally high exciton binding energies (exceeding 200 meV),[47] or valley polarization.[48–50] The last effect is a result of the inversion symmetry breaking in a monolayer form, for which the energetically degenerate valleys at K and K' points of the BZ (labeled in Fig. 1.2b), are inequivalent regarding the exciton spin and couple

selectively with either left- or right-handed circularly polarized light. This feature can be exploited in *valleytronics* – a branch of technology employing the valley degree of freedom and the possibility of accessing it externally to store information. Despite these impressive properties, Mo- and W-based TMDs exhibit rather poor electrical conductivity (typically of ~200 cm^2/Vs).[51]

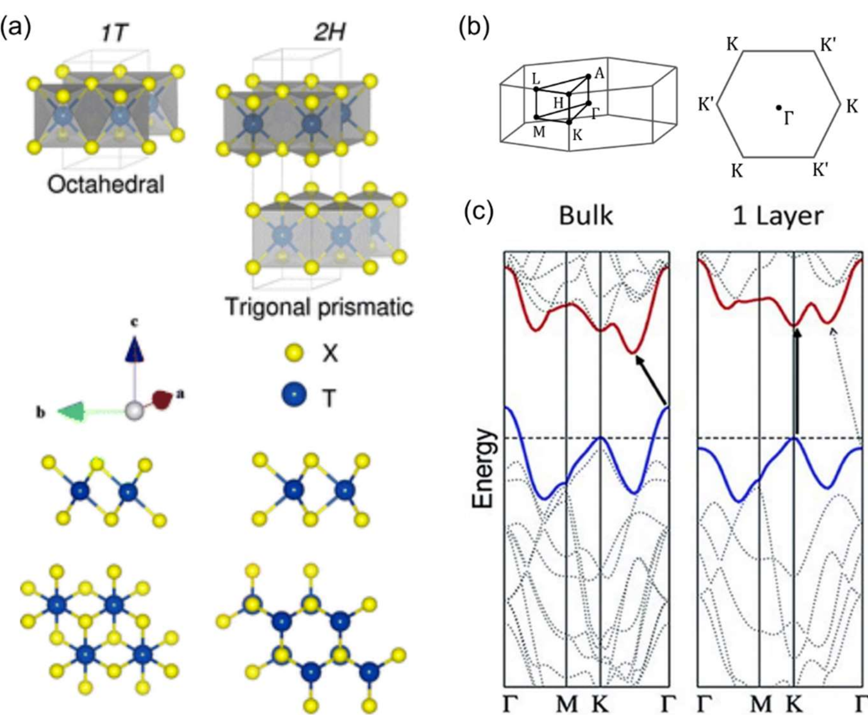

Fig. 1.2 (a) Crystal structure of the two phases of TMDs, octahedral 1T and trigonal prismatic 2H. Reprinted from Ref. [44] with permission of Royal Society of Chemistry; permission conveyed through Copyright Clearance Center, Inc. (b) Three-dimensional (left) and two-dimensional Brillouin zone corresponding to the crystal structure, with labeled high symmetry points, including inequivalent K and K' points in a monolayer form. (c) Band dispersion of bulk and monolayer MoS_2, illustrating the indirect-direct band gap transition in the monolayer limit. Reproduced from Ref. [46] with permission of Springer Nature.

A material combining the most desired properties of graphene and semiconducting TMDs is black phosphorus (BP) and its monolayer form – phosphorene.[10,52–54] In many aspects phosphorene is similar to graphene, as an elemental crystal. As presented in Fig. 1.3a, it crystalizes in a honeycomb structure, although the layer is not planar but puckered along one of the in-plane directions, as a result of sp^3 instead of sp^2 hybridization. While carbon atoms in graphene bond with three neighbors using three out of four valence electrons, leaving the remaining one delocalized, phosphorus has five valence electrons, forming three bonds and one lone electron pair in tetragonal coordination. The effective symmetry of the crystal is orthorhombic and characterized by strong in-plane anisotropy, affecting the fundamental properties of the material, such as conductivity, optical response, or mechanical parameters.[55–57] The phenomenon will be discussed in detail further in this work, with respect to IV-VI binary compounds analogous to BP.[11] The crystal structure and electron density distribution determine the electronic band dispersion, which, contrary to graphene, is characterized by an open band gap, relatively narrow in the bulk form (0.3 eV) but tunable with the sample thickness up to ~2 eV in the monolayer limit.[10,52,58–60] Importantly, the band gap character is direct

(independent of the number of layers), which is crucial for applications in light-emitting devices. Regarding the electrical conductivity, BP cannot compete with graphene, but exhibits properties superior to TMDs.[55,61–63] It should also be mentioned that even though BP is ambipolar (i.e. both n- and p-type doping can be easily achieved), the hole transport is favorable, with mobilities higher even by an order of magnitude.[55,64] With the above intermediate properties, BP is considered a material bridging the gap between relatively wide band gap TMDs and semimetallic graphene,[10,65] as visualized in a diagram in Fig. 1.3b.

Despite many advantages, the stability of BP is not sufficient for real-life applications. Thin layers are particularly prone to rapid degradation under atmospheric conditions.[66–68] One approach to prevent this process is the encapsulation of phosphorene flakes between layers of hexagonal boron nitride,[69–71] which, however, demands additional processing and is challenging to realize on a large scale. Therefore, group IV monochalcogenides - materials closely related to BP with similar properties but superior stability, which will be considered further in the text, are worth attention as an alternative.[11,72]

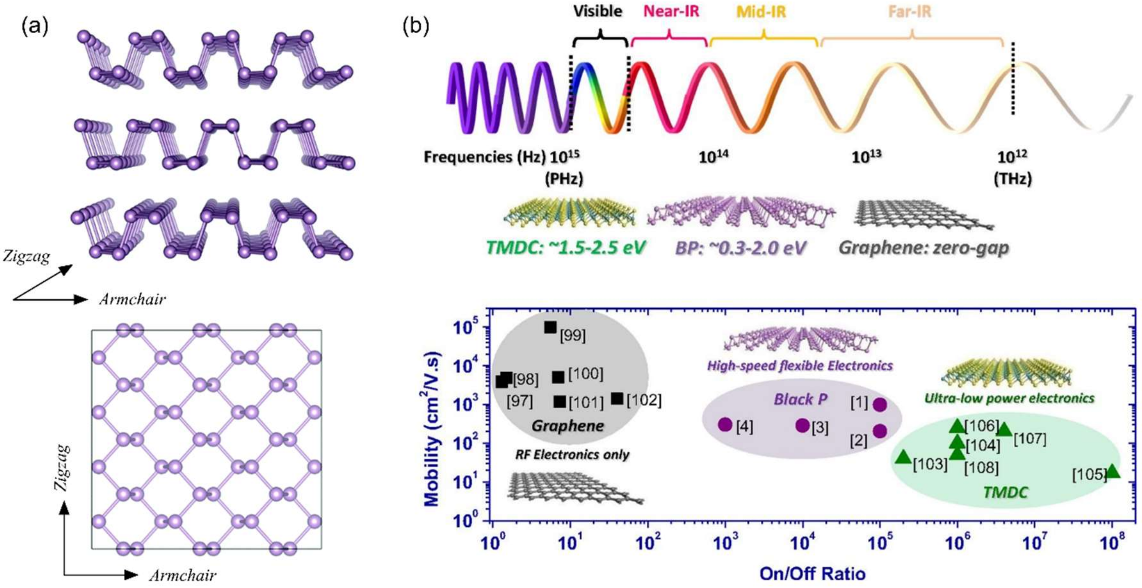

Fig. 1.3 (a) Crystal structure of BP. Reprinted from Ref. [64] with permission of Royal Society of Chemistry; permission conveyed through Copyright Clearance Center, Inc. (b) Diagram illustrating intermediate propertied of BP, compared to graphene and TMDs, regarding band gap, carrier mobility and on/off ratio of current response. Numbers in the figure correspond to references in the original work. Reprinted from Ref. [54] under educational permission. Copyright 2015 National Academy of Sciences.

Crystal growth and single layers isolation techniques

Bulk van der Waals crystals can be grown by multiple methods, including directional solidification (such as the Bridgman-Stockbarger technique), flux growth, and physical or chemical vapor transport.[73] The Bridgman-Stockbarger technique is a melt-based approach in which the grown crystal solidifies directly from the liquid phase of the material. In the flux growth, the crystals nucleate in a liquid (usually a molten metal, salt, or oxide), and the temperature dependence of the material solubility in a given solution is exploited to control the process. In vapor transport techniques the

substrates sublimate (physical transport) or undergo a chemical reaction with the transport agent (chemical transport) in the high-temperature zone of the growth chamber and are transported to a cooler zone, where they recrystallize to form a monocrystal. The choice of the most suitable growth method depends on the properties of the produced material, such as its melting point, solubility, reactivity, vapor pressure, etc.

Similarly to nanostructures of covalent crystals (quantum wells, wires, or dots), van der Waals monolayers and thin flakes can be obtained by various techniques, among which *top-down* or *bottom-up* procedures can be distinguished. In the top-down methods, layers are isolated from a thicker bulk crystal. The most common representative of this class of methods is mechanical exfoliation, in which flakes are detached by a scotch tape and transferred onto the desired substrate.[74,75] The technique allows to obtain high quality structures, however it remains hardly scalable. An alternative is liquid-phase exfoliation, in which the process takes place in a solution.[76] The solvent molecules intercalate between the van der Waals layers and weaken the interaction, leading to their disintegration. The method is often combined with sonication, i.e., applying ultrasounds to enhance the separation of layers. The resulting thin flakes can then be deposited from the solution. The technique is suitable for up-scaling, but the quality of the products is generally poorer compared to mechanical exfoliation, due to contamination with chemical agents residues.

The bottom-up methods are mainly different variants of epitaxy (including molecular beam epitaxy) or chemical vapor deposition (CVD), allowing to cover large areas with van der Waals monolayers.[77,78] The main drawbacks of CVD are its high cost and the tendency of van der Waals crystals to form clusters (such as triangular islands of TMDs) rather than uniform coatings.[79] Thin sheets can also be directly synthesized from a solution as products of chemical reactions and extracted in a similar manner to liquid-phase exfoliation.[80,81]

Van der Waals heterostructures

Today's electronics and optoelectronics strongly rely on the heterostructures and alloys of covalent crystals, with precisely designed composition and geometry, including simple *p-n* junctions, but also complex multilayer structures for advanced applications, such as tandem solar cells, quantum cascade lasers (and other light sources), Bragg reflectors, etc. The greatest challenge for heterostructures engineering is the requirement of similar lattice constants of the materials. Depending on the lattice mismatch, either strain is induced in the grown layers, or relaxation takes place, leading to the formation of structural defects at the interface, which may propagate through the entire structure, affecting its quality.

Analogously, heterostructures of van der Waals crystals can be assembled, however, providing considerably more freedom in the choice of the materials.[4] Just like in bulk van der Waals crystals, in heterostructures the constituent layers of different materials are held together by van der Waals interactions and do not form actual chemical bonds. Therefore, such systems are not limited by the condition of lattice matching, allowing for the design of heterostructures composed of layers with significantly different lattice parameters or even completely different symmetry,[82,83] as schematically illustrated in Fig. 1.4a. The structural differences of the stacked layers are not completely idle and, to some degree, may influence the interlayer interaction by inducing strain, but the effect is not as drastic as in the case of covalent crystals, regarding the structure quality. Actually, the misalignment of the

atoms in alternating layers may lead to the formation of moiré patterns and the emergence of novel properties.[84–86] Moiré patterns are effectively superlattices resulting from lattice parameter mismatch, twist, or strain of van der Waals bilayers, as demonstrated in Fig. 1.4c. By tuning these factors, different patterns can be obtained, characterized by a related deformation field (periodic variation of strain and atomic displacement), implying specific electronic behavior. An iconic example is the twisted bilayer graphene, for which superconductivity was observed.[35,36]

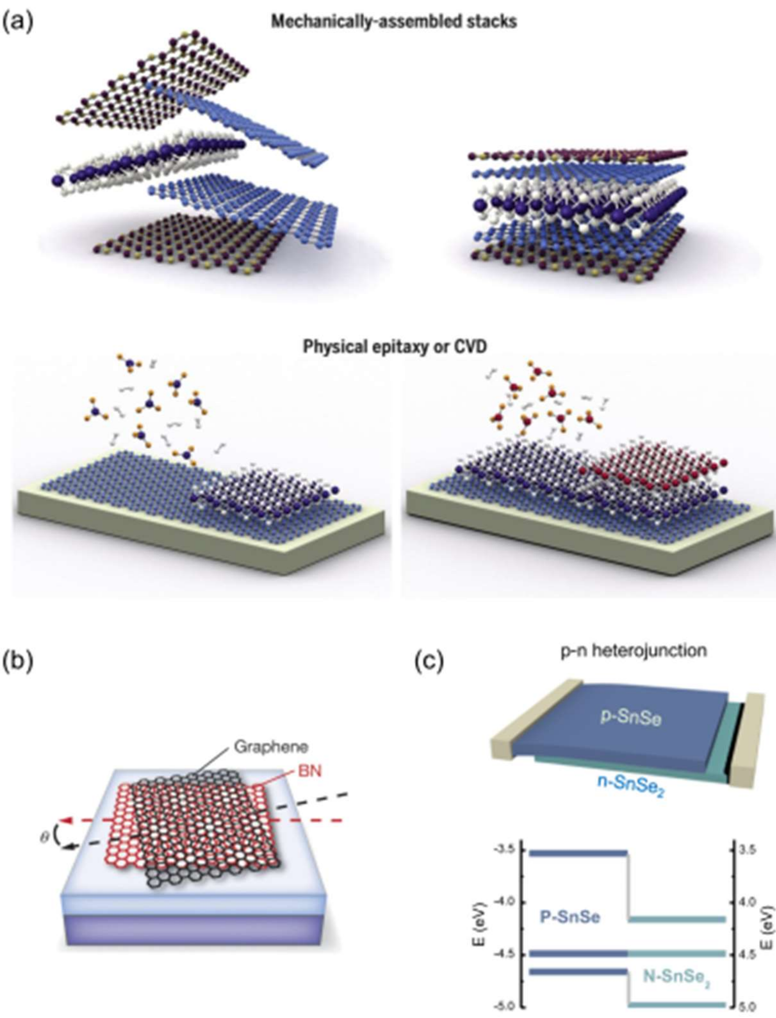

Fig. 1.4 (a) Schematic illustration of van der Waals heterostructures, visualizing the processes of mechanical assembly and epitaxial growth. Reprinted from Ref. [4] with permission of AAAS. (b) Sketch of a graphene/hBN twisted bilayer structure showing the emergence of a moiré pattern. Reproduced from Ref. [84] with permission of Springer Nature. (c) Schematic diagram (top) and band alignment (bottom) of a $SnSe/SnSe_2$ *p-n* heterojunction. Reprinted from Ref. [82] with permission of IOP Publishing; permission conveyed through Copyright Clearance Center, Inc.

An interesting idea of the heterostructure design is the combination of intrinsically *n*- and *p*-type semiconductors to form a *p-n* heterojunction, as shown in the diagram in Fig. 1.4c, without the need for introducing foreign atoms as dopants. Such a device was realized for $SnSe/SnSe_2$ structure,[82] with an additional advantage of the same elemental composition of the contributing materials, differing

only with stoichiometric ratio. Also worth mentioning is the fact that the two phases crystalize in entirely different crystallographic systems, orthorhombic (SnSe) and hexagonal ($SnSe_2$).

Van der Waals heterostructures offer plenty of new possibilities, however the efficient processes of their preparation still need to be developed for large-scale commercial applications. The two main approaches, mechanical assembly of the individual layers and direct epitaxial or CVD growth, are illustrated in the top and bottom sections of Fig. 1.4a, respectively.

1.2.2 Group IV monochalcogenides

Group IV monochalcogenides (MXs, where M = Ge, Sn, and X = S, Sn, Te) are a family of materials often referred to as phosphorene analogues,[11] as they are isoelectric to BP and inherit some of its properties, in a similar manner as GaAs (and other zinc-blend III-V compounds) is related to Si.

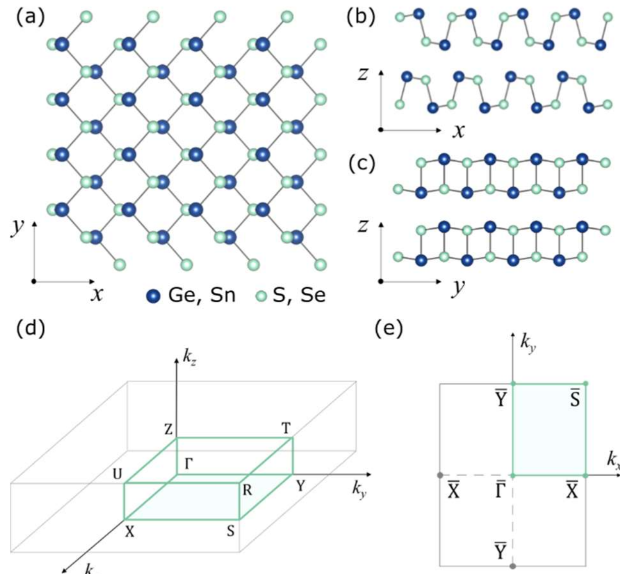

Fig. 1.5 Crystal structure of MXs. (a) Top view on a layer plane and side views along (b) *x* and (c) *y* directions. (d) three-dimensional and (e) two-dimensional Brillouin zone with labeled high symmetry points. Reprinted from Ref. [87] under CC-BY 4.0 license. Copyright 2023 A. K. Tołłoczko *et al.*

MXs crystalize in a distorted orthorhombic structure (space group *Pnma*, no. 62), illustrated in Fig. 1.5, with the characteristic anisotropic atomic arrangement in main in-plane crystallographic directions.[88] Along the *x* axis (also called *armchair*) the atoms form a puckered structure, while in the *y* direction (*zigzag*), the layer is ladder-like. This feature gives rise to strong directionality of the electronic structure, influencing the dielectric function and leading to strong linear dichroism of the optical response and general anisotropy of the fundamental properties.[89–96] The phenomenon, as one of the main topics of this work, was experimentally investigated by different methods of optical spectroscopy (especially the optical absorption) and is discussed in detail in the following chapters. In a bulk structure, the layers are sequenced in a centrosymmetric AB stacking (i.e., alternating layers have a slightly different atomic arrangement), however in a monolayer form the inversion symmetry is broken, resulting in the emergence of piezoelectric, multiferroic and nonlinear optical properties.[20,30,97,98]

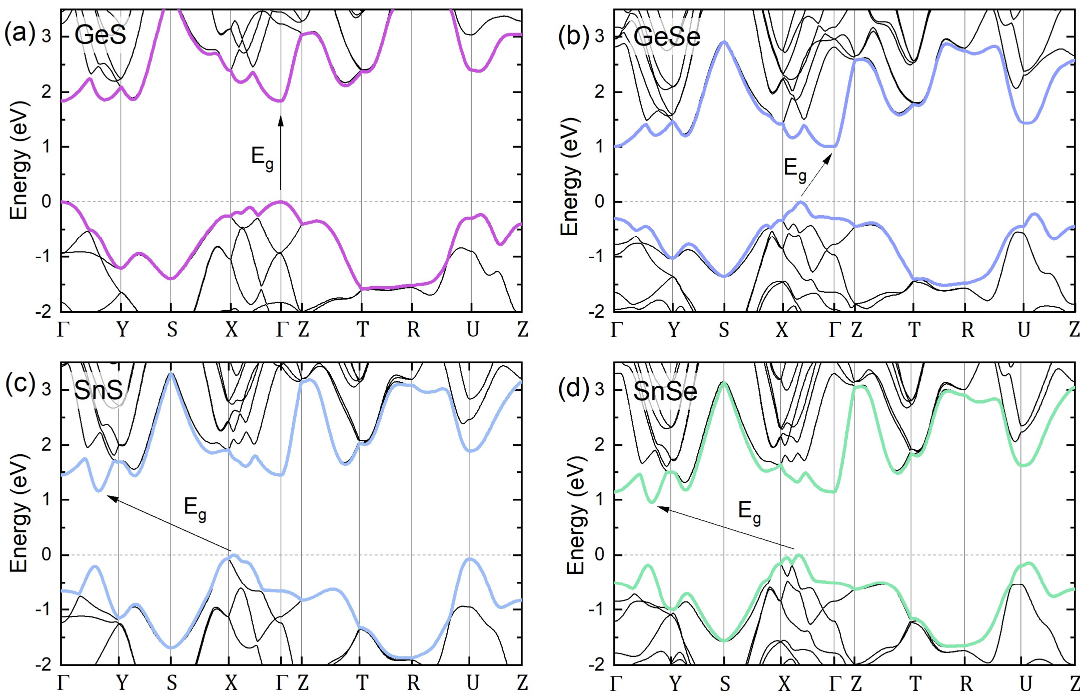

Fig. 1.6 Electronic band structures of GeS (a), GeSe (b), SnS (c), and SnSe (d) calculated by J. Ziembicki (a,c,d) and M. Błaszczak (b) employing mBJ exchange potential on top of the optimized geometry obtained within PBE+SO approach.

Regarding electronic behavior, MXs are semiconductors with usually indirect band gaps in the near-infrared or visible spectral range.[11] The materials are characterized by complex electronic band dispersion, featuring multiple energetically close valleys (in both valence and conduction band),[99,100] as presented in Fig. 1.6 for four representatives of the MX family, GeS, GeSe, SnS, and SnSe. Such a structure has consequences for the conductivity, as multiple valleys may contribute to electronic transport. It may also lead to difficulties in predicting the band gap character based solely on the electronic band dispersion calculations, as the choice of the computational method and parameters may affect the relative energies of the valleys. In other words, multiple band extrema can play the role of the conduction band minimum (CMB) and valence band maximum (VBM). Therefore, experimental verification of the accuracy of theoretical calculations is required. In the following chapters, different techniques are applied to resolve this issue. For GeS, ARPES investigation (see Chapter 5) allowed to determine the position of the VBM at the Γ point of the Brillouin zone, aligned with the theoretically predicted CBM, indicating the direct character of the band gap.[87] For the remaining three compounds, the band at Γ point is shifted towards higher binding energies, and a valley close to the X point is associated with the VBM, making the band gap indirect. The hypothesis is also confirmed by the lack of the photoluminescence emission. Nevertheless, for GeSe, the experiments (discussed in Chapter 2, but also independently shown by Murgatroyd *et al.*[101]) revealed domination of the optical absorption by direct transitions, suggesting a very small distance between the fundamental indirect and lowest direct band gap.[8] For SnS and SnSe, the two transitions could be resolved, exploiting the dependence on the incident light polarization,[102] as shown in Chapter 4.

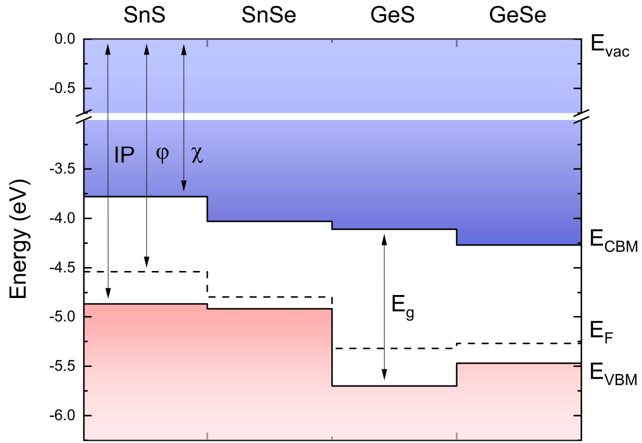

Fig. 1.7 Band alignment of GeS, GeSe, SnS, and SnSe crystals. Ionization potential, work function, electron affinity, and band gap are graphically defined as marked with arrows. Reprinted from Ref. [102] under CC-BY 4.0 license. Copyright 2024 A. K. Tołłoczko *et al.*

Another important property of MXs is their intrinsic *p*-type conductivity, resulting from the presence of native acceptor defects, such as metal (Ge or Sn) vacancies,[87,103–105] pinning the Fermi level close to the valence band top. Also worth attention is a related parameter, the ionization potential, determined by the VBM energy with respect to the vacuum level. Together with the work function and electron affinity, they are a set of parameters allowing to evaluate band offsets of a material. In Fig. 1.7, the three parameters are graphically defined, and the band offsets of MXs are plotted.[102,106] As can be seen from the figure, especially in the case of SnX crystals, the ionization potential is relatively low compared to other semiconductors (approximately 4.9 eV), which leads to serious consequences regarding the band alignment in heterostructures and the character of electrical contacts (Ohmic or Schottky) formed with different metals. This property is related to the presence of the stereochemically active lone electron pairs in the crystal structure.[102–104,107] The metal atom in the tetragonal coordination forms three bonds with chalcogen atoms and a lone electron pair is pushed to the fourth vertex of the tetrahedron, leading to distortion of the crystal lattice. According to the revised lone pairs model,[108] due to specific mixing of the valence M and X orbitals, the valence band top is shifted towards lower binding energies, reducing the ionization potential. The phenomenon is discussed in detail in Chapter 4.

Apart from optoelectronic applications, MXs are also promising for thermoelectric conversion.[22,23,93,94,99,109] Thermoelectric materials are extremely desired in the era of growing energy demand, as they allow to directly convert heat into electricity. A quantity describing the thermoelectric efficiency of a material is the thermoelectric figure of merit, given by the formula

$$zT = \frac{S^2 \sigma T}{\kappa_L + \kappa_e}, \tag{1}$$

where S is the Seebeck coefficient, σ is the electrical conductivity, κ_L and κ_e are the lattice and electronic thermal conductivities, respectively, and T is the temperature. Since it is challenging to simultaneously maximize both S and σ (the parameters are counter-dependent, therefore improving one usually leads to deterioration of the other), the state-of-the-art thermoelectric materials are

complex Pb compounds, exploiting heavy atoms and nanostructuring to minimize the thermal conductivity.[110,111] However, it was shown by Zhao *et al.*[22] that the pristine SnSe can reach zT of 2.6 (exceeding the Pb-based technology), thanks to its intrinsic low thermal conductivity, but also the multivalley electronic band structure, allowing to overcome the inverse relationship between S and σ. Other MXs, thanks to a similar band dispersion, also exhibit potential for thermoelectric applications, as considered in Chapter 5.

1.2.3 Group IV dichalcogenides

Group IV dichalcogenides (MX_2, where M = Ge, Sn, and X = S, Se), despite similar atomic composition, differ significantly from MXs due to the 1:2 stoichiometry. They crystalize in monoclinic (GeX_2) or hexagonal (SnX_2) structure. This work is focused mainly on tin compounds. The materials are suitable for a variety of applications, including optoelectronics, but also thermoelectric conversion, saturable absorbers for mode-locked lasers, photocatalysis, gas sensing, and water purification.[19,29,112–121] They are also perfect for integration with other stoichiometric phases of group IV chalcogenides (MX, M_2X_3) and with TMDs, crystalizing in a similar structure.

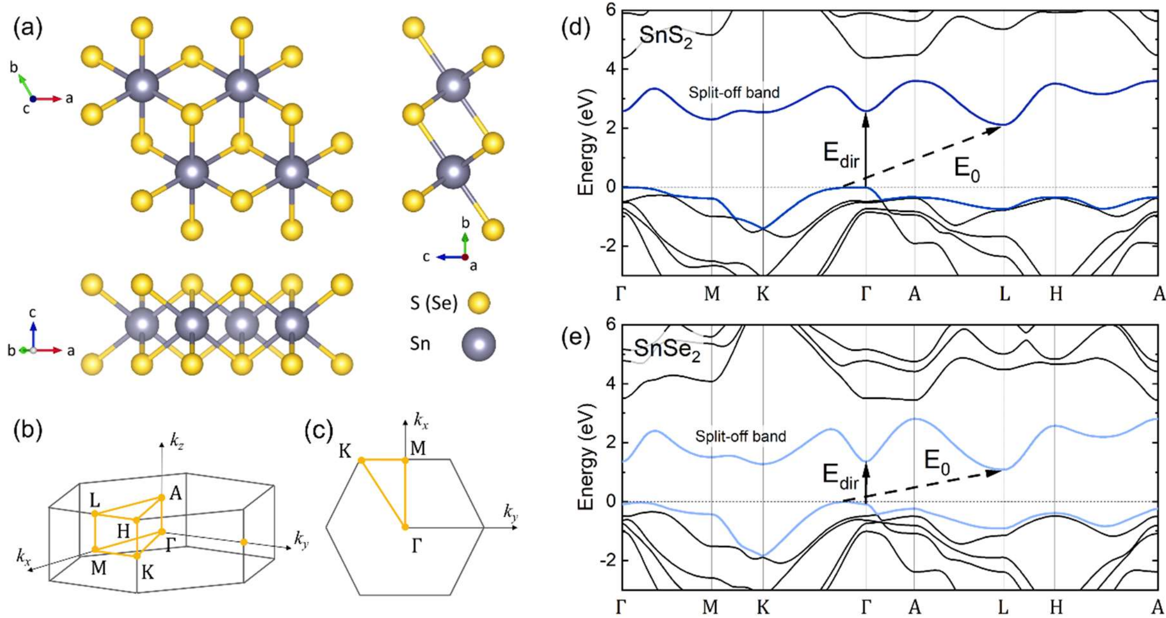

Fig. 1.8 (a) Hexagonal structure of SnX_2 crystals. Reprinted from Ref. [125] under CC-BY 4.0 license. Copyright 2024 A. K. Tołłoczko et al. (b) Three-dimensional and (c) two-dimensional Brillouin zone, with labeled high symmetry points. (d) Electronic band structures of SnS_2 and (d) $SnSe_2$ calculated by M. Rybak using mBJ exchange potential on top of the optimized geometry obtained within the PBE+SO approach. Fundamental indirect (E_0) and lowest direct (E_{dir}) band gaps are distinguished.

The crystal structure of SnX_2 materials, illustrated in Fig. 1.8a, belongs to space group $P\bar{3}m1$ (no. 164), often referred to as CdI_2-type.[122,123] The Sn atoms in an octahedral coordination form six bonds with chalcogens. The nomenclature regarding the structure present in the literature may lead to some confusion, as the phase is often referred to as 2H in the Ramsdell notation,[124] commonly used for CdI_2-like crystals. In this convention, the number 2 represents the number of chalcogen atomic layers

in the unit cell, while the letter H stands for the hexagonal arrangement. For TMDs, another notation is used, in which a phase with trigonal prismatic coordination of the metal atom is labeled 2H, where 2 describes the number of van der Waals layers (i.e. X-M-X layers) in the unit cell. Using this system, the $P\bar{3}m1$ SnX_2 crystals should be referred to as 1T polytype.

The electronic band structure of SnX_2, demonstrated in Fig. 1.11, reveals the indirect character of the fundamental band gap (of ~2.1 eV for SnS_2 and ~1.0 eV for $SnSe_2$), with the VBM in the Γ-K path and CBM in the L point of the BZ.[125] The lowest direct optical transition occurs in the Γ point. Similarly to MXs, the band structure has a multivalley character, however some other unique features can also be observed. One of them is an extremally flat valence band dispersion in the proximity of the Γ point, which has consequences regarding the electronic transport (high effective mass leads to low carrier mobility) and optical properties (significant broadening and band-nesting character of the optical transitions). Another interesting effect is the presence of a *split-off* band in the CB, i.e. the lowermost band is separated from the remaining part. As shown in Chapter 6, the band is composed of a mixture of Sn *s* and chalcogen *p* orbitals. The calculations of the transition matrix element between the topmost valence and the split-off conduction band resulted in very low values of the in-plane component (especially in the high symmetry points of the BZ), indicating the optical transitions between the bands are forbidden (or *quasi-forbidden*) by the selection rules.

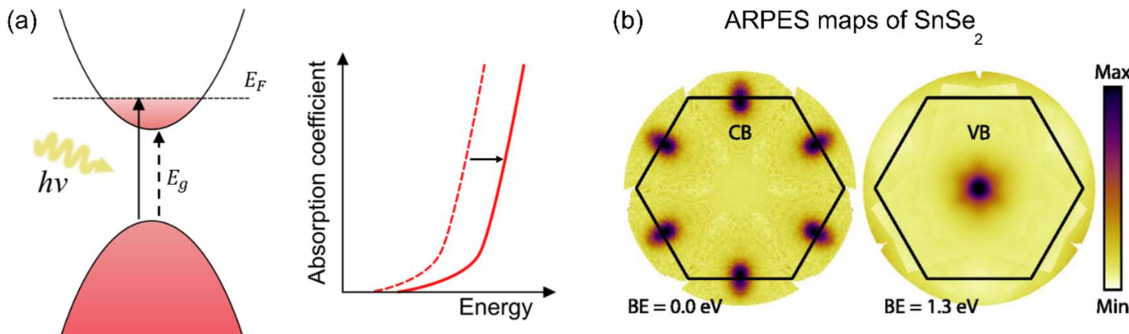

Fig. 1.9 (a) Graphical illustration of Burstein-Moss effect. Due to the population of the bottom CB states by electrons, only light of energy exceeding the lowest unoccupied state can be absorbed, which is experimentally observed as a blueshift of the absorption edge. (b) Evidence of the effect for $SnSe_2$ in the ARPES maps, revealing the CB valleys and Fermi level located above the band gap. Reprinted from Ref. [127] with permission of AIP Publishing.

In contrast to the monochalcogenide phase, MX_2 crystals exhibit intrinsic *n*-type conductivity induced by native donor defects (chalcogen vacancies and interstitial Sn).[82,105,126] The relatively high defect concentration leads to the Burstein-Moss effect (effective shift of the optical band gap energy due to population of the bottom conduction band states, schematically illustrated in Fig. 1.9a) visible in the optical absorption. As discussed in Chapter 6, the Burstein-Moss effect is most likely a primary cause of the discrepancies in the literature regarding the character and width of the energy gap of SnX_2 crystals, as different concentrations of the donor defects shift the absorption edge by different amounts. A direct evidence of the phenomenon in $SnSe_2$ is the work of Lochocki *et al.*,[127] where the authors detected a signal originating from the conduction band valley in the ARPES measurements, sensitive only to occupied electronic states. The examples of the acquired constant energy map at the

Fermi level and valence band top are presented in Fig. 9b. The importance of native defects in the material system is also shown by other studies, investigating their influence on properties such as photocatalytic efficiency or surface adsorption for gas detection.[28,120,121,128–130]

1.3 Experimental techniques

1.3.1 Optical spectroscopy

Optical absorption

Optical absorption spectroscopy is one of the fundamental analytical techniques adapted to study the interaction between light and matter. In solid-state physics, together with reflectance, they provide information about the dielectric function of the material, as absorption and reflection coefficients are related to, respectively, imaginary and real parts of the dielectric function. Unlike reflection, the absorption of the material cannot be measured directly, but is determined based on the light transmission through the sample using the Lambert-Beer relation

$$I_T = I_0 e^{-\alpha/d}, \tag{2}$$

where I_T is the transmitted light intensity, I_0 is the incident light intensity, α is the absorption coefficient and d is the sample thickness. If the reflection from the sample surface is significant (which is the case for most solid-state materials), the formula needs to be corrected by the reflected light intensity I_R, resulting in

$$I_T = (I_0 - I_R)\, e^{-\alpha/d}. \tag{3}$$

Then, the absorption coefficient can be calculated form the derived equation

$$\alpha = -\frac{1}{d} ln\left(\frac{I_T}{I_0 - I_R}\right). \tag{4}$$

In the investigation of semiconductors, particularly important is the spectral region close to the absorption edge, allowing to determine the fundamental band gap. The technique is sensitive to both direct and indirect optical transitions, characterized by different spectral dependences. In the analysis of the optical absorption, the relation between the imaginary part of the dielectric function and the joint density of states of the material is exploited, together with an assumption of parabolic and spherically-symmetrical dispersion of the bands at VBM and CBM (i.e. $E(k) \propto \frac{\hbar^2 k^2}{2m^*}$, where k is the wavevector and m^* is the effective mass of an electron or hole, for conduction and valence band, respectively).[131] Then, the analysis of the absorption coefficient spectra near the absorption edge can be simplified to considering the proportionality

$$\alpha(h\nu) \propto \frac{1}{h\nu}(h\nu - E_g)^{\frac{1}{2}}, \tag{5}$$

for direct optical transitions, and

$$\alpha(h\nu) \propto \frac{1}{h\nu}(h\nu - E_g \pm E_p)^2, \tag{6}$$

for indirect absorption edge, where $h\nu$ is the incident photon energy, E_g is the fundamental band gap, and E_p is the energy of the phonon involved in the indirect process. It should be noted that in the case of an indirect band gap, two absorption edges should be observed, corresponding to the processes with phonon absorption (minus sign in the equation) and emission (plus sign). In practice, the former is usually weak (especially at low temperatures), and the analysis is limited to the latter. The approach is generally referred to as the Tauc plot method,[132] in which the band gap is extracted from the absorption coefficient spectra by extrapolating the linear portions of the $(\alpha h\nu)^{\gamma}$ vs. $h\nu$ plot, where γ depends on the transition character (2 for direct allowed, 1/2 for indirect allowed, 2/3 for direct forbidden, and 1/3 for indirect forbidden transitions). Although the Tauc plot method is widely used and provides accurate results for covalent crystals, for which the condition of parabolic bands dispersion is fulfilled, it may fail for more complex structures characteristic for many van der Waals crystals. As shown in Chapter 6, an alternative can be the analysis of the derivative of the transmittance spectra (either calculated numerically or acquired from the modulated version of the experiment, analogous to the modulated reflectance considered further in this chapter), not restricted by assumptions of the electronic band shape. The approach is commonly employed in spectroscopic ellipsometry, as it allows to better visualize the critical points of the dielectric function.[133,134]

An experimental setup allowing to measure the light transmission is presented in Fig. 1.10. The sample, mounted on a transparent or holey holder enabling light transmission, is illuminated by radiation from a white light source (here, a tungsten halogen lamp), dispersed by a monochromator. The transmitted portion of the incident light is focused on a photodetector. Modulating the signal by a mechanical chopper and coupling it with a lock-in amplifier allows improving the sensitivity of the method. Additionally, for low-temperature or temperature-resolved measurements, the sample is placed in a cryostat.

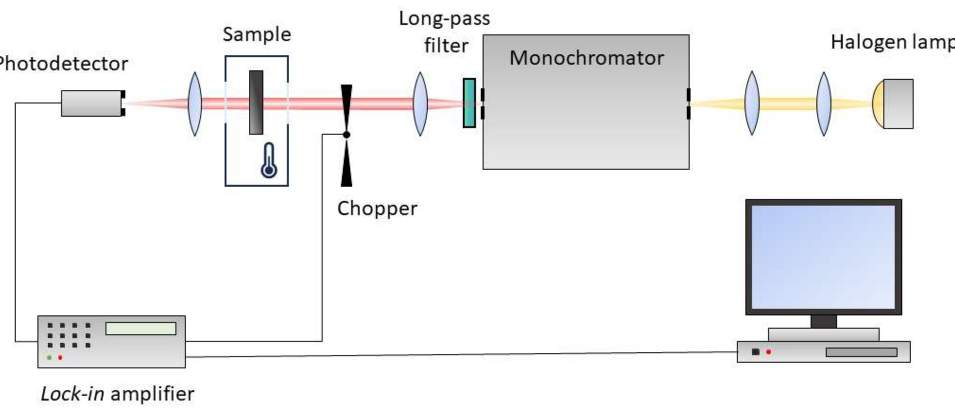

Fig. 1.10 Experimental setup for optical absorption measurements.

Modulated reflectance

Modulated reflectance is one of the methods of modulation spectroscopy, suitable for investigating the optical properties of a material by externally inducing periodic perturbation of the dielectric function and measuring its changes.[131] The differential character is one of the strongest advantages of modulation spectroscopy, as it ensures high sensitivity. The dielectric function is

generally composed of broad, slowly varying regions with superimposed rather weak but sharp features at the energies of van Hove critical points (corresponding to the joint density of states singularities). Therefore, it is often more convenient to analyze the derivatives of the spectra, in which rapid changes are enhanced over a locally monotonous background. The reflectance R of a material can be related to the perturbation of the dielectric function ε by a linearized formula

$$\frac{\Delta R}{R} = \beta_r \Delta\varepsilon_r + \beta_i \Delta\varepsilon_i, \tag{7}$$

where $\beta_r = \frac{\partial \ln R}{\partial \varepsilon_r}$ and $\beta_i = \frac{\partial \ln}{\partial \varepsilon_i}$ are the Seraphin coefficients,[135,136] ε_r and ε_i are the real and imaginary parts of the dielectric function, respectively, and $\Delta\varepsilon_r$ and $\Delta\varepsilon_i$ are their changes. Considering the spectral dependence of the Seraphin coefficients, close to the fundamental absorption edge β_i is negligible, which simplifies the analysis to only considering $\Delta\varepsilon_r$. The approximation is usually sufficient, although if needed the Kramers-Kronig relations can be used to connect the real and imaginary parts.[137]

The modulation of the dielectric function, and consequently the reflectance, can be achieved by influencing the sample temperature, internal strain, or applying an alternating electric field. Dependently on the modulated factor, different variants of the method can be distinguished, including thermoreflectance (TR), piezoreflectance (PzR), electroreflectance (ER) or its contactless modification (CER), and photoreflectance (PR). In principle, as demonstrated in Fig. 1.11, using the example of PR, the sample with applied external modulation is simultaneously illuminated by white light (or monochromatic portion of a spectrally broad source), and the reflected signal is collected. The use of a phase-sensitive lock-in amplifier allows separation of the constant component (not sensitive to the perturbation, also containing the characteristic response of the experimental setup) and varying component (reproducing the influence of the modulation). The ratio of the two components determines the relative change of the reflection coefficient, dependent only on the investigated structure properties.

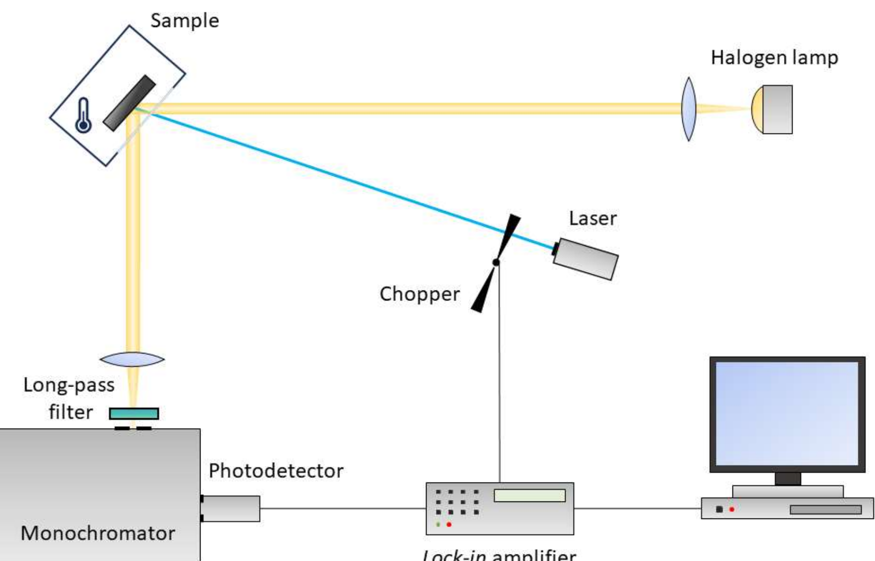

Fig. 1.11 Experimental setup for PR measurements.

In this work, the PR is employed to characterize MX and MX_2 crystals. In this variation of the modulated reflectance, periodic excitation of the sample with a mechanically chopped laser beam is applied. The technique is commonly qualified as a variant of electromodulation, however, it may also induce changes in the sample temperature, resulting in thermomodulation. Both processes are schematically illustrated in Fig. 1.12a,b. The former occurs in the presence of a built-in electric field in the structure, which is usually observed for covalent crystals and heterostructures. At the sample surface the translational symmetry is broken, as the boundary atoms lack further neighbors to bond with. As a consequence, there are so-called *dangling bonds* left, which need to be passivated by foreign atoms or in the process of surface reconstruction. Either way, additional electronic states form, typically within the band gap, which can be partly occupied by carriers. Then, at the crystal surface, the Fermi level is pinned at a different energy than in the bulk, which leads to bending of the electronic bands and induces the electric field. The field can be further influenced by the photovoltaic effect, as demonstrated in Fig. 1.12b. Under illumination, photogenerated electron-hole pairs are spatially separated by the electric field and modify it further. When the excitation is turned off, the carriers recombine and the electric field returns to its initial state. Unlike covalent materials, van der Waals crystals do not undergo surface reconstruction, therefore the non-uniform distribution of the electrical potential can only be related to some external impurities or oxidation of the surface layers, which is a rather weak effect. Hence, the thermomodulation mechanism dominates, in which the sample temperature is temporarily increased, as photogenerated carries thermalize to the lowest excited states, and the energy is dissipated as heat (Fig. 1.12.a). Both effects provide similar information, but the procedure of the analysis of the spectra differs. Thermomodulation is an isotropic effect, preserving the translational invariance in the structure, and influencing the dielectric function by slightly reducing the band gap when the sample is heated. Then, the relative changes in the reflectance spectra observed as a form of a resonance can be approximated by the first derivative of the Lorenzian line-shape, given by

$$\frac{\Delta R}{R}(h\nu) = Re\left(\sum_j C_j e^{i\phi_j}\left(h\nu - E_j + i\Gamma_j\right)^{-m}\right), \tag{8}$$

where C_j is the j-th resonance amplitude, ϕ_j is the phase, E_j is the optical transition energy, and Γ is the lifetime broadening. The parameter $m = 2$ for the first derivative analysis. The summation over j applies when more than one optical transitions occur within a narrow spectral range. Unlike the temperature, the built-in electric field is directional and affects the dielectric function by accelerating the charge carriers. It was shown by Aspnes,[138] that in the case of electromodulation the changes follows the third derivative line-shape. The influence of thermo- and electromodulation on the dielectric function is presented in Fig. 12 c and d, respectively.

Nevertheless, under the assumption of the parabolic band dispersion Eq. 8 can be used, with the value of the m parameter chosen depending on the critical point dimensionality (2.5 for 3D, 3 for 2D, and 3.5 for 1D) or the transition character (2 for excitonic transitions). Hence, in practice, for the analysis of the PR spectra, prior assessment of whether thermo- or electromodulation effects dominate is not critical, especially when the parameter of interest is mainly the optical transition

energy. It should be noted that the procedure described above is applicable under the conditions of a weak electric field, while beyond this regime, some additional effects emerge, such as Franz-Keldysh oscillations.[131] Since for pristine van der Waals crystals the built-in electric field is rather insignificant, the cases of intermediate and strong fields will not be discussed in this work.

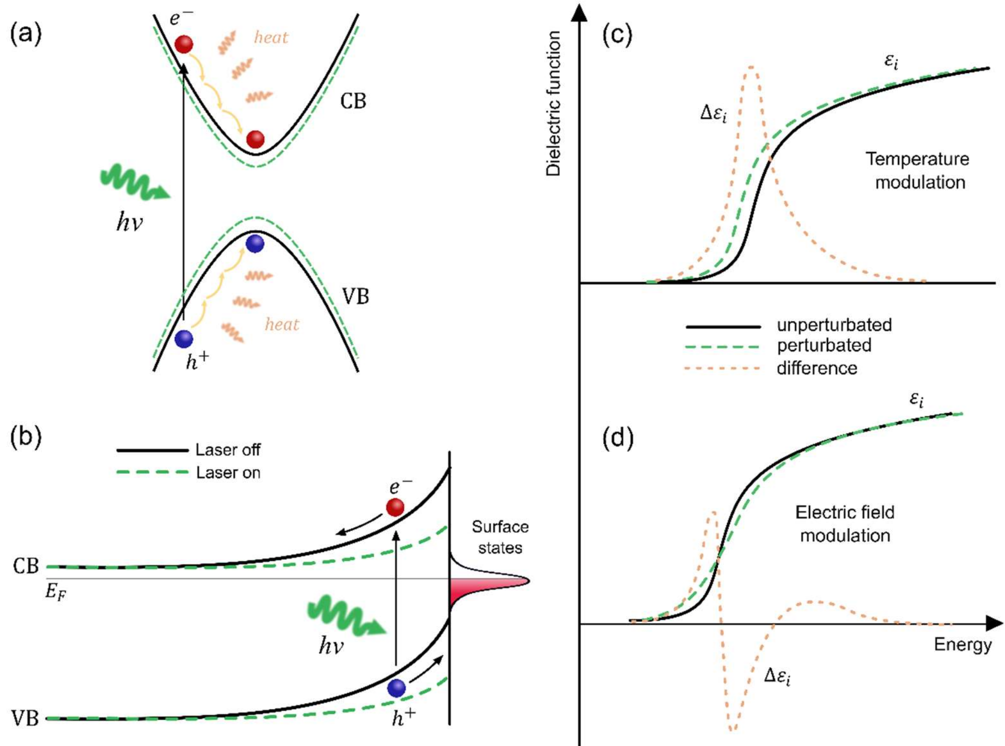

Fig. 1.12 Two mechanisms of dielectric function modulation by periodic excitation with a laser beam in PR technique: (a) increase of the sample temperature in the process of excited carriers thermalization from higher states to the bottom of CB and top of VB, and (b) reduction of the built-in electric field, compensated by spatial separation of photogenerated electron-hole pairs, on the example of *n*-type material. The influence of the effects of (c) thermomodulation and (d) electromodulation on the imaginary part of the dielectric function, illustrating expected shapes of differential spectra.

An experimental setup for PR measurements is proposed in Fig. 1.11. The tungsten halogen lamp is exploited as the white light source, and the mechanically chopped laser beam is used for sample excitation. In the figure a so-called *bright configuration* is presented, in which the sample is illuminated with white light, and the reflected signal is dispersed by a monochromator before being detected. The experiment can also be carried out in a *dark configuration*, analogous to the optical setup for absorption measurement illustrated in Fig. 1.10, where monochromatized light of wavelength scanned across the spectral range of interest is used as the probe beam.

Raman scattering

Raman scattering spectroscopy is an experimental technique exploiting inelastic scattering of light as a source of information about the structure and composition of the investigated materials. When the sample is illuminated, most of the light is scattered elastically (Rayleigh scattering), but a small

fraction interacts with the vibrational levels of the molecules in a process of inelastic (Raman) scattering, resulting in a slight increase (Stokes lines) or decrease (anti-Stokes lines) of the photon energy, as shown in a diagram in Fig. 1.13a. The energy difference between the incident and scattered light corresponds to the energy of vibrational (or rotational) modes of the molecules, which are compound-specific. Therefore, Raman spectroscopy can be treated as a fingerprint method, allowing identification of chemical substances by revealing the presence of specific functional groups, chemical bonds, and molecular structures. In solid-state physics, Raman spectroscopy is used to study phonons (quantized crystal lattice vibrations), which can provide insight into the crystallographic structure, phase, and lattice defects in materials. The activity of Raman modes depends on the crystal symmetry, and their frequency on the lattice parameters and chemical composition. It is also worth noting that only optical phonon modes can be investigated using this technique, due to the momentum conservation principle. Since the momentum of a photon is negligible compared to the momentum of an oscillating atom, light can only interact with phonons possessing non-zero energy at zero momentum, which is fulfilled for optical phonons, as shown in Fig. 1.13b. To study acoustic modes, different methods need to be employed, such as Brillouin light scattering and neutron scattering.

An experimental setup for Raman scattering measurements is schematically presented in Fig. 1.14. A monochromatic light source (here, a continuous wave laser) is focused on the sample surface by an objective lens, utilized also for the scattered light collection. The signal beam travels through a sharp cut-off optical filter, eliminating the elastically scattered light from the spectrum, and is introduced into the detection system, composed of a high-resolution monochromator and a CCD camera able to resolve the Raman lines.

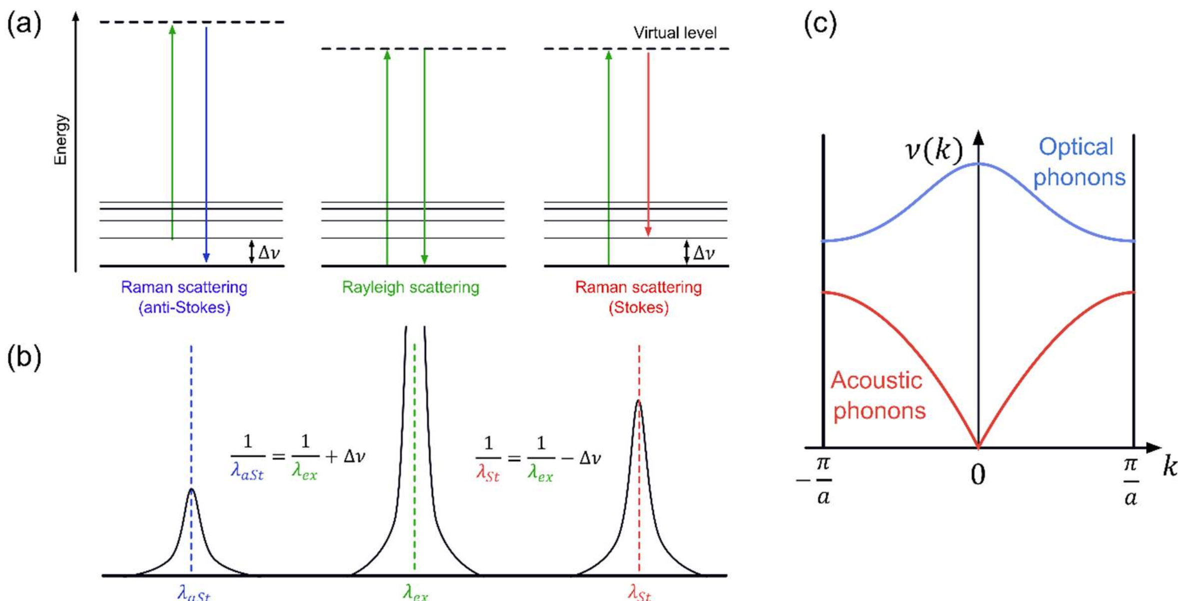

Fig. 1.13 Illustration of processes of elastic (Rayleigh) and inelastic (Raman) scattering (a) resulting Raman spectrum, including Rayleigh, Stokes and anti-Stokes lines (b), and phonon dispersion diagram, visualizing optical and acoustic branches (c).

Photoluminescence

Photoluminescence (PL) spectroscopy is used to investigate the radiative recombination processes. In principle, the sample is illuminated by monochromatic light (usually a laser beam) of energy equal to (resonant excitation) or exceeding (non-resonant excitation) the characteristic energy of the system. Typically, such energy is the band gap, but depending on the investigated structure, it may also be an impurity level, exciton energy, or generally any difference between discrete electronic states. The incident photons generate electron-hole pairs, which then thermalize (in the case of non-resonant excitation) and recombine. In radiative recombination, the energy is emitted in the form of photons, which can be detected, providing information about electronic states. The phenomenon is typical for direct band gap semiconductors, while for indirect band gap, non-radiative processes dominate. To preserve the momentum, additional particles, such as phonons, need to participate in the process, which severely deteriorates the probability of radiative recombination. For this reason, photoluminescence emission is not observed for the majority of indirect gap materials, allowing to preliminarily determine the band gap character. Nevertheless, the result may sometimes be misleading, as weak emission from indirect band gap or higher levels in the case of optical pumping (filling the lower states by high-intensity incident light) can sometimes be observed. On the other hand, in direct band gap semiconductors different mechanisms of photoluminescence quenching can be present, such as charge and energy transfer between electronic bands and impurities-related states. In this regard, additional signal can sometimes be detected in the PL spectra originating from the transitions between bands and defect levels within the band gap (or between different defect levels). Such emission is generally easy to distinguish from band-to-band and excitonic transitions, as the measured line often has significant spectral broadening and its intensity (I) varies with the excitation power (P_{ex}), following the relation $I \sim P_{ex}^{k}$, with the parameter $k < 1$. For excitonic and band-to-band emission k assumes values approximately equal or greater than 1, respectively.[139]

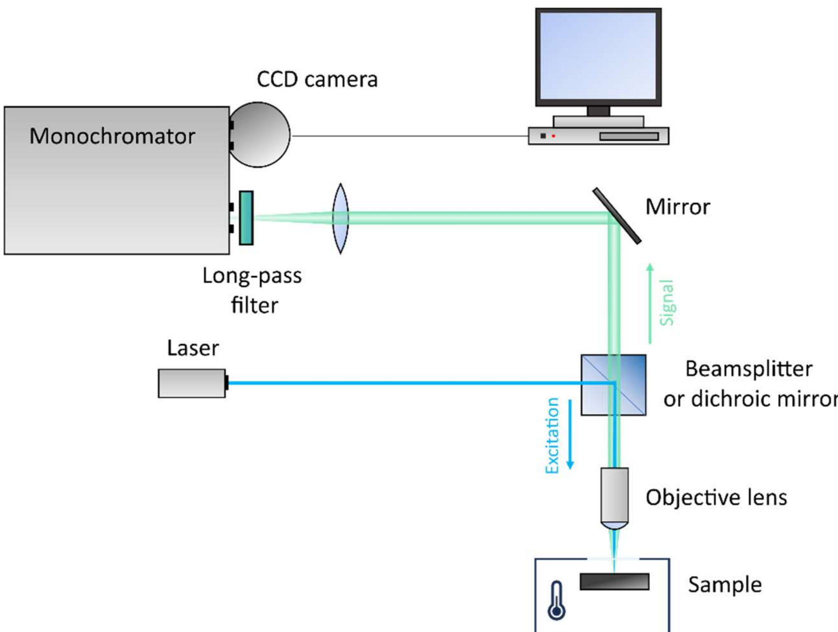

Fig. 1.14 Experimental setup for Raman scattering and μPL measurements.

In this work, PL spectroscopy was exploited for the investigation of defect-related emission in SnS_2 crystals, as for other materials no emission was observed. An example of an experimental setup is presented in Fig. 1.14, also used for Raman scattering measurements. The diagram illustrates microscopic configuration, allowing to detect signal from μm-size samples.

Polarization-resolved measurements

In order to investigate the anisotropy of the optical properties of van der Waals crystals the experimental methods described above were applied in a polarization-resolved configuration. The modifications of the experimental setups for optical absorption (Fig. 1.10) and photoreflectance (Fig. 1.12) involved placing additional elements in the optical axis: a Glan-Taylor polarizer to acquire linear polarization of the probing light, and a half-wave plate to rotate the polarization angle.

1.3.2 Photoemission spectroscopy

Photoemission spectroscopy (PES) is a technique exploiting the photoelectric effect to investigate the electronic structure of a material. By illuminating the sample with high-energy radiation (from the UV or X-ray region of the electromagnetic spectrum), the electrons are ejected from its surface. Their kinetic energy E_{kin} depends on the excitation energy and specific energies of the material as given by the formula

$$E_{kin} = h\nu - \varphi - E_b, \quad (9)$$

where φ is the work function (i.e., the position of the Fermi level with respect to vacuum energy), and E_b is the binding energy of the ejected electron. The photoemission process is schematically illustrated in Fig. 1.15a.

Depending on the energy regime, different variants of PES are distinguished, allowing to probe a broad range of electronic states of a material. UV photoemission spectroscopy (UPS) is typically used to examine the valence band states, at energies up to 20 eV. It can be used to visualize the valence band density of states and even, to some extent, investigate the orbital composition. In addition, fundamental electronic properties such as the work function, ionization energy, and electron affinity (if the energy gap is known) can be determined. X-ray photoemission spectroscopy (XPS) probes core-level states at higher binding energies. As a fingerprint method, it provides information about the elemental composition of the measured structure, but also its stoichiometry and chemical environment, as the position of the core-level orbital lines vary slightly depending on the oxidation state. A more advanced modification of the method is the angle-resolved photoemission spectroscopy (ARPES), enabling the observation of the valence band dispersion in the wavevector space, based on the fact that the electron momentum in-plane component is preserved in the photoemission process. All these methods require ultra-high vacuum conditions, specialized electron optics, and a hemispherical detector, suitable for resolving the emitted photoelectrons kinetic energies (by curving their trajectory in the magnetic field), as illustrated in Fig. 1.15b.

The choice of the excitation energy, besides determining the probing depth, has other implications. The photoemission intensity depends on the photoionization cross-section, varying for different orbitals and incident radiation energies. Generally, with increasing excitation energy, the photoionization cross-section decreases. Also, valence orbitals are characterized by smaller cross-

sections compared to core states. These tendencies make the high-energy XPS technique less optimal for measurements of the valence band (the photoemission intensity from this region is low), even though it is within the probed range. In the case of ARPES measurements the excitation energy also plays one more critical role. As mentioned, in the photoemission the in-plane component of the electron momentum is preserved, however the condition is not fulfilled for the out-of-plane component due to interaction with the surface atoms. Therefore, when examining a 3D crystal, the probed plane of the reciprocal space cannot be directly determined. In other words, considering the first Brillouin zone, the probed states do not necessarily belong to the central plane (containing the Γ point) or other plane of interest. In fact, in the ARPES maps several k_z states are projected onto the measured plane, forming so-called reduced 2D BZ. By varying the excitation energy, different regions along the k_z direction can be observed, visualizing the out-of-plane valence band dispersion. Van der Waals crystals are often characterized by weak dispersion in the k_z direction, although for multilayer structures it depends on the strength of the interlayer interaction and should not be neglected.

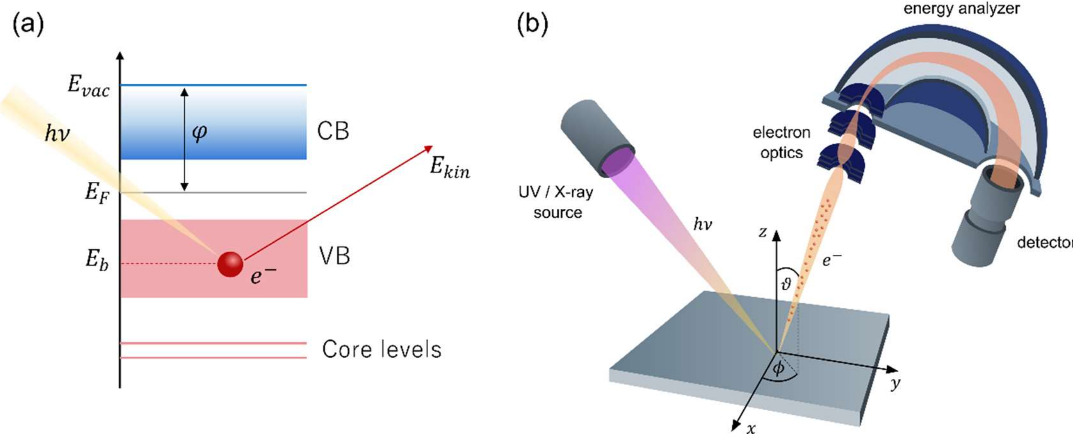

Fig. 1.15 Schematic illustration (a) of the photoemission process and (b) of the experimental procedure. The electrons are ejected from the sample surface at an angle corresponding to their in-plane momentum. The hemispherical analyzer allows to resolve the kinetic energy of electrons by curving their trajectory in the magnetic field.

Two modifications of PES, two-photon photoemission spectroscopy (2PPE) and inverse photoemission spectroscopy (IPS), are also worth mentioning, as they provide the possibility to investigate the unoccupied electronic states (above the Fermi level), and hence, being complementary to PES. The former is a time-resolved method, using a pumping laser pulse to excite the electrons to populate the energetically higher states, and a secondary pulse to eject them from the sample. Usually, the pumping beam energy is within the visible spectral range, and the probing radiation belongs to the UV range, sufficient for photoionization. Both wavelengths can be obtained by exploiting different harmonics of a femtosecond laser. The photoelectrons are analyzed in the same configuration as in PES. In the IPS technique, the sample is exposed to a beam of electrons, which couple to high-energy unoccupied states and decay to lower unoccupied states. In the process, electromagnetic radiation is emitted, providing information about the energy difference between involved levels.

In this work, three variants of PES were used to investigate the electronic structure of IV-VI monochalcogenides, as reported in Chapters 4 and 5.

CHAPTER 2

Optical properties of orthorhombic germanium selenide: an anisotropic layered semiconductor promising for optoelectronic applications

Agata K. Tołłoczko, Szymon J. Zelewski, Michał Błaszczak, Tomasz Woźniak, Anna Siudzińska, Alicja Bachmatiuk, Paweł Scharoch, Robert Kudrawiec

Journal of Materials Chemistry C, **9**, 14838 (2021)

Overview

The optical properties of GeSe were investigated by means of polarization-resolved optical absorption and photoreflectance measurements, supported by DFT calculations of the electronic band structure. The study revealed strong anisotropy and domination of the optical properties by direct transitions, despite the indirect character of the fundamental band gap. Additionally, the photoconversion performance of a simple Schottky-junction Ag/GeSe photodetector was characterized, showing promise for polarization-sensitive light detection applications.

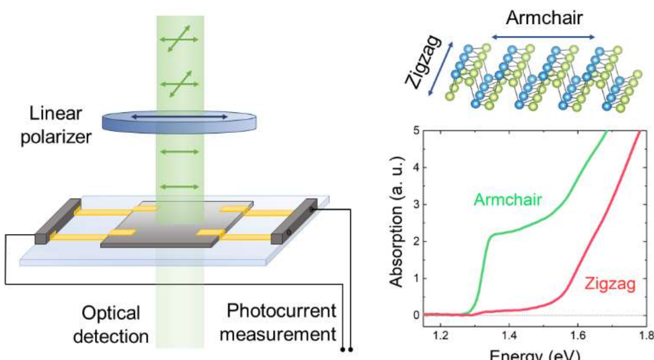

Fig. 2.1 Graphical abstract. Reprinted from Ref. [7] under CC-BY 4.0 license. Copyright 2021 A. K. Tołłoczko *et al.*

Author's contribution

Agata K. Tołłoczko (corresponding author) performed all the experimental investigation involving optical spectroscopy (PR, optical absorption, and Raman scattering) and electrical measurements of the photogenerated current, processed and analyzed the acquired data, prepared their graphical presentation, and wrote the manuscript.

Journal of
Materials Chemistry C

PAPER

View Article Online
View Journal | View Issue

Cite this: *J. Mater. Chem. C*, 2021, 9, 14838

Optical properties of orthorhombic germanium selenide: an anisotropic layered semiconductor promising for optoelectronic applications†

Agata Tołłoczko, *[a] Szymon J. Zelewski, [a] Michał Błaszczak,[a] Tomasz Woźniak, [a] Anna Siudzińska,[b] Alicja Bachmatiuk,[b] Paweł Scharoch[a] and Robert Kudrawiec[ab]

Received 8th September 2021,
Accepted 28th September 2021

DOI: 10.1039/d1tc04280g

rsc.li/materials-c

Group-IV monochalcogenides, such as germanium selenide (GeSe), are strongly anisotropic semiconducting van der Waals crystals isoelectronic to black phosphorus, with superior stability in air conditions. High optical absorption, good conductivity, and band gap ranging from 1 to 2 eV make these materials suitable for various optoelectronic applications; however more in-depth investigation of their fundamental properties is required. We present a comprehensive study of bulk GeSe by means of optical absorption and modulation spectroscopy, supported by theoretical density functional theory (DFT) calculations of the electronic band structure. Our experimental results reveal that the optical properties of GeSe are dominated by direct transitions; however the fundamental band gap might in fact be indirect and could not be observed in the experiment due to low oscillator strength. Such interpretation is in agreement with our calculations, providing the picture of the first Brillouin zone with multiple band extrema in close energy proximity. In order to investigate the anisotropy of the material, polarization-resolved measurements have been performed, revealing a strong dependence of the observed optical transitions on light polarization. Photogenerated current measurements resulted in reasonably high photoconversion efficiency and fast response time, implying that GeSe is a promising material for photoconversion applications.

Open Access Article. Published on 28 September 2021. Downloaded on 1/4/2024 1:07:00 PM.
This article is licensed under a Creative Commons Attribution 3.0 Unported Licence.

Introduction

Since the interest in two-dimensional (2D) materials and heterostructures has been boosted by the first successful exfoliation of atomically thin graphite flake, graphene,[1,2] a variety of other layered van der Waals crystals have been rediscovered as potentially more suitable for certain applications than semimetallic graphene. One of them is black phosphorus (BP), a promising direct band gap semiconducting material, which in analogy to graphene is called phosphorene in its monolayer form. BP is known to fill the gap between graphene and transition metal dichalcogenides (TMDs) – it combines open energy gap, characteristic for TMDs, with excellent conductivity, nearly comparable to graphene.[3–5] Unfortunately, despite being the most stable phosphorus allotrope, BP is prone to oxidation in air conditions, which severely limits its applications.[6,7]

Group IV monochalcogenides (MX, where M is a group IV element, such as Ge, Sn or Pb, and X is a chalcogen atom, such as S, Se, or Te) are a family of van der Waals crystals isoelectronic to black phosphorus, which are also known as phosphorene analogues,[2,8] as they share the most important features, but exhibit superior stability. MXs are semiconductors with an orthorhombic crystal structure (space group *Pcmn*). Atomic arrangement along main in-plane crystallographic directions is strongly anisotropic, which affects the material's fundamental properties.[9–14] An open band gap tunable from the near infrared to visible spectral range, high carrier mobility, and strong optical absorption make MXs perfect candidates for application in two-dimensional optoelectronics (photovoltaics, light detectors and emitters).[15–19] They do, however, exhibit other properties that can be exploited in different areas of technology, such as nonlinear optics,[20–23] transistors,[24,25] piezotronics,[26–28] multiferroics-based devices,[29–32] or photocatalytic water splitting.[33–36]

Germanium selenide (GeSe) has attracted the particular interest of researchers focused on photovoltaics.[15,16,37–40] The material exhibits low toxicity and is composed of earth-abundant elements. In its bulk form, the band gap of GeSe is

[a] *Department of Semiconductor Materials Engineering, Wrocław University of Science and Technology, Wybrzeże Wyspiańskiego 27, 50-370 Wrocław, Poland. E-mail: agata.tolloczko@pwr.edu.pl*
[b] *Łukasiewicz Research Network – PORT Polish Center for Technology Development, Stabłowicka 147, Wrocław, Poland*

† Electronic supplementary information (ESI) available. See DOI: 10.1039/d1tc04280g

This journal is © The Royal Society of Chemistry 2021

Open Access Article. Published on 28 September 2021. Downloaded on 1/4/2024 1:07:00 PM.
This article is licensed under a Creative Commons Attribution 3.0 Unported Licence.

most often reported between 1.1 and 1.3 eV (dependent on the experimental or theoretical method), which is close to the optimal value for maximum photoelectric conversion, according to the Shockley–Queisser detailed balance limit.[41] Moreover, it is possible to combine GeSe with other van der Waals crystals, especially group IV mono- and dichalcogenides, to form heterostructures,[42–45] which can be exploited as p–n-like junctions, due to relative band offsets,[46] or in the construction of tandem solar cells. With the selenium-rich analogue of GeSe, $GeSe_2$,[47,48] such heterostructure can be grown in one reaction chamber using the same precursors but by adjusting only the stoichiometric ratio, which allows the avoidance of impurities and unintentional doping, as reported for the $SnSe/SnSe_2$ heterostructure.[49] The CVD technique can also be exploited, which is important for large-scale device integration.

To date, there are a lot of discrepancies in the literature concerning the optical and electronic properties of GeSe, particularly the character and exact width of the fundamental band gap, crucial for the design of any semiconducting device. Based on the experimental investigation of the optical activity in GeSe, the majority of authors report an indirect fundamental band gap of ~1.2 eV at room temperature.[50–53] However, there are also reports of a direct band gap at slightly higher energies.[37] The reason for numerous various interpretations can be found in the electronic band structure, featuring flat bands and multiple band extrema within close energy proximity, characteristic of the whole MX family.[8,15,46] Unfortunately, density functional theory (DFT) calculations do not provide the unambiguous answer as well, as the width of the fundamental band gap of GeSe and its position in the Brillouin zone (BZ) are sensitive to lattice parameters and the computation method in general.[8,37,50,54,55]

In this work we present a comprehensive study of GeSe focused on its optical properties, anisotropy, and photoelectric conversion efficiency. The samples were characterized by high resolution transmission electron microscopy (HRTEM), selected area electron diffraction (SAED), electron energy loss spectroscopy (EELS), and Raman spectroscopy. The optical properties of GeSe were investigated using polarization- and temperature-resolved optical absorption and photoreflectance (PR), one of the methods of modulation spectroscopy. Optical absorption reveals the fundamental band gap of the material (either direct or indirect), while PR allows observation of energetically higher features, but it is only sensitive to direct optical transitions. Therefore, the two methods are considered complementary. *Ab initio* calculations of the electronic band structure have been performed to support experimental results and enable assignation of the measured optical transitions to certain BZ points. Eventually, the photoelectric conversion efficiency of a simple GeSe zero-bias photodetector has been studied, by means of photogenerated current measurements.

Results and discussion

Germanium selenide crystallizes in the orthorhombic phase (*Pcmn*), schematically presented in Fig. 1a. The lattice constants

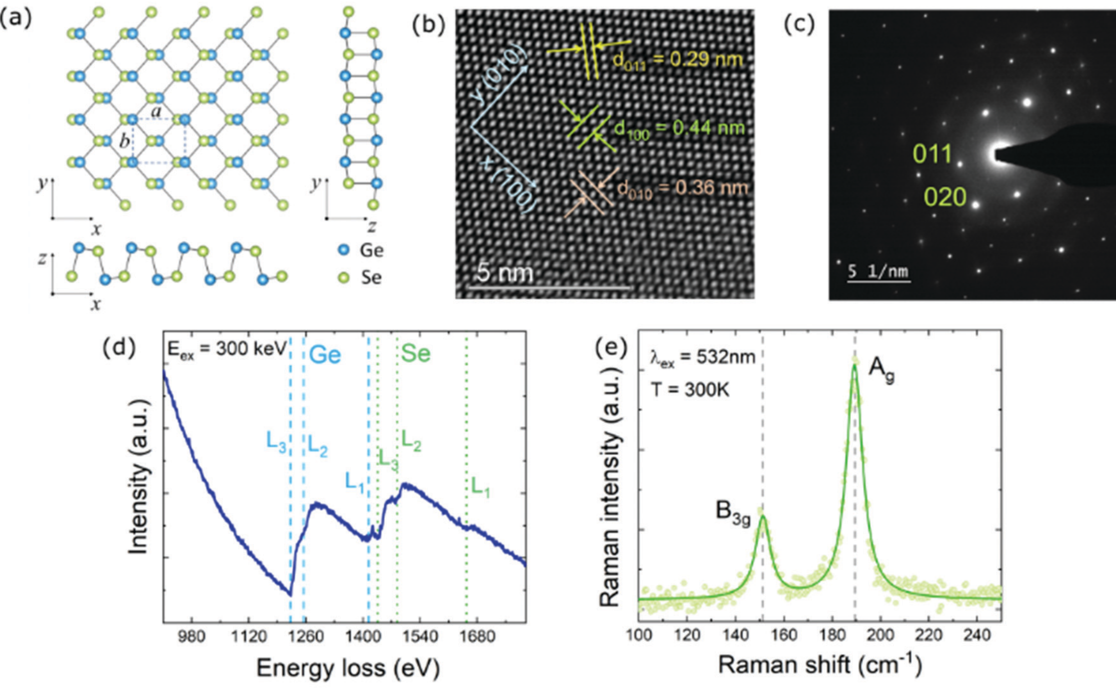

Fig. 1 (a) Schematic illustration of the GeSe orthorhombic crystal structure and atomic arrangement along main in-plane directions (armchair and zigzag), (b) HRTEM image of the GeSe flake with crystallographic directions and spacings between crystal planes marked, (c) SAED pattern with labeled reflexes corresponding to certain crystal planes, (d) EELS spectrum with labeled edges related to Ge and Se atoms, and (e) Raman scattering spectrum, acquired for a bulk GeSe sample with the excitation of a 532 nm laser beam, at room temperature.

Open Access Article. Published on 28 September 2021. Downloaded on 1/4/2024 1:07:00 PM.
This article is licensed under a Creative Commons Attribution 3.0 Unported Licence.

are a = 0.444 nm, b = 0.386 nm, and c = 1.081 nm,[56] where a and b are in-plane unit cell dimensions, and c is the lattice parameter perpendicular to the layer plane. DFT calculations yield a = 0.442 nm, b = 0.389 nm, and c = 1.092 nm, in excellent agreement with measured values. The atomic structure within a single layer is anisotropic. In the x (100) direction, called armchair, the layer is puckered, while in the orthogonal y (010) direction, called zigzag, the atoms are arranged in a ladder-like pattern. As can be seen in the HRTEM image and the SAED pattern presented in Fig. 1b and c, respectively, the investigated sample exhibits high crystallinity. In the HRTEM image the atomic sites are clearly visible, and an arrangement characteristic of the orthorhombic phase can be observed. The spacings between crystal planes in (100), (010), and (110) directions are 0.44, 0.36, and 0.29 nm, respectively. The atomic composition of the sample was determined by EELS measurements (Fig. 1c). In the obtained spectrum edges related to Ge and Se can be distinguished. The positions of the observed L–Ge edges, along with L–Se edges, are in perfect agreement with reference values.[57] The exact energies are listed in Table S1 of the ESI.† No other significant EELS features have been observed, indicating a low level of impurities in the crystal structure. In the Raman scattering spectrum (Fig. 1f) two peaks at frequencies of 152 cm^{-1} (19 meV) and 189 cm^{-1} (23 meV) are clearly visible. These modes can be assigned to B_{3g} and A_g symmetries, corresponding to in-plane shear vibrations of adjacent layers in the y and x directions, respectively.[58] Two other Raman peaks at frequencies of 81 and 176 cm^{-1} are often reported,[59,60] but have not been observed in our measurements.

Experimental investigations of the optical properties of GeSe reported in the literature exploit mostly optical absorption measurements, and the results are commonly perceived as the evidence of the indirect fundamental band gap between 1.10 and 1.25 eV (at room temperature).[50–53] Such interpretation is supported by the lack of photoluminescence emission from bulk GeSe, although other mechanisms may be responsible for photoluminescence quenching, such as intrinsic defects, creating paths of nonradiative recombination. However, Murgatroyd *et al.*[37] claim that the low-energy region of the absorption coefficient spectrum, previously attributed to the fundamental band-gap, in fact originates from defect-related absorption. The actual absorption edge occurs at ~1.3 eV, and above this energy the absorption coefficient spectrum is dominated by direct optical transitions due to higher oscillator strength. Nevertheless, the authors do not negate the presence of energetically close indirect transitions or state the character of the fundamental band-gap.

In our research, in order to experimentally verify the band gap nature of GeSe, along with optical absorption a complementary spectroscopic method, photoreflectance, was exploited. In Fig. 2, photoreflectance and optical absorption spectra collected at 20 K (panel a) and 300 K (panel b) are presented. The shaded areas correspond to moduli of observed PR resonances. Low-temperature PR spectra exhibit three strong optical transitions, namely E_1, E_2, and E_3. At room temperature only two closely lying transitions can be distinguished. The step-like shape of the absorption curve also indicates the contribution of

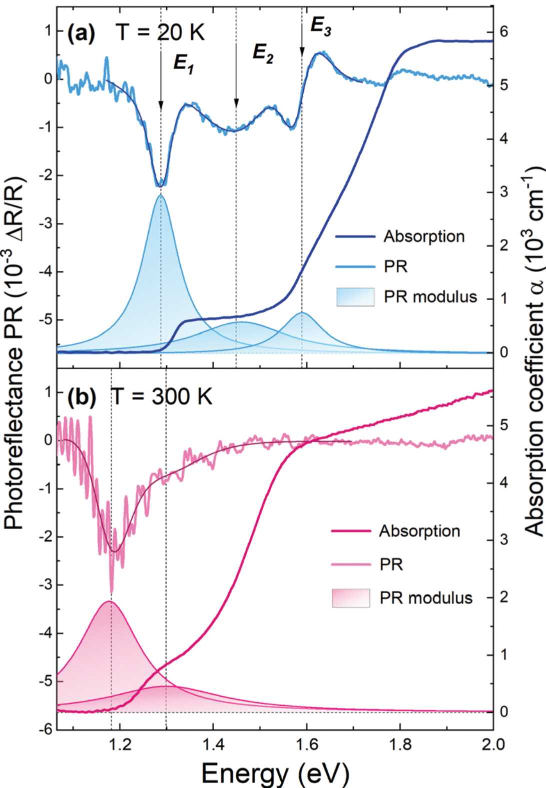

Fig. 2 Photoreflectance and optical absorption spectra of GeSe obtained at a temperature of 20 K (a) and 300 K (b), with assigned optical transitions. The darker solid lines over the PR plots are the curves fitted with the Aspnes formula (eqn (1)), and the colored areas beneath are the PR resonance moduli, calculated using eqn (2).

multiple optical transitions. The sharp rise of the absorption coefficient at an energy of ~1.3 eV at 20 K and ~1.2 eV at 300 K coincides with the energetically lowest PR resonance. Since photoreflectance is a method sensitive only to direct transitions, such agreement suggests the direct character of the band-gap of GeSe, or that a weak absorption edge from the fundamental indirect band-gap is predominated by a stronger signal from closely lying direct optical transition.

The exact energies of the observed PR resonances were determined by fitting the Aspnes formula[61] to experimental data,

$$\frac{\Delta R}{R}(\hbar\omega) = \mathrm{Re}\left(\sum C_i e^{i\varphi_i}(\hbar\omega - E_i + i\Gamma_i)^{-m}\right), \qquad (1)$$

where C_i is the amplitude of the i-th PR resonance, φ_i is the phase, Γ_i is the broadening and E_i is the energy. The parameter m is related to the type of the transition and is equal to 2 for excitonic and 2.5 for band-to-band transitions. The choice of the m parameter value does not affect the energy of the resonance, and therefore m = 2 was assumed as a good approximation, provided that van der Waals crystals often exhibit high exciton binding energies, even in the bulk form. Nevertheless, in the case of GeSe, the character of observed optical transitions may not be excitonic and need to be further investigated. Fitted curves are shown in the figure as smooth solid lines over the PR spectra. The energies of the transitions are as follows: E_1 = 1.29 eV,

This journal is © The Royal Society of Chemistry 2021

Open Access Article. Published on 28 September 2021. Downloaded on 1/4/2024 1:07:00 PM.
This article is licensed under a Creative Commons Attribution 3.0 Unported Licence.

E_2 = 1.52 eV, E_3 = 1.58 eV at 20 K, and E_1 = 1.21 eV, E_2 = 1.30 eV at 300 K. The uncertainties of the determined values are ~0.01 eV for E_1 and E_3, and ~0.05 eV for E_2. The PR resonance moduli (shaded areas under PR spectra in Fig. 2) were calculated from the equation

$$\Delta\rho_i(E) = \frac{|C_i|}{\left((E - E_i)^2 + \Gamma_i^2\right)^{\frac{m}{2}}}. \tag{2}$$

The area under the modulus curve, given by $A_i = \pi|C_i|/\Gamma_i$, is proportional to the transition oscillator strength.

In order to further investigate the influence of temperature on optical properties of GeSe, both PR and optical absorption were measured at different temperatures, covering the range from 20 up to 300 K. The results are presented in Fig. 3 (in panels a and b every second measured spectrum is plotted for clarity). The temperature dependence of PR (Fig. 3a) reveals that the energetically highest transition E_3, narrow and well defined at 20 K, diminishes rapidly with increasing temperature, to vanish completely at 100–120 K. Such a shape and behaviour suggest excitonic transition and allows one to estimate an exciton binding energy of 10 meV; however other factors can affect the transition strength (such as slightly band-nesting character of the transition, which will be discussed later) and the exciton binding energy may actually be higher. Above 120 K E_3 could still be optically active as a weaker band-to-band transition, with intensity below the detection threshold. Transitions E_1 and E_2 are still visible at room temperature, although due to increased broadening and a significantly larger E_2 temperature coefficient (see Fig. 3c), they blend together and become hard to distinguish.

In the absorption spectra (Fig. 3b) two sharp edges are visible. The energies of the edges were determined from extrapolation of linear approximation of a Tauc plot for direct allowed optical transitions ($(\alpha h\nu)^2$ *vs.* $h\nu$)[62] (see Fig. S1 in ESI†). Both values and temperature dependence of lower and higher absorption edge energies are in good agreement with transitions E_1 and E_3 observed in photoreflectance, as can be seen in Fig. 3c. The reason why E_3 is visible in absorption spectra throughout the whole temperature range may be due to the fact that only the signal from the band-to-band component was detected (no characteristic excitonic features are present in the absorption spectra). The same phenomenon could be responsible for the shift between E_1 energies determined from PR and absorption (however only at low temperatures; above 180 K the uncertainty of the PR resonance energy increases rapidly due to noise and proximity of E_2).

The temperature dependencies of each transition energy were approximated by Bose–Einstein[63] (solid lines in Fig. 3c) and Varshni[64] (not shown in the figure) formulas. The B–E approximation is derived from the Bose–Einstein distribution and is defined as

$$E(T) = E(0) - \frac{2a_B}{\exp\left(\frac{\theta_B}{T}\right) - 1}, \tag{3}$$

where $E(0)$ is the energy at a temperature of 0 K, a_B is the strength of the electron–phonon interaction, and θ_B is the average phonon temperature. The Varshni formula is semi-empirical and is given by

$$E(T) = E(0) - \frac{\alpha T^2}{\beta + T}, \tag{4}$$

where α and β are the Varshni coefficients.

The Varshni equation is commonly used for temperature dependence approximation; however the parameters in the formula have no direct physical interpretation and can only be used for empirical comparison. On the other hand, the B–E formula includes parameters that are dependent on material properties and follow the low-temperature experimental data with better accuracy. The fitting parameters from both methods are listed in Table 1. It is worth noting that the average phonon temperature between 202 and 205 K, corresponding to a thermal energy of 18 meV, coincides perfectly with the first

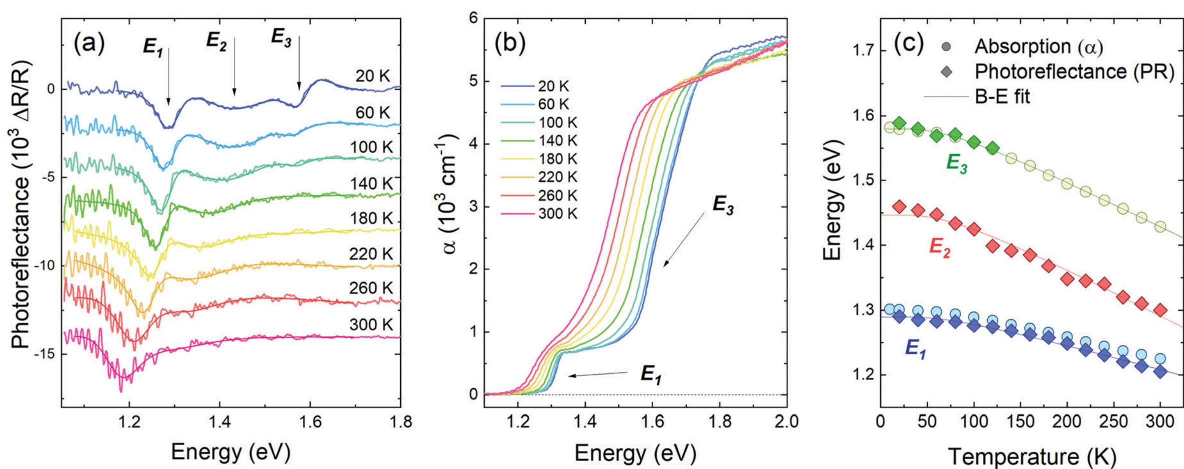

Fig. 3 Photoreflectance (a) and optical absorption (b) spectra measured at different temperatures from 20 to 300 K, and the temperature dependence of the optical transition energies observed in PR (diamond symbols) and absorption (circles), fitted with the Bose–Einstein formula given by eqn (3) (solid lines) (c).

Open Access Article. Published on 28 September 2021. Downloaded on 1/4/2024 1:07:00 PM.
This article is licensed under a Creative Commons Attribution 3.0 Unported Licence.

Table 1 Temperature coefficients for transitions E_1, E_2, and E_3 determined from fitting the dependencies with Varshni (eqn (4)) and Bose–Einstein (eqn (3)) formulas

	Varshni			Bose–Einstein		
Transition	$E(0)$ (eV)	α (10^{-4} eV K^{-1})	β (K)	$E(0)$ (eV)	a_B (meV)	θ_B (K)
E_1	1.451 ± 0.039	9.91 ± 0.45	245 ± 51	1.448 ± 0.036	76.4 ± 7.7	206 ± 32
E_2	1.583 ± 0.013	9.20 ± 0.69	229 ± 39	1.580 ± 0.010	71.5 ± 7.2	202 ± 10
E_3	1.292 ± 0.012	5.01 ± 0.14	225 ± 45	1.290 ± 0.013	40.0 ± 4.1	205 ± 16

Raman peak in the measured spectrum (Fig. 1e) and is close to average phonon energy determined using other methods (phonon dispersion calculations, Raman scattering).[60,65–67]

To explore the anisotropy of the optical activity of GeSe, a series of polarization-dependent measurements were performed. Photoreflectance and optical absorption were measured as a function of the linear polarization angle of the incident light parallel to the sample surface. In the orthorhombic crystal structure of GeSe two main in-plane orthogonal directions can be discerned – armchair and zigzag. As can be seen in Fig. 4a, in the PR spectrum acquired for armchair polarization only two out of three optical transitions are visible – E_1 and E_3. While rotating the polarization towards zigzag, E_1 and E_3 weaken to disappear entirely, and E_2 emerges. The polarization dependence is best visible in Fig. 4c, where the polar plot of the area under PR modulus curve (calculated using eqn (2)) is presented for transitions E_1, E_2 and E_3. The dependence was fitted with a formula derived from Malus' law,

$$f(\varphi) = f_{\parallel}\cos^2(\varphi - \varphi_0) + f_{\perp}\sin^2(\varphi - \varphi_0), \tag{5}$$

where φ is the polarization angle of the incidnet light, φ_0 is the polarization direction of the transition, and $f_{\parallel}$ and $f_{\perp}$ are the parallel and perpendicular components of the transition intensity, respectively. Using these parameters, the degree of polarization (*DOP*) can be defined as

$$\mathrm{DOP} = \frac{f_{\parallel} - f_{\perp}}{f_{\parallel} + f_{\perp}} \times 100\%, \tag{6}$$

where DOP = 100% indicates a fully polarized transition. Polarization degrees (and directions) for transitions E_1, E_2, and E_3 are 80% (armchair), 73% (zigzag) and 76% (armchair), respectively.

Absorption spectra are sensitive to polarization as well, as shown in Fig. 4b. The energetically lower absorption edge, corresponding to transition E_1, is best visible for the armchair polarization. The second component, attributed to transition E_3 based on temperature-dependent measurements, does not change significantly with the polarization, which is inconsistent with the PR results. Assuming the interpretation that in absorption spectra the band-to-band transition is visible, while the PR resonance is of excitonic nature, such discrepancy can be explained if the polarization selection rules do not apply to inter-band transition as strictly.

The experimental results can be further analysed and interpreted in terms of the electronic band structure of GeSe, in order to assign the observed optical transitions to certain Brillouin zone points and determine the position of the fundamental band gap. The DFT study revealed two competing valence band maxima (at the Γ point and on the Γ–X path) and three conduction band minima (at the Γ point, on the Γ–X and Γ–Y path), with relative energy dependent on the choice of the computation method and parameters.[8,37,50,54,55] In this work, theoretical calculations of the GeSe band structure were performed with the use of the mBJ-TB09 potential, which is proven to give satisfactory results for similar materials.[68] In Fig. 5a the Brillouin zone of GeSe is presented, with high symmetry points and directions marked. Fig. 5b shows the

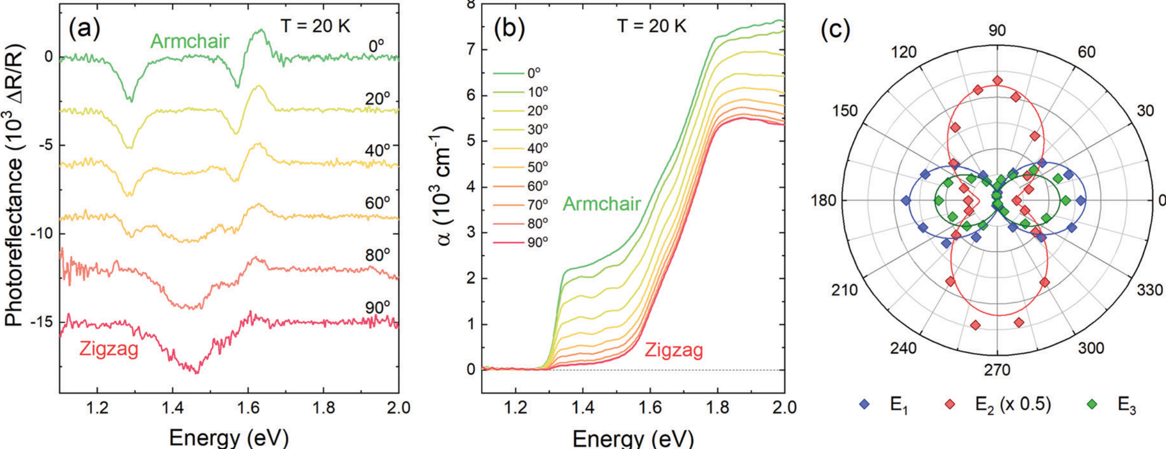

Fig. 4 Photoreflectance (a) and optical absorption (b) spectra acquired for light polarized linearly from 0° (along the armchair crystallographic direction) to 90° (along the zigzag direction). Polarization dependence of transition oscillator strength, calculated as the integrated area under the PR resonance modulus curve (c).

This journal is © The Royal Society of Chemistry 2021

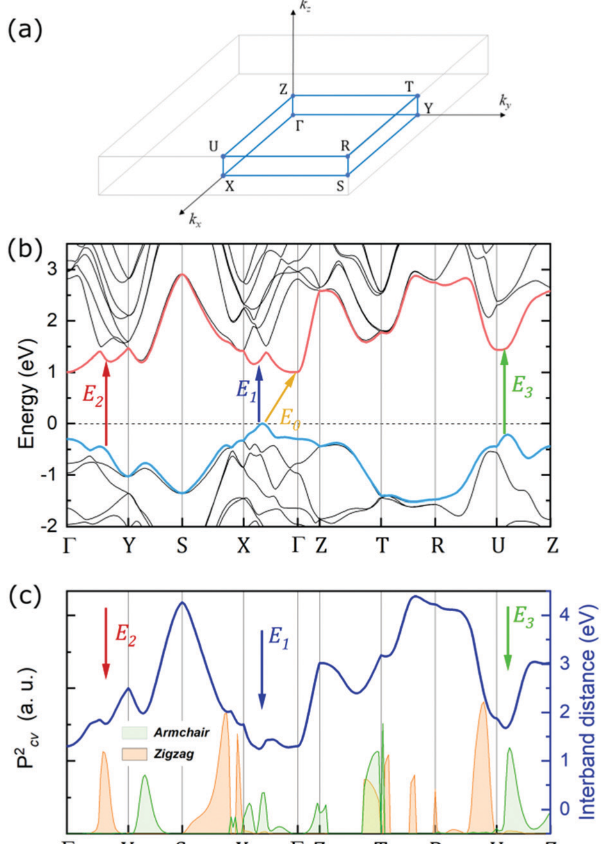

Fig. 5 (a) Schematic illustration of the BZ, with high symmetry points marked, (b) electronic band dispersion simulated with the mBJ-TB09 potential, along the high-symmetry path in the BZ, with optical transitions marked by arrows, (c) squared transition matrix element components in armchair (green areas) and zigzag (orange areas) directions, and the calculated distance between the valence and conduction band (solid dark blue line).

electronic band dispersion on high symmetry paths in the Brillouin zone. The valence band maximum (VBM) occurs on the Γ–X path, while the conduction band minimum (CBM) is at the Γ point. As a consequence, the fundamental band gap of GeSe (yellow arrow labelled E_0 in the figure) is indirect, with an energy of 0.99 eV. No absorption close to this energy was observed in the experiment, indicating that either the energy is underestimated, or the transition is not optically active. Optical transitions measured experimentally and discussed in this work were assigned to certain BZ points, based on their energy and polarization. To determine the theoretical polarization of each transition, the square of the transition matrix element (P_{cv}^2) between the topmost valence and lowermost conduction bands was calculated on a path in the BZ. Its components in armchair and zigzag directions are presented in Fig. 5c as green and orange areas, respectively. The theoretical DOP can be calculated using eqn (6), treating $f_{\parallel}$ and $f_{\perp}$ as matrix element components parallel and perpendicular to the transition polarization direction. In Fig. 5c additionally the distance between the valence and conduction band (direct band gap) is plotted (solid dark blue line, right axis), to better illustrate the critical points of the electronic band structure.

The lowest direct transition E_1 (blue arrow in the figure) was assigned to the point close to the VBM, on the Γ–X path, where the armchair component of the matrix element is high. The theoretical energy of this transition is 1.26 eV, which is very close to the experimental value of 1.29 eV (at 0 K, extrapolated from the temperature dependence). Although a similar energy is observed at Γ, the matrix element around this point is nearly zero. The second direct transition E_2 (red arrow) was assigned to a point on the Γ–Y path, due to the high zigzag matrix element component. The distance between bands at this point is 1.78 eV. In this case, the experimentally determined energy of 1.52 eV is significantly smaller; however it is the lowest allowed transition with confirmed zigzag polarization in the BZ. The discrepancy is most likely due to underestimation of the valence band energy by the calculations or high exciton binding energy. A similar observation has been reported and discussed for GeS.[68] Transition E_3 (green arrow), based on its armchair polarization, can be assigned to both Y–S and Z–U paths, although the energy matches the latter better. In the Z–U direction the distance between bands is 1.68 eV, slightly higher than the experimental energy of 1.58 eV. Experimental and theoretical energies and polarizations of each transition are presented in Table 2. Worth noting is also the band-nesting (van Hove singularity of the second type) character of each direct transition – valence band maxima and the corresponding conduction band minima do not occur at exactly the same energy, as can be seen in Fig. 5b. The difference is not significant at 0 K (as provided by DFT calculations); however it may extend and have serious consequences when the influence of the temperature is considered. One of them can be the aforementioned vanishing of the PR resonance corresponding to transition E_3 at $\sim$120 K.

Additional DFT calculations of transition energies were performed with the HSE06 hybrid functional. Table S2 (see ESI†) presents comparison of experimental and calculated transition

Table 2 Experimental and theoretical energies and polarizations of measured and predicted optical transitions, along with their assignation to certain BZ points. The experimental values correspond to a temperature of 0 K and are determined from the extrapolation of the temperature dependence

		Energy (eV)		Polarization, DOP	
Transition	Assignation	Experiment	Calculation	Experiment	Calculation
E_0	Γ–Y→ Γ		0.99	—	—
E_1	Γ–Y	1.29	1.29	Armchair, 80%	Armchair, 90%
E_2	Γ–X	1.52	1.78	Zigzag, 73%	Zigzag, 83%
E_3	Z–T	1.58	1.68	Armchair, 76%	Armchair, 93%

Open Access Article. Published on 28 September 2021. Downloaded on 1/4/2024 1:07:00 PM.
This article is licensed under a Creative Commons Attribution 3.0 Unported Licence.

Open Access Article. Published on 28 September 2021. Downloaded on 1/4/2024 1:07:00 PM.
This article is licensed under a Creative Commons Attribution 3.0 Unported Licence.

energies. It is clear that HSE06 significantly overestimates all the energies, while mBJ-TB09 yields much better agreement with measured values. This is in line with previous observations for another orthorhombic monochalcogenide, GeS.[68]

In order to investigate the functionality of GeSe in photoconversion applications, photocurrent (PC) measurements have been performed. In Fig. 6a the spectral dependence of generated photocurrent is presented (solid line), along with optical absorption (dashed line), measured at 20 K. The incident light power density used for the measurement was ~600 mW cm^{-2}, resulting in a photocurrent of an order of magnitude of pA. As can be seen in the figure, the absorption edge and step-like profile are in excellent agreement for both spectra. In PC a wide extremum occurs below the absorption edge, which can be attributed to ionized defects. Such conclusion has been made based on polarization dependent measurements (Fig. S2a in ESI†), revealing that above the absorption edge PC follows the optical absorption dependence on polarization, while in the energetically lower region the signal remains unchanged. It is best visible in panel b of Fig. S2 (ESI†), where the degree of polarization of the photocurrent is plotted. Below 1.3 eV the DOP is close to zero (the negative values originate from measurement artefacts and are not physical), indicating that there are no polarized features in this spectral region. As the optical properties of GeSe are strongly anisotropic (which is confirmed by theoretical calculations of the matrix element components across the Brillouin zone, presented in Fig. 5b), only defect states, insensitive to polarization, can contribute to light absorption and photocurrent generation. For energies above the absorption edge the polarization degree increases rapidly up to ~80%, which coincides with the value of *DOP* extracted from the photoreflectance spectra analysis. In Fig. 6b time-resolved photocurrent response obtained for three illumination powers (10 mW, 5 mW, and 1 mW) is plotted. The 532 nm laser beam was modulated at a frequency of 80 Hz. In the bottom panel of Fig. 6b a close-up of the photocurrent decay is presented. As can be seen from the figure, after the illumination is turned off, the photocurrent drops down to 10% of its maximal value in less than 80 μs. Such rapid decay is evidence of the fast response of the device (compared to other reports for this material system[18,24,65]). Fig. 6c and d show the photocurrent dependence on the illumination power density and modulation frequency, respectively, measured for two laser wavelengths: 405 nm and 532 nm. The power density dependence (panel c) follows the power law in nearly the whole investigated range. Above ~1 W cm^{-2} the experimental data drift from the trend, as the photocurrent saturates at the value exceeding 100 nA (for an excitation wavelength of 532 nm),

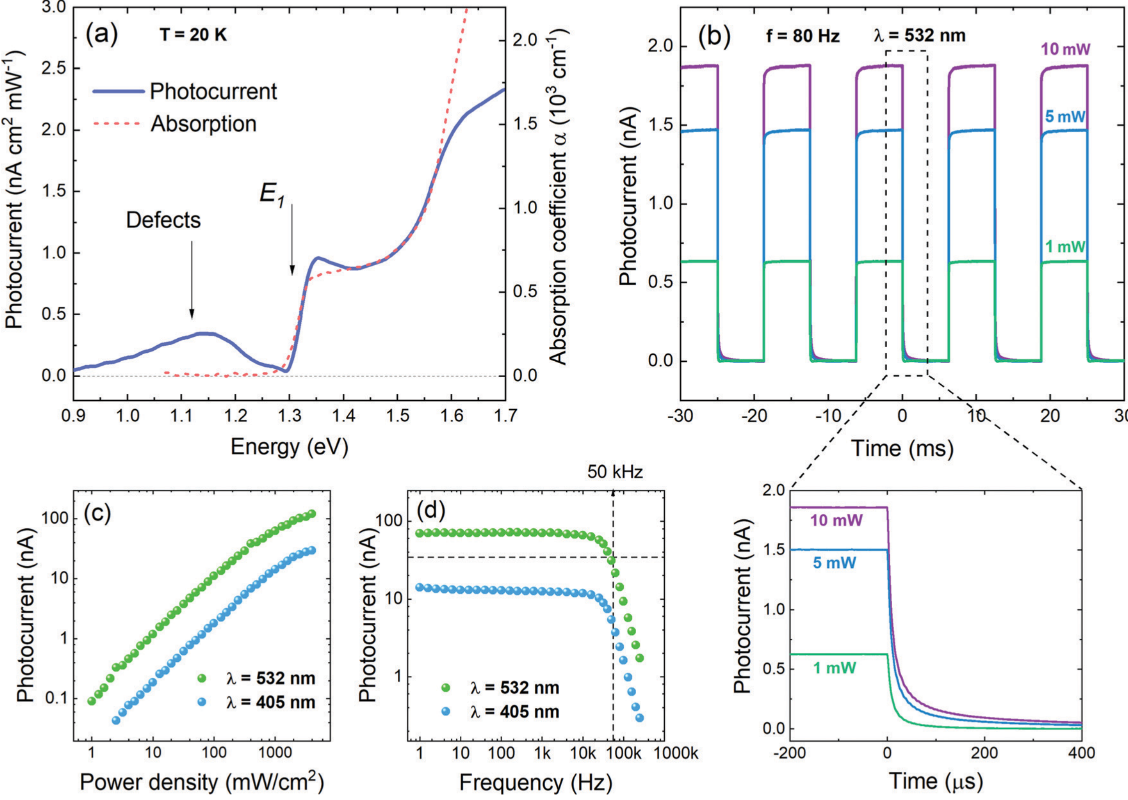

Fig. 6 (a) The comparison of the spectral characteristics of the photocurrent (solid line) and optical absorption (dashed line) of the GeSe sample under illumination with a monochromatic light of power density ~600 mW cm^{-2}, (b) the photocurrent time response measured under illumination with a 532 nm laser beam modulated at a frequency of 80 Hz, at an excitation power of 1, 5, and 10 mW. In the bottom panel the decay of the photocurrent can be seen more closely, allowing the estimation of the decay time. The dependence of photocurrent on (c) light power density and (d) frequency, measured for excitation wavelengths of 532 and 405 nm.

This journal is © The Royal Society of Chemistry 2021

Open Access Article. Published on 28 September 2021. Downloaded on 1/4/2024 1:07:00 PM.
This article is licensed under a Creative Commons Attribution 3.0 Unported Licence.

which is an excellent result for a measurement in zero-bias conditions. The photocurrent generated under 405 nm laser illumination is generally lower, due to the descent of the spectral characteristics. In the PC *vs.* frequency plot (panel d) the current is reduced by half at a frequency of ~50 kHz. This value is in good agreement with the estimated decay time (within the order of magnitude).

From the photocurrent measurement results, parameters commonly used to describe the efficiency of photoelectric conversion can be derived: photoresponsivity (R) and external quantum efficiency (EQE). Photosensitivity is defined as the photocurrent generated per unit illumination power and is given by

$$R = \frac{I_{\mathrm{ph}}}{\rho A}, \tag{7}$$

where I_{ph} is the photocurrent, ρ is the light power density, and A is the illuminated area. External quantum efficiency is defined by the equation

$$\mathrm{EQE} = \frac{hcR}{e\lambda}, \tag{8}$$

where h is Planck's constant, c is the speed of light, e is the elementary charge, and λ is the excitation wavelength. Under the illumination of a 532 nm laser beam of 1 mW power, R = 0.63 mA W^{-1} and EQE = 0.15%. The values cannot be directly compared with the corresponding results from the literature due to the fact that the reported measurements have been performed for thin flakes or nanosheets, under a fixed bias of 2–5 V, typically resulting in considerably higher photoresponsivity.[25,59,65,69] To the best of our knowledge, no reports of comprehensive photocurrent studies of bulk GeSe under zero-bias conditions are available.

Conclusions

In conclusion, the optical activity and anisotropy of a group-IV monochalcogenide, GeSe, have been investigated experimentally, exploiting two complementary methods of optical spectroscopy – optical absorption and photoreflectance. The measurements have been supported by density functional theory (DFT) calculations of the electronic band structure. The experimental study exposed that the absorption properties of GeSe are dominated by direct optical transitions, suggesting the direct character of the fundamental band gap, at an energy of (1.21 ± 0.05) eV at room temperature. Additionally, two energetically higher optical transitions have been observed. Polarization-resolved measurements revealed strong anisotropy of the acquired spectra, with the polarization degree of each observed transition exceeding 70% in one of the main in-plain crystallographic directions. The experimental results are in agreement with the theoretical study, although according to DFT calculations the fundamental band gap of GeSe is indirect, at slightly lower energy than that of the lowest direct transition. Such inconsistency can be explained by the fact that the indirect transition is significantly weaker and in the experiment may not be possible to discern from the closely lying direct transition, characterized by higher oscillator strength. Therefore, the fundamental band gap of GeSe may in fact be indirect, but with the lowest direct transition within close energy proximity.

Finally, we performed an investigation of the photoelectric properties of GeSe, by means of photocurrent measurements. The obtained photoresponsivity of 0.63 mA W^{-1} and external quantum efficiency of 0.15% are satisfactory, considering the experimental conditions (zero-bias) and the simplicity of the exploited setup. The fast response of the device (both rise and decay time of the photocurrent) is an excellent result, promising for application in photodetection technology.

We believe that our research will contribute to the general knowledge of the fundamental properties of van der Waals crystals and provide the background essential for future development of two-dimensional optoelectronics.

Methods

Experimental details

The investigated samples were bulk GeSe crystals, grown by the flux method, and were purchased from the 2D Semiconductors company (USA).[56] Crystals' purity was over 99.995%, as confirmed by XRD and EDX data provided by the manufacturer. For optical measurements flakes of thickness between 10 and 100 μm and lateral dimensions of ~2 mm were selected. The top layer of each sample was exfoliated with Kapton tape in order to obtain a clear surface. For photocurrent measurements a larger (5 mm) and thicker (500 μm) sample was used.

Structural characterization of GeSe samples was performed using high resolution transmission electron microscopy, selected area electron diffraction, and electron energy loss spectroscopy. HRTEM images and SAED patterns were acquired using a double-aberration corrected FEI Titan3 60-300 (S)TEM microscope. GeSe crystals were mechanically exfoliated onto a carbon lacey grid and subsequently imagined at an accelerating voltage of 300 kV, with spherical aberration correction. EELS analysis was performed in the STEM mode, using a Gatan Continuum (model 1077) EELS spectrometer, under the following experimental parameters: operating voltage 300 kV, beam current 120 pA, 5 mm of EELS aperture size, and dispersion of 0.3 eV ch^{-1}.

Raman scattering measurements were performed on the micro-PL setup, consisting of a 550 mm focal length grating monochromator coupled with a liquid nitrogen cooled CCD array detector camera and a 532 nm laser line (output power 50 μW). A 50×, NA = 0.55 magnifying objective lens was used to focus the laser beam and collect the light scattered at the sample surface. Raman characterization was conducted in the backscattering mode at room temperature and under ambient conditions.

Photoreflectance (PR) and optical absorption measurements were performed using dedicated optical setups. The sample was mounted inside a cryostat connected to a closed-cycle helium cryocooler, to allow measurements from room temperature down to 20 K. For both measurements a quartz tungsten

Open Access Article. Published on 28 September 2021. Downloaded on 1/4/2024 1:07:00 PM.
This article is licensed under a Creative Commons Attribution 3.0 Unported Licence.

halogen (QTH) lamp was used as the white probing light source. The signal was detected with a Si photodiode and a lock-in amplifier (Stanford Research Systems SR830). For PR measurements, a 405 nm laser modulated by a mechanical chopper at a frequency of ~300 Hz was employed. For polarization-resolved measurements a Glan–Taylor calcite linear polarizer and an achromatic half-wave plate were placed in the optical axis.

In order to investigate the photoelectric response of GeSe, photocurrent measurements were performed. The sample was mounted on a sapphire substrate (1 mm thick) to provide good thermal conduction (allowing low-temperature measurements) and electric insulation from the cold head. Four silver electric contacts were deposited on each corner of the sample. The measurements were performed under zero-bias conditions, with a Stanford Research Systems SR570 transconductance preamplifier to convert the generated photocurrent to a corresponding voltage signal, further demodulated with a lock-in amplifier. For spectral dependence measurements a mechanical chopper was used to modulate the incident light. For power, frequency, and time dependence, laser beams (405 and 532 nm) were modulated with acoustooptic modulators (AA Optoelectronics). The photocurrent time response was acquired using a high-resolution (10 bit) digital signal oscilloscope (Rohde & Schwarz RTB2000 series).

Computation details

Calculations employing DFT were performed with the use of the Vienna *Ab Initio* Simulation Package (VASP).[70] Atomic cores were represented by relativistic projector-augmented wave (PAW) datasets[71] within the Perdew–Burke–Ernzerhof (PBE) parametrization of the generalized gradient approximation (GGA) to the exchange–correlation functional.[72] The geometric structure was optimized until interatomic forces were lower than 0.01 eV A^{-1} which resulted in stress tensor components lower than 0.5 kbar. A semi-empirical vdW correction of Tkatchenko and Scheffler was used.[73] Convergence tests revealed that a plane wave basis cutoff of 650 eV combined with a $10 \times 8 \times 4$ Monkhorst Pack k-point grid is sufficient for convergence of lattice constants up to 0.01 A. The PBE functional is commonly known to underestimate the electronic band gap; therefore the modified Becke–Johnson (mBJ-TB09) exchange potential[74] and Heyd–Scuseria–Ernzerhof (HSE06) hybrid functional[75] were used. Spin–orbit coupling was employed during all the calculations. Polarization of direct optical transitions was determined from the matrix elements of the transitions obtained within Density Functional Perturbation Theory.[76]

Conflicts of interest

There are no conflicts to declare.

Acknowledgements

This work was supported by the National Science Centre (NCN) Poland OPUS 15 no. 2018/29/B/ST7/02135. S. J. Z. is a beneficiary of the START scholarship from the Foundation for Polish Science. Computational studies were supported by WCSS and PLGrid Infrastructure.

References

1 K. S. Novoselov, A. K. Geim, S. V. Morozov, D. Jiang, Y. Zhang, S. V. Dubonos, I. V. Grigorieva and A. A. Firsov, *Science*, 2004, **306**, 666–669.
2 K. S. Novoselov, A. Mishchenko, A. Carvalho and A. H. C. Neto, *Science*, 2016, **353**, aac9439.
3 A. Khandelwal, K. Mani, M. H. Karigerasi and I. Lahiri, *Mater. Sci. Eng., B*, 2017, **221**, 17–34.
4 A. Castellanos-Gomez, *J. Phys. Chem. Lett.*, 2015, **6**, 4280–4291.
5 J. Qiao, X. Kong, Z.-X. Hu, F. Yang and W. Ji, *Nat. Commun.*, 2014, **5**, 4475.
6 M. Kim, H. Kim, S. Park, J. S. Kim, H. J. Choi, S. Im, H. Lee, T. Kim and Y. Yi, *Angew. Chem., Int. Ed.*, 2019, **58**, 3754–3758.
7 Q. Li, Q. Zhou, L. Shi, Q. Chen and J. Wang, *J. Mater. Chem. A*, 2019, **7**, 4291–4312.
8 L. C. Gomes and A. Carvalho, *Phys. Rev. B: Condens. Matter Mater. Phys.*, 2015, **92**, 085406.
9 X. Zhou, X. Hu, B. Jin, J. Yu, K. Liu, H. Li and T. Zhai, *Adv. Sci.*, 2018, **5**, 1800478.
10 L. Huang, F. Wu and J. Li, *J. Chem. Phys.*, 2016, **144**, 114708.
11 J. Liu and S. T. Pantelides, *Appl. Phys. Express*, 2018, **11**, 101301.
12 G. Shi and E. Kioupakis, *Nano Lett.*, 2015, **15**, 6926–6931.
13 D. Tan, H. E. Lim, F. Wang, N. B. Mohamed, S. Mouri, W. Zhang, Y. Miyauchi, M. Ohfuchi and K. Matsuda, *Nano Res.*, 2017, **10**, 546–555.
14 Y. Yang, S.-C. Liu, Y. Wang, M. Long, C.-M. Dai, S. Chen, B. Zhang, Z. Sun, Z. Sun, C. Hu, S. Zhang, L. Tong, G. Zhang, D.-J. Xue and J.-S. Hu, *Adv. Opt. Mater.*, 2019, **7**, 1801311.
15 P. Zhao, H. Yang, J. Li, H. Jin, W. Wei, L. Yu, B. Huang and Y. Dai, *J. Mater. Chem. A*, 2017, **5**, 24145–24152.
16 P. D. Antunez, J. J. Buckley and R. L. Brutchey, *Nanoscale*, 2011, **3**, 2399–2411.
17 X. Fan, L. Su, F. Zhang, D. Huang, D. K. Sang, Y. Chen, Y. Li, F. Liu, J. Li, H. Zhang and H. Xie, *ACS Appl. Mater. Interfaces*, 2019, **11**, 47197–47206.
18 C. Lan, C. Li, Y. Yin, H. Guo and S. Wang, *J. Mater. Chem. C*, 2015, **3**, 8074–8079.
19 E. Sutter and P. Sutter, *ACS Appl. Nano Mater.*, 2018, **1**, 1042–1049.
20 A. Dasgupta, J. Gao and X. Yang, *Laser Photonics Rev.*, 2020, **14**, 1900416.
21 H. Ahmad, R. Ramli, A. A. Kamely, M. Z. Samion, N. Yusoff, L. Bayang, S. N. Aidit and K. Thambiratnam, *IEEE J. Quantum Electron.*, 2020, **56**, 1–8.
22 Y. I. Jhon, J. Lee, M. Seo, J. H. Lee and Y. M. Jhon, *Adv. Opt. Mater.*, 2019, **7**, 1801745.
23 Y. Jia, Z. Li, M. Saeed, J. Tang, H. Cai and Y. Xiang, *Opt. Express*, 2019, **27**, 20857–20873.

This journal is © The Royal Society of Chemistry 2021

Open Access Article. Published on 28 September 2021. Downloaded on 1/4/2024 1:07:00 PM.
This article is licensed under a Creative Commons Attribution 3.0 Unported Licence.

24 R. Ulaganathan, Y.-Y. Lu, C.-J. Kuo, S. Tamalampudi, R. Sankar, K. M. Boopathi, A. Anand, K. Yadav, R. Mathew, C.-R. Liu, F. Chou and Y.-T. Chen, *Nanoscale*, 2016, **8**, 2284–2292.
25 H. Zhao, Y. Yang, C. Wang, D. Zhou, X. Shi, Y. Li and Y. Mao, *ACS Appl. Mater. Interfaces*, 2019, **11**, 38031–38038.
26 R. Fei, W. Li, J. Li and L. Yang, *Appl. Phys. Lett.*, 2015, **107**, 173104.
27 L. C. Gomes, *Phys. Rev. B: Condens. Matter Mater. Phys.*, 2015, **92**, 214103.
28 A. I. Lebedev, *J. Appl. Phys.*, 2018, **124**, 164302.
29 R. Fei, W. Kang and L. Yang, *Phys. Rev. Lett.*, 2016, **117**, 097601.
30 S. R. Panday, S. Barraza-Lopez, T. Rangel and B. M. Fregoso, *Phys. Rev. B*, 2019, **100**, 195305.
31 H. Wang and X. Qian, *2D Mater.*, 2017, **4**, 015042.
32 M. Wu and X. C. Zeng, *Nano Lett.*, 2016, **16**, 3236–3241.
33 G. Bianca, M. I. Zappia, S. Bellani, Z. Sofer, M. Serri, L. Najafi, R. Oropesa-Nuñez, B. Martín-García, T. Hartman, L. Leoncino, D. Sedmidubský, V. Pellegrini, G. Chiarello and F. Bonaccorso, *ACS Appl. Mater. Interfaces*, 2020, **12**, 48598–48613.
34 C. Chowdhury, S. Karmakar and A. Datta, *J. Phys. Chem. C*, 2017, **121**, 7615–7624.
35 K. Wang, D. Huang, L. Yu, K. Feng, L. Li, T. Harada, S. Ikeda and F. Jiang, *ACS Catal.*, 2019, **9**, 3090–3097.
36 X. Lv, W. Wei, Q. Sun, F. Li, B. Huang and Y. Dai, *Appl. Catal., B*, 2017, **217**, 275–284.
37 P. A. E. Murgatroyd, M. J. Smiles, C. N. Savory, T. P. Shalvey, J. E. N. Swallow, N. Fleck, C. M. Robertson, F. Jäckel, J. Alaria, J. D. Major, D. O. Scanlon and T. D. Veal, *Chem. Mater.*, 2020, **32**, 3245–3253.
38 S.-C. Liu, Y. Yang, Z. Li, D.-J. Xue and J.-S. Hu, *Mater. Chem. Front.*, 2020, **4**, 775–787.
39 X. Lv, W. Wei, C. Mu, B. Huang and Y. Dai, *J. Mater. Chem. A*, 2018, **6**, 5032–5039.
40 D.-J. Xue, S.-C. Liu, C.-M. Dai, S. Chen, C. He, L. Zhao, J.-S. Hu and L.-J. Wan, *J. Am. Chem. Soc.*, 2017, **139**, 958–965.
41 W. Shockley and H. J. Queisser, *J. Appl. Phys.*, 1961, **32**, 510–519.
42 K. Cheng, Y. Guo, N. Han, Y. Su, J. Zhang and J. Zhao, *J. Mater. Chem. C*, 2017, **5**, 3788–3795.
43 L. Peng, C. Wang, Q. Qian, C. Bi, S. Wang and Y. Huang, *ACS Appl. Mater. Interfaces*, 2017, **9**, 40969–40977.
44 S. Ahmed, T. Taher, R. Chakraborty and S. Subrina, *J. Electron. Mater.*, 2019, **48**, 6735–6741.
45 C. Xia, J. Du, X. Huang, W. Xiao, W. Xiong, T. Wang, Z. Wei, Y. Jia, J. Shi and J. Li, *Phys. Rev. B*, 2018, **97**, 115416.
46 A. K. Singh and R. G. Hennig, *Appl. Phys. Lett.*, 2014, **105**, 042103.
47 Y. Yan, W. Xiong, S. Li, K. Zhao, X. Wang, J. Su, X. Song, X. Li, S. Zhang, H. Yang, X. Liu, L. Jiang, T. Zhai, C. Xia, J. Li and Z. Wei, *Adv. Opt. Mater.*, 2019, **7**, 1900622.
48 K. Yumigeta, C. Brayfield, H. Cai, D. Hajra, M. Blei, S. Yang, Y. Shen and S. Tongay, *RSC Adv.*, 2020, **10**, 38227–38232.
49 Y. Zhong, L. Zhang, W. Chen and H. Zhu, *Nanotechnology*, 2020, **31**, 385203.
50 B. Chen, Y. Ruan, J. Li, W. Wang, X. Liu, H. Cai, L. Yao, J.-M. Zhang, S. Chen and G. Chen, *Nanoscale*, 2019, **11**, 3968–3978.
51 C. R. Kannewurf and R. J. Cashman, *J. Phys. Chem. Solids*, 1961, **22**, 293–298.
52 A. M. Elkorashy, *Phys. Status Solidi B*, 1986, **135**, 707–713.
53 S.-C. Liu, Y. Mi, D.-J. Xue, Y.-X. Chen, C. He, X. Liu, J.-S. Hu and L.-J. Wan, *Adv. Electron. Mater.*, 2017, **3**, 1700141.
54 F. M. Gashimzade, D. G. Guliev, D. A. Guseinova and V. Y. Shteinshrayber, *J. Phys.: Condens. Matter*, 1992, **4**, 1081–1091.
55 L. Makinistian and E. A. Albanesi, *J. Phys.: Condens. Matter*, 2007, **19**, 186211.
56 Germanium Selenide (GeSe), https://www.2dsemiconductors.com/germanium-selenide-gese/, (accessed July 22, 2021).
57 EELS Atlas, https://eels.info/atlas, (accessed July 22, 2021).
58 D. Tan, X. Wang, W. Zhang, H. E. Lim, K. Shinokita, Y. Miyauchi, M. Maruyama, S. Okada and K. Matsuda, *Small*, 2018, **14**, 1704559.
59 H. Zhao, Y. Mao, X. Mao, X. Shi, C. Xu, C. Wang, S. Zhang and D. Zhou, *Adv. Funct. Mater.*, 2018, **28**, 1704855.
60 A. Taube, A. Lapińska, J. Judek, N. Wochtman and M. Zdrojek, *J. Phys. D: Appl. Phys.*, 2016, **49**, 315301.
61 D. E. Aspnes, *Surf. Sci.*, 1973, **37**, 418–442.
62 J. Tauc, *Mater. Res. Bull.*, 1968, **3**, 37–46.
63 L. Viña, S. Logothetidis and M. Cardona, *Phys. Rev. B: Condens. Matter Mater. Phys.*, 1984, **30**, 1979–1991.
64 Y. P. Varshni, *Physica*, 1967, **34**, 149–154.
65 Z. Wang, M. Li, X. P. A. Gao and Z. Zhang, *ACS Appl. Electron. Mater.*, 2019, **1**, 2236–2243.
66 F. M. Gashimzade, D. A. Guseinova, Z. A. Jahangirli and M. A. Nizametdinova, *Phys. Solid State*, 2013, **55**, 1802–1807.
67 G. Ding, G. Gao and K. Yao, *Sci. Rep.*, 2015, **5**, 1–7.
68 R. Oliva, T. Woźniak, F. Dybala, A. Tołłoczko, J. Kopaczek, P. Scharoch and R. Kudrawiec, *Phys. Rev. B*, 2020, **101**, 235205.
69 P. Ramasamy, D. Kwak, D.-H. Lim, H.-S. Ra and J.-S. Lee, *J. Mater. Chem. C*, 2016, **4**, 479–485.
70 G. Kresse and J. Furthmüller, *Phys. Rev. B: Condens. Matter Mater. Phys.*, 1996, **54**, 11169–11186.
71 G. Kresse and D. Joubert, *Phys. Rev. B: Condens. Matter Mater. Phys.*, 1999, **59**, 1758–1775.
72 J. P. Perdew, K. Burke and M. Ernzerhof, *Phys. Rev. Lett.*, 1996, **77**, 3865–3868.
73 A. Tkatchenko and M. Scheffler, *Phys. Rev. Lett.*, 2009, **102**, 073005.
74 F. Tran and P. Blaha, *Phys. Rev. Lett.*, 2009, **102**, 226401.
75 A. V. Krukau, O. A. Vydrov, A. F. Izmaylov and G. E. Scuseria, *J. Chem. Phys.*, 2006, **125**, 224106.
76 M. Gajdoš, K. Hummer, G. Kresse, J. Furthmüller and F. Bechstedt, *Phys. Rev. B: Condens. Matter Mater. Phys.*, 2006, **73**, 045112.

Electronic Supplementary Material (ESI) for Journal of Materials Chemistry C.
This journal is © The Royal Society of Chemistry 2021

Supporting Information

Optical properties of orthorhombic germanium selenide: an anisotropic layered semiconductor promising for optoelectronic applications

Agata Tołłoczko[*a], Szymon J. Zelewski[a], Michał Błaszczak[a], Tomasz Woźniak[a], Anna Siudzińska[b], Alicja Bachmatiuk[b], Paweł Scharoch[a], Robert Kudrawiec[ab]*

[1] Department of Semiconductor Materials Engineering,
Wrocław University of Science and Technology,
Wybrzeże Wyspiańskiego 27, 50-370 Wrocław, Poland

[2] Łukasiewicz Research Network – PORT Polish Center for Technology Development,
Stabłowicka 147, Wrocław, Poland

*Corresponding author.

E-mail address: agata.tolloczko@pwr.edu.pl

Table S1. Experimental and reference[a)] energies of the EELS edges observed in the acquired spectra.

EELS edge	Energy (eV)			
	Ge		Se	
	Experiment	Reference	Experiment	Reference
L_1	1413	1414	1655	1654
L_2	1255	1248	1479	1476
L_3	1221	1217	1436	1436

a) EELS Atlas, https://eels.info/atlas

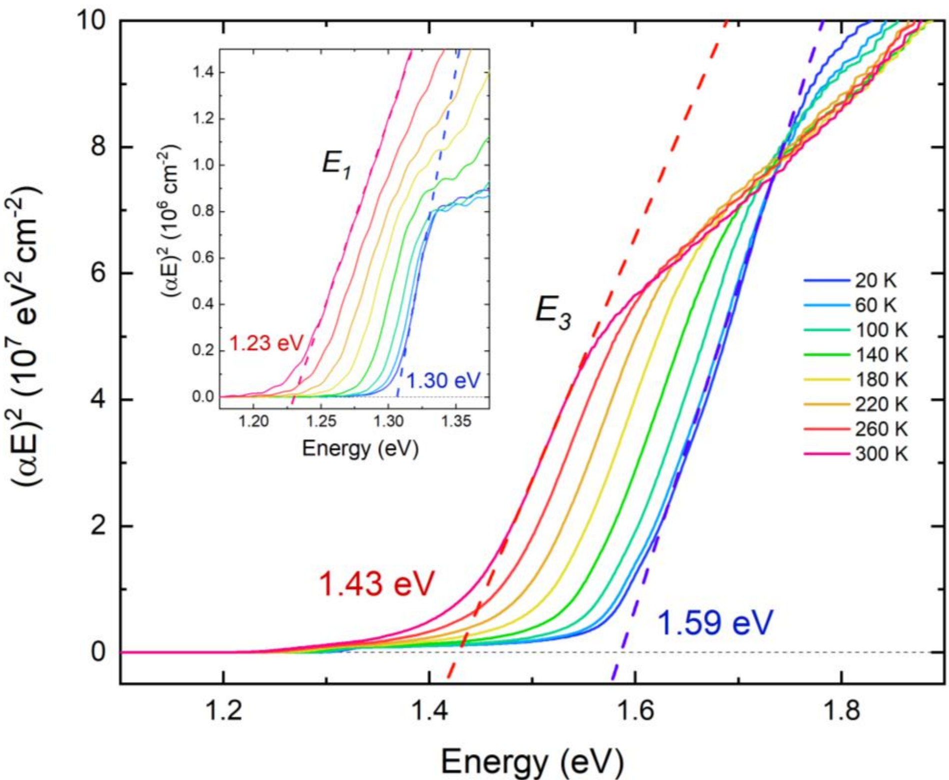

Fig. S1. Temperature dependence and linear approximation of Tauc plot of GeSe optical absorption, assuming allowed direct character of the observed absorption edge, corresponding to transition E_3. The inset shows the weaker absorption edge at the energy of 1.30 eV (at 20 K), corresponding to transition E_1.

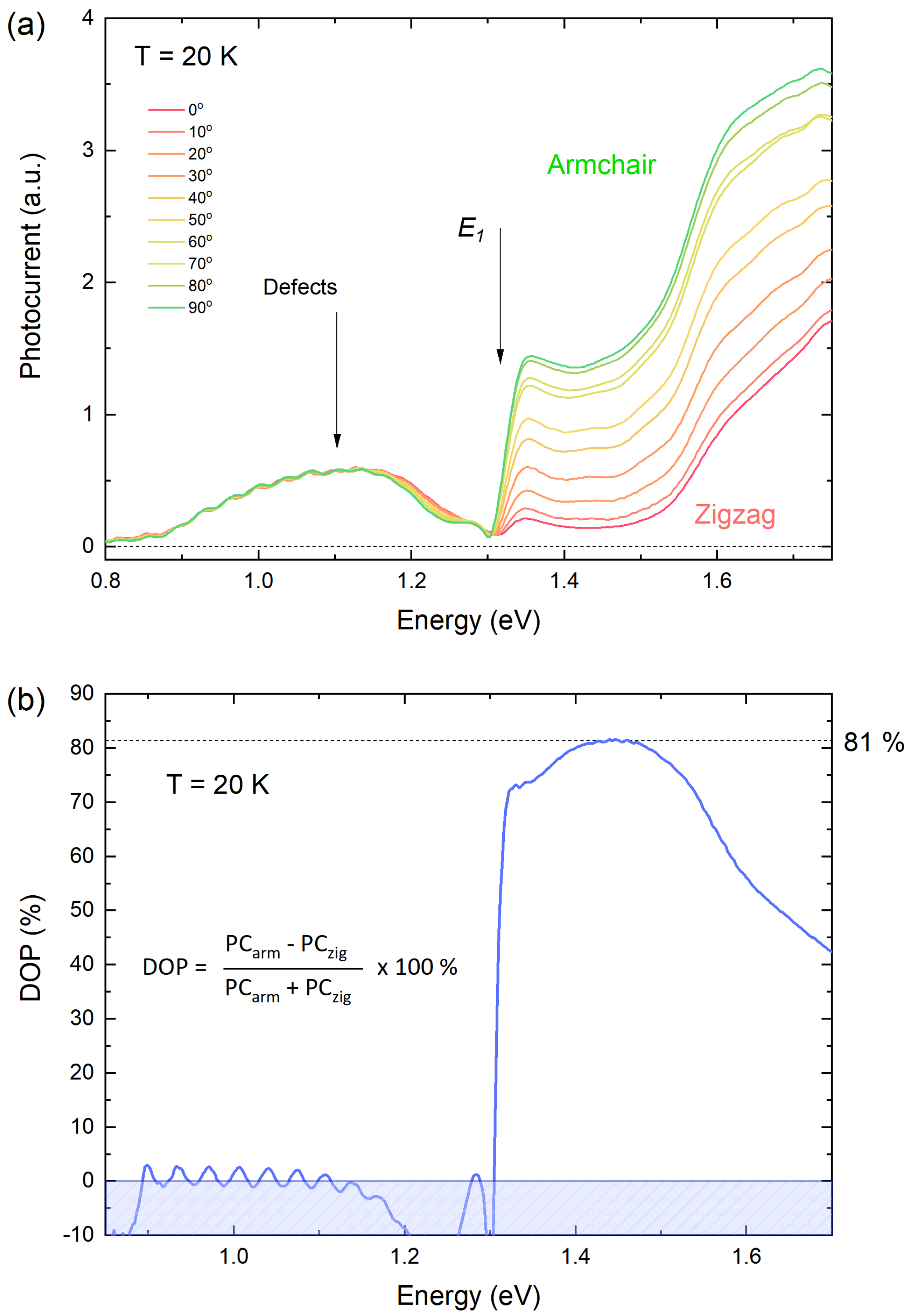

Fig. S2. (a) Polarization dependence of the photocurrent, measured at the temperature of 20 K, in zero-bias conditions and (b) the photocurrent degree of polarization (DOP), calculated using the equation from the figure.

Table S2. Transition energies from experiment and calculations with mBJ-TB09 and HSE06.

Transition	Energy (eV)		
	Exp	mBJ-TB09	HSE06
E_0	–	0.99	1.18
E_1	1.29	1.29	1.38
E_2	1.52	1.78	2.07
E_3	1.58	1.68	1.88

Chapter 3

Valley polarization investigation of GeS under high pressure

Robert Oliva, Tomasz Woźniak, Filip Dybała, Agata K. Tołłoczko, Jan Kopaczek, Paweł Scharoch, Robert Kudrawiec

Physical Review B, **101**, 235205 (2020)

Overview

The influence of high hydrostatic pressure on the electronic band structure of GeS was investigated by polarization-resolved high-pressure photoreflectance measurements combined with *ab initio* calculations. The experimental results confirmed the predictions of nondegenerate valleys, which can be individually selected through linearly polarized light. The effect of pressure on the electronic band structure is discussed in terms of orbital composition.

Author's contribution

Agata K. Tołłoczko participated in the optical experiments (pressure and polarization dependent PR), interpretation of the results, and writing of the manuscript. The work is a continuation of a previous study performed as AKT's Master's Degree project, in which the author performed characterization of GeS crystals in ambient pressure and vacuum conditions by means of polarization- and temperature-resolved PR and optical absorption. The obtained results revealed strong anisotropy of the material. The idea for the analogous pressure-dependent investigation and interpretation of the results are therefore strongly based on AKT's preliminary studies, which is an additional contribution to the presented work.

PHYSICAL REVIEW B **101**, 235205 (2020)

Valley polarization investigation of GeS under high pressure

R. Oliva,[*,†] T. Woźniak,[*] F. Dybala, A. Tołłoczko, J. Kopaczek, P. Scharoch, and R. Kudrawiec
Department of Semiconductor Materials Engineering, Wroclaw University of Science and Technology, Wybrzeże Wyspiańskiego 27, 50–370, Wroclaw, Poland

(Received 26 April 2020; revised manuscript received 28 May 2020; accepted 1 June 2020; published 19 June 2020)

GeS and its analog compounds exhibit unique properties that combine some of the most desired features of other two-dimensional compounds, such as transition-metal dichalcogenides and graphene. These include high electron mobilities or valley physics that result in strong optical and electronic anisotropy. Here, we present an experimental and theoretical study of the electronic band structure of GeS at high hydrostatic pressures. Polarization-resolved high-pressure photoreflectance measurements allow us to extract the energies, optical dichroic ratios, and pressure coefficients of the direct optical transitions. These findings are discussed in view of first-principles calculations, which predict that nondegenerate states in different valleys can be individually selected through linearly polarized light. Based on this, an assignation of the direct optical transitions to the electronic band structure is provided. Finally, the effect of pressure on the electronic band structure is discussed in terms of orbital composition. These results provide evidence that GeS is a strong candidate for valleytronic applications in nondegenerate systems.

DOI: 10.1103/PhysRevB.101.235205

I. INTRODUCTION

The discovery of graphene [1] triggered enormous research interest in two-dimensional (2D) compounds, owing to their exotic fundamental properties. Intensive research on 2D materials, such as transition-metal dichalcogenides (TMDs), revealed their remarkable electronic and optical properties. These include strong light-matter coupling [2], large excitonic binding energies, the easiness of producing heterostructures by stacking monolayers held by van der Waals (vdW) forces [3,4], as well as the presence of spin-polarized bands that couple to new degrees of freedom such as degenerate valleys or adjacent layers, even in their bulk form [5,6]. Despite the highly promising properties observed in TMDs for many optoelectronic and spintronic applications, alternative 2D materials with complementary properties are being researched. For example, black phosphorus (BP) exhibits superior high carrier mobilities and a sizable gap that can be tuned by adjusting the number of layers, thus combining the most desired features of TMDs and graphene [7,8]. Also, the group-IV monochalcogenides, which are isostructural to BP, have shown to retain many useful properties of BP, such as high carrier mobilities or strong in-plane optical anisotropy that is believed to arise from rich valley physics. In order to fully exploit this family of 2D materials for developing novel optoelectronic devices, it is crucial to further characterize their optical and electronic properties.

Amongst group-IV monochalcogenides, GeS has received particular interest owing to its high electron mobility (larger than 3000 $\mathrm{cm^2V^{-1}s^{-1}}$ in its monolayer form [9]), band-gap value (≈1.6 eV), low toxicity, and high optical anisotropy. These properties are very desirable for photodetectors [10,11], solar cells [12,13], or light-emitting devices [14]. Despite the vast technological potential, the electronic band structure of GeS is not yet accurately known, in particular an assignation of the optical features is still under research. Early polarization-resolved optical absorption measurements revealed that GeS exhibits two optical transitions, E_0 and E_1, polarized along the *zigzag* and *armchair* directions, respectively, and tentatively assigned them to either direct and indirect transitions [15–17]. More recently, polarization-resolved modulation spectroscopy measurements such as photoreflectance (PR) [18] or thermoreflectance [12,14] allowed measuring the first two direct transitions, namely E_1 and E_2, polarized along the *armchair* and *zigzag* directions, respectively. However, these transitions have not yet been unambiguously assigned due to difficulties in band-structure calculations such as those based on density-functional theory (DFT). The results of these calculations are highly sensitive to the particular values of lattice parameters, exchange-correlation functionals, van der Waals corrections, or electron-phonon coupling [19–26]. Hence, in order to provide an accurate description of the electronic band structure of GeS, it is desirable to test the state of the art DFT methods by confrontation with optical measurements under different experimental conditions.

High-pressure (HP) modulation spectroscopy represents a unique tool that allows one to obtain detailed information about the electronic band structure [27]. In particular, HP PR measurements allow one to extract the energies of direct transitions and their pressure dependencies, which can be used as a benchmark to test the calculation methods (such as those based on DFT) on challenging systems such as 2D materials [28,29]. To date, many theoretical works reported the effect of strain and pressure on the fundamental properties of GeS.

[*]These authors contributed equally to this work.
[†]robert.oliva.vidal@pwr.edu.pl

 ©2020 American Physical Society

These studies revealed that the electronic band structure can be strain tuned for ferroelastic switching applications [30] or the band gap can be reduced under compression [9], followed by a semiconductor to semimetal transition. [31,32] These results were confirmed by high-pressure experimental works, which showed that at high pressure GeS exhibits a structural phase transition followed by a metallization [33]. Despite these studies, the effect of pressure on the electronic band structure has been scarcely investigated. Only high-pressure optical absorption measurements reported the shift of the absorption edge with pressure, but the measured optical features were not assigned to the electronic band structure. [34]

In the present work, we perform high-pressure PR measurements in order to assign the optical transitions to the electronic band structure of GeS. Polarization-resolved measurements performed at different pressures are used to resolve the energetically close E_1 and E_2 direct excitonic transitions, as well as to investigate into the anisotropic properties under compression conditions. These results, combined with first-principles calculations, provide valuable information about the electronic band structure of GeS at both ambient and high-pressure conditions. Finally, the anisotropic optical properties are discussed in terms of valley polarization as defined by the selection rules, and the effect of pressure on the electronic band structure is discussed in the context of bands' orbital composition.

II. METHODS

A. Samples

High-purity (>99.995% confirmed) germanium sulfide samples were synthesized by the chemical vapor deposition method. The samples were commercially obtained from the HQ Graphene company. The excellent crystallinity of the samples was confirmed by x-ray diffraction and energy-dispersive x-ray spectroscopy; details can be found elsewhere [35]. An ≈200-μm-thick flake was selected for the high-pressure experiments. A picture of the sample selected for the high-pressure experiments is shown in Fig. 1(a). The sample is mounted on the top of a 5-mm-diameter sapphire window of the high-pressure piston-cylinder cell. The orientation of the sample can be inferred from its elongated shape, since GeS typically cleaves forming rectangles, having the largest side along the zigzag direction (*b* lattice parameter). The orientation of the sample has been confirmed by polarization-resolved photoreflectance measurements (the polarization direction along sample's long edge is set to 0°). The crystal structure, as represented by the VESTA software, is shown in Fig. 1(b) [36].

B. Computational methods

DFT calculations were performed using Vienna *Ab initio* Simulation Package (VASP) [37]. Atomic electronic structures were represented by projector-augmented waves datasets within the Perdew-Burke-Ernzerhof (PBE) parametrization of generalized gradients approximation to exchange-correlation functional [38,39]. A plane-wave basis cutoff of 550 eV and $4 \times 11 \times 9\Gamma$-centered k-point grid were found to assure convergence of both structural parameters and electronic gaps with precision of 0.001 Å and 0.01 eV, respectively.

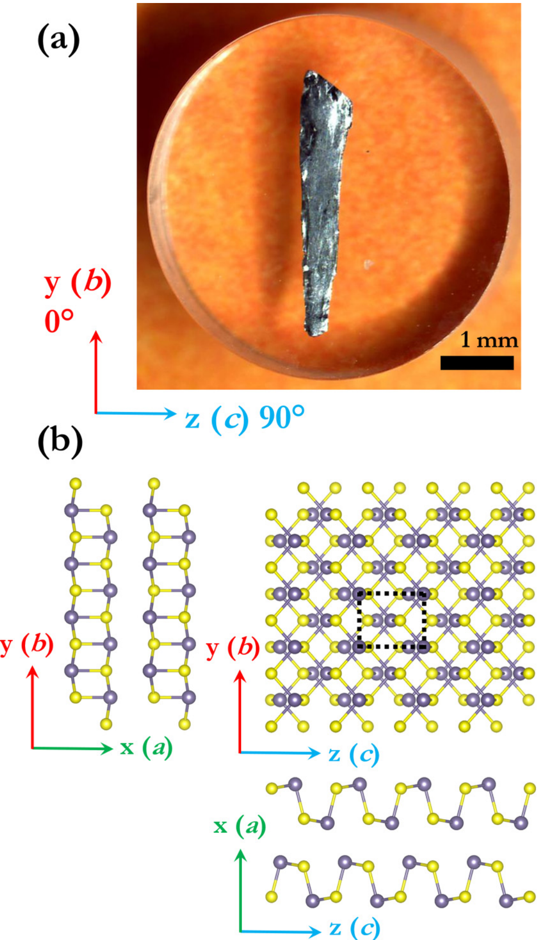

FIG. 1. (a) GeS flake mounted on a sapphire cylindrical window of a piston-cylinder high-pressure cell. GeS flakes typically cleave in rectangular shapes. (b) Representation of the crystal structure of GeS. The armchair and zigzag directions are shown in relation to the crystal orientation and lattice parameters.

Several methods to represent van der Waals interactions and related functionals were tested to evaluate their effect on the geometry. These are semiempirical corrections: D2 [40], D3 [41], D3 with Becke-Johnson damping (D3+BJ) [42], Tkachenko-Scheffler [43], Tkatchenko-Scheffler with Hirshfeld partitioning (TS+HP), [44] many-body dispersion energy (MBD), [45] dDcS [46], and van der Waals functionals: vdW-DF1 [47] with revPBE, [48] optPBE, optB88, and optB86b [49,50] functionals and vdW-DF2 [51] with rPW86 [52] and B86R [53] functionals. Optimized lattice parameters for all these methods are shown in Table S1 of the Supplemental Material (see Ref. [54] and references therein [55–58]). In the table, calculated lattice parameters are compared to the experimental values. The best agreement is found for the TS, TS+HP, and MBD functionals (corresponding mean absolute relative error, MARE, with respect experimental values is lower than 1%). From the table it is clear that the values of optimized lattice constants, both in plane and out of plane, are sensitive to the vdW method applied. In general, vdW functionals tend to significantly overestimate the lattice

parameters (up to MARE ≈6%). Therefore the band-structure calculations were performed only for the structures obtained with the semiempirical corrections (see Table S2 in Supplemental Material (SM) [54]). For the present work we used the semiempirical correction of Tkachenko and Scheffler (TS) for vdW interactions for the optimization of lattice constants and atomic positions since it reproduces best the experimental lattice parameters. [43] The geometrical parameters were optimized until all the interatomic forces and isotropic stress were lower than 10^{-3} eV/Å and 0.05 kbar, respectively.

For the electronic band-structure calculations a couple of methods (including local-density approximation, LDA, and PBE exchange-correlation functionals, Heyd-Scuseria-Ernzerhof HSE06 hybrid functional and mBJ-TB09 potential) were tested for all optimized structures as well as for experimental lattice constants (with optimized atomic positions only). Calculated energies with the modified Becke-Johnson exchange potential combined with the LDA correlation (mBJ-TB09) for different optimized structures are shown in Table S2 of the SM. [54] In the present work we conclude that the electronic band structure is best reproduced (in terms of both calculated transition energies and pressure coefficients) by the Tran and Blaha exchange-correlation potential, which consists of the mBJ-TB09) [59]. It is worth noting that qualitatively similar results were obtained with the HSE06 functional (results shown in Table S3 only). The effect of spin-orbit interaction on the lattice parameters and on the transition energies at ambient pressure was lower than 0.001 Å and 0.007 eV, respectively; thus, they were omitted in the high-pressure calculations. The optical matrix elements were obtained from the wave-function derivatives that are calculated within density-functional perturbation theory. [60]

C. Experimental setup

High-pressure hydrostatic measurements were performed by mounting the GeS flake (≈4 mm in diameter and ≈200 μm thickness) inside a UNIPRESS piston-type cylinder cell. The chosen pressure hydrostatic medium was Daphne 7474, which remained hydrostatic and transparent during the whole experiment, up to a pressure of 18 kbar. The pressure was determined by measuring the resistivity of the InSb gauge by the four-probe method. This method provides a 0.1-kbar sensitivity. A sapphire window guaranteed an optical access to the sample. For the PR measurements, white light from a halogen lamp was focused onto the sample and reflectivity signal was detected by a Si pin diode after the light was dispersed by a 0.55-m focal length single-grating monochromator. Reflectivity on the sample was modulated by a chopped (270 Hz) 405-nm laser line. Phase-sensitivity detection of the PR signal was processed with a lock-in amplifier. A sketch of the whole PR setup is shown in the SM (Fig. S1) [54]. Further details on the experimental setup can be found elsewhere [61].

III. RESULTS AND DISCUSSION

We conducted high-pressure PR measurements in order to determine the pressure dependence of the first direct optical transitions. The PR spectra obtained at different pressures are shown in Fig. 2. As it can be seen in the figure, two PR features

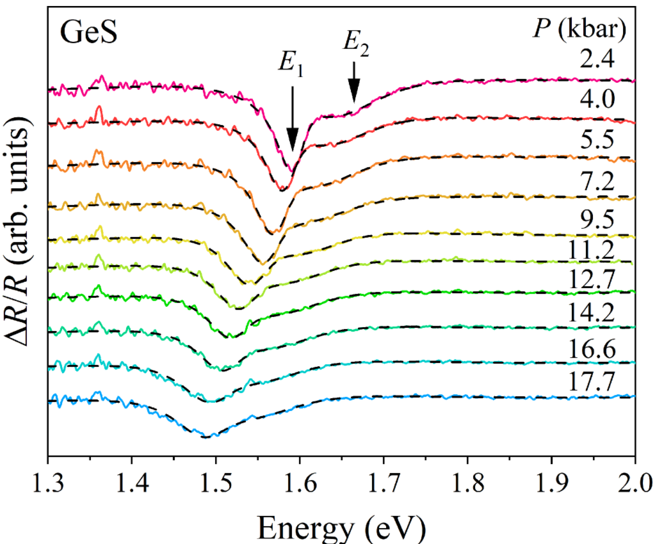

FIG. 2. PR spectra acquired at different pressure values. PR features corresponding to the transitions E_1 and E_2 are shown with labels. Fits to the data are presented as dashed black lines.

show up at $E_1 = 1.61$ eV and $E_2 = 1.66$ eV, whose energies decrease with increasing pressure. These optical transitions have been previously reported from thermoreflectance [12,14] and from polarization-resolved transmittance measurements [17,62]. Calculations predict that GeS is a quasidirect semiconductor with the indirect band gap ≈ 50 meV below the first direct transition (i.e., the indirect transition, not observed in the PR spectra, should be around $E_0 \approx 1.56$ eV at ambient temperature) [26]. To extract the energies of transitions E_1 and E_2, the PR spectra in Fig. 2 are fitted (dashed lines in the figure) with the Aspnes formula [63],

$$\frac{\Delta R}{R}(\hbar\omega) = Re\Big(\sum C_i e^{i\varphi_i}(\hbar\omega - E_i + i\Gamma_i)^{-m}\Big), \qquad (1)$$

where C_i, φ_i, Γ_i, and E_i are the resonance amplitude, phase, broadening, and energy of the ith transition ($i = 1, 2$), respectively. These transitions are properly fitted with an excitoniclike resonance profile ($m = 2$), as expected, since the excitonic binding energy is believed to be larger than the thermal energy at room temperature [21]. From the figure it can be seen that, with increasing pressure, both resonances redshift and broaden. At high pressure, both transitions merge, due to an increased pressure coefficient of transition E_2.

Since the energetic difference between transitions E_1 and E_2 is on the same order of magnitude as their broadening (Γ parameter of the Aspnes formula), polarization-resolved measurements were performed to determine the energies of each transition separately. As can be seen in Fig. 3, the PR profile obtained at 9.4 kbar strongly depends on the polarization angle. At a polarization of 90° (0°) the signal from transition E_1 (E_2) is maximum, which coincides with the direction of the main in-plane lattice parameters c (90°, armchair direction) and b (0°, zigzag direction). This finding is in perfect agreement with previous polarization-resolved absorption [10,12,16,17], thermoreflectance [12,14], and photoluminescence [14,17] measurements, which reported photoluminescence (PL) signal polarized along the armchair direction

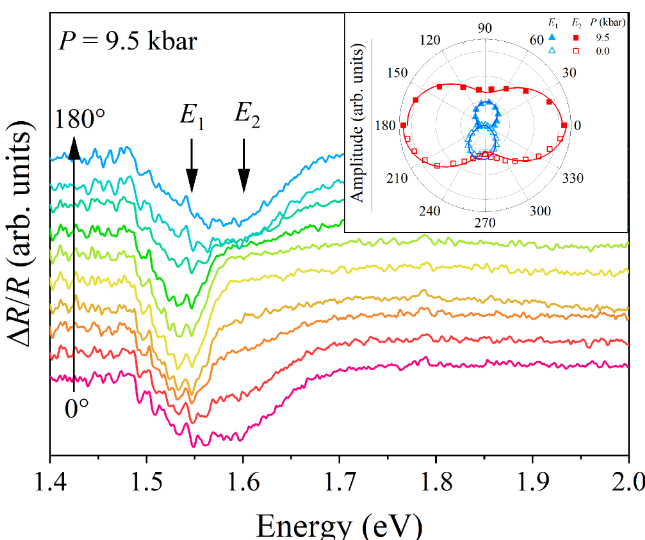

FIG. 3. PR spectra acquired at 9.5 kbar at different polarization directions, from zigzag (0°) to armchair (90°). Inset: Polar plot of the amplitude of transitions E_1 and E_2 at 9.5 kbar (top half) and ambient pressure (bottom half).

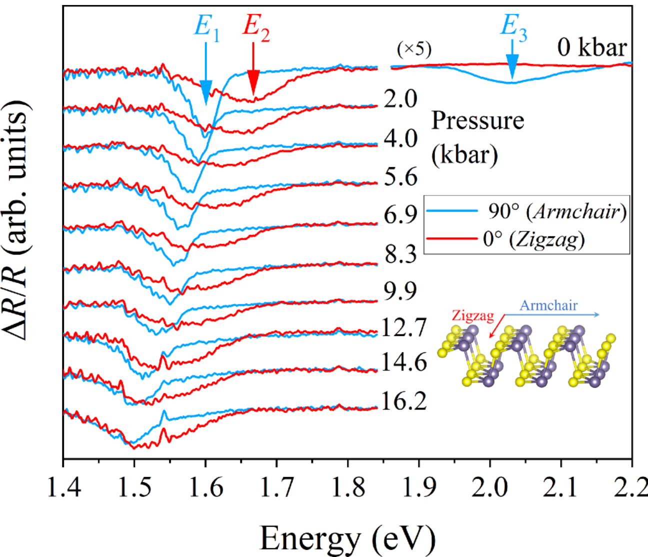

FIG. 4. PR spectra acquired at different pressures with light polarized along the two main crystallographic directions; zigzag (red line) and armchair (blue line). The crystal structure of a GeS layer is shown at the right bottom.

at the same energy as the absorption edge measured with the same polarization direction. Thermoreflectance and optical absorption measurements with polarization along the zigzag direction revealed a transition around 50–100 meV higher in energy, which is close to our measured difference of energy ($\Delta E = 49$meV) between transitions E_1 and E_2.

The polar dependence of the amplitude (C_i) of each transition is shown in the inset of Fig. 3 for both high pressure (top half of the plot) and ambient pressure (bottom half). As it can be seen in the inset, the amplitudes corresponding to transition E_1 (blue dots) and E_2 (red dots) exhibit maximum at 90° (armchair direction) and 0° (zigzag), respectively. It is worth noting that the fitted amplitude of E_2 is significantly larger than E_1; this is due to the fact that the broadening of E_2 is larger than that of transition E_1. Indeed, the oscillation strength, which is proportional to $|C_i|/\ \Gamma_i$, is practically identical between both transitions. The polar dependence (solid curves) is fitted by using a modified Malus law,

$$f(\varphi) = f_{||}\cos^2(\varphi - \varphi_0) + f_{\perp}\sin^2(\varphi - \varphi_0), \qquad (2)$$

where φ is the light polarization angle, φ_0 is the polarization direction of the transition, and $f_{||}$ and $f_{\perp}$ are the parallel and perpendicular components of the oscillator strength, respectively. While transition E_1 is fully polarized (i.e., $f_{\perp} \approx 0$), the E_2 transition has a significant out of plane component ($f_{\perp} \approx 0.3 f_{||}$). The associated optical dichroic anisotropy is around 2000 and 300% for transitions E_1 and E_2, respectively. These values are on the same order of magnitude as those reported for SnS, around 600% [64]. Here we propose that the decreased optical polarization degree of transition E_2 is caused by parasitic band to band signal from the E_1 transition. Band to band signal is expected as long as the excitonic binding energy of E_1 has a value similar to the ambient thermal energy, around $k_B T_{amb} = 25$ meV. While no excitonic binding energies have been reported so far for bulk GeS, an excitonic binding energy around 30 meV would result in some band to band PR signal around the energy of transition E_2, which is just 49 meV above transition E_1, but with a perpendicular polarization direction, hence resulting in $f_{\perp} > 0$ for the current fit, as experimentally observed. More work is desirable to clarify the excitonic binding energies of transitions E_1 and E_2.

In order to individually track the pressure dependence of each optical transition, high-pressure PR measurements with polarizations along the armchair and zigzag directions were performed during the downstroke pressure cycle. The obtained spectra are shown in Fig. 4, where it can be seen that, by using the armchair polarization, two transitions are fully visible. These are E_1 and E_3 (the latter measured at ambient pressure only, due to lack of signal), while transition E_2 shows up only when the zigzag polarization is used. At ambient pressure these transitions are located at 1.61, 1.66, and 1.96 eV, in perfect agreement with previously reported polarization-resolved thermoreflectance measurements that established their energies at 1.59, 1.67, and 2.06 eV, respectively [12]. From Fig. 4 it is clear that the energy difference between transition E_1 and E_2 becomes smaller with increasing pressure. This is due to the increased pressure coefficient of transition E_2, as discussed below.

Fitted energies by using the Aspnes formula during both the upstroke and downstroke are shown as a functions of pressure in Fig. 5. As it can be seen in the figure, good agreement is found between upstroke (full symbols) and downstroke (open symbols) cycles. For the fitting procedure, the phase and broadening parameters (φ_i, Γ_i) were set at fixed values extracted from fits to polarized spectra at room pressure, and only the amplitude and transition energy parameters (C_i, E_i) were left as free parameters to fit high-pressure spectra. Within this approach, pressure coefficients were obtained from linear fits to the data; dE/dP (meV/kbar) $= -6.9(2)$ and $-8.3(9)$ for transitions E_1 and E_2, respectively. The

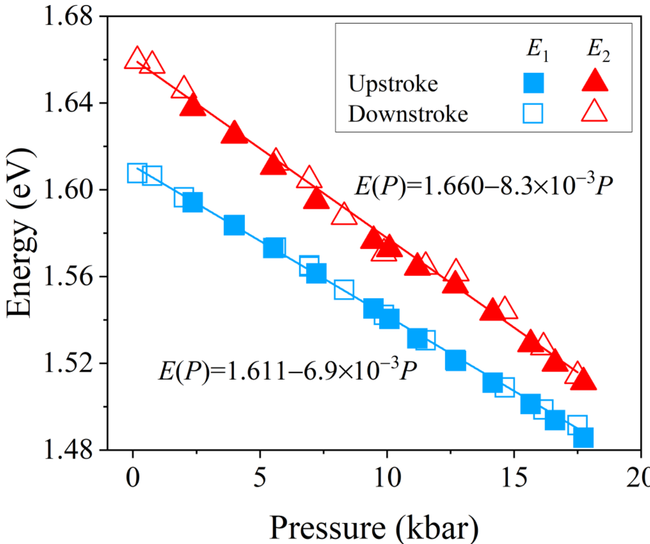

FIG. 5. Pressure dependence of the fitted direct transitions E_1 (squares) and E_2 (triangles) for spectra acquired during the upstroke (full symbols) and downstroke (open symbols) pressure cycles. Linear fits to the data are used to extract the pressure coefficients.

pressure coefficients obtained here are in good agreement with the values from optical absorption measurements reported previously, around -6.0 ± 1.5 meV/kbar for the absorption edge measured under armchair polarization direction (corresponding to the direct transition E_1) and -9.0 ± 1.5 meV/kbar measured under zigzag polarization direction (corresponding to signal arising from both the indirect transition E_0 and the direct transition E_2) [34]. From these results, energetic degeneracy of transitions E_1 and E_2 is expected to take place around 35 kbar. Since the pressure coefficients of transitions E_1 and E_2 are different, it is easier to assign them to the electronic band structure calculated at different pressures.

The calculated electronic band structure is shown in Fig. 6 for zero pressure (black lines) and 20 kbar (gray lines). These calculations predict that the indirect gap (shown as a green arrow) takes place from the valence-band maximum (VBM) close to the Z k-point to the conduction-band minimum (CBM) located around 2/3 of Γ-Y (labeled as Δ in the figure). The first three direct transitions are labeled E_1, E_2, and E_3 and take place at Γ, Δ, and close to Z, respectively. The two latter, which take place at non-high-symmetry k points with an enhanced joint density of states, are band-nesting transitions. These types of transitions have been previously reported in other families of layered compounds such as TMDs [65,66]. More importantly, the electronic band structure shown in Fig. 6 is composed of three valleys, one at Γ and two in the Γ-Z and Γ-Y reciprocal directions corresponding to the armchair and zigzag perpendicular crystallographic directions, respectively. Analog compounds such as SnS, SnSe, and GeSe exhibit a similar electronic dispersion but with a decreased band gap [67]. Interestingly, the two lowest transitions of these compounds in their monolayer form take place only around Z and Δ, while for GeS, a valley at Γ persists even in its monolayer form [68].

It can be shown that the three nondegenerate valleys of GeS can be individually selected by using linearly polarized

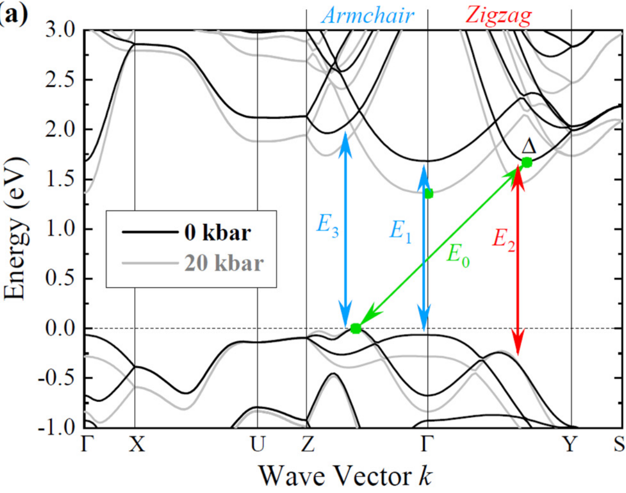

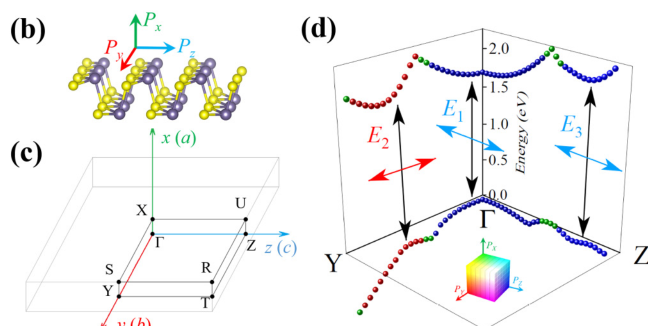

FIG. 6. (a) Electronic band structure calculated along the main high-symmetry points of the Brillouin zone at a pressure of 0 kbar (black curves) and 20 kbar (gray curves). The proposed indirect E_0 transition is indicated (green arrow) as well as the direct transitions E_1, E_2, and E_3 (blue and red arrows). CBM and VBM are indicated with green dots. (b) Light polarization directions as defined with respect to the crystal lattice. (c) Brillouin zone with labeled high-symmetry k points. The directions of the lattice parameters are included for clarity. (d) 3D plot of the electronic band-structure lines from (a) in the Y-Γ-Z region of the Brillouin zone. Three valleys are shown to have different polarization directions. For each valley, the matrix elements are shown as a RGB color code (P_y, P_x, and P_z, respectively).

light as a consequence of the selection rules of the crystal $Pnma - D_{2h}^{16}$ space group [69]. This feature can be exploited in designing a variety of valleytronic devices; for instance, transverse nonlinear conductivity has been demonstrated for the SnS analog [70]. In order to investigate the valley polarizability in GeS, optical matrix elements have been calculated along the Y-Γ-Z k-path. Results are shown as a color map in Fig. 6(d) where matrix elements contributing to the directions x, y, and z are represented by colors green, red, and blue, respectively. Our calculations reveal that all transitions are practically fully polarized (i.e., the matrix element for the perpendicular direction is zero), in good agreement with our experiments, which found small or negligible out of plane components of the PR signal (i.e., $f_\perp/f_{||} < 0.3$, as previously discussed). It is worth noting that calculated matrix elements within the present method have shown to accurately reproduce the relative photoluminescence intensity of TMDs [71], and

TABLE I. Assignation of direct optical transitions to different points of the BZ. Their respective experimental and calculated energies, polarization directions, and relative pressure coefficients are given.

		Energy (eV)		Polarization		$(1/E)dE/dP$ (10^{-3}kbar^{-1})	
Transition	Assignation	Experiment	Calc.	Experiment	Calc.	Experiment	Calc.
E_1	Γ	1.61	1.68	Armchair	Armchair	−4.3(1)	−3.1
E_2	Δ	1.66	2.05	Zigzag	Zigzag	−5.0(5)	−6.9
E_3	$\approx Z$	1.96	2.06	Armchair	Armchair		−6.6

are in perfect agreement with $\boldsymbol{k}\cdot\boldsymbol{p}$ theory for the selection rules of the *Pnma* space group [70].

The here proposed assignation of the direct excitonic transitions E_1, E_2 and E_3 to Brillouin-zone (BZ) points is summarized in Table I and has been performed considering the following factors; (i) transition energies, (ii) transition polarization directions, and (iii) pressure coefficients. As can be seen in Table I, the agreement between experimental and theoretical polarization directions is excellent. Within present limitations (no thermal or excitonic effects were considered in the calculations), the agreement between experimental and theoretical transition energies E_1 and E_3 is good (thermal and excitonic effects on the optical energy is expected to be smaller than $\Delta E \approx 250\,\text{meV}$) [14]. The relative pressure coefficients $(1/E)dE/dP$ are qualitatively in good agreement, where the pressure coefficient of transition E_2 is more pronounced. The calculated here pressure coefficients (−16.0 meV/kbar, −5.2 and −14.1 meV/kbar for the E_0, E_1, and E_2 transitions, respectively) are similar to those reported by Makinistian and Albanesi [24] from DFT calculations with GW corrections (−13.0, −4.8, and −9.5 meV/kbar for the E_0, E_1, and E_2 transitions, respectively). At higher pressures, the pressure coefficients decrease, and our calculations predict a transition to a semimetallic state at 130 kbar (see Fig. S3 in the SM) [54]. This result is consistent with high-pressure structural and electrical measurements, which revealed a phase transition at 90 kbar (phase $P21/m$), followed by a metallization around 150–200 kbar. [33]

The presented high-pressure optical results are useful to evaluate the effect of interlayer coupling on the electronic band structure. The orbital composition of the band structure in the Z-Γ-Y region of the BZ is shown in Fig. 7, where it can be seen that Ge (S) atoms contribute mostly to the conduction- (valence-) band states [see Figs. 7(a) and 6(b), respectively]. Calculated electron density isosurfaces associated with k points corresponding to each of the three direct optical transitions are shown in Fig. 7(c) [Fig. 7(d)] for the conduction (valence) band. From the figures, it is clear that the out of plane component (i.e., x direction) of the orbital composition is dominant at Γ. The pressure dependence positions of the states at Γ result from two competing contributions, on the one hand the destabilization of out of plane p_x orbitals as the interlayer distance diminish and on the other hand the stabilization of the p_x orbitals with contraction of in-plane lattice parameters, resulting in a redshift and a blueshift of the states, respectively. This is in perfect agreement with previously reported uniaxial and biaxial strain calculations, which show that under compression the CB exhibits a redshift around Γ while the VB a blueshift around Z [9,30–32]. Additional calculations under uniaxial strain, both compressive and tensile, on the electronic band structure further support this interpretation (results are shown in Fig. S2 of the SM). Under hydrostatic pressure, an overall redshift of the states at Γ take place. Indeed, our calculations reveal that with increased pressure, the band gap narrows mostly due to a relative increase of the VB around Z and a decrease of the CB at Γ, which becomes the CBM at 20 kbar [CBM and VBM are represented as green dots in Fig. 6(a)]. Moreover, our calculations show that the gap is closed at 130 kbar for a CBM located at Γ and VBM at Z (see Fig. S3 of the SM) [54]. In general, the effect of increased pressure has a similar impact on the band structure as increasing the number of layers, from monolayer to bulk. This trend has been observed for all GeS analogs, where increasing the interlayer interaction from monolayer to bulk results in an overall decrease of the CBM located at Γ and an increase of the VBM at Z [67]. Similar conclusions have been found for other layered compounds such as MoS_2 and ReS_2 [28].

The clear agreement between calculated and experimental polarization directions (all transitions being fully polarized), qualitative agreement on pressure coefficients and transition energies E_1 and E_3 as shown in Table I, allow us to unambiguously assign the first three optical transitions in the Z-Γ-Y region of the BZ. However, the calculated energy of transition E_2 is significantly overestimated. The fact that GeS analogs (i.e., SnS, SnSe, GeSe) clearly exhibit a prominent valence-band local maxima around Δ, from their monolayer form up to bulk [20,67,68], suggests that calculations fail to reproduce the valence-band electronic dispersion in the Γ-Y region. Similar results are reported in the literature, where most DFT calculations reported decrease [17,20,23,25,26,67] or are inexistent [67,68] VB local maximum around Δ in either bulk or monolayer forms. Angle-resolved photoemission fine-structure spectroscopy measurements show that the local VB at Δ should be ≈250 meV below the VBM at Z [72]. From these results, it seems that our calculations underestimate the energy of the VB at Δ by just 150 meV. Since the energetic difference between calculations and experiments is larger (i.e., $\Delta E = 390\,\text{meV}$, from Table I), we expect that transition E_2 has a large excitonic binding energy, around 240 meV. Such value could be valid in GeS since, in its monolayer form, excitonic binding energies are as large as 0.7–1.2 eV. [22] However, excitonic binding energies are not yet experimentally established for bulk GeS and more work is desirable both experimentally and theoretically to understand the exact electronic dispersion of the valence band in the Γ-Y region of the BZ.

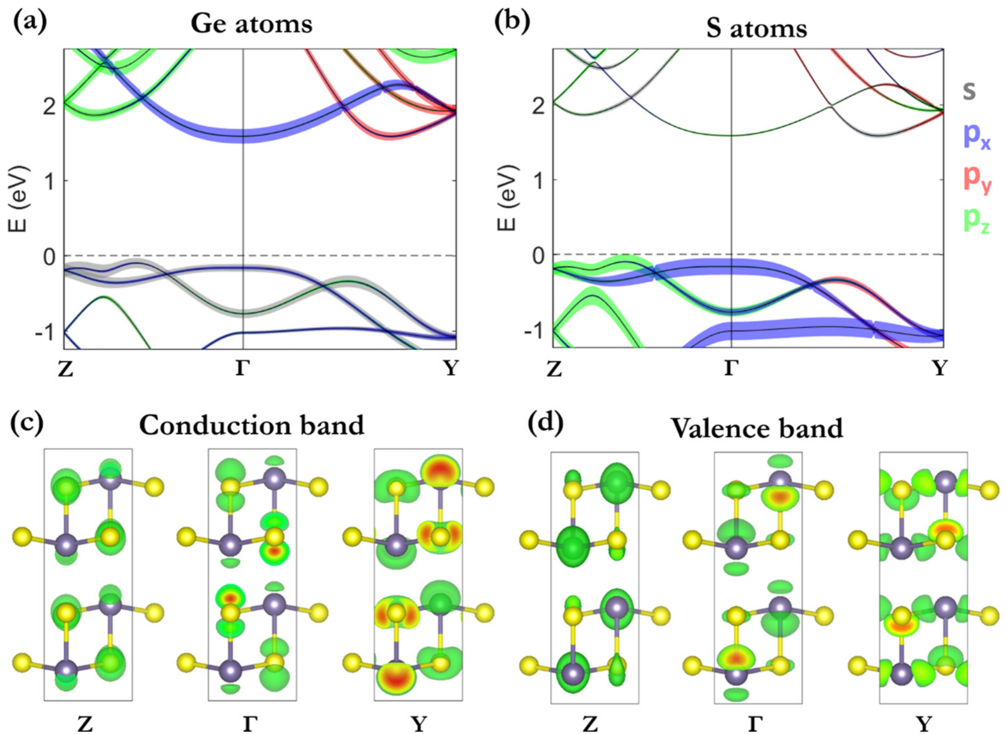

FIG. 7. (a), (b) Calculated band structure in the Z-Γ-Y region of the BZ at zero pressure. The calculated orbital composition for Ge and S atoms (left and right panel, respectively) is represented with different colors (see the legend on the right) and is proportional to the line thickness. Calculations are performed within the PBE functional with TS correction. (c), (d) Plots of calculated electron density isosurfaces (surface level 0.0057 e/Å^3) calculated at k points corresponding to each of the three direct optical transitions (close to the Z, Γ, and Y k points) for conduction-band electrons and valence-band electrons. The view plane is defined by the zigzag- (y) and out of plane (x) directions.

IV. CONCLUSIONS

To summarize, we performed polarization-resolved high-pressure PR measurements on GeS. We found that the first and third direct optical transitions were polarized in the armchair direction while the second was polarized in the zigzag direction with dichroic ratios of 2000 and 300%, respectively. Fits to the spectra acquired during the upstroke (unpolarized measurements) and downstroke (polarized measurements) allowed us to extract the pressure dependence of the first two direct optical transitions. The obtained pressure coefficient for the first (second) optical transition is −6.9 meV/kbar (−8.3 meV/kbar). First-principles calculations were used to explore the valley physics in GeS. Calculated matrix elements, transition energies, and pressure coefficients allowed us to unambiguously assign the experimentally measured optical transitions. Finally, the effect of pressure and number of layers on the electronic band structure was discussed in terms of orbital composition. Our results provide a comprehensive picture of the electronic band structure and optical properties of GeS and validate its potential for valleytronic applications in nondegenerate systems.

ACKNOWLEDGMENTS

This work was supported by the National Science Centre (NCN) Poland OPUS 11 Grant No. 2016/21/B/ST3/00482. R.O.V. acknowledges the support by POLONEZ 3 Grant No. 2016/23/P/ST3/04278. This project is carried out under the POLONEZ program which has received funding from the European Union's Horizon 2020 research and innovation program under the Marie Sklodowska-Curie Grant Agreement No. 665778. T.W. acknowledges support within the "Diamond Grant" No. 0026/DIA/2016/45 from the Polish Ministry of Science and Higher Education. DFT calculations were performed in Wroclaw Centre for Networking and Supercomputing.

[1] K. S. Novoselov, A. K. Geim, S. V. Morozov, D. Jiang, Y. Zhang, S. V. Dubonos, I. V. Grigorieva, and A. A. Firsov, Science **306**, 666 (2004).

[2] X. Liu, T. Galfsky, Z. Sun, F. Xia, E. Lin, Y.-H. Lee, S. Kéna-Cohen, and V. M. Menon, Nat. Photonics **9**, 30 (2015).

[3] M. Samadi, N. Sarikhani, M. Zirak, H. Zhang, H.-L. Zhang, and A. Z. Moshfegh, Nanoscale Horiz. **3**, 90 (2018).

[4] A. V. Kolobov and J. Tominaga, *Two-Dimensional Transition-Metal Dichalcogenides* (Springer International Publishing, Cham, 2016).

[5] R. Oliva, T. Wozniak, F. Dybala, J. Kopaczek, P. Scharoch, and R. Kudrawiec, Mater. Res. Lett. **8**, 75 (2020).

[6] X. Zhang, Q. Liu, J.-W. Luo, A. J. Freeman, and A. Zunger, Nat. Phys. **10**, 387 (2014).

[7] A. Castellanos-Gomez, J. Phys. Chem. Lett. **6**, 4280 (2015).
[8] A. Khandelwal, K. Mani, M. H. Karigerasi, and I. Lahiri, Mater. Sci. Eng.: B **221**, 17 (2017).
[9] F. Li, X. Liu, Y. Wang, and Y. Li, J. Mater. Chem. C **4**, 2155 (2016).
[10] Z. Li, Y. Yang, X. Wang, W. Shi, D.-J. Xue, and J.-S. Hu, ACS Appl. Mater. Interfaces **11**, 24247 (2019).
[11] R. K. Ulaganathan, Y.-Y. Lu, C.-J. Kuo, S. R. Tamalampudi, R. Sankar, K. M. Boopathi, A. Anand, K. Yadav, R. J. Mathew, C.-R. Liu, F. C. Chou, and Y.-T. Chen, Nanoscale **8**, 2284 (2016).
[12] H.-C. Hsueh, J.-X. Li, and C.-H. Ho, Adv. Opt. Mater. **6**, 1701194 (2018).
[13] P. Zhao, H. Yang, J. Li, H. Jin, W. Wei, L. Yu, B. Huang, and Y. Dai, J. Mater. Chem. A **5**, 24145 (2017).
[14] C.-H. Ho and J.-X. Li, Adv. Opt. Mater. **5**, 1600814 (2017).
[15] J. D. Wiley, A. Breitschwerdt, and E. Schönherr, Solid State Commun. **17**, 355 (1975).
[16] A. M. Elkorashy, J. Phys. C: Solid State Phys. **21**, 2595 (1988).
[17] D. Tan, H. E. Lim, F. Wang, N. B. Mohamed, S. Mouri, W. Zhang, Y. Miyauchi, M. Ohfuchi, and K. Matsuda, Nano Res. **10**, 546 (2017).
[18] S. J. Zelewski and R. Kudrawiec, Sci. Rep. **7**, 15365 (2017).
[19] A. K. Singh and R. G. Hennig, Appl. Phys. Lett. **105**, 042103 (2014).
[20] B. D. Malone and E. Kaxiras, Phys. Rev. B **87**, 245312 (2013).
[21] L. C. Gomes, P. E. Trevisanutto, A. Carvalho, A. S. Rodin, and A. H. Castro Neto, Phys. Rev. B **94**, 155428 (2016).
[22] B. R. Tuttle, S. M. Alhassan, and S. T. Pantelides, Phys. Rev. B **92**, 235405 (2015).
[23] L. Makinistian and E. A. Albanesi, Phys. Rev. B **74**, 045206 (2006).
[24] L. Makinistian and E. A. Albanesi, Comput. Mater. Sci. **50**, 2872 (2011).
[25] A. Rathor, V. Sharma, N. L. Heda, Y. Sharma, and B. L. Ahuja, Radiat. Phys. Chem. **77**, 391 (2008).
[26] C. E. P. Villegas, A. R. Rocha, and A. Marini, Phys. Rev. B **94**, 134306 (2016).
[27] T. Suski and W. Paul, *High Pressure in Semiconductor Physics I and II, Semiconductors and Semimetals* (Academic Press, San Diego, 1998).
[28] R. Oliva, M. Laurien, F. Dybala, J. Kopaczek, Y. Quin, S. Tongay, O. Rubel, and R. Kudrawiec, Npj 2D Mater. Appl. **3**, 20 (2019).
[29] F. Dybała, M. P. Polak, J. Kopaczek, P. Scharoch, K. Wu, S. Tongay, and R. Kudrawiec, Sci. Rep. **6**, 26663 (2016).
[30] B. W. Li, Y. Wang, Y. Q. Xie, L. Zhu, and K. L. Yao, Nanotechnology **28**, 435202 (2017).
[31] K. D. Pham, C. V. Nguyen, H. V. Phuc, T. V. Vu, N. V. Hieu, B. D. Hoi, L. C. Nhan, V. Q. Nha, and N. N. Hieu, Superlattices Microstruct. **120**, 501 (2018).
[32] S. Zhang, N. Wang, S. Liu, S. Huang, W. Zhou, B. Cai, M. Xie, Q. Yang, X. Chen, and H. Zeng, Nanotechnology **27**, 274001 (2016).
[33] R. P. Dias, M. Kim, and C.-S. Yoo, Phys. Rev. B **93**, 104107 (2016).
[34] G. Valiukonis, D. A. Guseinova, G. Keivaitb, and A. Sileika, Phys. Status Solidi B **135**, 299 (1986).
[35] GeS - Germanium sulfide, http://www.hqgraphene.com/GeS.php (2020).
[36] K. Momma and F. Izumi, J Appl Crystallogr. **44**, 1272 (2011).
[37] G. Kresse and J. Furthmüller, Phys. Rev. B **54**, 11169 (1996).
[38] G. Kresse and D. Joubert, Phys. Rev. B **59**, 1758 (1999).
[39] J. P. Perdew, K. Burke, and M. Ernzerhof, Phys. Rev. Lett. **77**, 3865 (1996).
[40] S. Grimme, J. Comput. Chem. **27**, 1787 (2006).
[41] S. Grimme, J. Antony, S. Ehrlich, and H. Krieg, J. Chem. Phys. **132**, 154104 (2010).
[42] S. Grimme, S. Ehrlich, and L. Goerigk, J. Comput. Chem. **32**, 1456 (2011).
[43] A. Tkatchenko and M. Scheffler, Phys. Rev. Lett. **102**, 073005 (2009).
[44] T. Bučko, S. Lebègue, J. G. Ángyán, and J. Hafner, J. Chem. Phys. **141**, 034114 (2014).
[45] A. Tkatchenko, R. A. DiStasio, R. Car, and M. Scheffler, Phys. Rev. Lett. **108**, 236402 (2012).
[46] S. N. Steinmann and C. Corminboeuf, J. Chem. Phys. **134**, 044117 (2011).
[47] M. Dion, H. Rydberg, E. Schröder, D. C. Langreth, and B. I. Lundqvist, Phys. Rev. Lett. **92**, 246401 (2004).
[48] Y. Zhang and W. Yang, Phys. Rev. Lett. **80**, 890 (1998).
[49] J. Klimeš, D. R. Bowler, and A. Michaelides, J. Phys.: Condens. Matter **22**, 022201 (2009).
[50] J. Klimeš, D. R. Bowler, and A. Michaelides, Phys. Rev. B **83**, 195131 (2011).
[51] K. Lee, É. D. Murray, L. Kong, B. I. Lundqvist, and D. C. Langreth, Phys. Rev. B **82**, 081101(R) (2010).
[52] É. D. Murray, K. Lee, and D. C. Langreth, J. Chem. Theory Comput. **5**, 2754 (2009).
[53] I. Hamada, Phys. Rev. B **89**, 121103(R) (2014).
[54] See Supplemental Material at http://link.aps.org/supplemental/10.1103/PhysRevB.101.235205 for the sketch of the experimental setup, electronic bandstructure under strain and higher pressures and tables of calculated lattice parameters and transition energies.
[55] W. H. Zachariasen, Phys. Rev. **40**, 917 (1932).
[56] G. Bissert and K.-F. Hesse, Acta Crystallogr. B **34**, 1322 (1978).
[57] H. Wiedemeier and H. G. von Schnering, Z. Kristallogr. **148**, 295 (1978).
[58] H. C. Hsueh, M. C. Warren, H. Vass, G. J. Ackland, S. J. Clark, and J. Crain, Phys. Rev. B: Condens. Matter **53**, 14806 (1996).
[59] F. Tran and P. Blaha, Phys. Rev. Lett. **102**, 226401 (2009).
[60] M. Gajdoš, K. Hummer, G. Kresse, J. Furthmüller, and F. Bechstedt, Phys. Rev. B **73**, 045112 (2006).
[61] R. Kudrawiec and J. Misiewicz, Appl. Surf. Sci. **253**, 80 (2006).
[62] F. Lukeš, E. Schmidt, J. Humlíček, and P. Dub, Phys. Status Solidi B **122**, 675 (1984).
[63] D. E. Aspnes, Surf. Sci. **37**, 418 (1973).
[64] S. Lin, A. Carvalho, S. Yan, R. Li, S. Kim, A. Rodin, L. Carvalho, E. M. Chan, X. Wang, A. H. Castro Neto, and J. Yao, Nat. Commun. **9**, 1455 (2018).
[65] A. Carvalho, R. M. Ribeiro, and A. H. Castro Neto, Phys. Rev. B **88**, 115205 (2013).
[66] J. Kopaczek, M. P. Polak, P. Scharoch, K. Wu, B. Chen, S. Tongay, and R. Kudrawiec, J. Appl. Phys. **119**, 235705 (2016).

[67] L. C. Gomes and A. Carvalho, Phys. Rev. B **92**, 085406 (2015).
[68] R. Li, H. Cao, and J. Dong, Phys. Lett. A **381**, 3747 (2017).
[69] M. S. Dresselhaus, G. Dresselhaus, and A. Jorio, *Group Theory: Application to the Physics of Condensed Matter* (Springer-Verlag, Berlin, 2008).
[70] A. S. Rodin, L. C. Gomes, A. Carvalho, and A. H. Castro Neto, Phys. Rev. B **93**, 045431 (2016).
[71] T. Woźniak, P. E. F. Junior, G. Seifert, A. Chaves and J. Kunstmann, Phys. Rev. B **101**, 235408 (2020).
[72] T. Grandke and L. Ley, Phys. Rev. B **16**, 832 (1977).

Supplementary Material

Valley polarization investigation of GeS under high pressure

R. Oliva,* T. Woźniak, F. Dybala, A. Tołłoczko, J. Kopaczek, P. Scharoch, and R. Kudrawiec

*robert.oliva.vidal@pwr.edu.pl

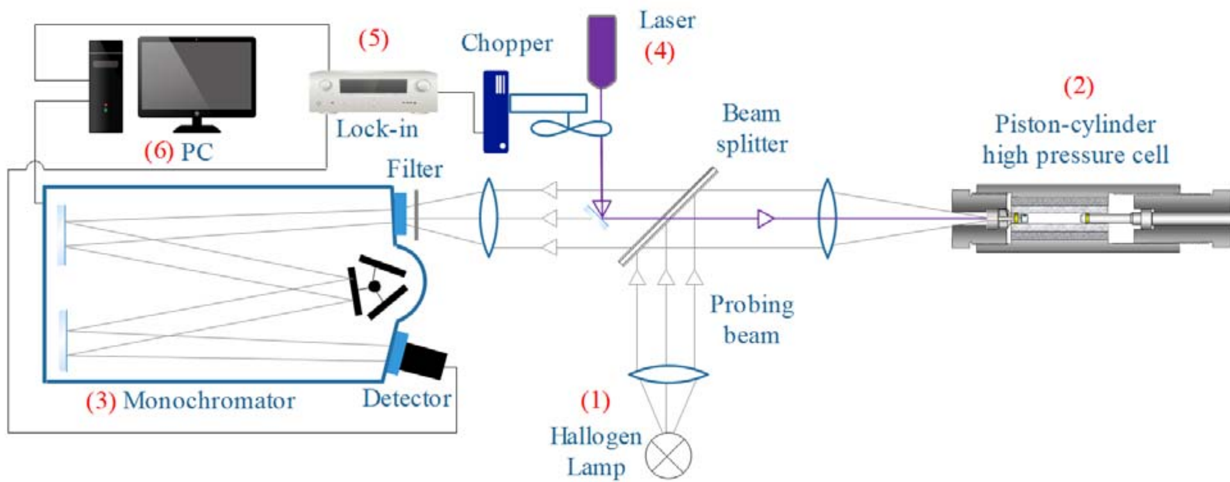

Fig. S1. Sketch of the experimental setup used for high-pressure photoreflectance measurements. A white light from halogen lamp (1) is directed into the piston-cylinder high-pressure cell (2), where the GeS sample is mounted. Reflected signal is focused by means of lenses into the monochromator (3). The reflectivity is modulated by a chopped 405-nm solid state laser (4). The signal is processed by a lock-in amplifier (5) and collected in the computer (6).

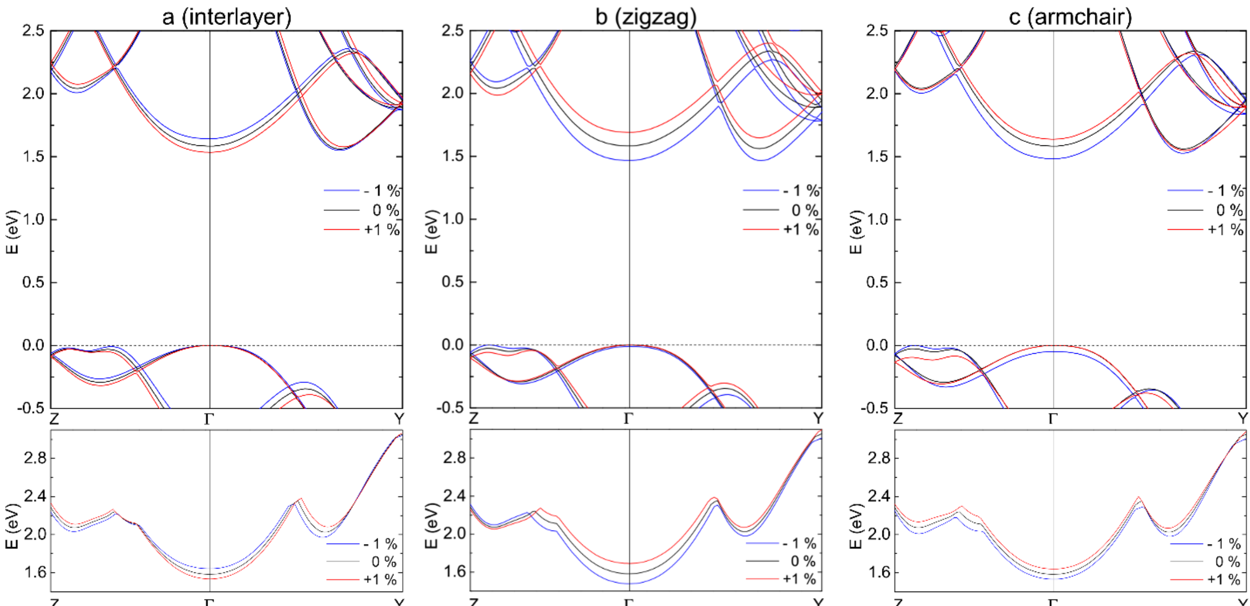

Fig. S2. Effect of uniaxial strain, applied in three different directions, on the calculated electronic band structure.

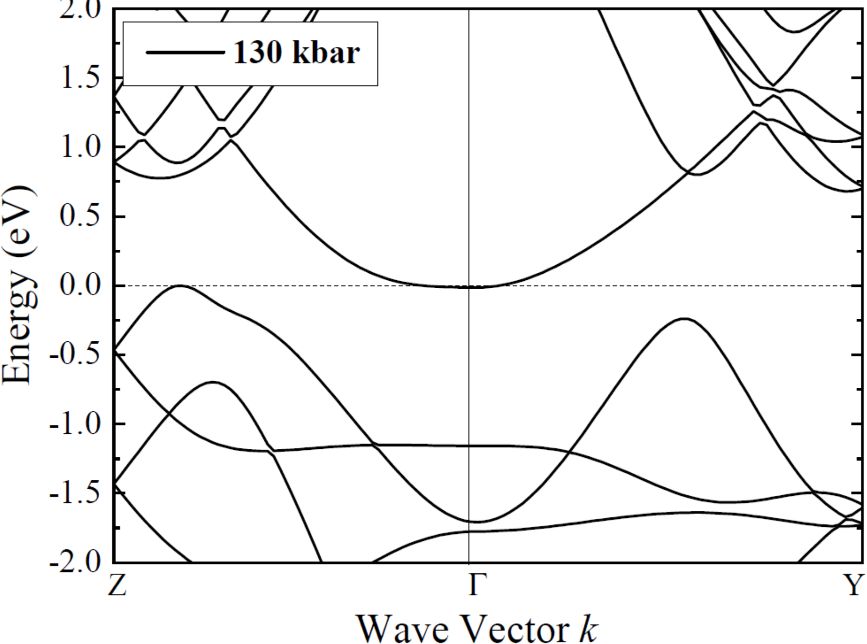

Fig. S3. Electronic band structure at a pressure of 130 kbar.

Table S1. Calculated lattice constants, relative errors with respect to the experimental values and mean absolute relative error (MARE). In the last row, average experimental values reported in Refs [1-4] and references therein are presented.

DFT method		Lattice constants (Å)			Relative error (%)			MARE (%)
		a	***b***	***c***	***a***	***b***	***c***	
Semi-empirical corrections	D2	10.655	3.654	4.364	1.65	0.29	1.48	1.14
	D3	10.642	3.658	4.471	1.53	0.40	3.97	1.97
	D3+BJ	10.657	3.679	4.357	1.67	0.98	1.32	1.32
	TS	10.461	3.666	4.359	−0.17	0.62	1.36	0.72
	TS+HP	10.556	3.665	4.316	0.71	0.59	0.36	0.55
	MBD	10.437	3.673	4.254	−0.43	0.81	−1.08	0.77
	dDsC	10.424	3.670	4.210	−0.55	0.73	−2.10	1.13
van der Waals functionals	revPBE	11.026	3.699	4.553	5.19	1.53	5.88	4.20
	optPBE	11.026	3.698	4.554	5.19	1.50	5.90	4.20
	optB88	11.026	3.699	4.553	5.19	1.53	5.88	4.20
	optB86b	11.027	3.698	4.553	5.20	1.50	5.88	4.19
	rPW86	11.177	3.703	4.62	6.63	1.64	7.43	5.23
	B86r	11.173	3.795	4.615	6.59	4.16	7.32	6.02
Experimental values	Average	10.482	3.643	4.300				

Table S2. Calculated transition energies (with mBJ-TB09 potential) with experimental and optimized lattice constants taken from Table S1, relative errors with respect to the experimental values and mean absolute relative error (MARE).

Lattice constants	vdW method	Transition energies (eV)				Relative error (%)				MARE (%)
		E_0	E_1	E_2	E_3	E_0	E_1	E_2	E_3	
experimental	D2	1.677	1.975	1.954	1.531	−1.4	9.9	−6.8	−9.2	9.1
	D3	1.601	1.977	1.981	1.492	−5.9	10.0	−5.5	−11.5	11.0
	D3+BJ	1.689	1.968	1.966	1.496	−0.7	9.5	−6.3	−11.2	9.2
	TS	1.597	1.986	1.993	1.473	−6.1	10.5	−4.9	−12.6	11.4
	TS+HP	1.762	1.983	1.962	1.500	3.6	10.4	−6.4	−11.0	10.5
	MBD	1.585	1.995	1.952	1.468	−6.8	11.0	−6.9	−12.9	12.5
	dDsC	1.588	1.949	1.883	1.467	−6.6	8.5	−10.2	−13.0	12.8
optimized	D2	1.717	2.129	2.086	1.668	1.0	18.5	−0.5	−1.0	7.0
	D3	1.749	2.228	2.253	1.654	2.8	24.0	7.4	−1.8	12.0
	D3+BJ	1.747	2.086	2.132	1.666	2.7	16.1	1.7	−1.1	7.2
	TS	1.684	2.059	2.051	1.681	−1.0	14.6	−2.2	−0.2	6.0
	TS+HP	1.800	2.056	1.997	1.582	5.8	14.4	−4.8	−6.1	10.4
	MBD	1.624	1.919	1.908	1.463	−4.5	6.8	−9.0	−13.2	11.2
	dDsC	1.565	1.860	1.834	1.339	−8.0	3.5	−12.5	−20.5	14.9
	Experimental values	1.701	1.797	2.097	1.685					

Table S3. Calculated transition energies (with HSE06 functional) with experimental and optimized lattice constants from Table S1, relative errors with respect to the experimental values and mean absolute relative error (MARE).

Lattice constants	vdW method	Transition energies (eV)				Relative error (%)				MARE (%)
		E_0	E_1	E_2	E_3	E_0	E_1	E_2	E_3	
experimental	D2	1.805	2.245	2.092	1.653	6.1	24.9	−0.2	−1.9	11.1
	D3	1.718	2.241	2.115	1.606	1.0	24.7	0.9	−4.7	10.4
	D3+BJ	1.815	2.236	2.100	1.608	6.7	24.4	0.1	−4.6	11.9
	TS	1.711	2.248	2.120	1.577	0.6	25.1	1.1	−6.4	11.1
	TS+HP	1.888	2.251	2.092	1.605	11.0	25.2	−0.2	−4.8	13.8
	MBD	1.701	2.215	2.128	1.579	0.0	23.2	1.5	−6.3	10.4
	dDsC	1.751	2.174	2.042	1.578	2.9	21.0	−2.6	−6.4	11.0
optimized	D2	1.835	2.407	2.224	1.789	7.9	34.0	6.0	6.2	18.0
	D3	1.860	2.510	2.396	1.793	9.4	39.7	14.3	6.4	23.2
	D3+BJ	1.868	2.404	2.221	1.780	9.8	33.8	5.9	5.6	18.4
	TS	1.875	2.322	2.183	1.802	10.2	29.2	4.1	6.9	16.8
	TS+HP	1.914	2.325	2.130	1.690	12.5	29.4	1.6	0.3	14.6
	MBD	1.751	2.174	2.042	1.578	2.9	21.0	−2.6	-6.4	11.0
	dDsC	1.691	2.109	1.974	1.460	−0.6	17.4	−5.8	-13.4	12.4
	Experimental values	1.701	1.797	2.097	1.685					

References

1. W. H. Zachariasen, Phys. Rev., 1932, 40, 917–922.

2. G. Bissert and K.-F. Hesse, Acta Crystallogr. B, 1978, 34, 1322–1323.

3. H. Wiedemeier and H. Georg von Schnering, Z. Krist., , DOI:10.1524/zkri.1978.148.3-4.295.

4. H. C. Hsueh, M. C. Warren, H. Vass, G. J. Ackland, S. J. Clark and J. Crain, Phys. Rev. B, 1996, 53, 14806–14817.

CHAPTER 4

Linear dichroism of the optical properties of SnS and SnSe van der Waals crystals

Agata K. Tołłoczko, Jakub Ziembicki, Miłosz Grodzicki, Jarosław Serafińczuk, Seth A. Tongay, Melike Erdi, Natalia Olszowska, Marcin Rosmus, Robert Kudrawiec

Submitted to ACS Photonics, DOI: 10.48550/arXiv.2409.17412

Overview

SnS and SnSe crystals were characterized by means of optical spectroscopy and photoemission spectroscopy, supported by *ab initio* calculations. The studies revealed high sensitivity of the optical response of both materials to the incident light polarization, which is interpreted with regard to the orbital composition of the electronic bands and symmetry-related selection rules. From the photoemission investigation, we determined the ionization potential, electron affinity, and work function of SnS and SnSe.

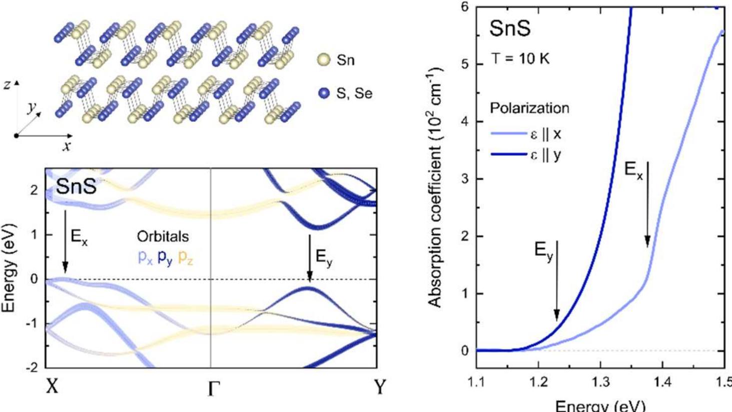

Fig. 4.1 Graphical abstract. Reprinted from Ref. [102] under CC-BY 4.0 license. Copyright 2024 A. K. Tołłoczko *et al.*

Author's contribution

Agata K. Tołłoczko (corresponding author) carried the optical spectroscopy (PR, optical absorption) and UV photoemission spectroscopy experiments, processed and analyzed the acquired data, prepared their graphical presentation, proposed the interpretation, and wrote the manuscript.

Linear dichroism of the optical properties of SnS and SnSe van der Waals crystals

Agata K. Tołłoczko,*[a] Jakub Ziembicki,[a] Miłosz Grodzicki,[ab] Jarosław Serafińczuk,[ab] Natalia Olszowska,[d] Marcin Rosmus,[d] Seth A. Tongay,[c] Melike Erdi,[c] and Robert Kudrawiec[ab]

[a] Department of Semiconductor Materials Engineering, Wrocław University of Science and Technology, Wybrzeże Wyspiańskiego 27, 50-370 Wrocław, Poland

[b] Łukasiewicz Research Network – PORT Polish Center for Technology Development, Stabłowicka 147, Wrocław, Poland

[c] School for Engineering of Matter, Transport and Energy Arizona State University Tempe, AZ 85287, USA

[d] Solaris National Synchrotron Radiation Centre, Jagiellonian University, Czerwone Maki 98, 30-392 Kraków, Poland

KEYWORDS van der Waals crystals, anisotropy, linear dichroism, optical absorption, photoemission, tin sulfide, tin selenide

ABSTRACT: Tin monochalcogendies SnS and SnSe, belonging to a family of van der Waals crystals isoelectronic to black phosphorus, are known as environmentally-friendly materials promising for thermoelectric conversion applications. However, they exhibit other desired functionalities, such as intrinsic linear dichroism of the optical and electronic properties originating from strongly anisotropic orthorhombic crystal structure. This property makes them perfect candidates for polarization-sensitive photodetectors working in near infrared spectral range. We present a comprehensive study of the SnS and SnSe crystals by means of optical spectroscopy and photoemission spectroscopy, supported by ab initio calculations. The studies revealed the high sensitivity of the optical response of both materials to the incident light polarization, which we interpret in terms of the electronic band dispersion and orbital composition of the electronic bands, dictating the selection rules. From the photoemission investigation we determine the ionization potential, electron affinity and work function, which are parameters crucial for the design of devices based on semiconductor heterostructures.

INTRODUCTION

The unique layered structure and possibility of obtaining atomically thin flakes make van der Waals (vdW) crystals[1,2] perfect candidates for applications in two-dimensional electronics and optoelectronics, such as photodetectors, solar cells, and light emitters. An interesting class of devices are polarization-sensitive photodetectors, as their responsivity depends on the incident light polarization. Such technology can be exploited for detection of light polarization changes after traveling through a birefringent medium, including various solids, liquid crystals, but also biological systems, such as protein solutions.[3] In the case of the latter, the measured polarization angle shift may allow to determine presence of certain proteins in a sample, which is extremally important in diagnostics. Unfortunately, the state-of-the-art polarization-sensitive photodetectors are rather complex, as they demand integration of multiple optical components. The design, however, can be significantly simplified by exploiting the materials with intrinsic anisotropy of the optical properties.[4–6] Among vdW crystals, such properties was observed for black phosphorus (BP)[6–8] and its binary analogues, group IV monochalcogenides (MX, where M = Ge, Sn, and X = S, Se).[9–16] Since MXs exhibit stability in atmospheric conditions superior to BP,[9,17] they are more suitable for most applications, including photodetection. The origin of the anisotropy is the structure of the materials. Similarly to BP, MXs crystalize in a distorted orthorhombic structure (space group *Pnma*, no. 62) with strong in-plane anisotropy of the atomic arrangement, as schematically presented in Figure 1a. Along the x axis the structure is puckered, while a ladder-like pattern is observed in the y direction. The anisotropy of the crystal lattice induces directionality of the electronic band dispersion, which then determines the dielectric function and the optical properties. For the considered 1:1 stoichiometry, the metal atom is in the +2 oxidation state and forms three bonds with chalcogen atoms and a lone electron pair in the tetragonal coordination.[18] The presence of the stereochemically active lone pairs is also know to reduce the ionization potential of a material[19–21] and influence the photoconversion efficiency, as in the case of metal-halide perovskites.[22,23]

Among the MX family, tin monochalcogenides are characterized by relatively narrow indirect band gaps in the near infrared spectral range (1.1 and 0.9 eV for SnS and SnSe, respectively),[24,25] high absorption coefficient, and intrinsic p-type conductivity, enhanced by

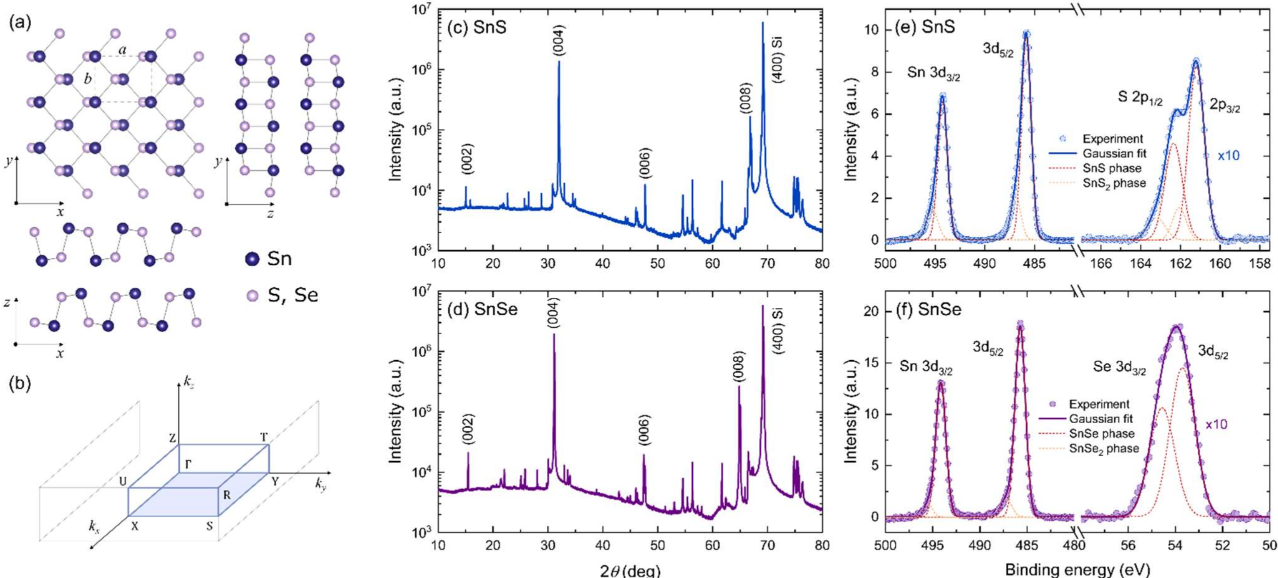

Figure 1. Schematic illustration of the crystal structure created with VESTA software[26] (a), the first Brillouin zone of the reciprocal orthorhombic structure (b), the results of XRD characterization for SnS (c) and SnSe (d), and core level XPS spectra of SnS (e) and SnSe (f). In panels e and f the Gaussian line-shape (dark solid lines) were fitted to the experimental points (circles). The components of the Gaussian fits corresponding to SnX and SnX_2 phases are plotted with dashed red and yellow lines, respectively.

the presence of native acceptor defects,[27–31] making them perfect candidates for infrared polarization-sensitive photodetectors. Apart from optoelectronics, SnX crystals poses vast potential for applications as thermoelectric materials,[32–35] extremally desired in the era of growing energy demand. For SnSe, Zhao *et al.*[32] reported unexpectedly high thermoelectric figure of merit of 2.6, exceeding the performance of typical state-of-the-art Pb-based materials.[36]

In this work we investigate the linear dichroism of the optical properties of SnS and SnSe by means of optical spectroscopy and search for its origins in the electronic band structure, studied by combined density functional theory (DFT) calculations and photoemission spectroscopy. We discuss the influence of the stereochemical activity of the lone electron pairs on the energies of the electronic bands with respect to the vacuum level, crucial for the engineering of semiconductor heterostructures and metal contacts.[28,37–40] The obtained results provide in-depth understanding of the mechanisms responsible for the observed phenomena at the fundamental level and reflect the empirical implications of the selection rules.

RESULTS AND DISCUSSION

Structural characterization

SnS and SnSe crystalize in a distorted orthorhombic phase, schematically presented in Figure 1a. In Figure 1b the first Brillouin zone (BZ) of the reciprocal space is illustrated, with marked high-symmetry points. The structure of the investigated samples was confirmed by X-ray diffraction measurements (XRD), revealing characteristic reflexes, assigned according to the PDF-4 database[41] (SnS card no. 00-067-0519, SnSe card no. 00-048-1224), as shown in Figure 1c. For both crystals, a dominant [001] orientation was observed in the diffraction patterns. In addition, a reflection from Si (400) plane was detected. The lattice parameter *c* (corresponding to the out-of-plane crystallographic direction) equals 11.18 and 11.48 Å for SnS and SnSe, respectively, in agreement with previous reports.[42]

An investigation of the chemical composition was performed using core level X-ray photoemission spectroscopy (XPS) (Figure 1d,e). The full-scale spectra, plotted in Figure S1 of the Supporting Information (SI), only show the presence of Ge or Sn and S or Se atoms, with negligible traces of oxygen and carbon, indicating high purity of the sample surface. In Figure 1d,e regions of the spectra with characteristic features related to contributing elements are presented, for SnS (panel d) and SnSe (panel e), identified after Moulder *et al.*[43] The energies of individual orbital levels were determined by fitting the Gaussian line-shape to the acquired data. For S in SnS a doublet corresponding to 2*p* orbitals was observed, with the expected $p_{3/2} : p_{1/2}$ intensity ratio of ~2:1. For Se in SnSe, a 3*d* doublet can be identified, with the $d_{5/2} : d_{3/2}$ intensity ratio of ~3:2. For Sn atoms, signal associated with 3*d* orbitals was detected. The exact energies and spin-orbit splitting values of the observed lines are summarized in Table S1 of the SI. Along with the core levels corresponding to the SnX phase (with Sn at the +2 oxidation state), plotted as red dashed components of the Gaussian fits, a weak signal originating from the SnX_2 phase (Sn at the +4 oxidation state, yellow dashed lines) was observed as an asymmetrical broadening of the XPS lines. The contribution of side-lines could not be resolved for the SnSe Se 3*d* peak due to close position of $d_{3/2}$ and $d_{5/2}$ components, but is apparent for other measured lines, indicating presence of chalcogen-rich domains at the sample surface, which is not unusual (tin vacancies are one of the most stable native defects in the system, responsible for the intrinsic *p*-type character).[44–46]

Optical properties

The optical properties of SnS and SnSe crystals were investigated by means of complementary methods of optical spectroscopy: photoreflectance (PR), sensitive to direct optical transitions,[47–49] and optical absorption allowing to detect both direct and indirect band gap. In Figure 2, a comparison of the photoreflectance and optical absorption spectra acquired at the temperature of 20 K for SnS

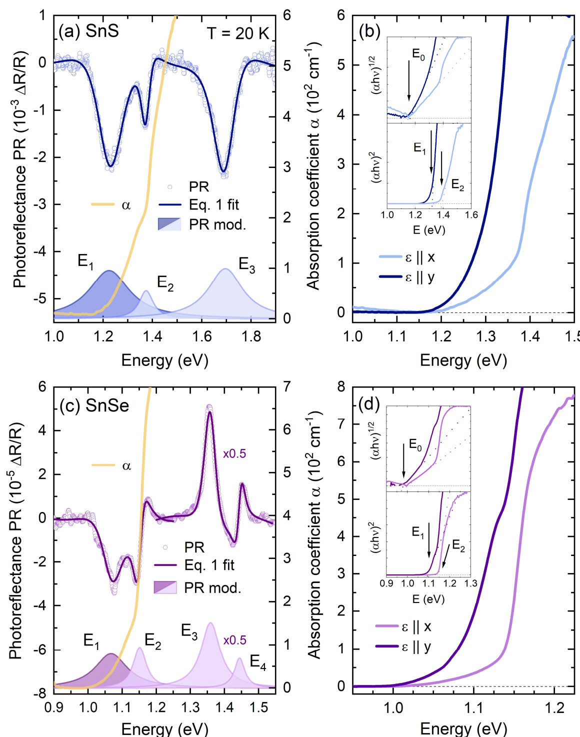

Figure 2. (a, c) The unpolarized photoreflectance and optical absorption spectra acquired for SnS (a) and SnSe (c). The fit with the Aspnes formula (dark solid lines) is superimposed over the experimental PR data (circles). The absorption coefficient α is plotted with solid yellow lines. Shaded areas at the bottom of each panel are the PR resonances moduli (Eq. 2), with the dark and light colour corresponding to y and x polarization of the optical transition, respectively. In panel c, the E_3 and E_4 resonances and corresponding moduli are scaled by the factor of 0.5 for clarity. (b, d) The optical absorption spectra measured at the incident light polarized along x (bright solid lines) and y (dark solid lines) crystallographic direction for SnS (b) and SnSe (d). In the insets Tauc plots for indirect and direct absorption edge are shown.

(Figure 2a) and SnSe (Figure 2c) is presented. For both materials, in the PR spectra (plotted with blue and purple circles) multiple resonances are visible, indicating contribution of three and four optical transitions for SnS and SnSe, respectively, labelled E_1-E_4 in the figure. In order to determine the energies of the transitions, the Aspnes formula,[50] given by

$$\frac{\Delta R}{R}(\hbar\omega) = Re\left(\sum C_i e^{i\varphi_i}(\hbar\omega - E_i + i\Gamma_i)^{-2}\right) \qquad (1)$$

was fitted to the experimental data. In the equation, C_i is the amplitude of the i-th PR resonance, φ_i is the phase, Γ_i is the broadening and E_i is the energy. The energies corresponding to the temperature of 20 K are summarized in Table 1. Based on the fitting parameters, the resonance moduli, plotted as shaded areas in Figure 2a,c, were calculated, using the formula

$$\Delta\rho_i(E) = \frac{|C_i|}{(E - E_i)^2 + \Gamma_i^2}. \qquad (2)$$

The area under the modulus curve is related to the transition oscillator strength.

The PR resonances visible in the spectra exhibit strong polarization dependence, as shown by Ho *et al.*[51] and Herninda *et al.*[52] and confirmed by our preliminary results. E_1 transition, for both SnS and SnSe, is polarized along the y direction, while all the energetically higher features manifest the x polarization, as illustrated by different shades of the moduli plots (dark for y and light for x polarization) corresponding to the measured PR resonances. The optical absorption coefficient spectra (yellow solid lines in Figure 2a,c) exhibit a characteristic step-like shape, also suggesting contribution of multiple optical transitions, with the two branches corresponding well to the E_1 and E_2 PR resonances. Above ~1.5 eV for SnS and ~1.3 eV for SnSe the measured signal is saturated and no features attributed to the higher transitions could be observed, however below the first resonance energy, an absorption tail is present, which may be an evidence of the indirect character of the fundamental band gap. The indirect absorption edge could be better resolved in the spectra acquired for the incident light polarized along one of the main crystallographic directions (i.e. the electric component of the EM field ε || x or ε || y), presented in Figure 2b,d. A significant shift of the direct absorption edge with varying polarization can be observed, related to the changes of the probability of individual transitions, in-line with the PR resonances polarization dependence. From the Tauc plots[53] of the absorption coefficient spectra, presented in the insets of panels b and d, the energies of the individual optical transitions were extracted. For the x polarization the linear region in the $(ahv)^{1/2}$ plot is clearly visible, allowing to determine the fundamental indirect band gaps E_0 of 1.16 eV for SnS and 0.99 eV for SnSe. The $(ahv)^2$ plots of the energetically higher regions of the spectra for both polarizations provided the energies of direct transitions E_1 and E_2, in perfect agreement with PR, as compared in Table 1. Some minor discrepancies may result from the fact that the Tauc plot method is best applicable for materials with simple electronic band dispersion, exhibiting the absorption edge originating from an optical transitions between well-defined parabolic-like valleys.

To better understand the optical activity of SnXs, temperature dependent experiments were carried. The obtained results are presented in Figure 3. The temperature evolution of the PR spectra (Figure 3a,d) reveals the expected thermal redshift of PR resonances energies and a decrease of their amplitude. In the case of optical absorption, the influence of the temperature was investigated using either unpolarized light (Figure 3b,e) or light polarized linearly along x and y direction (Figure S2 of the SI).

Temperature dependences of E_0 and E_1 transitions energies (Figure 3c,f) were approximated by Bose-Einstein (B-E)[54] and Varshni[55] formulas, providing information about the electron-phonon interaction strength. The equations and obtained values of the fitting parameters values are given in the SI (Table S2). Both approaches allow to reproduce the temperature dependence with good accuracy, although the B-E procedure is more accurate at low temperatures. For the energetically higher transitions the fits did not converge or provided non-physical values, which may be related to the uncommon shape of the plot, resulting from the uncertainties of the energies extracted from the PR spectra, especially at higher temperatures.

Electronic band structure

Based on the absolute energies and polarizations of the optical transitions observed in the experiment, we propose an assignation to

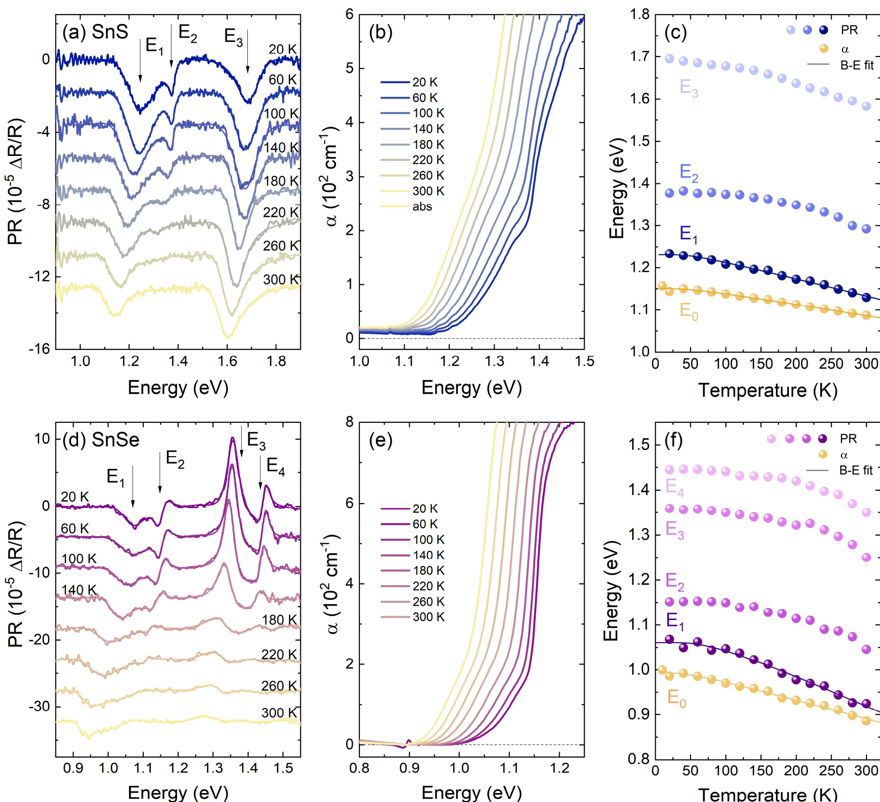

Figure 3. The temperature evolution of the photoreflectance (a,d) and optical absorption (b,e) spectra acquired for SnS (a,b) and SnSe (d,e). Temperature dependence of the optical transitions energies determined based on the optical absorption (E_0) and PR (E_1 - E_4) measurements for SnS (c) and SnSe (f). The experimental data (circles) are approximated by Bose-Einstein formula (solid lines).

certain Brillouin zone points. In Figure 4a,c the electronic band structure is presented, calculated employing DFT, with the use of Heyd-Scuseria-Ernzerhof (HSE06) hybrid functional (for the computational details see *Methods* section). The calculations confirm the multivalley character of the band dispersion, with the conduction band minimum (CBM) in the Γ-Y path and a characteristic shape of the valence band maximum (VBM) in the Γ-X path, composed of two hole pockets. The band shape has been observed experimentally in the angle-resolved photoemission spectroscopy measurements and strongly influences the thermoelectric efficiency of the materials.[56–58] The band dispersion is generally similar to germanium monochalcogenides (GeS, GeSe), except for the valence band in the Γ point, pushed towards higher binding energies relative to the VBM.[13,14,58,59] Hence, the quasi-direct band gap character observed for GeS[59] and GeSe[13,14] is not present for SnS and SnSe crystals. In Figure 4b,e the relative distance between highest valence band and lowest conduction band is plotted, along with in-plane components of the transition squared matrix element (shaded areas), determining the transition oscillator strength and, as a consequence, its probability. The matrix element distribution is governed by the selection rules and indicates for which polarization a transition is allowed. By comparing the experimental results to the calculated band structure we assign the observed optical transitions as labelled in Figure 4b,e and summarized in Table 1. The E_0 transition can be attributed to the indirect fundamental band gap between VBM and CBM. The lowest direct transition E_1, polarized along *y* direction, correspond to the valley in the Γ-Y path, while E_2, active for the *x* polarization, occurs in the Γ-X path, close to the X point. The transition E_3 can be assigned to the U point, and E_4, visible only for SnSe, to a critical point in the Y-S path. The agreement between experimental and theoretical energies is excellent for E_0, but poorer for the higher transitions. Such discrepancies are not unusual, as DFT calculations, burdened with approximations and sensitive to the computational parameters, often reproduce the band shapes accurately, but fail to evaluate the absolute energies. Therefore, to find a plausible interpretation of the experimental results we focus mainly on the polarization and the matrix element in-plane components ratio.

The anisotropy of the matrix element distribution and, as a consequence, the polarization of the optical transitions is related to the orbital composition of the electronic bands. In Figure 4c,f the density of states (DOS) is plotted, including both total DOS (shaded areas) and partial contribution of Sn and X valence orbitals (dashed lines): Sn 5*s*, 5*p* and S 3*s*, 3*p* or Se 4*s*, 4*p*. According to DFT calculations, also *d* orbitals (often referred to as semi-core states) have minor contribution to the total DOS, which is not plotted in the figure for clarity. It was shown that either including the *d* states to the band structure calculation, or treating them as core-levels, provides nearly identical results.[19,20] The conduction band of both materials is mainly composed of Sn 5*p* orbitals, with addition of X *p* states. In the valence band three regions can be distinguished, labelled A, B, and C in Figure 4c,f, as was also shown for other MXs.[20,52] The A band is composed of a mixture of Sn 5*s*, 5*p* and X *p* orbitals, the B region is dominated by X *p* states, with contribution of Sn *p* orbitals, and the C peak almost entirely consists of Sn 5*s* states. The contribution of the

Table 1. Experimental and theoretical energies and polarizations of measured and predicted optical transitions, along with their assignation to certain BZ points. The experimental values correspond to the temperature of 20 K.

	Transition	BZ point	Polarization	Energy (eV)		
				Experiment (20 K)		DFT (0 K)
				Absorption	PR	
SnS	E_0	Γ-X→ Γ-Y	-	1.16	-	1.16
	E_1	Γ-Y	y	1.23	1.23	1.39
	E_2	Γ-X	x	1.38	1.38	1.75
	E_3	U	x	-	1.70	1.97
SnSe	E_0	Γ-X→ Γ-Y	-	0.99	-	0.95
	E_1	Γ-Y	y	1.09	1.07	1.16
	E_2	Γ-X	x	1.14	1.15	1.31
	E_3	U	x	-	1.36	1.63
	E_4	Y-S	x	-	1.45	1.72

5*s* orbitals to the upper valence band is a consequence of the presence of stereochemically active s^2 lone electron pairs in the crystal structure and will be discussed further in the text. In Figure 4a,d, the contribution of the three spatial components of the *p* orbital (p_x, p_y, p_z), oriented along respective crystallographic axes, is superimposed over the band dispersion. In the figure, *p* states of both Sn and X atoms are combined. More detailed picture, including also the *s* states and resolving contribution of different elements, is presented in Figure S3 of the SI. In the orbital composition plots the size of the points is proportional to the contribution of an orbital to certain band. The distribution of the three components across the BZ is particularly interesting regarding the topmost valence and lowermost conduction band, as it affects the optical properties observed in the experiment. In the proximity of the X and U points of the BZ, the bands are mainly composed of p_x orbitals, resulting in high k_x matrix element component, and consequently polarization of the optical transition along the *x* direction. Similarly, in the Γ-Y and Z-T paths p_y orbitals dominate, giving rise to high k_y matrix element component and determining the *y* polarization of the optical transitions. It can also be seen that in the BZ regions where both valence and conduction bands consists mainly of p_z states (Γ, Z, S, and R points), the in-plane matrix element vanishes, as a result of small value of the overlap integral. Therefore, in the applied experimental configuration, no optical transition attributed to the Γ point of the BZ was observed, despite relatively low energy with respect to the fundamental band gap.

Photoemission study

The valence band DOS can be experimentally investigated by means of photoemission spectroscopy. In this study we apply two techniques, exploiting different radiation sources and excitation energies. The lab-based XPS, utilizing the Al K_α line of $h\nu = 1486.6$ eV, allows observation of core-level states, confirming the material composition and quality, and the high energy secondary electron cut-off, providing direct information about the work function of the investigated sample. In terms of valence band investigation, for high excitation energies the photoionization cross-section of the valence orbitals is relatively small, resulting in low photoemission intensity. Therefore, the second applied method was UV photoemission spectroscopy (UPS), exploiting monochromatic synchrotron radiation of $h\nu = 100$ eV. The technique and the experimental setup provide significantly improved resolution and sensitivity, along with possibility of angle-resolved measurements, which are reported in our previous work.[58] Both techniques allow measurements of the valence band, however UPS is more suitable, considering the photoionization cross-section of the valence orbitals up to two orders of magnitude higher for the excitation energy of 100 eV compared to 1.5 keV.[60,61] In Figure 5a,c the UPS spectra (top plot of each panel) are compared with the simulated valence band (bottom plots), obtained by applying following procedure to the calculated partial DOS: first, the contribution from the orbitals was weighted using the photoemission cross-sections corresponding to the excitation energy of 100 eV, according to Yeh and Lindau.[60] Next, to introduce the broadening of the electronic states, the partial DOS was convolved with Lorenzian (natural broadening) and Gaussian (thermal broadening) functions. The UPS spectra were corrected by subtracting the background originating from the inelastic electron scattering. It can be seen for both SnS and SnSe that after taking into account the photoionization cross-section, the signal from A and B bands (as labelled in Figure 4c,d) is strongly dominated by X *p* orbitals, and the contribution of Sn 5*s* states is distinct only in the C band. The simulated curves are in perfect agreement with the experimental spectra in the B and C regions, but diverges in the A region. In the calculations, the intensity of the A band is lower with respect to the B band, but in the experiment we observe opposite relation. The discrepancy may result from the fact that in the measurement light polarized linearly was used, interacting differently with the three spatial components of *p* orbitals. Effectively, the photoionization cross-section for *p* states might be smaller than predicted, while estimated correctly for s orbitals, insensitive to the polarization. Then, the contribution of the Sn 5*s* states to the photoemission from the A region should be greater, resulting in higher overall detected intensity. Another factor which may influence the respective bands intensity ratio is the possibility that DFT calculations underestimate the contribution of the Sn 5*s* states to the topmost region of the valence band.

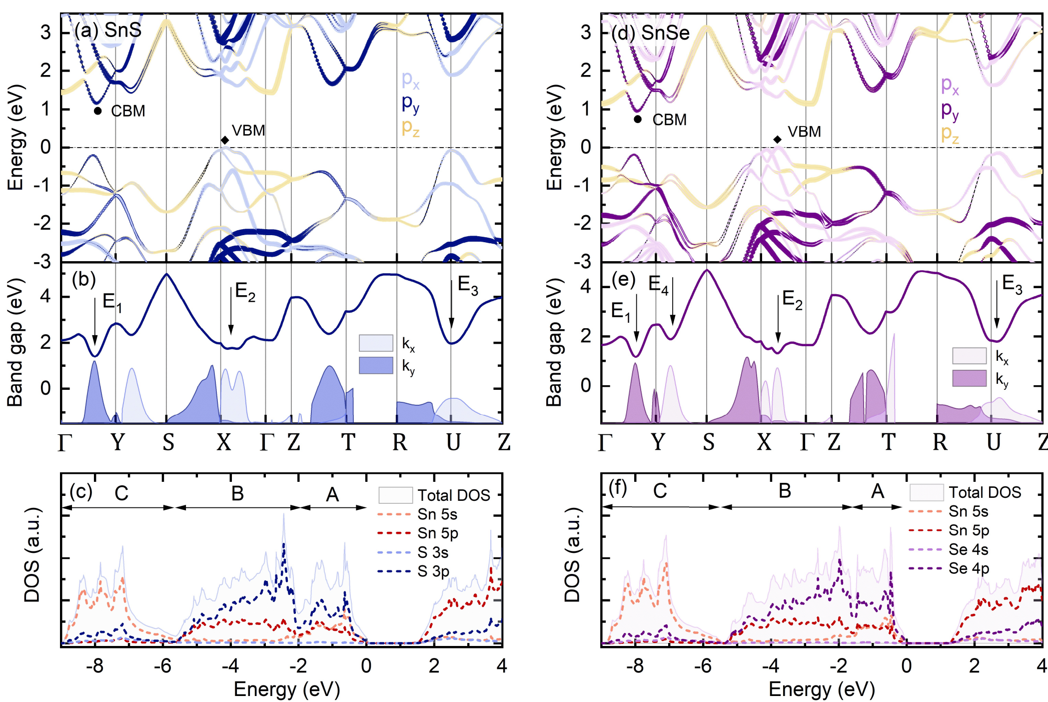

Figure 4. (a, d) The electronic band dispersion of SnS (a) and SnSe (d) along high-symmetry BZ paths with superimposed contribution of the *x*, *y*, and *z* components of the Sn and X *p* orbitals. (b,e) The interband distance (solid line) and transition squared matrix element k_x and k_y components (bright and dark shaded areas, respectively). The optical transitions observed in the experiment are assigned to certain BZ points by arrows. (c,f) The calculated total (shaded areas) and partial (dashed lines) density of states, corresponding to individual orbitals. The energy scale is relative to the VBM energy ($E_{VBM} = 0$). In panels a, b, and c results for SnS are presented, while d, e, and f correspond to SnSe.

The XPS spectra acquired for SnS and SnSe, visualizing the secondary electron cut-off and valence band maximum are presented in Figure 5b,d. From the extrapolation of the linear region at high binding energy side of the spectrum the cut-off energy $E_{cut\text{-}off}$ was determined. The valence band maximum energy E_{VBM} can also be estimated (with respect to the Fermi level), however considering the spectral resolution and intensity of the signal originating from the valence band more reliable and precise values of E_{VBM} are extracted from the UPS data, as shown in the insets of Figure 5a,c. It can be noticed that the VBM is observed at slightly higher energies in XPS measurements. Such shift can be explained by the fact that the DOS at VBM (close to the X point of the BZ) is low and cannot be resolved in the XPS measurements. In the UPS spectra a characteristic step attributed to the VBM is clearly visible, followed by a rapid rise of the photoemission signal originating from a band in the Γ point.

The values of E_{VBM} obtained for SnS and SnSe are 0.33 eV and 0.12 eV, respectively. The material work function (φ) can be calculated from the relation

$$\varphi = h\nu - E_{cut-off}. \tag{3}$$

Then, the ionization potential (*IP*) is given by

$$IP = \varphi + E_{VBM}, \tag{4}$$

and the electron affinity (χ) can be defined as

$$\chi = IP - E_g, \tag{5}$$

where E_g is the fundamental energy gap determined from the optical absorption measurements. The values of the above parameters for SnS and SnSe (compared with GeS and GeSe investigated in our previous work[62]) are summarized in Table 2 and Figure 6, visualizing the band alignment of the four MXs with respect to the vacuum energy. It should be noted that the work function, related to the Fermi level position inside the band gap, may vary depending on the intrinsic defect or intentional dopants concentration, therefore the parameter more suitable for comparison with other studies is the *IP*, i.e. the VBM position with respect to vacuum level.

The obtained values of the *IP* are relatively low compared to other semiconducting van der Waals crystals, which leads to some significant consequences considering potential applications, such as band alignment with window layers for photovoltaics, affecting the device efficiency, or with metals for electrical contacts, determining the ohmic or Schottky character of the junction. The reason for this is the aforementioned contribution of the metal s^2 lone electron pairs to the high energy region of the valence band, confirmed by previous studies.[19,63] In all MXs the metal atom is in the +2 oxidation state. For group IV metals it implies either tetrahedral or octahedral coordination. The former characterize with three bonds with chalcogen atoms and one lone electron pair in the fourth vertex of the tetrahedron, forming a distorted orthorhombic crystal lattice. In the latter, six M-X bonds result in perfectly symmetric rocksalt structure.[18,21] The lattice distortion is related to the stereochemical activity of the s^2 lone pairs, observed for GeS, GeSe, GeTe, SnS and SnSe, but not for other group IV-VI compounds with the same stoichiometry, such

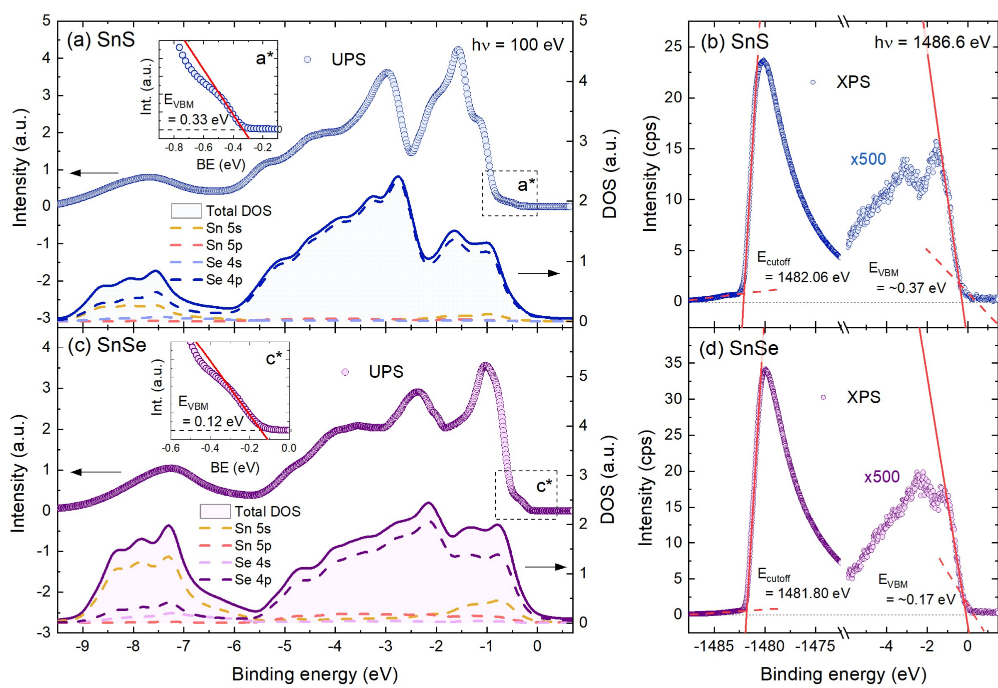

Figure 5. (a,c) The results of the UPS measurements (circles, top of each panel) acquired with the use of synchrotron radiation at the excitation energy of 100 eV, compared with the simulated valence band (solid and dashed lines, bottom of each panel) based on the calculated DOS, corrected by the photoionization cross-section for individual orbitals and broadening of the electronic states. In the insets the boxed regions of the experimental spectra labeled a* and c* are enlarged to better illustrate the VBM and determine E_{VBM}. (b,d) The low (valence band) and high (secondary electron cut-off) binding energy regions of the lab-based XPS spectra (acquired with the use of Al K_α line of 1486.6 eV), allowing to extract the $E_{cut\text{-}off}$ and E_{VBM} (less accurate than from UPS spectra). The valence band regions of the spectra are scaled by the factor of 500 for better visualization.

as SnTe, PbS, PbSe, and PbTe. The phenomenon can be partly explained by the revised lone pair model proposed by Walsh *et al.*[21] In the considered materials the metal valence *s* orbitals hybridize with chalcogen *p* states, forming bonding and anti-bonding states (as schematically illustrated in Figure 7), contributing to the high (C band) and low (A band) binding energy regions of the valence band, respectively. The amount of the contribution of the M *s* orbitals to the anti-bonding state is determined by the relative energy of M *s* and X *p* levels, yielding higher contribution for smaller energy distance. For strong M *s* component, the interaction of the unoccupied M *p* orbitals with the anti-bonding state leads to asymmetric electron density distribution with a directional lone electron pair. When M *s* contribution is minor, the interaction is weak and stereochemically active lone pairs do not form. The relative positions of M *s* and X *p* valence levels for group IV and VI elements is presented in a diagram in Figure 7, with the energies adapted after Mann *et al.*[64] It can be seen that due to lowest energy distance, most prominent lone pairs form for oxides, and the X *p* energy increases down the VI group. For metal atoms, the Sn 5*s* state is positioned higher relative to both Ge 4*s* and Pb 6*s* levels, reducing the effective distance to X *p* states, which explains the significantly lower *IP* observed for SnX compared to GeX. Considering only tin compounds, we should expect stronger mixing of Sn 5*s* orbitals with S 3*p* than with Se 4*p* states, and therefore greater contribution to the A band for SnS. In Figure S5 of the SI the Sn 5*s* contribution to the total DOS is plotted for both investigated materials, confirming the predictions.

The revised lone pair model is in agreement with the experimental results obtained for SnX crystals, however does not explain formation of the stereochemically active lone pairs in GeX compounds and their absence in PbXs. An attempt of justification of the phenomenon was made by Smiles *et al.*,[20] who proposed that the atomic radius and bond lengths may affect the resulting favorable structure. The theoretical study performed by the authors for GeS and GeSe, simulating the influence of the bond length on the optimized geometry by varying the unit cell volume, did not resolve the issue, however other evidence that the explanation might be valid can be found in the literature. XRD studies of pressure-induced structural phase transition of PbX crystals revealed a transformation from the perfectly symmetric rock-salt to distorted orthorhombic structure with space group *Cmcm* (a supergroup of *Pnma*).[65–67] Furthermore, in the investigations of the thermal expansion of GeX materials, a phase transition from the orthorhombic (GeSe) or rhombohedral (GeTe) to cubic system was observed.[68,69] GeS did not undergo any phase transition up to the melting point, indicating superior stability of the distorted structure.[69] The observed behavior of both Pb and Ge chalcogenides is in-line with the hypothesis that the

Table 2. Ionization potential, work function, electron affinity, and room temperature energy gap determined for SnS, SnSe, GeS, and GeSe. The values for GeX crystals are adapted from Ref. [62]

	IP (eV)	φ (eV)	χ (eV)	E_g (eV)
SnS	4.87	4.54	3.78	1.09
SnSe	4.92	4.80	4.03	0.89
GeS	5.70	5.32	4.11	1.59
GeSe	5.47	5.27	4.27	1.20

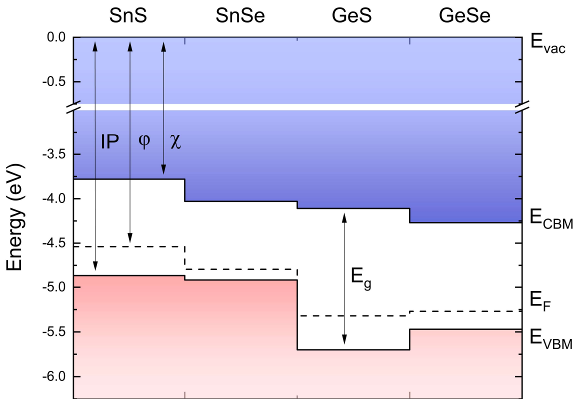

Figure 6. The band alignment diagram for the group IV-IV chalcogenides SnS, SnSe, GeS, and GeSe, with respect to vacuum energy E_{vac}. The values for GeX crystals are adapted from Ref. [62].

interatomic distance may influence the stereochemical activity of the lone electron pairs. In the case of the former, increasing the hydrostatic pressure leads to effective reduction of the interatomic distance and induce stronger interaction between Pb and X orbitals, resulting in the crystal lattice distortion. For the latter, the thermal expansion causes an opposite effect, weakening the interaction and observed as a phase transition to a structure with higher symmetry.

Considering the Sn chalcogenides, it is worth mentioning that in the high-temperature regime (above ~800 K) the *Cmcm* phase appears, although the transition is only related to the relative change of the lattice parameters (at the transition temperature a = b, resulting in higher symmetry of the structure) and does not involve major atomic rearrangement.[70] The result confirms the trends predicted based on the atomic orbital energies regarding the relation between the stability of the s^2 lone pairs and the energy distance between M *s* and X *p* valence states.

CONCLUSIONS

In conclusion, the optical properties of SnS and SnSe van der Waals crystals were investigated by complementary methods of optical spectroscopy (modulated reflectance and optical absorption) combined with *ab initio* calculations of the electronic band structure and density of states. The experimental studies confirmed the predicted indirect character of the fundamental band gap of SnS (1.09 eV at room temperature) and SnSe (0.89 eV), and revealed strong linear dichroism of the energetically higher direct optical transitions. The anisotropy of the optical properties originates from the electronic band structure and orbital composition of the individual bands, determining the selection rules and transition probability dependent on the incident light polarization angle.

By means of UV and X-ray photoemission spectroscopy the valence bands of SnS and SnSe were examined experimentally, remaining in good agreement with the simulations based on the calculated density of states corrected by the photoionization cross-section of the individual orbitals. The measurements also allowed to determine the work functions, ionization potentials and electron affinities of the materials, providing information about the band alignment with other semiconductors for heterostructures engineering. The obtained relatively low values of the ionization potential (4.87 eV and 4.92 eV for SnS and SnSe, respectively) can be attributed to the presence of the stereochemically active Sn 5*s* lone electron pairs in the crystal structure. Their formation is governed by the interaction between unoccupied Sn 5*p* orbitals and the anti-bonding state of hybridized Sn 5*s* and S or Se valence *p* orbitals. Along with SnX, we discuss the phenomenon and its consequences also for other group IV monochalcogenides.

In general, our results explain the origins of the linear dichroism of the optical properties of SnS and SnSe and point towards potential applications in polarization-sensitive photodetectors, but also possibilities of integration with other crystals to form van der Waals heterostructures.

METHODS

Experimental details

The investigated samples were SnS and SnSe single crystals synthesized using modified Bridgman technique using 6N Sn, S and Se precursors. Prior to synthesis, as received precursors were purified using float zone technique to reach 6N purity. Stoichiometric ratio of Sn and chalcogen were mixed in nugget form into Bridgman ampoule with a sharp tip to limit nucleation density and enable single crystal formation. Typical growth temperature was set above the melting point of SnS and SnSe, usually at 950 °C. The crystallization occurred by lowering rate of 1 mm per week from 950 °C hot zone to 300 °C cold zone.

For structural characterization, X-ray diffraction (XRD) measurements were performed on a Marvel Panalytical Empyrean diffractometer in a Bragg-Brentano configuration using a Cu $K_{\alpha 1}$ $\lambda = 1.540598$ Å x-ray tube and a Pixcel3D detector. A small piece of bulk crystal was placed on a Si/SiO_2 substrate and a diffraction curve was recorded. The measurement range spread from 10 to 75 degrees under normal conditions.

For the optical spectroscopy measurements (photoreflectance and optical absorption) the samples were exfoliated to obtain clear surface and mounted on a brass carrier, ensuring good thermal contact, inside a cryostat coupled with a closed-cycle helium cryocooler. The experiments were carried with the use of a dedicated optical

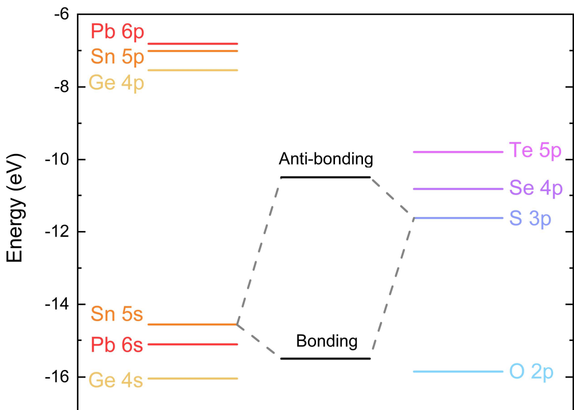

Figure 7. Diagram of the electronic configuration energies of the atomic valence *s* and *p* orbital for group IV elements Ge, Sn, and Pb, and group VI elements O, S, Se, and Te. The orbital energies are adapted from Ref. [64]. The hybridized bonding and anti-bonding states are only presented for the illustration of the phenomenon and does not correspond to the values on the energy scale.

setups, composed of a quartz tungsten halogen lamp (a probing white light source), a 550 mm focal length grating monochromator and a detection system, including Si or InGaAs photodiode and a lock-in amplifier (Stanford Research Systems SR830). For the photoreflectance measurement the modulation was achieved by periodic excitation with a 532 nm continuous wave laser, mechanically chopped at the frequency of ~300 Hz. For polarization-resolved optical absorption measurements a Glan-Taylor calcite linear polarizer and an achromatic half-wave plate were placed in the optical axis.

The photoemission studies were performed using two techniques, exploiting different radiation sources. For both variants the samples were exfoliated under ultra-high vacuum condition inside a preparation chamber. UV photoemission spectroscopy experiments were carried with the use of the synchrotron radiation (excitation energy of 100 eV) of the URANOS beamline at SOLARIS National Synchrotron Radiation Centre (Kraków, Poland).[71] The photoemission signal was detected with Scienta-Omicron DA30-L electron analyzer. The measurements were performed at the temperature of 77 K (achieved in a flow-type liquid nitrogen cryostat) and base pressure below 5 x 10^{-11} mbar. X-ray photoemission spectroscopy (including core-level XPS) exploiting monochromatic Al K_α line (1486.6 eV) were carried at room temperature. In this technique, the photoelectrons were detected with a hemispherical analyzer Argus CU.

Computational details

Ab initio calculations were performed within the framework of density functional theory (DFT) with the use of the relativistic projector-augmented waves (PAW) datasets[72] in Vienna Ab Initio Simulation Package (VASP).[73] The Perdew-Burke-Ernzerhof (PBE) parametrization of generalized gradients approximation (GGA) to the exchange-correlation functional was employed.[74] Monkhorst-Pack k-point grid of 12 x 12 x 3, plane wave energy cutoff of 600 eV, and a semi-empirical DFT-D3 correction for vdW interactions were used.[75] The electronic band structures were calculated with the use of Heyd-Scuseria-Ernzerhof (HSE06) hybrid functional.[76]

ASSOCIATED CONTENT

Supporting Information. Broad energy range core-level XPS spectra, biding energies of characteristic core-level lines, temperature evolution of the optical absorption spectra, Bose-Einstein and Varshni formulas and values of the parameters, contribution of the Sn 5*s* orbitals to total DOS, detailed orbital composition of the electronic bands.

AUTHOR INFORMATION

Corresponding Author

*Agata K. Tołłoczko, Department of Semiconductor Materials Engineering, Wrocław University of Science and Technology, Wybrzeże Wyspiańskiego 27, 50-370 Wrocław, Poland
Email: agata.tolloczko@pwr.edu.pl

Author Contributions

A.K.T. carried the optical spectroscopy and UPS experiments, analyzed the data, prepared graphics, and wrote the manuscript. J.Z. performed the theoretical calculations. M.G. performed the XPS measurements. J.S. performed the XRD measurements. N.O. and M.R. assisted and supervised the photoemission experiments at SOLARIS National Synchrotron Radiation Centre as beamline scientists. S.A.T. and M.E. synthesized the samples. R.K. supervised the project and provided funding. All authors edited the manuscript.

Notes

The authors declare no conflict of interest.

ACKNOWLEDGMENT

This work was supported by the National Science Centre (NCN) Poland OPUS 23 no. 2022/45/B/ST7/02750. The publication was partially developed under the provision of the Polish Ministry of Science and Higher Education project "Support for research and development with the use of infrastructure of the National Synchrotron Radiation Centre SOLARIS" under contract no. 1/SOL/2021/2. The authors acknowledge the SOLARIS Centre for the access to the Beamline URANOS, where the measurements were performed. Computational studies were supported by WCSS and PLGrid Infrastructure. S.A.T. acknowledges primary support from DOE-SC0020653 (materials synthesis), Lawrence Semiconductors, NSF CMMI 2129412, NSF DMR 2330110, and NSF CMR 2111812.

REFERENCES

(1) Novoselov, K. S.; Geim, A. K.; Morozov, S. V.; Jiang, D.; Zhang, Y.; Dubonos, S. V.; Grigorieva, I. V.; Firsov, A. A. Electric Field Effect in Atomically Thin Carbon Films. *Science* **2004**, *306* (5696), 666–669. https://doi.org/10.1126/science.1102896.

(2) Novoselov, K. S.; Mishchenko, A.; Carvalho, A.; Neto, A. H. C. 2D Materials and van Der Waals Heterostructures. *Science* **2016**, *353* (6298), aac9439. https://doi.org/10.1126/science.aac9439.

(3) Taylor, E. W.; Cramer, W. Birefringence of Protein Solutions and Biological Systems. *Biophys J* **1963**, 3 (2), 143–154.

(4) Hsueh, H.-C.; Li, J.-X.; Ho, C.-H. Polarization Photoelectric Conversion in Layered GeS. *Advanced Optical Materials* **2018**, *6* (4), 1701194. https://doi.org/10.1002/adom.201701194.

(5) Liu, C.; Zheng, T.; Shu, K.; Shu, S.; Lan, Z.; Yang, M.; Zheng, Z.; Huo, N.; Gao, W.; Li, J. Polarization-Sensitive Self-Powered Schottky Photodetector with High Photovoltaic Performance Induced by Geometry-Asymmetric Contacts. *ACS Appl. Mater. Interfaces* **2024**, *16* (11), 13914–13926. https://doi.org/10.1021/acsami.3c16047.

(6) Yuan, H.; Liu, X.; Afshinmanesh, F.; Li, W.; Xu, G.; Sun, J.; Lian, B.; Curto, A. G.; Ye, G.; Hikita, Y.; Shen, Z.; Zhang, S.-C.; Chen, X.; Brongersma, M.; Hwang, H. Y.; Cui, Y. Polarization-Sensitive Broadband Photodetector Using a Black Phosphorus Vertical p–n Junction. *Nature Nanotech* **2015**, *10* (8), 707–713. https://doi.org/10.1038/nnano.2015.112.

(7) Qiao, J.; Kong, X.; Hu, Z.-X.; Yang, F.; Ji, W. High-Mobility Transport Anisotropy and Linear Dichroism in Few-Layer Black Phosphorus. *Nature Communications* **2014**, *5*, 4475. https://doi.org/10.1038/ncomms5475.

(8) Xia, F.; Wang, H.; Jia, Y. Rediscovering Black Phosphorus as an Anisotropic Layered Material for Optoelectronics and Electronics. *Nature Communications* **2014**, *5*, 4458. https://doi.org/10.1038/ncomms5458.

(9) Gomes, L. C.; Carvalho, A. Phosphorene Analogues: Isoelectronic Two-Dimensional Group-IV Monochalcogenides with Orthorhombic Structure. *Phys. Rev. B* **2015**, *92* (8), 085406. https://doi.org/10.1103/PhysRevB.92.085406.

(10) Chen, Z.; Hwang, W.; Cho, M.; Hoang, A. T.; Kim, M.; Kim, D.; Kim, D. H.; Kim, Y. D.; Kim, H. J.; Ahn, J.-H.; Soon, A.; Choi, H.-J. In-Plane Optical and Electrical Anisotropy in Low-Symmetry Layered GeS Microribbons. *NPG Asia Mater* **2022**, *14* (1), 1–11. https://doi.org/10.1038/s41427-022-00390-8.

(11) Ishihara, Y.; Ohno, Y.; Nakada, I. Anisotropic Electrical Properties of GeSe. *physica status solidi (b)* **1984**, *121* (1), 407–412. https://doi.org/10.1002/pssb.2221210143.

(12) Le, V. L.; Cuong, D. D.; Nguyen, H. T.; Nguyen, X. A.; Kim, B.; Kim, K.; Lee, W.; Hong, S. C.; Kim, T. J.; Kim, Y. D. Anisotropic Behavior of Excitons in Single-Crystal α-SnS. *AIP Advances* **2020**, *10* (10), 105003. https://doi.org/10.1063/5.0021690.

(13) Tan, D.; Lim, H. E.; Wang, F.; Mohamed, N. B.; Mouri, S.; Zhang, W.; Miyauchi, Y.; Ohfuchi, M.; Matsuda, K. Anisotropic Optical and Electronic Properties of Two-Dimensional Layered Germanium Sulfide. *Nano Res.* **2017**, *10* (2), 546–555. https://doi.org/10.1007/s12274-016-1312-6.

(14) Tołłoczko, A.; Zelewski, S. J.; Błaszczak, M.; Woźniak, T.; Siudzińska, A.; Bachmatiuk, A.; Scharoch, P.; Kudrawiec, R. Optical Properties of Orthorhombic Germanium Selenide: An Anisotropic Layered Semiconductor Promising for Optoelectronic Applications. *J. Mater. Chem. C* **2021**, *9* (41), 14838–14847. https://doi.org/10.1039/D1TC04280G.

(15) Zhang, Z.; Yang, J.; Zhang, K.; Chen, S.; Mei, F.; Shen, G. Anisotropic Photoresponse of Layered 2D SnS-Based near Infrared Photodetectors. *J. Mater. Chem. C* **2017**, *5* (43), 11288–11293. https://doi.org/10.1039/C7TC02865B.

(16) Xue, D.-J.; Tan, J.; Hu, J.-S.; Hu, W.; Guo, Y.-G.; Wan, L.-J. Anisotropic Photoresponse Properties of Single Micrometer-Sized GeSe Nanosheet. *Adv. Mater. Weinheim* **2012**, *24* (33), 4528–4533. https://doi.org/10.1002/adma.201201855.

(17) Li, Q.; Zhou, Q.; Shi, L.; Chen, Q.; Wang, J. Recent Advances in Oxidation and Degradation Mechanisms of Ultrathin 2D Materials under Ambient Conditions and Their Passivation Strategies. *J. Mater. Chem. A* **2019**, *7* (9), 4291–4312. https://doi.org/10.1039/C8TA10306B.

(18) Walsh, A.; Watson, G. W. Influence of the Anion on Lone Pair Formation in Sn(II) Monochalcogenides: A DFT Study. *J. Phys. Chem. B* **2005**, *109* (40), 18868–18875. https://doi.org/10.1021/jp051822r.

(19) Jones, L. A. H.; Linhart, W. M.; Fleck, N.; Swallow, J. E. N.; Murgatroyd, P. A. E.; Shiel, H.; Featherstone, T. J.; Smiles, M. J.; Thakur, P. K.; Lee, T.-L.; Hardwick, L. J.; Alaria, J.; Jäckel, F.; Kudrawiec, R.; Burton, L. A.; Walsh, A.; Skelton, J. M.; Veal, T. D.; Dhanak, V. R. Sn $5{s}^{2}$ Lone Pairs and the Electronic Structure of Tin Sulphides: A Photoreflectance, High-Energy Photoemission, and Theoretical Investigation. *Phys. Rev. Mater.* **2020**, *4* (7), 074602. https://doi.org/10.1103/PhysRevMaterials.4.074602.

(20) Smiles, M. J.; Skelton, J. M.; Shiel, H.; Jones, L. A. H.; Swallow, J. E. N.; Edwards, H. J.; Murgatroyd, P. A. E.; Featherstone, T. J.; Thakur, P. K.; Lee, T.-L.; Dhanak, V. R.; Veal, T. D. Ge 4s2 Lone Pairs and Band Alignments in GeS and GeSe for Photovoltaics. *J. Mater. Chem. A* **2021**, *9* (39), 22440–22452. https://doi.org/10.1039/D1TA05955F.

(21) Walsh, A.; Payne, D. J.; Egdell, R. G.; Watson, G. W. Stereochemistry of Post-Transition Metal Oxides: Revision of the Classical Lone Pair Model. *Chem. Soc. Rev.* **2011**, *40* (9), 4455–4463. https://doi.org/10.1039/C1CS15098G.

(22) Fabini, D. H.; Seshadri, R.; Kanatzidis, M. G. The Underappreciated Lone Pair in Halide Perovskites Underpins Their Unusual Properties. *MRS Bulletin* **2020**, *45* (6), 467–477. https://doi.org/10.1557/mrs.2020.142.

(23) Ganose, A. M.; Savory, C. N.; Scanlon, D. O. Beyond Methylammonium Lead Iodide: Prospects for the Emergent Field of Ns2 Containing Solar Absorbers. *Chem. Commun.* **2016**, *53* (1), 20–44. https://doi.org/10.1039/C6CC06475B.

(24) Lambros, A. P.; Geraleas, D.; Economou, N. A. Optical Absorption Edge in SnS. *Journal of Physics and Chemistry of Solids* **1974**, *35* (4), 537–541. https://doi.org/10.1016/S0022-3697(74)80008-9.

(25) Elkorashy, A. M. Optical Absorption in Tin Monoselenide Single Crystal. *Journal of Physics and Chemistry of Solids* **1986**, *47* (5), 497–500. https://doi.org/10.1016/0022-3697(86)90048-X.

(26) Momma, K.; Izumi, F. VESTA 3 for Three-Dimensional Visualization of Crystal, Volumetric and Morphology Data. *J Appl Cryst* **2011**, *44* (6), 1272–1276. https://doi.org/10.1107/S0021889811038970.

(27) Whittles, T. J.; Burton, L. A.; Skelton, J. M.; Walsh, A.; Veal, T. D.; Dhanak, V. R. Band Alignments, Valence Bands, and Core Levels in the Tin Sulfides SnS, SnS2, and Sn2S3: Experiment and Theory. *Chem. Mater.* **2016**, *28* (11), 3718–3726. https://doi.org/10.1021/acs.chemmater.6b00397.

(28) Zhong, Y.; Zhang, L.; Chen, W.; Zhu, H. Macro van Der Waals P-n Heterojunction Based on SnSe and SnSe2. *Nanotechnology* **2020**, *31* (38), 385203. https://doi.org/10.1088/1361-6528/ab9a77.

(29) Huang, Y.; Wang, C.; Chen, X.; Zhou, D.; Du, J.; Wang, S.; Ning, L. First-Principles Study on Intrinsic Defects of SnSe. *RSC Adv.* **2017**, *7* (44), 27612–27618. https://doi.org/10.1039/C7RA03367B.

(30) Zhou, Y.; Li, W.; Wu, M.; Zhao, L.-D.; He, J.; Wei, S.-H.; Huang, L. Influence of Defects on the Thermoelectricity in SnSe: A Comprehensive Theoretical Study. *Phys. Rev. B* **2018**, *97* (24), 245202. https://doi.org/10.1103/PhysRevB.97.245202.

(31) Ullah, H.; Noor-A-Alam, M.; Kim, H. J.; Shin, Y.-H. Influences of Vacancy and Doping on Electronic and Magnetic Properties of Monolayer SnS. *Journal of Applied Physics* **2018**, *124* (6), 065102. https://doi.org/10.1063/1.5022151.

(32) Zhao, L.-D.; Lo, S.-H.; Zhang, Y.; Sun, H.; Tan, G.; Uher, C.; Wolverton, C.; Dravid, V. P.; Kanatzidis, M. G. Ultralow Thermal Conductivity and High Thermoelectric Figure of Merit in SnSe Crystals. *Nature* **2014**, *508* (7496), 373–377. https://doi.org/10.1038/nature13184.

(33) Hu, Z.-Y.; Li, K.-Y.; Lu, Y.; Huang, Y.; Shao, X.-H. High Thermoelectric Performances of Monolayer SnSe Allotropes. *Nanoscale* **2017**, *9* (41), 16093–16100. https://doi.org/10.1039/C7NR04766E.

(34) Čermák, P.; Hejtmánek, J.; Plecháček, T.; Navrátil, J.; Kašparová, J.; Holý, V.; Zmrhalová, Z.; Jarošová, M.; Beneš, L.; Drašar, Č. Thermoelectric Properties and Stability of Tl-Doped SnS. *Journal of Alloys and Compounds* **2019**, *811*, 151902. https://doi.org/10.1016/j.jallcom.2019.151902.

(35) Ding, G.; Gao, G.; Yao, K. High-Efficient Thermoelectric Materials: The Case of Orthorhombic IV-VI Compounds. *Sci Rep* **2015**, *5* (1), 9567. https://doi.org/10.1038/srep09567.

(36) Biswas, K.; He, J.; Blum, I. D.; Wu, C.-I.; Hogan, T. P.; Seidman, D. N.; Dravid, V. P.; Kanatzidis, M. G. High-Performance Bulk Thermoelectrics with All-Scale Hierarchical Architectures. *Nature* **2012**, *489* (7416), 414–418. https://doi.org/10.1038/nature11439.

(37) Cheng, K.; Guo, Y.; Han, N.; Su, Y.; Zhang, J.; Zhao, J. Lateral Heterostructures of Monolayer Group-IV Monochalcogenides: Band Alignment and Electronic Properties. *J. Mater. Chem. C* **2017**, *5* (15), 3788–3795. https://doi.org/10.1039/C7TC00595D.

(38) Mao, Y.; Xu, C.; Yuan, J.; Zhao, H. A Two-Dimensional GeSe/SnSe Heterostructure for High Performance Thin-Film Solar Cells. *J. Mater. Chem. A* **2019**, *7* (18), 11265–11271. https://doi.org/10.1039/C9TA01219B.

(39) Rahim, A.; Haider, W.; Khan, A.; Khan, H.; Din, H. U.; Shafiq, M.; Amin, B.; Idrees, M. Electronic and Thermoelectric Properties of Group IV–VI van Der Waals Heterostructures. *J Comput Electron* **2022**, *21* (4), 725–732. https://doi.org/10.1007/s10825-022-01894-w.

(40) Peng, L.; Wang, C.; Qian, Q.; Bi, C.; Wang, S.; Huang, Y. Complete Separation of Carriers in the GeS/SnS Lateral Heterostructure by Uniaxial Tensile Strain. *ACS Appl. Mater. Interfaces* **2017**, *9* (46), 40969–40977. https://doi.org/10.1021/acsami.7b11613.

(41) Gates-Rector, S.; Blanton, T. The Powder Diffraction File: A Quality Materials Characterization Database. *Powder Diffraction* **2019**, *34* (4), 352–360. https://doi.org/10.1017/S0885715619000812.

(42) Wiedemeier, H.; Georg von Schnering, H. Refinement of the Structures of GeS, GeSe, SnS and SnSe. *Zeitschrift fur Kristallographie* **1978**, *148*. https://doi.org/10.1524/zkri.1978.148.3-4.295.

(43) Moulder, J. F.; Chastain, J. *Handbook of X-Ray Photoelectron Spectroscopy: A Reference Book of Standard Spectra for Identification and Interpretation of XPS Data*; Physical Electronics Division, Perkin-Elmer Corporation, 1992.

(44) Albers, W.; Haas, C.; van der Maesen, F. The Preparation and the Electrical and Optical Properties of SnS Crystals. *Journal of Physics and Chemistry of Solids* **1960**, *15* (3), 306–310. https://doi.org/10.1016/0022-3697(60)90253-5.

(45) Vidal, J.; Lany, S.; d'Avezac, M.; Zunger, A.; Zakutayev, A.; Francis, J.; Tate, J. Band-Structure, Optical Properties, and Defect Physics of the Photovoltaic Semiconductor SnS. *Appl. Phys. Lett.* **2012**, *100* (3), 032104. https://doi.org/10.1063/1.3675880.

(46) Malone, B. D.; Gali, A.; Kaxiras, E. First Principles Study of Point Defects in SnS. *Phys. Chem. Chem. Phys.* **2014**, *16* (47), 26176–26183. https://doi.org/10.1039/C4CP03010A.

(47) Kopaczek, J.; Polak, M. P.; Scharoch, P.; Wu, K.; Chen, B.; Tongay, S.; Kudrawiec, R. Direct Optical Transitions at K- and H-Point of Brillouin Zone in Bulk MoS2, MoSe2, WS2, and WSe2. *Journal of Applied Physics* **2016**, *119* (23), 235705. https://doi.org/10.1063/1.4954157.

(48) Zelewski, S. J.; Kudrawiec, R. Photoacoustic and Modulated Reflectance Studies of Indirect and Direct Band Gap in van Der Waals Crystals. *Scientific Reports* **2017**, *7* (1), 15365. https://doi.org/10.1038/s41598-017-15763-1.

(49) Kopaczek, J.; Zelewski, S. J.; Polak, M. P.; Gawlik, A.; Chiappe, D.; Schulze, A.; Caymax, M.; Kudrawiec, R. Direct and Indirect Optical Transitions in Bulk and Atomically Thin MoS2 Studied by Photoreflectance and Photoacoustic Spectroscopy. *Journal of Applied Physics* **2019**, *125* (13), 135701. https://doi.org/10.1063/1.5080300.

(50) Aspnes, D. E. Third-Derivative Modulation Spectroscopy with Low-Field Electroreflectance. *Surface Science* **1973**, *37*, 418–442. https://doi.org/10.1016/0039-6028(73)90337-3.

(51) Ho, C.-H.; Lin, W.-Y.; Chao, L.-C.; Lee, K.-Y.; Inagaki, J.; Hsueh, H.-C. Study of Structural, Thermoelectric, and Photoelectric Properties of Layered Tin Monochalcogenides SnX (X = S, Se) for Energy Application. *ACS Appl. Energy Mater.* **2020**, *3* (5), 4896–4905. https://doi.org/10.1021/acsaem.0c00481.

(52) Herninda, T. M.; Hsu, C. E.; Hsueh, H.-C.; Ho, C.-H. Structural, Opto-Electrical, and Band-Edge Properties of Full-Series Multilayer SnS1-xSex ($0 \leq x \leq 1$) Compounds with Strong in-Plane Anisotropy. *Materials Today Advances* **2023**, *18*, 100379. https://doi.org/10.1016/j.mtadv.2023.100379.

(53) Tauc, J. Optical Properties and Electronic Structure of Amorphous Ge and Si. *Materials Research Bulletin* **1968**, *3* (1), 37–46. https://doi.org/10.1016/0025-5408(68)90023-8.

(54) Viña, L.; Logothetidis, S.; Cardona, M. Temperature Dependence of the Dielectric Function of Germanium. *Phys. Rev. B* **1984**, *30* (4), 1979–1991. https://doi.org/10.1103/PhysRevB.30.1979.

(55) Varshni, Y. P. Temperature Dependence of the Energy Gap in Semiconductors. *Physica* **1967**, *34* (1), 149–154. https://doi.org/10.1016/0031-8914(67)90062-6.

(56) Kuroki, K.; Arita, R. "Pudding Mold" Band Drives Large Thermopower in NaxCoO2. *J. Phys. Soc. Jpn.* **2007**, *76* (8), 083707. https://doi.org/10.1143/JPSJ.76.083707.

(57) Pletikosić, I.; von Rohr, F.; Pervan, P.; Das, P. K.; Vobornik, I.; Cava, R. J.; Valla, T. Band Structure of the IV-VI Black Phosphorus Analog and Thermoelectric SnSe. *Phys. Rev. Lett.* **2018**, *120* (15), 156403. https://doi.org/10.1103/PhysRevLett.120.156403.

(58) Tołłoczko, A. K.; Zelewski, S. J.; Ziembicki, J.; Olszowska, N.; Rosmus, M.; Woźniak, T.; Tongay, S.; Kudrawiec, R. Photoemission Study of the Thermoelectric Group IV-VI van Der Waals Crystals (GeS, SnS, and SnSe). *Advanced Optical Materials* **2024**, *12* (6), 2302049. https://doi.org/10.1002/adom.202302049.

(59) Tołłoczko, A.; Oliva, R.; Woźniak, T.; Kopaczek, J.; Scharoch, P.; Kudrawiec, R. Anisotropic Optical Properties of GeS Investigated by Optical Absorption and Photoreflectance. *Mater. Adv.* **2020**, *1* (6), 1886–1894. https://doi.org/10.1039/D0MA00146E.

(60) Yeh, J. J.; Lindau, I. Atomic Subshell Photoionization Cross Sections and Asymmetry Parameters: $1 \leqslant Z \leqslant 103$. *Atomic Data and Nuclear Data Tables* **1985**, *32* (1), 1–155. https://doi.org/10.1016/0092-640X(85)90016-6.

(61) Scofield, J. H. *Theoretical Photoionization Cross Sections from 1 to 1500 keV.*; UCRL-51326; CALIFORNIA UNIV., LIVERMORE. LAWRENCE LIVERMORE LAB., 1973. https://doi.org/10.2172/4545040.

(62) Grodzicki, M.; Tołłoczko, A. K.; Majchrzak, D.; Hommel, D.; Kudrawiec, R. Band Alignments of GeS and GeSe Materials. *Crystals* **2022**, *12* (10), 1492. https://doi.org/10.3390/cryst12101492.

(63) Suzuki, I.; Kawanishi, S.; Tanaka, K.; Omata, T.; Tanaka, S. Contribution of the Sn 5s State to the SnS Valence Band: Direct Observation via ARPES Measurements. *Electron. Struct.* **2022**, *4* (2), 025004. https://doi.org/10.1088/2516-1075/ac6ea8.

(64) Mann, J. B.; Meek, T. L.; Allen, L. C. Configuration Energies of the Main Group Elements. *J. Am. Chem. Soc.* **2000**, *122* (12), 2780–2783. https://doi.org/10.1021/ja992866e.

(65) Chattopadhyay, T.; von Schnering, H. G.; Grosshans, W. A.; Holzapfel, W. B. High Pressure X-Ray Diffraction Study on the Structural Phase Transitions in PbS, PbSe and PbTe with Synchrotron Radiation. *Physica B+C* **1986**, *139–140*, 356–360. https://doi.org/10.1016/0378-4363(86)90598-X.

(66) Grzechnik, A.; Friese, K. Pressure-Induced Orthorhombic Structure of PbS. *J. Phys.: Condens. Matter* **2010**, *22* (9), 095402. https://doi.org/10.1088/0953-8984/22/9/095402.

(67) Knorr, K.; Ehm, L.; Hytha, M.; Winkler, B.; Depmeier, W. The High-Pressure α/β Phase Transition in Lead Sulphide (PbS). *Eur. Phys. J. B* **2003**, *31* (3), 297–303. https://doi.org/10.1140/epjb/e2003-00034-6.

(68) Wiedemeier, H.; Siemers, P. A. The Thermal Expansion and High Temperature Transformation of GeSe. *Zeitschrift für anorganische und allgemeine Chemie* **1975**, *411* (1), 90–96. https://doi.org/10.1002/zaac.19754110110.

(69) Wiedemeier, H.; Siemers, P. A. The Thermal Expansion of GeS and GeTe. *Zeitschrift für anorganische und allgemeine Chemie* **1977**, *431* (1), 299–304. https://doi.org/10.1002/zaac.19774310134.

(70) Chattopadhyay, T.; Pannetier, J.; Von Schnering, H. G. Neutron Diffraction Study of the Structural Phase Transition in SnS and SnSe. *Journal of Physics and Chemistry of Solids* **1986**, *47* (9), 879–885. https://doi.org/10.1016/0022-3697(86)90059-4.

(71) Szlachetko, J.; Szade, J.; Beyer, E.; Błachucki, W.; Ciochoń, P.; Dumas, P.; Freindl, K.; Gazdowicz, G.; Glatt, S.; Guła, K.; Hormes, J.; Indyka, P.; Klonecka, A.; Kołodziej, J.; Kołodziej, T.; Korecki, J.; Korecki, P.; Kosiorowski, F.; Kosowska, K.; Kowalski, G.; Kozak, M.; Kozioł, P.; Kwiatek, W.; Liberda, D.; Lichtenberg, H.; Madej, E.; Mandziak, A.; Marendziak, A.; Matlak, K.; Maximenko, A.; Nita, P.; Olszowska, N.; Panaś, R.; Partyka-Jankowska, E.; Piszak, M.; Prange, A.; Rawski, M.; Roman, M.; Rosmus, M.; Sikora, M.; Sławek, J.; Sobol, T.; Sowa, K.; Spiridis, N.; Stępień, J.; Szczepanik, M.; Ślęzak, T.; Tyliszczak, T.; Ważny, G.; Wiechecki, J.; Wilgocka-Ślęzak, D.; Wolanin, B.; Wróbel, P.; Wróbel, T.; Zając, M.; Wawrzyniak, A.; Stankiewicz, M. SOLARIS National Synchrotron Radiation Centre in Krakow, Poland. *Eur. Phys. J. Plus* **2023**, *138* (1), 10. https://doi.org/10.1140/epjp/s13360-022-03592-9.

(72) Kresse, G.; Joubert, D. From Ultrasoft Pseudopotentials to the Projector Augmented-Wave Method. *Phys. Rev. B* **1999**, *59* (3), 1758–1775. https://doi.org/10.1103/PhysRevB.59.1758.

(73) Kresse, G.; Furthmüller, J. Efficient Iterative Schemes for Ab Initio Total-Energy Calculations Using a Plane-Wave Basis Set. *Phys. Rev. B* **1996**, *54* (16), 11169–11186. https://doi.org/10.1103/PhysRevB.54.11169.

(74) Perdew, J. P.; Burke, K.; Ernzerhof, M. Generalized Gradient Approximation Made Simple. *Phys. Rev. Lett.* **1996**, *77* (18), 3865–3868. https://doi.org/10.1103/PhysRevLett.77.3865.

(75) Grimme, S.; Antony, J.; Ehrlich, S.; Krieg, H. A Consistent and Accurate Ab Initio Parametrization of Density Functional Dispersion Correction (DFT-D) for the 94 Elements H-Pu. *The Journal of Chemical Physics* **2010**, *132* (15), 154104. https://doi.org/10.1063/1.3382344.

(76) Krukau, A. V.; Vydrov, O. A.; Izmaylov, A. F.; Scuseria, G. E. Influence of the Exchange Screening Parameter on the Performance of Screened Hybrid Functionals. *J. Chem. Phys.* **2006**, *125* (22), 224106. https://doi.org/10.1063/1.2404663.

Supporting Information

Linear dichroism of the optical properties of SnS and SnSe van der Waals crystals

Agata K. Tołłoczko,[*a] Jakub Ziembicki,[a] Miłosz Grodzicki,[ab] Jarosław Serafińczuk,[a] Seth A. Tongay,[c] Natalia Olszowska,[d] Marcin Rosmus,[d] and Robert Kudrawiec[ab]*

[a] Department of Semiconductor Materials Engineering,
Wrocław University of Science and Technology,
Wybrzeże Wyspiańskiego 27, 50-370 Wrocław, Poland

[b] Łukasiewicz Research Network – PORT Polish Center for Technology Development,
Stabłowicka 147, Wrocław, Poland

[c] School for Engineering of Matter, Transport and Energy Arizona State University
Tempe, AZ 85287, USA

[d] Solaris National Synchrotron Radiation Centre, Jagiellonian University, Czerwone
Maki 98, 30-392 Kraków, Poland

*Corresponding author.

E-mail address: agata.tolloczko@pwr.edu.pl

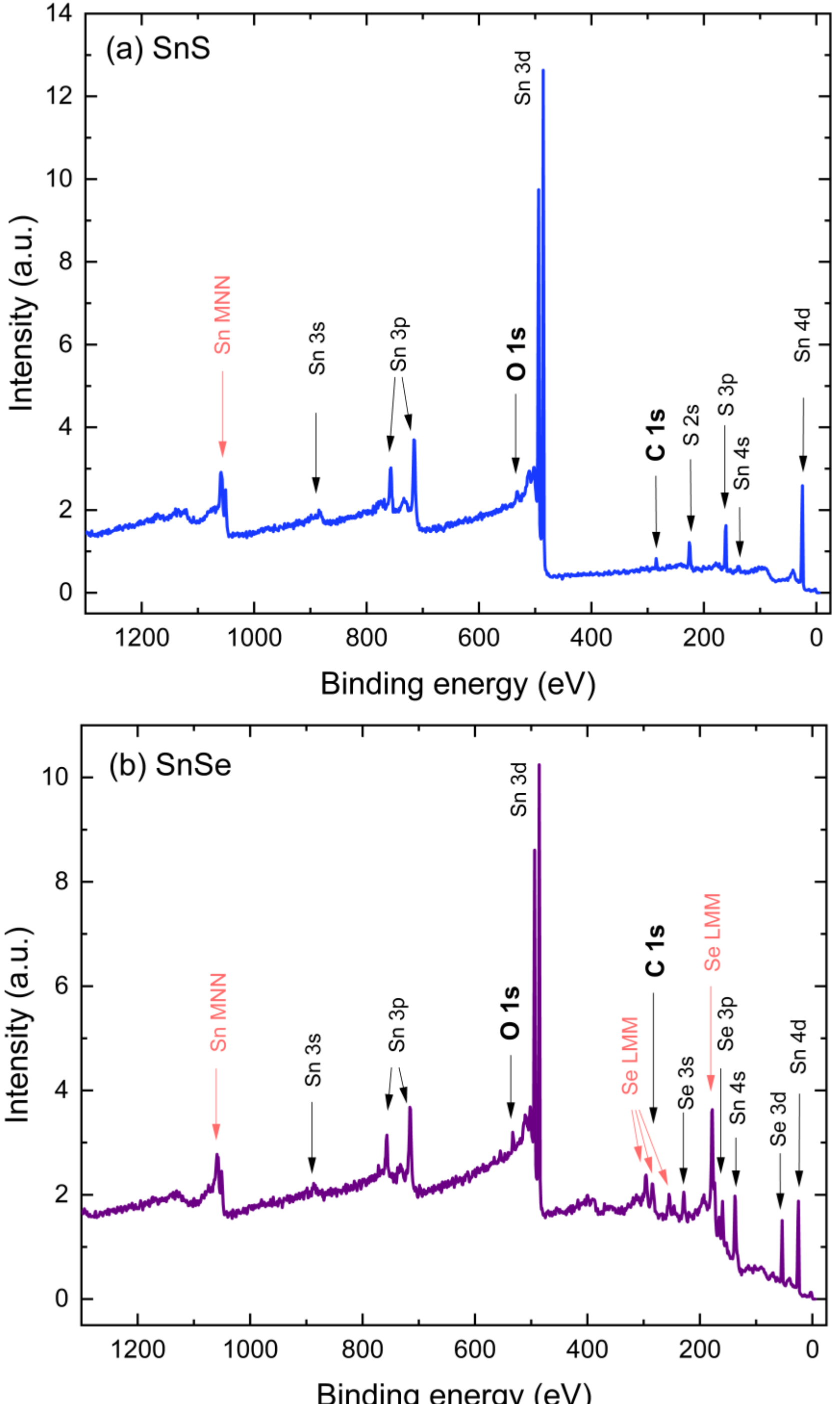

Fig. S1. Full-scale core-level XPS spectra acquired for SnS (a) and SnSe (b). Lines corresponding to individual atomic orbitals are identified. Auger lines are marked with red arrows and labels. Along with the signal originating from Sn and S or Se, weak contribution of O 1s (at the biding energy of 532.5 eV) and C 1s (284.7 eV) states was observed. The spectra are interpreted with regard to Ref. [S1].

Table S1. Binding energies of the core-level XPS lines (with SO splitting given in parentheses) measured for SnS and SnSe.

	SnS	SnSe
XPS line (SO splitting)	Binding energy (eV)	
S $2p_{3/2}$	161.2 (1.1)	-
Sn $3d_{5/2}$	485.8 (8.5)	485.7 (8.4)
Se $3d_{5/2}$	-	53.7 (0.9)

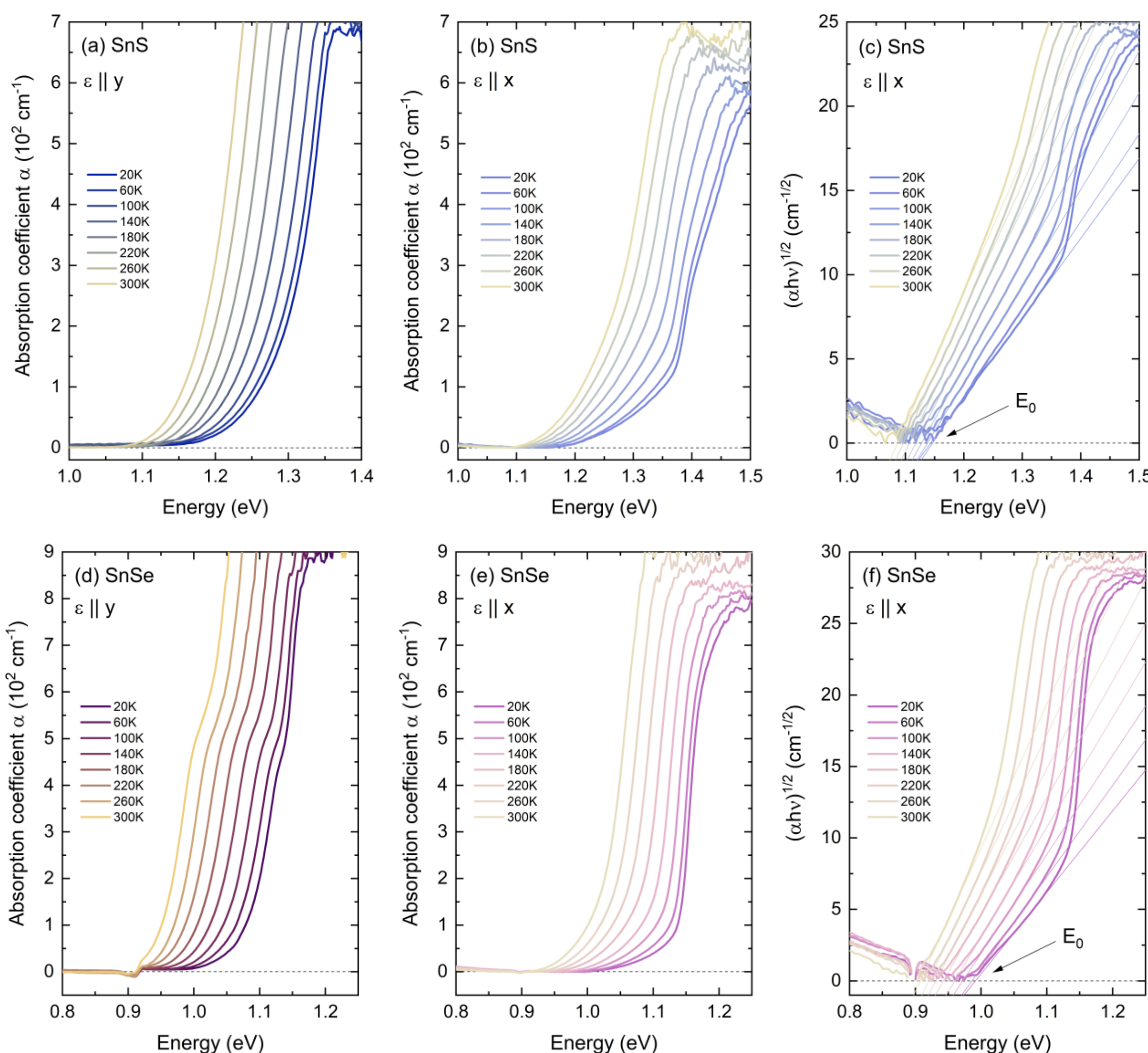

Fig. S2. Temperature dependence of the optical absorption measured of SnS (a,b) and SnSe (d,e) with incident light polarized along *y* (a, d) and *x* (b,e) in-plane crystallographic directions. Tauc plots hv vs. $(\alpha hv)^{1/2}$ of the *x*-polarized absorption, allowing to determine the fundamental indirect band gap E_0 of SnS (c), and SnSe (f).

Temperature dependence of the optical transition energy analysis

Bose-Einstein formula[S2]

$$E(T) = E(0) - \frac{2a_B}{\exp\left(\frac{\theta_B}{T}\right) - 1} \qquad \text{(Eq. S1)}$$

$E(0)$ - energy at the temperature of 0 K,

a_B - electron-phonon interaction strength,

θ_B - average phonon temperature.

Varshni formula[S3]

$$(T) = E(0) - \frac{\alpha T^2}{\beta + T} \qquad \text{(Eq. S2)}$$

$E(0)$ - energy at the temperature of 0 K,

α, β - semi-empirical Varshni coefficients.

Table S2. Temperature coefficients of the energies of the fundamental indirect (E_0) and lowest direct (E_1) optical transitions, determined from fitting the dependencies with Bose-Einstein (Eq. S1) and Varshni (Eq. S2) formulas.

	Transition	Bose-Einstein			Varshni		
		$E(0)$ (eV)	a_B (meV)	θ_B (K)	$E(0)$ (eV)	α (10^{-4} eV K^{-1})	β (K)
SnS	E_0	1.15	19.2	140	1.15	3.02	110
	E_1	1.23	27.7	133	1.23	4.67	112
SnSe	E_0	0.99	28.4	133	0.99	4.85	119
	E_1	1.06	78.6	223	1.07	8.75	230

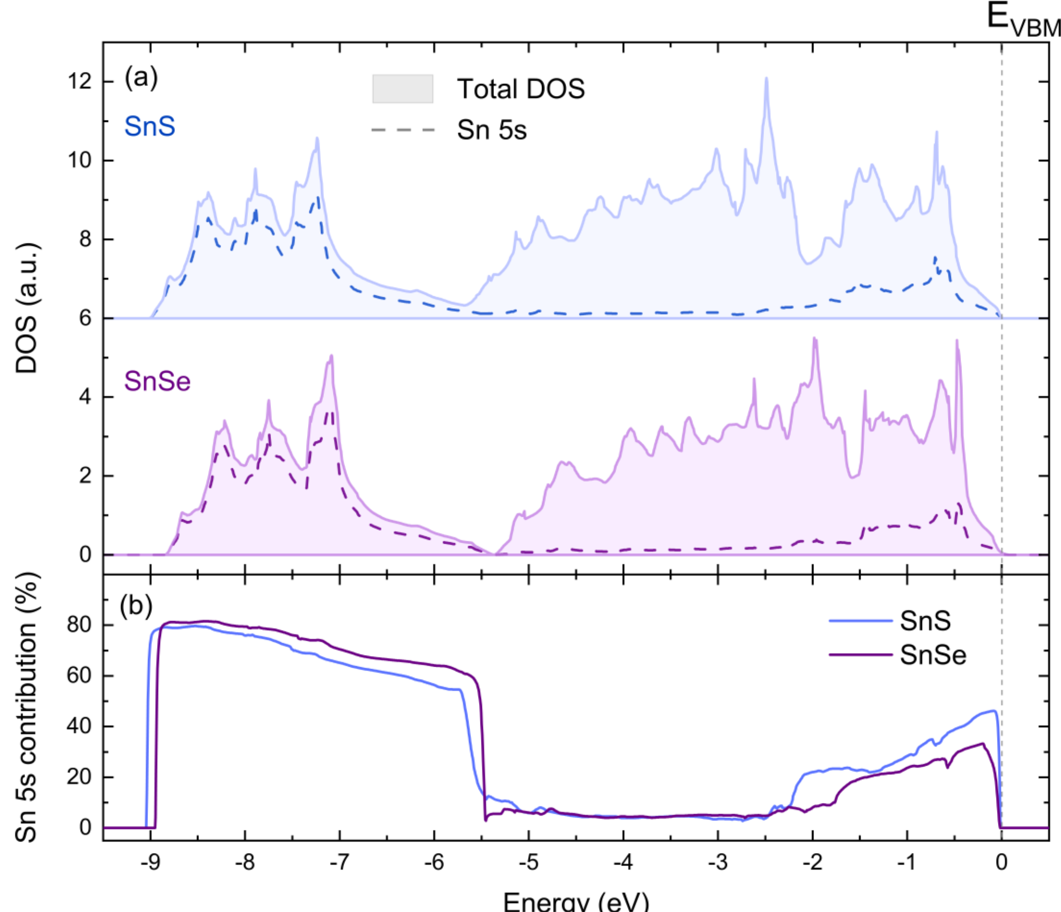

Fig. S3. (a) Total (shaded areas) and partial Sn 5*s* (dashed lines) DOS calculated for SnS (top plot) and SnSe (bottom plot). (b) The percentage contribution of the Sn 5*s* orbital to total DOS.

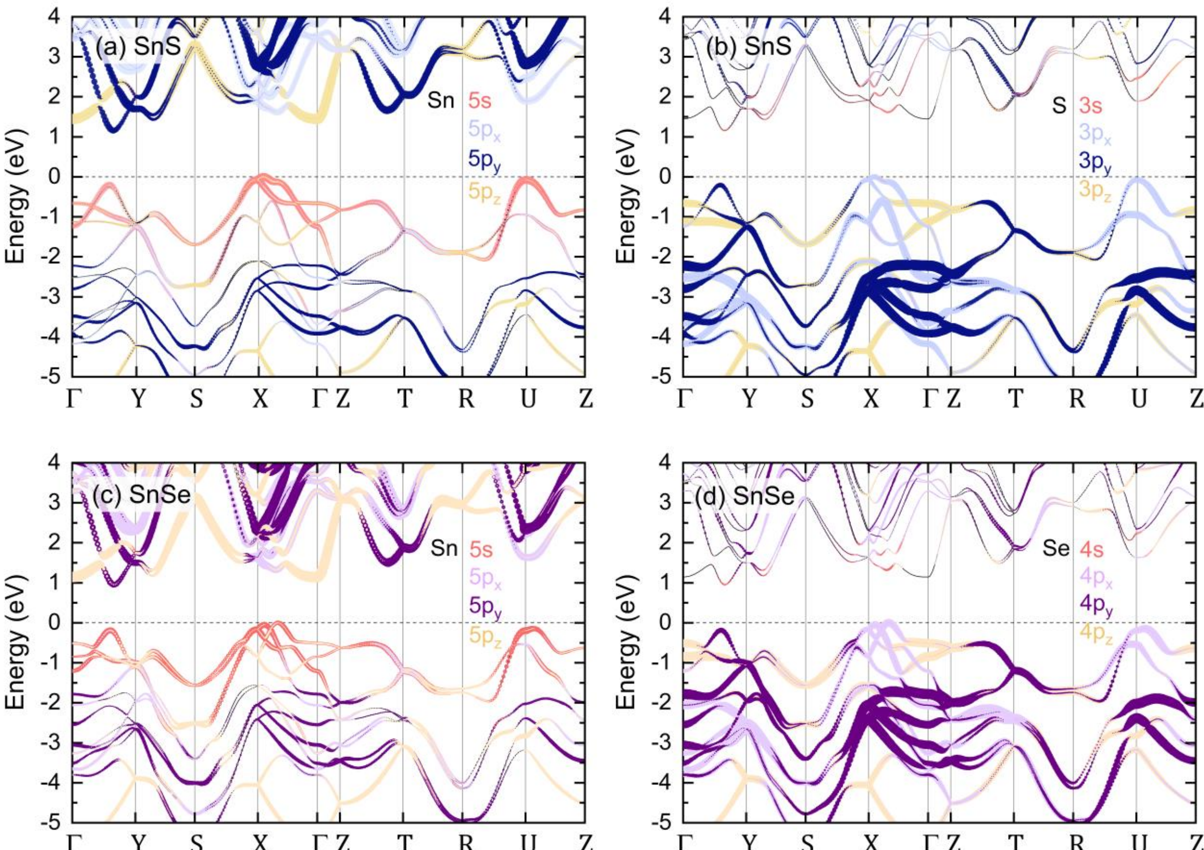

Fig. S4. The electronic band structure calculated with the use of mBJ exchange potential for SnS (a,b) and SnSe (c,d), with superimposed contribution of the valence *s* and *p* (with three spatial components p_x, p_y, p_z) orbitals of Sn (a,c), S (b) and Se (c) atoms, illustrated with the size of the plot points.

References

S1 J. F. Moulder and J. Chastain, *Handbook of X-ray Photoelectron Spectroscopy: A Reference Book of Standard Spectra for Identification and Interpretation of XPS Data*, Physical Electronics Division, Perkin-Elmer Corporation, 1992.

S2 L. Viña, S. Logothetidis and M. Cardona, Phys. Rev. B, 1984, 30, 1979–1991.

S3 Y. P. Varshni, Physica, 1967, 34, 149–154.

Chapter 5

Photoemission Study of the Thermoelectric Group IV-VI van der Waals Crystals (GeS, SnS, and SnSe)

Agata K. Tołłoczko, Szymon J. Zelewski, Jakub Ziembicki, Natalia Olszowska, Marcin Rosmus, Tomasz Woźniak, Sefaattin Tongay, and Robert Kudrawiec

Advanced Optical Materials, **12**, 2302049 (2024)

Overview

The electronic band structure of GeS, SnS, and SnSe was experimentally measured by angle-resolved photoemission spectroscopy. The acquired maps allowed to observe the valence band dispersion and resolve a subtle splitting of the valence band maximum close to the X point of the Brillouin zone, which is a feature predicted to enhance the thermoelectric properties of the materials. Additionally, hole effective masses were directly determined from the curvature of the valence band valleys. The accuracy of the theoretically calculated band structure is verified.

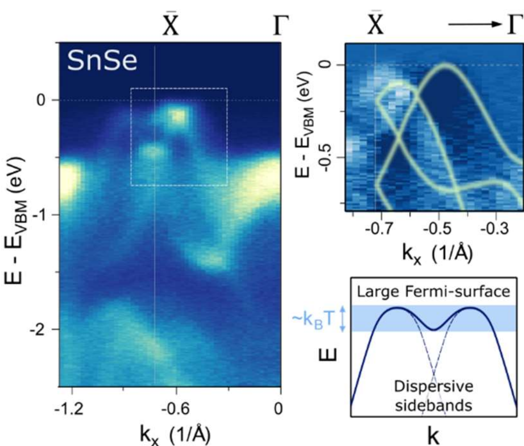

Fig. 5.1 Graphical abstract. Reprinted from Ref. [87] under CC-BY 4.0 license. Copyright 2024 A. K. Tołłoczko *et al.*

Author's contribution

Agata K. Tołłoczko (corresponding author) performed the angle-resolved photoemission spectroscopy experiments (with assistance from Marcin Rosmus and Natalia Olszowska, beamline scientists at the SOLARIS National Synchrotron Radiation Centre) and optical measurements (optical absorption and Raman scattering), processed and analyzed the acquired data, prepared their graphical presentation, proposed the interpretation, and wrote the manuscript.

RESEARCH ARTICLE
ADVANCED OPTICAL MATERIALS
www.advopticalmat.de

Photoemission Study of the Thermoelectric Group IV-VI van der Waals Crystals (GeS, SnS, and SnSe)

Agata K. Tołłoczko, Szymon J. Zelewski, Jakub Ziembicki, Natalia Olszowska, Marcin Rosmus, Tomasz Woźniak, Sefaattin Tongay, and Robert Kudrawiec*

Group IV-VI van der Waals crystals (MX, where M = Ge, Sn, and X = S, Se) are receiving increasing attention as semiconducting thermoelectric materials with nontoxic, earth-abundant composition. Among them, SnSe is considered the most promising as it exhibits a remarkably high thermoelectric figure of merit (*ZT*), initially attributed to its low lattice thermal conductivity. However, it has been shown that the electronic band structure plays an equally important role in thermoelectric performance. A certain band shape, described as a "pudding mold" and characteristic for all MXs, has been predicted to significantly improve *ZT* by combining good electrical conductivity with high Seebeck coefficient. This subtle feature is explored experimentally for GeS, SnS, and SnSe by means of angle-resolved photoemission spectroscopy. The technique also allows for the determination of the effective mass and Fermi level position of as-grown undoped crystals. The findings are supported by ab initio calculations of the electronic band structure. The results greatly contribute to the general understanding of the valence band dispersion of MXs and reinforce their potential as high-performance thermoelectric materials, additionally giving prospects for designing systems consisting of van der Waals heterostructures.

1. Introduction

A family of van der Waals crystals isoelectronic to black phosphorus called group IV monochalcogenides (MXs)[1] are known to be promising for application in two-dimensional (2D) optoelectronics (light detectors, solar cells)[2–7] and piezotronics.[8–10] Recently, they have also been rediscovered as potentially excellent thermoelectric materials,[11–13] extremely desired in the era of growing energy demand, as they possess the ability to convert waste heat into electricity. A quantity dictating the efficiency of thermoelectric conversion is a dimensionless thermoelectric figure of merit $ZT = \frac{S^2 \sigma T}{\kappa_L + \kappa_e}$, where S is the Seebeck coefficient (or thermopower), σ is the electrical conductivity, κ_L and κ_e are, respectively, lattice and electronic thermal conductivities, and T is the temperature. Materials with high ZT values (>2.0) are desired for efficient thermoelectric devices, unfortunately the parameters involved in the equation are interdependent, thus improving one often leads to deterioration of the other. Two strategies are commonly exploited to obtain high ZT: minimizing the thermal conductivity, and maximizing the power factor $PF = S^2\sigma$. The former is commonly realized by nanostructuring, dimensionality reduction, and introducing heavy atoms, which reduce the lattice thermal conductivity.[14–16] The latter can be achieved by electronic band structure engineering and adjustment of the Fermi level position by changing the charge carrier concentration.[17–21] Fermi level pinned deep inside the semiconductor band gap and high density of states at the band top (in the case of materials with simple band structure, dominated by a single valley, ensured by large effective mass) are favorable for large Seebeck coefficient, but result in poor electrical conductivity. However, it has been found that more complex band dispersion, with multiple valleys in the proximity of chemical potential, may allow to combine these two properties, by providing sufficient density of states and simultaneously preserving low effective mass.[22,23] What is more, Kuroki and Arita[24] discovered that these conditions can be fulfilled by a single electronic band of a certain shape, described as "pudding mold", characterized by effectively flat band top and strongly dispersive sidebands. Both features (multivalley transport and "pudding mold" shape) can be found in the band structure of group IV monochalcogenides. The representatives of MXs attracting increasing attention are GeS, GeSe, SnS, and SnSe – layered semiconductors composed of earth-abundant and nontoxic elements, crystalizing in orthorhombic *Pnma* structure. Out of the four,

A. K. Tołłoczko, S. J. Zelewski, J. Ziembicki, T. Woźniak, R. Kudrawiec
Department of Semiconductor Materials Engineering
Wrocław University of Science and Technology
Wybrzeże Wyspiańskiego 27, Wrocław 50-370, Poland
E-mail: agata.tolloczko@pwr.edu.pl
N. Olszowska, M. Rosmus
Solaris National Synchrotron Radiation Centre
Jagiellonian University
Czerwone Maki 98, Kraków 30-392, Poland
S. Tongay
School for Engineering of Matter, Transport and Energy
Arizona State University
Tempe, AZ 85287, USA
The ORCID identification number(s) for the author(s) of this article can be found under https://doi.org/10.1002/adom.202302049

© 2023 The Authors. Advanced Optical Materials published by Wiley-VCH GmbH. This is an open access article under the terms of the Creative Commons Attribution License, which permits use, distribution and reproduction in any medium, provided the original work is properly cited.

DOI: 10.1002/adom.202302049

21951071, 2024, 6, Downloaded from https://onlinelibrary.wiley.com/doi/10.1002/adom.202302049 by Wroclaw University Of Science, Wiley Online Library on [26/09/2024]. See the Terms and Conditions (https://onlinelibrary.wiley.com/terms-and-conditions) on Wiley Online Library for rules of use; OA articles are governed by the applicable Creative Commons License

SnSe has been the most thoroughly studied[17,18,25–31] since Zhao et al.[32] reported a remarkably high ZT of 2.63 at 923 K. Considering the state-of-the-art nanostructured PbTe-based thermoelectric materials with $ZT = 2.2$,[14] such result was unexpected for a simple as-grown crystal composed of relatively light atoms. The authors attribute this property to ultralow intrinsic lattice thermal conductivity, resulting from strong lattice anharmonicity,[33,34] although later complementary explanations have been proposed, involving the electronic band structure.[17,27] Soon characteristic multivalley and pudding-mold band dispersion predicted by Density Functional Theory (DFT) calculations has been confirmed by angle resolved photoemission spectroscopy (ARPES).[17,27,29,30] Good thermoelectric performance has also been theoretically predicted for other MXs,[11,12] but significantly less attention was paid compared to SnSe. The second most popular is SnS, for which ZT exceeding 1 was achieved and the electronic band structure was experimentally investigated.[19,35–38] GeSe follows tin chalcogenides with several reports of ARPES[39,40] and thermoelectric properties measurements,[41,42] while for GeS only computational simulations have been published to date.[43–46] Therefore, especially for this material an experimental investigation is required to provide insight into its most fundamental properties and verify the calculations. Generally, according to both theoretical predictions and empirical studies, compared to SnSe other MXs exhibit poorer thermoelectric performance, which however does not necessarily exclude them from applications in thermoelectric devices. It has been shown that high ZT values can be obtained for heterostructures,[47,48] and, what is more, the increased efficiency of Peltier cooling can be reached by introducing a gradient of Seebeck coefficient across the device.[49]

In this work we present an in-depth investigation of the electronic band structure of GeS, SnS, and SnSe by combined ARPES measurements and DFT calculations. ARPES is the only technique allowing to experimentally observe the valence band dispersion, and additionally determine other important properties of the material, such as Fermi level position and hole effective mass. The obtained results are discussed in terms of thermoelectric performance of MXs and other potential applications. For SnS and SnSe previous findings are confirmed and augmented with investigations at higher binding energies. For GeS a first-to-date comprehensive experimental study of the valence band dispersion allowing to observe the “pudding mold” band shape is presented.

2. Results and Discussion

2.1. Crystal Structure and Simulated Electronic Band Dispersion

In **Figure 1**a–c schematic diagrams of MX crystal structure are presented. MXs crystalize in orthorhombic phase belonging to space group *Pnma* (no. 62), with two characteristic orthogonal crystallographic directions, armchair (x) and zigzag (y). A single layer is composed of two rows of atoms bound covalently, as can be seen in the side view of a layer in Figure 1b,c. The armchair direction is characterized by a peculiar puckered atomic arrangement, absent in the zigzag direction, which leads to strong in-plane anisotropy of these materials.[34,50–57] In a multilayer structure the layers are sequenced in a centrosymmetric AB stacking (particular atoms are positioned differently in alternating layers),

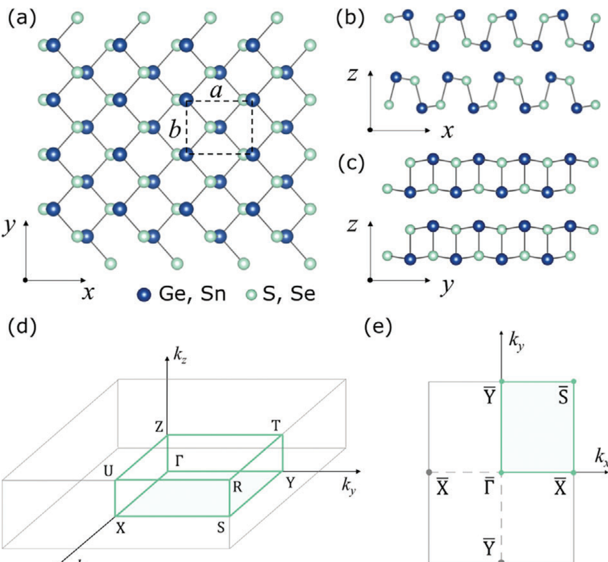

Figure 1. Schematic diagrams of crystal structure of the MXs, visualizing the atomic arrangement in a) a layer plane, and b) along the armchair, and c) the zigzag directions. d) 3D and e) reduced 2D Brillouin zone of the orthorhombic lattice, with marked high-symmetry points.

but again only in the armchair direction (see Figure 1b). In a monolayer (or few, odd-number layer flakes) the inversion symmetry is broken, resulting in piezoelectric,[8–10] multiferroic,[58–60] and nonlinear optical properties.[61–64]

An investigation of the electronic band dispersion, either experimentally or theoretically, demands an understanding of the reciprocal lattice of MXs. In Figure 1d the first Brillouin zone (BZ) of a simple orthorhombic structure is presented, with marked high symmetry points. Such picture represents the three-dimensional (3D) BZ, characteristic for bulk crystals. Directions parallel to k_x and k_y wavevector components correspond to the in-plane armchair and zigzag directions of the real space, respectively, and k_z corresponds to the direction perpendicular to the layer plane. However, in ARPES technique the results are usually analyzed with regard to the 2D (surface) BZ, presented in Figure 1e. In this case four characteristic high-symmetry points ($\bar{\Gamma}$, $\bar{Y}$, $\bar{X}$, and $\bar{S}$) are the projections along k_z of the respective points of the 3D BZ. Further, we also introduce the Λ and Δ symbols in order to label characteristic points in the Γ-X (close to X point) and Γ-Y (approximately in half of the distance between Γ and Y) paths, respectively, where the valence band local maxima occur. Analogously, their projections onto the 2D reduced BZ are referred to as $\bar{\Lambda}$ and $\bar{\Delta}$.

The electronic band structure along the high symmetry paths of the 3D BZ obtained from DFT calculations with the use of HSE06 hybrid functional for each investigated material is illustrated in **Figure 2**. Both valence and conduction band dispersions are plotted, allowing to determine the type and theoretical width of the electronic energy gap. The computation procedure (see the Experimental Section for details) did not involve the determination of the Fermi level position, therefore the energy scale is relative to the energy of the highest valence band maximum (VBM) of each structure. As can be seen from Figure 2, a common feature

© 2023 The Authors. Advanced Optical Materials published by Wiley-VCH GmbH

ADVANCED SCIENCE NEWS
www.advancedsciencenews.com

ADVANCED OPTICAL MATERIALS
www.advopticalmat.de

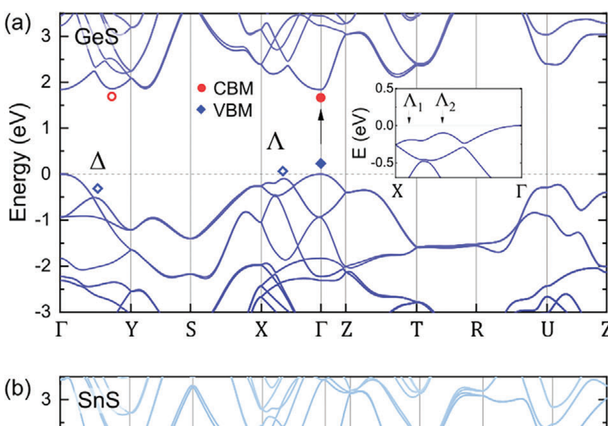

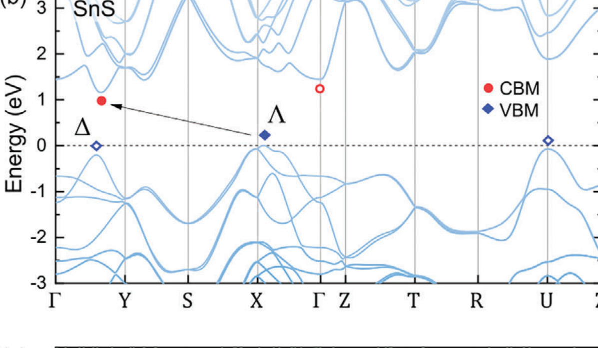

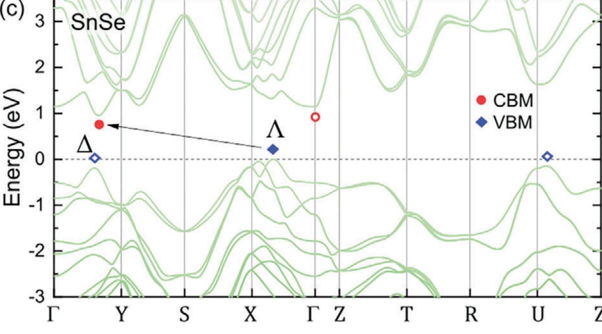

Figure 2. Electronic band structure predicted by DFT calculations with the HSE06 hybrid functional for a) GeS, b) SnS, and c) SnSe. The red circles and blue diamond symbols mark conduction band minima and valence band maxima, respectively. Solid symbols correspond to main extrema of the structure. The inset of panel (a) illustrates the separation of the band apices in the Λ region. The energy of the highest VBM is assumed as E = 0 eV.

of all MXs is the presence of multiple band extrema within a narrow energy range, marked with red circles (conduction band minimum, CBM) and blue diamond symbols (VBM). Solid symbols correspond to the lowest CBM and highest VBM, determining the band gap, whereas hollow ones denote secondary extrema. For tin chalcogenides, the main VBM is located in the Γ-X path close to the X point, in a k-region labeled Λ. The topmost band forms a characteristic pudding mold shape,[17,24] with two closely lying maxima separated by a shallow minimum (a saddle point). In the case of GeS, an analogous feature is also present, although the valley at the Γ point plays the role of the highest VBM. To better resolve the pudding mold structure, a close-up of the Λ region is presented in the inset of Figure 2a for GeS. The exact k-points where the maxima occur are referred to as $Λ_1$ (closer to the X point) and $Λ_2$ (farther from the X point). The same nomenclature is used for SnS and SnSe. The predicted band shape diverges from an ideal pudding mold, as the band tops in $Λ_1$ and $Λ_2$ are located at slightly different energies, as demonstrated in Figure S1 (Supporting Information). Another important feature is the secondary VBM located in approximately half of the Γ-Y path, in a point labeled Δ, at the energy of ≈100 meV below the Λ maximum for SnS and SnSe, and ≈500 meV for GeS. A high energy valley is also present in (or close to) the U point, which is located above the X point in the k_z direction of the BZ. It is worth noticing that the splitting into the $Λ_1$ and $Λ_2$ apices vanishes away from the central plane of the BZ to form a single broad maximum in the U point. The energies of the discussed features are summarized in Table S2 (Supporting Information).

The conduction band dispersion of the MXs is similarly complex. For GeS the lowest CBM is located at Γ, suggesting a direct character of the band gap, although there are two other valleys, in the Γ-Y and Y-S paths, at nearly the same energy (≈10 and ≈30 meV higher, respectively). With such small differences, it is not possible to unambiguously determine the band gap character of GeS based solely on the DFT simulations, although regarding the proximity of multiple valleys, either in the valence and conduction band, a direct-like behavior can be expected to manifest in the material properties. The domination of the optical properties by direct optical transitions, despite the indirect fundamental band gap, has been shown for another group IV monochalcogenide – GeSe.[52,65] In the case of SnS and SnSe the CBM appears near the Δ point, however at not the same k-value as the $VBM_Δ$. According to these observations, tin chalcogenides have an indirect energy gap. The theoretical values of the band gaps can be found in Table 2.

The simulations discussed above were performed with the use of the HSE06 hybrid functional, which is established as a method allowing to accurately reproduce the band dispersion. Nevertheless, DFT calculations are always burdened with approximations and the final result may vary depending on the choice of the computational method and parameters. According to our overall experience with the MX family, it is the lattice optimization procedure that affect the resulting band dispersions most severely. In our previous work regarding GeS, the structure optimization was performed applying the same procedure (see Experimental Section), but with different parameters and van der Waals correction.[54] The resulting band structure varied from the one presented here, with the most significant discrepancies being the positions of the highest VBM (in the Λ region instead of Γ point) and lowest CBM (in the Γ-Y path instead of Γ point), and, as a consequence, indirect instead of direct band gap character. In this work, for an optimized crystal structure, we compare two methods of the electronic dispersion calculation: the commonly used HSE06 hybrid functional, and modified Becke-Johnson exchange potential (mBJ-TB09), which characterizes with significantly lower computational cost. A comparison of the electronic band structures calculated for GeS, SnS, and SnSe acquired with the two methods is presented in Figure S2 (Supporting Information). The differences in the dispersion near the valence band top are minor, and become more distinct at deeper energy levels, where the bands obtained from HSE06 calculations are visibly shifted toward higher binding energies with respect to mBJ. Most importantly, the relative energies of the

© 2023 The Authors. Advanced Optical Materials published by Wiley-VCH GmbH

21951071, 2024, 6, Downloaded from https://onlinelibrary.wiley.com/doi/10.1002/adom.202302049 by Wroclaw University Of Science, Wiley Online Library on [26/09/2024]. See the Terms and Conditions (https://onlinelibrary.wiley.com/terms-and-conditions) on Wiley Online Library for rules of use; OA articles are governed by the applicable Creative Commons License

21951071, 2024, 6, Downloaded from https://onlinelibrary.wiley.com/doi/10.1002/adom.202302049 by Wroclaw University Of Science, Wiley Online Library on [26/09/2024]. See the Terms and Conditions (https://onlinelibrary.wiley.com/terms-and-conditions) on Wiley Online Library for rules of use; OA articles are governed by the applicable Creative Commons License

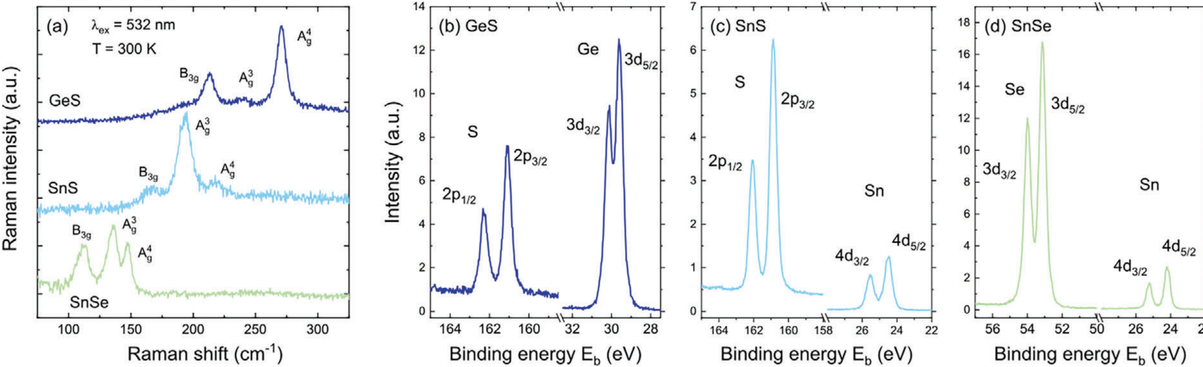

Figure 3. a) Raman scattering spectra with identified vibrational modes, and core level XPS lines observed for b) GeS, c) SnS, and d) SnSe.

band extrema are preserved. Eventually, mBJ calculations result in slightly narrower band gaps, however the differences are less than 60 meV. Therefore, it can be concluded that for the purpose of the band dispersion reproduction in proximity of the band gap, both methods provide similar results, with the mBJ-TB09 being considerably less resource- and time-consuming.

An electronic structure with multiple band extrema leads to some major consequences, that need to be discussed. First of all, a multivalley structure may significantly improve the thermoelectric properties of a material (effectively increased density of states leads to the enhancement of the Seebeck coefficient).[22,23,26] Bands in close vicinity of the Fermi level can contribute to the electronic transport through thermal excitation or increasing the carrier concentration by doping. Importantly, the pudding mold shape of a band is considered a feature responsible for combining good conductivity with large thermopower. In Figure S1a (Supporting Information) a simplified pudding mold structure is schematically presented. When the separation between the maxima and the central minimum is within the order of magnitude of thermal energy $k_B T$, where k_B is the Boltzmann constant, and T is the temperature, a significant part of the band is effectively flat, resulting in high-effective-mass-like conditions, favorable for large thermopower. Meanwhile, strongly dispersive sidebands (correlated with low effective mass) ensure good conductivity. The influence of the pudding mold band shape on thermoelectric properties of the material is discussed in detail by Kuroki and Arita.[24]

According to previous reports, the valence band of the MXs is composed of a mixture of chalcogen atom p orbitals (S 3p or Se 4p) and group-IV atom s orbitals (Ge 4s or Sn 5s). The conduction band is dominated by the Ge 4p or Sn 5p states, with minor contribution from S or Se.[53,54]

In the following sections, the calculated band dispersion is discussed with regard to the experimentally observed valence band structure, acquired with the use of ARPES technique.

2.2. Structural Characterization

The measured samples were bulk undoped crystals, grown by chemical vapor transport (CVT) method. The quality and purity of the crystals were confirmed by Raman scattering and x-ray photoemission spectroscopy (XPS). Raman scattering measurements (**Figure 3**a) revealed only vibrational modes characteristic for the considered crystallographic system (symmetric A_g and asymmetric B_{3g} shear vibrations[66,67]), with no evidence of chalcogen-rich phase, indicating high structural quality of the examined crystals. An investigation of the qualitative chemical composition was performed using core level XPS (Figure 3b–d). The full-scale spectra, plotted in Figure S3 (Supporting Information), only show the presence of Ge or Sn and S or Se atoms in the measured binding energy range. Investigations of oxygen-related levels, laying outside the range for which the beamline equipment is optimized, are not considered relevant due to the process of sample preparation, involving exfoliation under ultra-high vacuum ($<10^{-9}$ mbar), allowing to minimize surface oxidation. In Figure 2b–e regions of the spectra with characteristic features related to particular elements are presented, for GeS (panel b), SnS (c), and SnSe (d). For S in GeS and SnS a doublet corresponding to 2p orbitals was observed, with spin-orbit (SO) splitting of 1.16 eV, and expected $p_{3/2} : p_{1/2}$ intensity ratio of ≈2:1. For Se in SnSe, a 3d doublet can be identified, with SO splitting of 0.86 eV, and the $d_{5/2} : d_{3/2}$ intensity ratio of ≈3:2. For Ge (Sn) atoms, signal associated with 3d (4d) orbitals was detected, with SO splitting of 0.54 eV (1.04 eV). Additionally, for GeS a weak contribution from Ge 3p orbitals was measured (see inset of Figure S3a, Supporting Information). The obtained values of binding energy indicate either +2 or −2 oxidation state of metal and chalcogen atoms, respectively, and no sidebands originating from other phases (MX_2, M_2X_3), oxides, or elemental forms were observed.[68,69] Raman modes and XPS core level lines observed in the experiments, with corresponding frequencies, binding energies, and SO splitting values, are summarized in the Supporting Information (Table S1).

2.3. Photoemission Study

An experimental investigation of the electronic band structure performed by means of ARPES measurements is a straightforward way to observe the actual valence band dispersion and verify the accuracy of the theoretical model used for its prediction indicating the directions for future improvements. It allows to directly connect certain features occurring in the band structure with the resulting properties of the material, such as thermoelectric performance, band gap character, and optical transitions

 © 2023 The Authors. Advanced Optical Materials published by Wiley-VCH GmbH

21951071, 2024, 6, Downloaded from https://onlinelibrary.wiley.com/doi/10.1002/adom.202302049 by Wroclaw University Of Science, Wiley Online Library on [26/09/2024]. See the Terms and Conditions (https://onlinelibrary.wiley.com/terms-and-conditions) on Wiley Online Library for rules of use; OA articles are governed by the applicable Creative Commons License

(including their anisotropy), without the influence of approximations and corrections.

For the interpretation and discussion of ARPES results we assume a 2D BZ, presented in Figure 1e. The choice of the k_x-k_y plane containing the center of the BZ, i.e., the Γ point, is justified in this case. While for covalent 3D materials the electronic bands dispersion in the k_z direction is usually significant, most vdW crystals characterize with quasi-2D structure, which leads to weak dispersion in the direction corresponding to the layers stacking axis. Nevertheless, the considered surface BZ is a projection of the bulk BZ, therefore a contribution of other states along k_z may still be visible in the photoemission maps. In the experiment, different values of k_z can be probed by adjusting the incident photons energy. Such test scans within the energy range from 40 to 100 eV were performed and no apparent dispersion was in fact observed, which is consistent with reports of Pletikosić et al. regarding SnSe.[27] Follow-up experiments were carried out at a constant photon energy of 100 eV, allowing to acquire a picture of a large region of the reciprocal space.

In **Figure 4** the results of ARPES measurements are summarized and set with DFT calculations of the electronic band structure, obtained using the HSE06 hybrid functional. Panels a, b, and c demonstrate maps acquired for GeS, SnS, and SnSe, respectively. For clarity, each panel has been divided into subpanels indexed from 1 to 6. In this section the energy corresponding to the highest VBM (E_{VBM}) for each sample is assumed as relative zero ($E_{VBM} = 0$), and all results are presented with respect to this energy. The Fermi level position and actual binding energies of the VBMs are discussed later.

An important mode of the ARPES technique is the investigation of constant energy contours in the k_x-k_y plane. Subpanels (1) and (2) for each material present maps of photoemission intensity as a function of the in-plane wavevector. White dashed rectangles represent the boundaries of the first BZ, with high symmetry points labeled in Figure 4a$_2$. In subpanels (1) maps corresponding to the energy close to the highest VBM of each material are shown, and in subpanels (2) features below VBM are visualized. In Figure 4a$_2$ a constant energy contour corresponding to 3.0 eV below the VBM of GeS reveals four equivalent valleys in S points, revealing the rectangular shape of the BZ and allowing to directly determine its dimensions. For SnS and SnSe a similar structure appears at slightly different energies, as presented in Figure S4 (Supporting Information). Figure 4b$_2$ and c$_2$ show maps at energies of -0.40 eV and -0.36 eV, respectively, where secondary VBMs of tin chalcogenides become distinct. Another approach in the analysis of ARPES results, allowing more in-depth investigation of the electronic structure, its anisotropy, and direct interpretation in terms of DFT calculations, is to map photoemission along selected high-symmetry directions in wide binding energy range. Such scans can be compared side-by-side with band structure predicted by DFT. Subpanels (3) and (5) show ARPES maps along X-Γ-X and Y-Γ-Y paths of the 2D BZ. In subpanels (4) and (6) calculated valence band dispersion is superimposed over the second derivative of the photoemission map.

As can be seen from the figures, each investigated material exhibits anisotropy of the band dispersion, with the pudding mold shape of the topmost band in the Λ region (labeled in Figure 4c$_1$). Although the characteristic splitting into Λ_1 and Λ_2 valleys is challenging to detect experimentally, thanks to high angular resolution of the utilized setup we were able to observe it. This feature was clearly visible for SnSe (see Figure 4c), and less conspicuous for GeS and SnS. Close-ups of the photoemission maps and their second derivatives containing the Λ region are presented in Figure S5 (Supporting Information). The measured dispersion does not exactly follow the calculated one, which may be attributed to the influence of other k_z states. DFT predicts different energies of the maxima in Λ_1 and Λ_2 points, separated by up to 70 meV, while in the case of GeS and SnSe the shape observed in the photoemission maps is more symmetrical. Both maxima occur at approximately equal energy, and the central minimum is significantly shallower, which makes each hole pocket accessible simultaneously. Such a shape is also closer to an ideal pudding mold. For SnS the agreement with calculations is better – the VBM in Λ_2 is located below Λ_1, which may partly account for poorer thermoelectric performance compared to SnSe.

In the case of GeS, there is a crucial discrepancy between experiment and theory regarding the position of the main VBM. According to calculations, the highest VBM occurs at the Γ point, and the Λ valleys lay ≈100 meV below, whereas in the ARPES maps in Figure 4a$_1$,a$_3$ it is clearly visible, that all three maxima correspond to nearly equal binding energy. Assuming the lowest CBM in the Γ point, GeS turns out to be a direct or a quasi-direct semiconductor, which is consistent with previously reported optical spectroscopy investigations,[50,70,71] however in order to definitely determine the band gap character, also the conduction band dispersion needs to be investigated experimentally.

For SnS and SnSe there are distinct differences between calculated and measured band dispersion around the Γ point, especially in the k_x direction. In the calculated structure the bands are extremely flat and form a saddle point (with positive curvature in the k_x direction, and negative in the k_y). In the experiment, an isotropic parabolic maximum was observed, with stronger dispersion. The bands energy, however, still remains significantly below the VBM_Λ, and therefore their contribution to optoelectronic properties of the material is minor.

The secondary VBM in the Δ point is clearly visible for tin chalcogenides, and its position can be most accurately determined from constant energy contours, corresponding to an energy at which the band emerges (see Figure S4, Supporting Information). For SnSe the VBM_Δ is located at −0.22 eV, and for SnS at −0.26 eV, however the photoemission originating from this BZ region is weak, preventing us from a more precise estimation of the energy. The results for both compounds are in agreement with our DFT HSE06 calculations (predicting the energies of −0.19 and −0.20 eV, respectively), as well as with previous experimental studies on SnSe (reporting a distance from the VBM_Λ of 0.20–0.26 eV[26–28]). For GeS this feature could not be resolved in the ARPES measurements due to high-intensity band around Γ, overlapping photoemission originating from the Δ valley, although the observed band shape follows the simulated dispersion (see Figure 4a$_6$).

In general, considering a wide binding energy range, the valence band dispersion obtained from ARPES measurements is in outstanding agreement with DFT predictions, and the observed discrepancies can be explained and justified. To begin with, the ARPES maps are projections of the 3D band structure onto a 2D plane, while the DFT calculations discussed here only simulate the dispersion along high symmetry paths in the bulk BZ.

© 2023 The Authors. Advanced Optical Materials published by Wiley-VCH GmbH

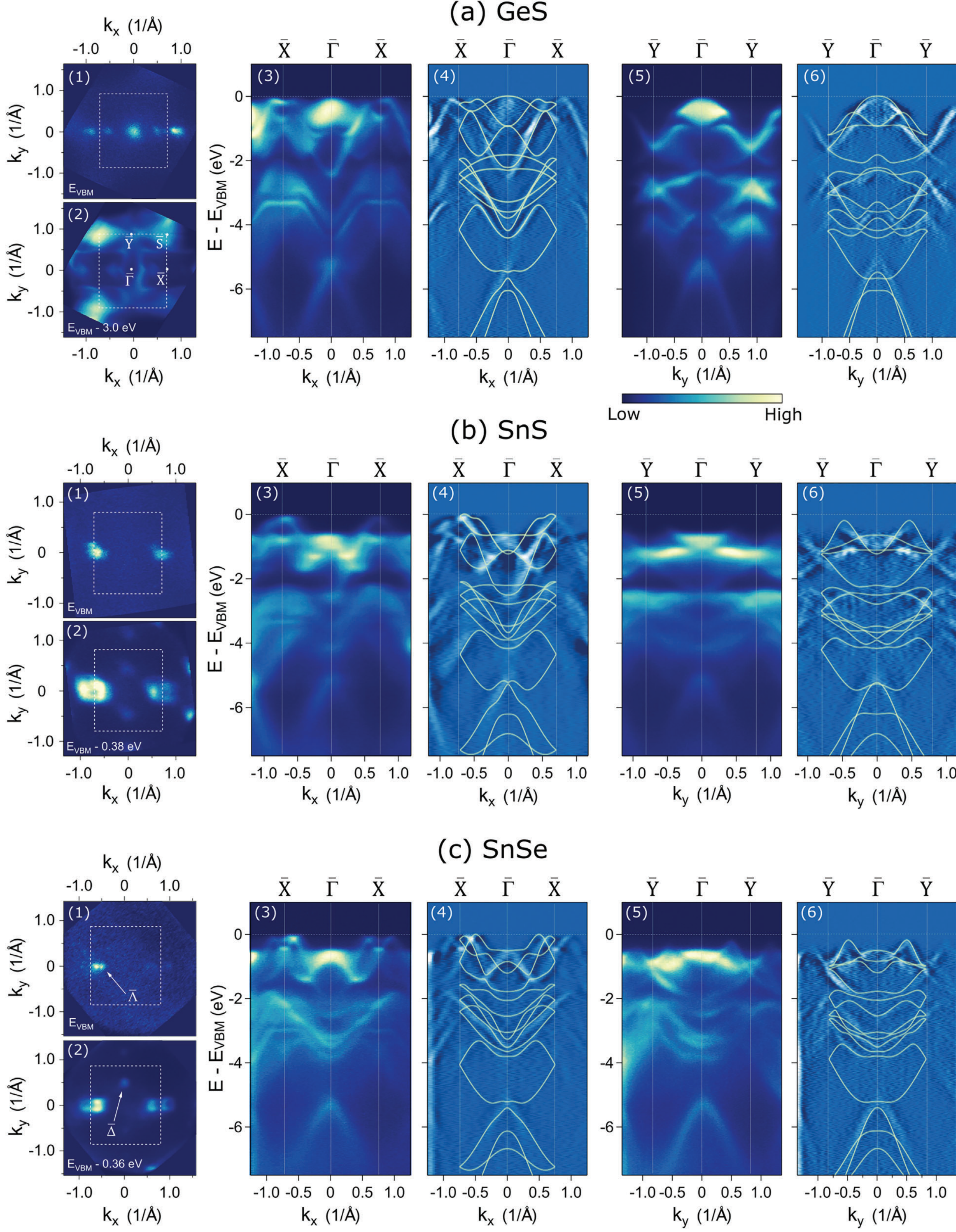

Figure 4. The results of ARPES measurements of valence band dispersion for a) GeS, b) SnS, and c) SnSe. Subpanels (1) and (2) present constant energy contours acquired at the band tops and energies at which other important features occur. White dashed rectangles mark the boundaries of the first BZ. In subpanels (3) and (5) photoemission maps in kx and ky directions, respectively, are shown, and in subpanels (4) and (6) valence band structure calculated with the HSE06 hybrid functional is superimposed over second derivative of the corresponding photoemission maps.

 © 2023 The Authors. Advanced Optical Materials published by Wiley-VCH GmbH

21951071, 2024, 6, Downloaded from https://onlinelibrary.wiley.com/doi/10.1002/adom.202302049 by Wroclaw University Of Science, Wiley Online Library on [26/09/2024]. See the Terms and Conditions (https://onlinelibrary.wiley.com/terms-and-conditions) on Wiley Online Library for rules of use; OA articles are governed by the applicable Creative Commons License

21951071, 2024, 6, Downloaded from https://onlinelibrary.wiley.com/doi/10.1002/adom.202302049 by Wroclaw University Of Science, Wiley Online Library on [26/09/2024]. See the Terms and Conditions (https://onlinelibrary.wiley.com/terms-and-conditions) on Wiley Online Library for rules of use; OA articles are governed by the applicable Creative Commons License

The measurement resolution is also limited by the experimental setup and configuration (temperature, width of the detector slits, incident photon energy, etc.), which does not apply to theoretical predictions. On the other hand, the DFT calculation results strongly depend on the choice of computational method and vdW correction, as discussed in Section 2.1, and to some degree do not accurately reproduce the actual electronic band structure. At last, the experimentally observed intensity of particular bands depends on the photoemission matrix element, which may result in weak or even invisible bands. There is, though, an interesting feature common for all investigated crystals present in the ARPES spectra, but not in the calculated band structure, which is unusual. In the X point of the BZ a narrow band emerges at the energy of ≈3 eV below the VBM, which exhibits remarkably flat dispersion in the k_x direction in quite wide wavevector range, implying strong localization. One explanation for such a picture might be a superposition of multiple bands with weak dispersion, resulting in one effectively flat band, although in such case we would expect larger broadening. The contribution from other k_z states should be considered, however no comparably flat bands at the corresponding energies were predicted in the U point of the 3D BZ either. This feature could be also interpreted as a measurement artifact (a ghost band resulting from step-like character of the sample surface), yet it is highly unlikely, as it appears for each sample. The most probable explanation is to attribute this band to some kind of an intrinsic defect level, common for the whole MX family, which explains both the flat dispersion (strong localization) and the lack of corresponding feature in the calculated band structure (assuming perfect crystal lattice). Nevertheless, to determine and understand the true origin of the discussed band, further investigation is required.

2.4. Effective Mass

The effective mass m^* of a material is determined by the curvature of the electronic band and given by $m^* = \frac{\hbar^2}{2}\left(\frac{\partial E^2}{\partial^2 k}\right)^{-1}$, where E is the energy, and k is the wavevector. Assuming parabolic approximation around the band top, m^* can be evaluated by fitting the dispersion with quadratic function. Such approach can be exploited for both theoretically and experimentally obtained band structure, however in the case of ARPES maps multiple factors may affect the result. The estimated band curvature strongly depends on the choice of the points indicating the band edge, which is often to some extent arbitrary, considering the image resolution and steepness of the observed feature. For this reason, significant discrepancies can be found in the literature. Most works regarding the hole effective mass focus on the SnSe compound.[26–29,38,72,73] The reported values of m_h^* in the Λ region of the BZ in the k_x direction range from 0.12 m_0[26] to 0.24 m_0,[73] and in the k_y direction from 0.1 m_0[38] up to 0.38 m_0[29] (where m_0 is the free electron mass). Also the ratio of the effective mass components in k_x and k_y directions varies, in some works reported as greater than 1, in others below 1.

Here we were able to evaluate the hole effective mass for SnS and SnSe around VBMs in the Λ_1 and Λ_2 points separately. In the case of GeS the photoemission originating from this BZ region was too weak to precisely determine m_h^*, and only estimations were made, burdened with high uncertainties. As the secondary VBM, the Γ point was analyzed for GeS, and the Δ point for SnS and SnSe. The m_h^* values were obtained by fitting of the parabolic function to the band edges visible in the photoemission second derivative maps, as presented in **Figure 5**. For each material (Figure 5b–d) the index of the subpanel (1-5) corresponds to a particular cut through the BZ, as labeled in Figure 5a. The determined values are summarized in **Table 1**. For SnSe we obtained good agreement with previously reported results. Besides a slightly higher effective mass at the Λ valley in the k_x direction, the values coincide perfectly with those reported by Pletikosić et al.[27] ($m_x^\Lambda = 0.21\, m_0$, $m_y^\Lambda = 0.18\, m_0$, $m_y^\Delta = 0.24\, m_0$), which we consider the most reliable due to quality and resolution of the acquired ARPES maps. The experimental effective masses are generally in accordance with theoretical values, listed in Table S3 (Supporting Information), obtained by fitting the parabolic function to calculated band dispersion around VBMs. The values closest to the experiment were found for SnSe (in Λ_1, Λ_2, and Δ points) and GeS (in the Γ point). The most significant discrepancies occurred for the Λ_1 point in the case of GeS, and the Λ_2 point in the case of SnS.

The effective mass is a parameter directly influencing the carrier mobility ($\mu = \frac{e\tau_c}{m^*}$, where e is the elementary charge, and τ_c is the mean free time between collisions), and, as a consequence, the electrical conductivity of a given type ($\sigma = en\mu$, where n is the carrier concentration). Therefore, the ratio of the values corresponding to respective crystallographic directions can be compared. In the Δ region the m_x/m_y ratio is generally greater than 1 for tin chalcogenides and below 1 for GeS. The exact values are listed in Table 1. This result is in agreement with reports of hole mobility and conductivity measured in armchair and zigzag directions. According to Tian et al.,[36] for SnS the hole mobility ratio $\mu_y/\mu_x = 1.67$. For SnSe Zhao et al.[32] report $\mu_y/\mu_x = 2$, but along with the electrical conductivity ratio of $\sigma_y/\sigma_x = 1.2$. Such comparison may not be entirely accurate due to the influence of τ_c parameter, which along with the effective mass often exhibits anisotropy and is affected by the presence of defects. Nevertheless, we can see that the general tendency is preserved: for tin chalcogenides the conductivity is better in the zigzag direction, while for GeS the armchair direction is preferable (like in the case of black phosphorus[74]).

2.5. Fermi Level Position

In the previous sections we assumed the energy corresponding to the highest VBM as the relative zero level, in order to conveniently compare the acquired photoemission maps with DFT predictions. However, for the design of electronic devices and heterostructures the position of Fermi level needs to be investigated. In ARPES measurements the Fermi level energy (E_F) can be determined by using a reference gold sample. Accordingly, the VBM position (E_{VBM}) with respect to the E_F was found for GeS, SnS, and SnSe corresponding to the energies of 0.67, 0.38, and 0.14 eV, respectively. The value obtained for GeS is larger than reported by Smiles et al. (0.46 eV),[69] however their experiment was carried out at room temperature, not 77 K, as in the case of this work, and the shift of the E_F toward the valence band may be a consequence of thermal activation of intrinsic acceptors. For SnS and SnSe our results are in line

© 2023 The Authors. Advanced Optical Materials published by Wiley-VCH GmbH

ADVANCED SCIENCE NEWS
www.advancedsciencenews.com

ADVANCED OPTICAL MATERIALS
www.advopticalmat.de

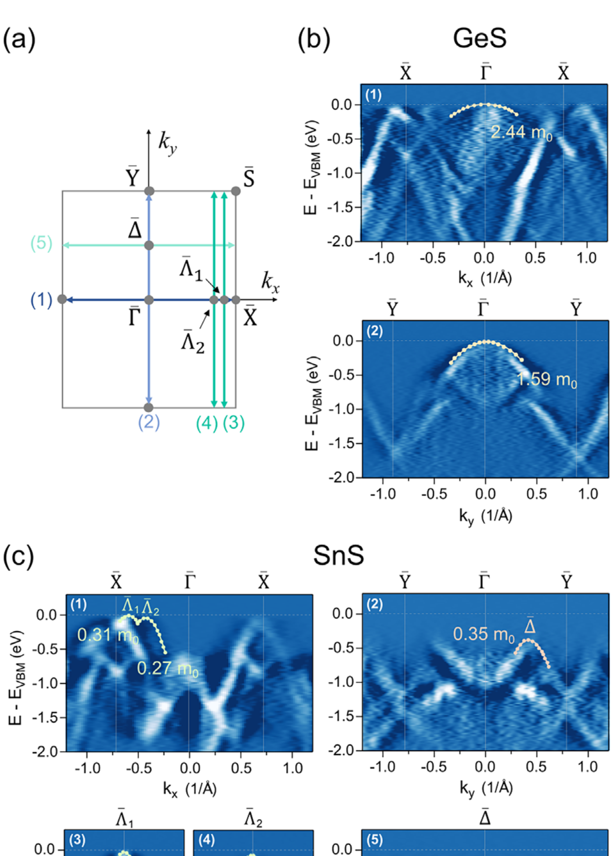

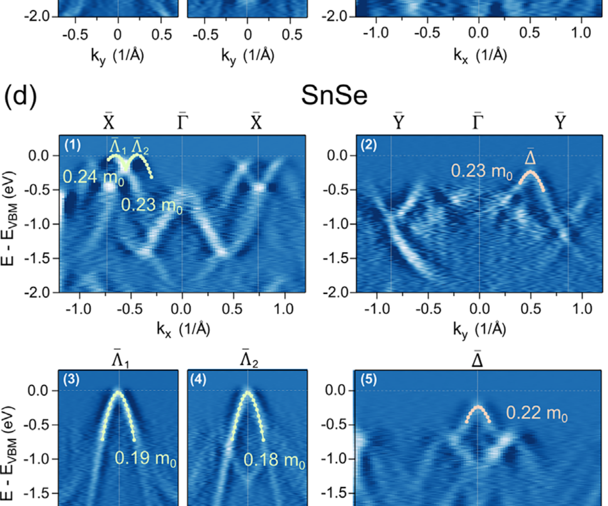

Figure 5. a) 2D Brillouin zone of MXs with marked cuts, along which the effective mass was investigated. Photoemission second derivative maps of the VBMs in the Λ region and the Γ or the Δ point of the BZ acquired for b) GeS, c) SnS, and d) SnSe, with results of fitting the parabolic function to dispersion at the band tops, in order to extract the hole effective mass. The subpanels (1)–(5) correspond to the respective cuts given in panel (a).

Table 1. Hole effective masses of GeS, SnS, and SnSe in the Λ_1, Λ_2, and Γ or Δ points of the BZ, along k_x and k_y directions, determined from ARPES maps. The values are given as fractions of the free electron mass m_0.

BZ point	Λ_1			Λ_2			Γ or Δ		
	m_x	m_y	m_x/m_y	m_x	m_y	m_x/m_y	m_x	m_y	m_x/m_y
GeS	≈0.3	≈0.7	≈0.43	–	–	–	2.44 (Γ)	1.59 (Γ)	1.53
SnS	0.31	0.25	1.24	0.27	0.28	0.96	0.28 (Δ)	0.35 (Δ)	0.80
SnSe	0.24	0.19	1.26	0.23	0.18	1.28	0.22 (Δ)	0.23 (Δ)	0.96

with Whittles et al. (≈0.38 eV for SnS)[68] and Pletikosić et al. (0.12 eV for SnSe).[27]

In order to assess the CBM position (E_{CBM}) relative to E_F, the energy gap (E_g) of each material is necessary. E_g can be determined from DFT calculations of the electronic band structure, although such approach i) provides the value at temperature of 0 K, and ii) may vary dependently on the choice of the computational method. Therefore, we performed experimental investigation by means of the optical absorption spectroscopy, at the temperature of ≈80 K. From the Tauc plots[75] of the acquired spectra (presented in Figure S6, Supporting Information) we obtained the band gaps of 1.69 eV for GeS, 1.15 eV for SnS, and 0.98 eV for SnSe. In the case of GeS the direct character of the band gap was assumed (for the reasons explained before), contrary to tin chalcogenides. Considering these results, the Fermi level position indicates p-type character for all materials, which is in accordance with previous reports.[68,69,76] The determined values of E_{VBM}, E_{CBM}, and E_g are summarized in **Table 2**, and in **Figure 6** the band alignment with respect to the Fermi level of the investigated samples is presented. Based on the obtained results an important observation can be made, that GeS forms type I heterojunction with either SnS or SnSe. On the other hand, a composition of the two tin chalcogenides results in a type II structure. In terms of thermoelectric efficiency, the position of E_F closer to the band top is favorable for maximizing the PF. Additionally, by comparing the experimental band gaps with theoretical ones, it can be decided which computational method provides a more accurate value. As it turns out, for GeS both procedures result in similar energies and overestimate the band gap by more than 100 meV. For tin chalcogenides the agreement with the experiment is generally better, and the HSE06 hybrid functional allows to obtain more accurate values.

Table 2. Valence and conduction band energies with respect to the Fermi level of GeS, SnS, and SnSe, together with band gaps determined from optical absorption measurements. All experiments were performed at the temperature of ≈80 K. Theoretical band gaps (E_g^{theor}) were obtained from DFT calculations (performed with either HSE06 or mBJ-TB09 procedure) and correspond to the temperature of 0 K.

	E_{VBM} [eV]	E_{CBM} [eV]	E_g^{exp} [eV]	E_g^{theor} [eV]	
				HSE06	*mBJ-TB09*
GeS	−0.67	1.02	1.69	1.84	1.83
SnS	−0.38	0.77	1.15	1.16	1.10
SnSe	−0.12	0.84	0.98	0.95	0.89

© 2023 The Authors. Advanced Optical Materials published by Wiley-VCH GmbH

21951071, 2024, 6, Downloaded from https://onlinelibrary.wiley.com/doi/10.1002/adom.202302049 by Wroclaw University Of Science, Wiley Online Library on [26/09/2024]. See the Terms and Conditions (https://onlinelibrary.wiley.com/terms-and-conditions) on Wiley Online Library for rules of use; OA articles are governed by the applicable Creative Commons License

ADVANCED SCIENCE NEWS
www.advancedsciencenews.com
ADVANCED OPTICAL MATERIALS
www.advopticalmat.de

21951071, 2024, 6, Downloaded from https://onlinelibrary.wiley.com/doi/10.1002/adom.202302049 by Wroclaw University Of Science, Wiley Online Library on [26/09/2024]. See the Terms and Conditions (https://onlinelibrary.wiley.com/terms-and-conditions) on Wiley Online Library for rules of use; OA articles are governed by the applicable Creative Commons License

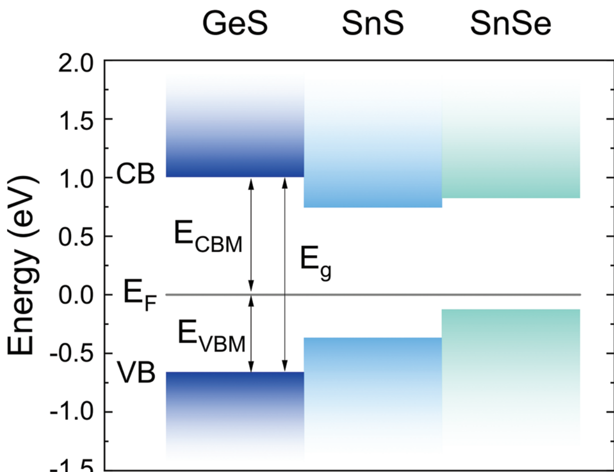

Figure 6. A band diagram of a hypothetical GeS/SnS/SnSe heterostructure with conduction and valence band alignment with respect to the Fermi level, determined for the investigated materials.

3. Conclusion

In conclusion, we performed a series of experiments exploiting the ARPES technique on orthorhombic group IV monochalcogenides GeS, SnS, and SnSe, along with complementary DFT calculations of the electronic band structure. The obtained results were analyzed in terms of the influence of the valence band dispersion on the thermoelectric performance and other properties of the materials. In the acquired high-resolution photoemission maps we were able to observe multiple valleys in the proximity of chemical potential and characteristic pudding mold shape of the band near the X point of the Brillouin zone, with two hole pockets separated by a shallow minimum. These two features are responsible for combining high Seebeck coefficient with good conductivity and play an important role in increasing the thermoelectric figure of merit (ZT).[22,24,26] From the obtained results hole effective masses and Fermi level positions of each sample were determined. Additionally, band gaps were found using optical absorption measurements. SnSe turned out to exhibit the lowest effective mass of ≈0.20 m_0, VBM energy closest to Fermi level, at −0.14 eV, and narrowest band gap of 0.98 eV at 80 K. These findings are in line with reports of the superior electrical conductivity of SnSe, and along with low lattice thermal conductivities contribute to remarkably high ZT of 2.62.[32] Due to wider band gaps and Fermi levels farther from the VBM, intrinsic GeS and SnS exhibit poorer conductive properties, these features are however favorable for high Seebeck coefficient. The obtained experimental results are generally in accordance with DFT predictions, although a few discrepancies were noticed, reinforcing the importance of the experimental investigation. In the case of GeS, most importantly, a step toward the band gap character determination was made by experimental observation of two valence band apices (in the Γ and Λ points) at equal binding energies (not predicted by the simulations). Although for a complete picture of the band structure the conduction band dispersion needs to be yet examined, our results, combined with previous optical measurements, are in favor of direct or quasi-direct energy gap, crucial for multiple applications.

A direction worth exploring is also the investigation of MX-based heterostructures and alloys, as it has been found that certain combinations of the materials can result in either type I or type II heterojunction, and introducing a gradient of ZT across a thermoelectric device (Peltier cooler) may in some conditions improve its performance.[49]

4. Experimental Section

The investigated samples were nominally undoped GeS, SnS, and SnSe single crystals, grown by iodine-assisted chemical vapor transport technique in vacuum-sealed quartz ampoules (15 cm in length, 2.4 cm outer diameter, 2.0 cm inner diameter). The growth temperature and pressure were 900–1100 °C and ≈10^{-5} mbar, respectively. To initiate nucleation and facilitate the transport of the precursors a temperature difference of ≈50 °C between hot and cold zones of the ampule was created.

Preparation of the samples for photoemission experiments (ARPES, XPS) involved mechanical exfoliation in ultra-high vacuum conditions (<10^{-9} mbar), at room temperature. For Raman and optical absorption spectroscopies flakes of a thickness of 50–100 nm were selected. No special treatment was needed.

Raman scattering measurements were conducted exploiting a custom optical setup, consisting of a 550 mm focal length grating monochromator coupled with a liquid nitrogen cooled CCD array detector camera. For sample excitation a 532 nm laser diode was used, with incident power of 250 µW and laser spot size of ≈5 µm, focused by a 50×, NA = 0.55 magnifying objective lens, also allowing signal collection in the backscattering mode. The experiment was carried in ambient conditions.

The photoemission studies (ARPES, XPS) were performed using synchrotron radiation at the URANOS beamline of the SOLARIS National Synchrotron Radiation Centre (Kraków, Poland),[77] The photoemission signal was detected with Scienta-Omicron DA30-L electron analyzer. The measurements were performed at the temperature of 77 K (achieved in a flow-type liquid nitrogen cryostat) and base pressure below 5×10^{-11} mbar. Along with GeS, SnS, and SnSe, an attempt to perform complementary measurements for the fourth member of the MX family, GeSe, was made. Unfortunately, the sample suffered degradation under the illumination with high-energy photons, making it impossible to acquire satisfactory results.

Optical absorption spectra, allowing to determine the energy gap of the investigated materials, were acquired with a dedicated optical set up, composed of a quartz tungsten halogen lamp as the source of the white light, 300 mm focal length grating monochromator, and Si (for GeS) or InGaAs (for SnX) photodetector coupled with a lock-in amplifier (Stanford Research Systems SR830). The temperature of ≈80 K was achieved and maintained during the experiment with the use of a closed-cycle helium cryocooler and a heating system.

Ab initio calculations were performed within the framework of density functional theory (DFT) with the use of the relativistic projector-augmented waves (PAW) datasets[78] in Vienna Ab Initio Simulation Package (VASP).[79] The Perdew-Burke-Ernzerhof (PBE) parametrization of generalized gradients approximation (GGA) to the exchange-correlation functional was employed.[80] Monkhorst-Pack k-point grid of 12×12×3, plane wave energy cutoff of 600 eV, and a semi-empirical DFT-D3 correction for vdW interactions were used.[81] The electronic band structures were calculated with the use of two methods: Heyd-Scuseria-Ernzerhof (HSE06) hybrid functional,[82] and modified Becke-Johnson (mBJ-TB09) exchange potential.[83]

Supporting Information

Supporting Information is available from the Wiley Online Library or from the author.

© 2023 The Authors. Advanced Optical Materials published by Wiley-VCH GmbH

ADVANCED SCIENCE NEWS
www.advancedsciencenews.com

ADVANCED OPTICAL MATERIALS
www.advopticalmat.de

Acknowledgements

This work was supported by the National Science Centre (NCN) Poland OPUS 15 no. 2018/29/B/ST7/02135. The publication was partially developed uder the provision of the Polish Ministry of Science and Higher Education project "Support for research and development with the use of infrastructure of the National Synchrotron Radiation Centre SOLARIS" under contract no. 1/SOL/2021/2. The authors acknowledge the SOLARIS Centre for the acces to the Beamline URANOS, where the measurements were performed. Computational studies were supported by the Wroclaw Centre for Networking and Supercomputing and the Interdisciplinary Centre for Mathematical and Computational Modelling, University of Warsaw. S.T. acknowledges NSF DMR-1955889, NSF CMMI-1933214, NSF 1904716, NSF 1935994, NSF ECCS 2052527, DMR 2111812, and CMMI 2129412.

Conflict of interest

The authors declare no conflict of interest.

Data Availability Statement

The data that support the findings of this study are available from the corresponding author upon reasonable request.

Keywords

ARPES, photoemission, thermoelectric materials, van der Waals crystals

Received: August 23, 2023
Published online: October 18, 2023

[1] L. C. Gomes, A. Carvalho, *Phys. Rev. B* **2015**, *92*, 085406.
[2] R. E. Banai, M. W. Horn, J. R. S. Brownson, *Sol. Energy Mater. Sol. Cells* **2016**, *150*, 112.
[3] K. Kushnir, M. Wang, P. D. Fitzgerald, K. J. Koski, L. V. Titova, *ACS Energy Lett.* **2017**, *2*, 1429.
[4] P. Zhao, H. Yang, J. Li, H. Jin, W. Wei, L. Yu, B. Huang, Y. Dai, *J. Mater. Chem. A* **2017**, *5*, 24145.
[5] S.-C. Liu, Y. Mi, D.-J. Xue, Y.-X. Chen, C. He, X. Liu, J.-S. Hu, L.-J. Wan, *Adv. Electron. Mater.* **2017**, *3*, 1700141.
[6] X. Zhou, X. Hu, B. Jin, J. Yu, K. Liu, H. Li, T. Zhai, *Adv. Sci.* **2018**, *5*, 1800478.
[7] X. Fan, L. Su, F. Zhang, D. Huang, D. K. Sang, Y. Chen, Y. Li, F. Liu, J. Li, H. Zhang, H. Xie, *ACS Appl. Mater. Interfaces* **2019**, *11*, 47197.
[8] L. C. Gomes, A. Carvalho, A. H. Castro Neto, *Phys. Rev. B* **2015**, *92*, 214103.
[9] R. Fei, W. Li, J. Li, L. Yang, *Appl. Phys. Lett.* **2015**, *107*, 173104.
[10] A. I. Lebedev, *J. Appl. Phys.* **2018**, *124*, 164302.
[11] G. Ding, G. Gao, K. Yao, *Sci. Rep.* **2015**, *5*, 9567.
[12] A. Shafique, Y.-H. Shin, *Sci. Rep.* **2017**, *7*, 506.
[13] R. Guo, X. Wang, Y. Kuang, B. Huang, *Phys. Rev. B* **2015**, *92*, 115202.
[14] K. Biswas, J. He, I. D. Blum, C.-I. Wu, T. P. Hogan, D. N. Seidman, V. P. Dravid, M. G. Kanatzidis, *Nature* **2012**, *489*, 414.
[15] M. Rakshit, D. Jana, D. Banerjee, *J. Mater. Chem. A* **2022**, *10*, 6872.
[16] B. Ul Haq, S. Alfaify, A. Laref, R. Ahmed, M. F. M. Taib, *Ceram. Int.* **2019**, *45*, 15122.
[17] Z. Wang, C. Fan, Z. Shen, C. Hua, Q. Hu, F. Sheng, Y. Lu, H. Fang, Z. Qiu, J. Lu, Z. Liu, W. Liu, Y. Huang, Z.-A. Xu, D. W. Shen, Y. Zheng, *Nat. Commun.* **2018**, *9*, 47.
[18] K. Zhang, K. Deng, J. Li, H. Zhang, W. Yao, J. Denlinger, Y. Wu, W. Duan, S. Zhou, *Phys. Rev.* **2018**, *2*, 054603.
[19] J. Cui, C. Chen, W. He, J. Avila, L.-D. Zhao, M. C. Asensio, J. He, Y. Chen, *J. Mater. Chem. A* **2018**, *6*, 24588.
[20] S. Li, J. Sun, Y. Zhang, Y. Fan, X. Tang, G. Tan, *Z. Anorg. Allg. Chem.* **2022**, *648*, e202200038.
[21] H. Tang, J.-F. Dong, F.-H. Sun, Asfandiyar, P. Shang, J.-F. Li, *Sci. China Mater.* **2019**, *62*, 1005.
[22] Y. Pei, X. Shi, A. Lalonde, H. Wang, L. Chen, G. J. Snyder, *Nature* **2011**, *473*, 66.
[23] J. Q. Li, N. Yang, S. M. Li, Y. Li, F. S. Liu, W. Q. Ao, *J. Electron. Mater.* **2018**, *47*, 205.
[24] K. Kuroki, R. Arita, *J. Phys. Soc. Jpn.* **2007**, *76*, 083707.
[25] L.-D. Zhao, G. Tan, S. Hao, J. He, Y. Pei, H. Chi, H. Wang, S. Gong, H. Xu, V. P. Dravid, C. Uher, G. J. Snyder, C. Wolverton, M. G. Kanatzidis, *Science* **2016**, *351*, 141.
[26] C. W. Wang, Y. Y. Y. Xia, Z. Tian, J. Jiang, B. H. Li, S. T. Cui, H. F. Yang, A. J. Liang, X. Y. Zhan, G. H. Hong, S. Liu, C. Chen, M. X. Wang, L. X. Yang, Z. Liu, Q. X. Mi, G. Li, J. M. Xue, Z. K. Liu, Y. L. Chen, *Phys. Rev. B* **2017**, *96*, 165118.
[27] I. Pletikosic, F. Von Rohr, P. Pervan, P. K. Das, I. Vobornik, R. J. Cava, T. Valla, *Phys. Rev. Lett.* **2018**, *120*, 156403.
[28] Q. Lu, M. Wu, D. Wu, C. Chang, Y.-P. Guo, C.-S. Zhou, W. Li, X.-M. Ma, G. Wang, L.-D. Zhao, L. Huang, C. Liu, J. He, *Phys. Rev. Lett.* **2017**, *119*, 116401.
[29] T. Nagayama, K. Terashima, T. Wakita, H. Fujiwara, T. Fukura, Y. Yano, K. Ono, H. Kumigashira, O. Ogiso, A. Yamashita, Y. Takano, H. Mori, H. Usui, M. Ochi, K. Kuroki, Y. Muraoka, T. Yokoya, *Jpn. J. Appl. Phys.* **2017**, *57*, 010301.
[30] K. Peng, B. Zhang, H. Wu, H. Che, X. Sun, J. Ying, G. Wang, Z. Sun, G. Wang, X. Zhou, X. Chen, *J. Mater. Chem. C* **2020**, *8*, 9345.
[31] M. Maeda, K. Yamamoto, T. Mizokawa, N. L. Saini, M. Arita, H. Namatame, M. Taniguchi, G. Tan, L. D. Zhao, M. G. Kanatzidis, *Phys. Rev. B* **2018**, *97*, 121110.
[32] L.-D. Zhao, S.-H. Lo, Y. Zhang, H. Sun, G. Tan, C. Uher, C. Wolverton, V. P. Dravid, M. G. Kanatzidis, *Nature* **2014**, *508*, 373.
[33] Y. Xiao, C. Chang, Y. Pei, D. Wu, K. Peng, X. Zhou, S. Gong, J. He, Y. Zhang, Z. Zeng, L.-D. Zhao, *Phys. Rev. B* **2016**, *94*, 125203.
[34] J. Carrete, N. Mingo, S. Curtarolo, *Appl. Phys. Lett.* **2014**, *105*, 101907.
[35] W. He, D. Wang, J.-F. Dong, Y. Qiu, L. Fu, Y. Feng, Y. Hao, G. Wang, J. Wang, C. Liu, J.-F. Li, J. He, L.-D. Zhao, *J. Mater. Chem. A* **2018**, *6*, 10048.
[36] Z. Tian, C. Guo, M. Zhao, R. Li, J. Xue, *ACS Nano* **2017**, *11*, 2219.
[37] I. Suzuki, S. Kawanishi, K. Tanaka, T. Omata, S.-I. Tanaka, *Electron. Struct.* **2022**, *4*, 025004.
[38] I. Suzuki, Z. Lin, S. Kawanishi, K. Tanaka, Y. Nose, T. Omata, S.-I. Tanaka, *Phys. Chem. Chem. Phys.* **2022**, *24*, 634.
[39] P. Mishra, H. Lohani, A. K. Kundu, R. Patel, G. K. Solanki, K. S. R. Menon, B. R. Sekhar, *Semicond. Sci. Technol.* **2015**, *30*, 075001.
[40] Z. Muhammad, Y. Li, G. Abbas, M. Usman, Z. Sun, Y. Zhang, Z. Lv, Y. Wang, W. Zhao, *Adv. Electron. Mater.* **2022**, *8*, 2101112.
[41] X. Zhang, J. Shen, S. Lin, J. Li, Z. Chen, W. Li, Y. Pei, *J. Materiomics* **2016**, *2*, 331.
[42] L. Shaabani, S. Aminorroaya-Yamini, J. Byrnes, A. Akbar Nezhad, G. R. Blake, *ACS Omega* **2017**, *2*, 9192.
[43] W. Li, C. Yang, *AIP Adv.* **2022**, *12*, 085111.
[44] Y. Wang, X. Yang, Y. Shang, *Phys. Lett. A* **2019**, *383*, 2499.
[45] W. Li, C. Yang, *J. Appl. Phys.* **2022**, *132*, 214302.
[46] M. Rakshit, S. Nath, S. Chowdhury, R. Mondal, D. Banerjee, D. Jana, *Phys. Scr.* **2022**, *97*, 125804.
[47] A. Rahim, W. Haider, A. Khan, H. Khan, H. U. Din, M. Shafiq, B. Amin, M. Idrees, *J Comput Electron* **2022**, *21*, 725.
[48] A. Marjaoui, M. Ait Tamerd, M. Zanouni, A. El Kasmi, M. Assebban, M. Diani, *Mater. Sci. Eng., B* **2022**, *281*, 115737.

© 2023 The Authors. Advanced Optical Materials published by Wiley-VCH GmbH

21951071, 2024, 6, Downloaded from https://onlinelibrary.wiley.com/doi/10.1002/adom.202302049 by Wroclaw University Of Science, Wiley Online Library on [26/09/2024]. See the Terms and Conditions (https://onlinelibrary.wiley.com/terms-and-conditions) on Wiley Online Library for rules of use; OA articles are governed by the applicable Creative Commons License

[49] Z. Bian, H. Wang, Q. Zhou, A. Shakouri, *Phys. Rev. B* **2007**, *75*, 245208.
[50] D. Tan, H. E. Lim, F. Wang, N. B. Mohamed, S. Mouri, W. Zhang, Y. Miyauchi, M. Ohfuchi, K. Matsuda, *Nano Res.* **2017**, *10*, 546.
[51] J. Liu, S. T. Pantelides, *Appl. Phys. Express* **2018**, *11*, 101301.
[52] A. Tolloczko, S. J. Zelewski, M. Blaszczak, T. Wozniak, A. Siudzinska, A. Bachmatiuk, P. Scharoch, R. Kudrawiec, *J. Mater. Chem. C* **2021**, *9*, 14838.
[53] V. L. Le, D. D. Cuong, H. T. Nguyen, X. A. Nguyen, B. Kim, K. Kim, W. Lee, S. C. Hong, T. J. Kim, Y. D. Kim, *AIP Adv.* **2020**, *10*, 105003.
[54] R. Oliva, T. Wozniak, F. Dybala, A. Tolloczko, J. Kopaczek, P. Scharoch, R. Kudrawiec, *Phys. Rev. B* **2020**, *101*, 235205.
[55] Y. Cui, Z. Zhou, X. Wang, X. Wang, Z. Ren, L. Pan, J. Yang, *Nano Res.* **2021**, *14*, 2224.
[56] Z. Chen, W. Hwang, M. Cho, A. T. Hoang, M. Kim, D. Kim, D. H. Kim, Y. D. Kim, H. J. Kim, J.-H. Ahn, A. Soon, H.-J. Choi, *NPG Asia Mater* **2022**, *14*, 41.
[57] C.-H. Ho, W.-Y. Lin, L.-C. Chao, K.-Y. Lee, J. Inagaki, H.-C. Hsueh, *ACS Appl. Energy Mater.* **2020**, *3*, 4896.
[58] H. Wang, X. Qian, *2D Mater.* **2017**, *4*, 015042.
[59] R. Fei, W. Kang, L. Yang, *Phys. Rev. Lett.* **2016**, *117*, 097601.
[60] M. Wu, X. C. Zeng, *Nano Lett.* **2016**, *16*, 3236.
[61] Y. I. Jhon, J. Lee, M. Seo, J. H. Lee, Y. M. Jhon, *Adv. Opt. Mater.* **2019**, *7*, 1801745.
[62] H. R. Yang, X. M. Liu, *Appl. Phys. Lett.* **2017**, *110*, 171106.
[63] A. Dasgupta, J. Gao, X. Yang, *Laser Photonics Rev.* **2020**, *14*, 1900416.
[64] M. Zhu, M. Zhong, X. Guo, Y. Wang, Z. Chen, H. Huang, J. He, C. Su, K. P. Loh, *Adv. Opt. Mater.* **2021**, *9*, 2101200.
[65] P. A. E. Murgatroyd, M. J. Smiles, C. N. Savory, T. P. Shalvey, J. E. N. Swallow, N. Fleck, C. M. Robertson, F. Jäckel, J. Alaria, J. D. Major, D. O. Scanlon, T. D. Veal, *Chem. Mater.* **2020**, *32*, 3245.
[66] J. D. Wiley, W. J. Buckel, R. L. Schmidt, *Phys. Rev. B* **1976**, *13*, 2489.
[67] H. R. Chandrasekhar, R. G. Humphreys, U. Zwick, M. Cardona, *Phys. Rev. B* **1977**, *15*, 2177.
[68] T. J. Whittles, L. A. Burton, J. M. Skelton, A. Walsh, T. D. Veal, V. R. Dhanak, *Chem. Mater.* **2016**, *28*, 3718.
[69] M. J. Smiles, J. M. Skelton, H. Shiel, L. A. H. Jones, J. E. N. Swallow, H. J. Edwards, P. A. E. Murgatroyd, T. J. Featherstone, P. K. Thakur, T.-L. Lee, V. R. Dhanak, T. D. Veal, *J. Mater. Chem. A* **2021**, *9*, 22440.
[70] P. Sutter, S. Wimer, E. Sutter, *Nature* **2019**, *570*, 354.
[71] N. Zawadzka, L. Kipczak, T. Wozniak, K. Olkowska-Pucko, M. Grzeszczyk, A. Babinski, M. R. Molas, *Nanomaterials* **2021**, *11*, 3109.
[72] V. Tayari, B. V. Senkovskiy, D. Rybkovskiy, N. Ehlen, A. Fedorov, C.-Y. Chen, J. Avila, M. Asensio, A. Perucchi, P. Di Pietro, L. Yashina, I. Fakih, N. Hemsworth, M. Petrescu, G. Gervais, A. Grüneis, T. Szkopek, *Phys. Rev. B* **2018**, *97*, 045424.
[73] P. Wu, B. Zhang, K. L. Peng, M. Hagihala, Y. Ishikawa, M. Kofu, S. H. Lee, H. Kumigashira, C. S. Hu, Z. M. Qi, K. Nakajima, G. Y. Wang, Z. Sun, T. Kamiyama, *Phys. Rev. B* **2018**, *98*, 094305.
[74] A. Khandelwal, K. Mani, M. H. Karigerasi, I. Lahiri, *Mater. Sci. Eng., B* **2017**, *221*, 17.
[75] J. Tauc, *Mater. Res. Bull.* **1968**, *3*, 37.
[76] Y. Zhong, L. Zhang, W. Chen, H. Zhu, *Nanotechnology* **2020**, *31*, 385203.
[77] J. Szlachetko, J. Szade, E. Beyer, W. Blachucki, P. Ciochon, P. Dumas, K. Freindl, G. Gazdowicz, S. Glatt, K. Gula, J. Hormes, P. Indyka, A. Klonecka, J. Kolodziej, T. Kolodziej, J. Korecki, P. Korecki, F. Kosiorowski, K. Kosowska, G. Kowalski, M. Kozak, P. Koziol, W. Kwiatek, D. Liberda, H. Lichtenberg, E. Madej, A. Mandziak, A. Marendziak, K. Matlak, A. Maximenko, et al., *Eur Phys J Plus* **2023**, *138*, 10.
[78] G. Kresse, D. Joubert, *Phys. Rev. B* **1999**, *59*, 1758.
[79] G. Kresse, J. Furthmüller, *Phys. Rev. B* **1996**, *54*, 11169.
[80] J. P. Perdew, K. Burke, M. Ernzerhof, *Phys. Rev. Lett.* **1996**, *77*, 3865.
[81] S. Grimme, J. Antony, S. Ehrlich, H. Krieg, *J. Chem. Phys.* **2010**, *132*, 154104.
[82] A. V. Krukau, O. A. Vydrov, A. F. Izmaylov, G. E. Scuseria, *J. Chem. Phys.* **2006**, *125*, 224106.
[83] F. Tran, P. Blaha, *Phys. Rev. Lett.* **2009**, *102*, 226401.

© 2023 The Authors. Advanced Optical Materials published by Wiley-VCH GmbH

21951071, 2024, 6, Downloaded from https://onlinelibrary.wiley.com/doi/10.1002/adom.202302049 by Wroclaw University Of Science, Wiley Online Library on [26/09/2024]. See the Terms and Conditions (https://onlinelibrary.wiley.com/terms-and-conditions) on Wiley Online Library for rules of use; OA articles are governed by the applicable Creative Commons License

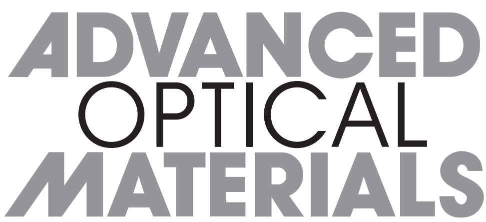

Supporting Information

for *Adv. Optical Mater.*, DOI 10.1002/adom.202302049

Photoemission Study of the Thermoelectric Group IV-VI van der Waals Crystals (GeS, SnS, and SnSe)

Agata K. Tołłoczko, Szymon J. Zelewski, Jakub Ziembicki, Natalia Olszowska, Marcin Rosmus, Tomasz Woźniak, Sefaattin Tongay and Robert Kudrawiec*

WILEY-VCH

Supporting Information

for

Photoemission study of the thermoelectric group IV-VI van der Waals crystals (GeS, SnS, and SnSe)

Agata K. Tołłoczko, Szymon J. Zelewski, Jakub Ziembicki, Natalia Olszowska, Marcin Rosmus, Tomasz Woźniak, Sefaattin Tongay, and Robert Kudrawiec*

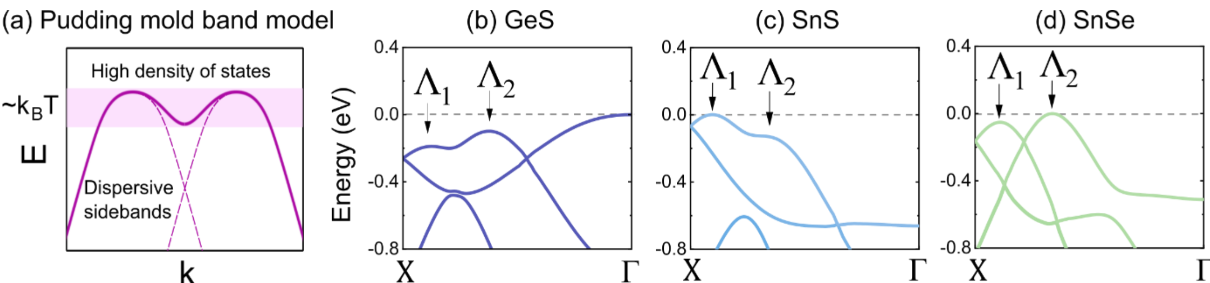

Figure S1. a) Schematic illustration of the pudding-mold-shaped band, and the valence band dispersion in the Λ region calculated for b) GeS, c) SnS, and d) SnSe.

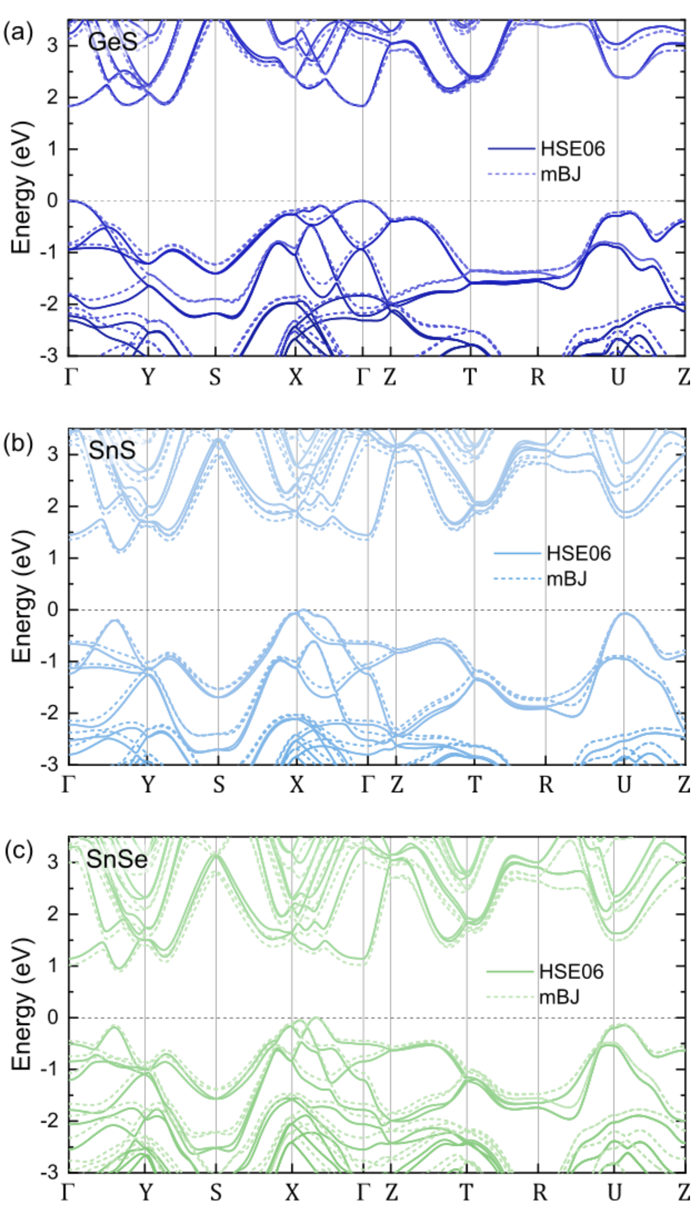

Figure S2. Electronic band structure predicted by DFT calculations with HSE06 hybrid functional (solid lined) and mBJ-TB09 exchange potential (dashed lines) for a) GeS, b) SnS, and c) SnSe.

WILEY-VCH

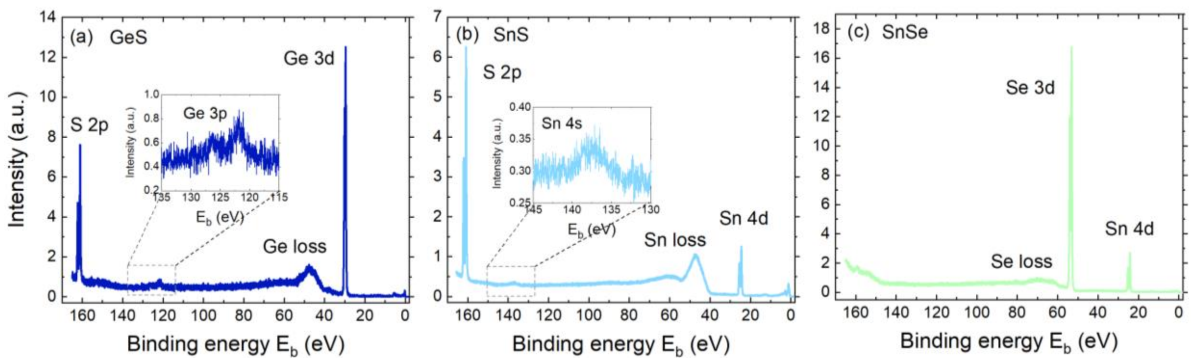

Figure S3. Wide energy range core level XPS spectra, revealing lines corresponding to expected orbital transitions for a) GeS, b) SnS, and c) SnSe.

Table S1. Raman modes frequencies and core level XPS lines energies (with spin-orbit splitting) measured for GeS, SnS, and SnSe.

	GeS	SnS	SnSe
Raman mode		(cm^{-1})	
B_{3g}	213	167	112
A_g^3	239	193	134
A_g^4	271	217	149
XPS line (SO splitting)		(eV)	
Ge $3d_{5/2}$	29.6 (0.5)	-	-
S $2p_{3/2}$	161.1 (1.2)	160.9 (1.2)	-
Sn $4d_{5/2}$	-	24.5 (1.0)	24.2 (1.0)
Se $3d_{5/2}$	-	-	53.1 (0.9)

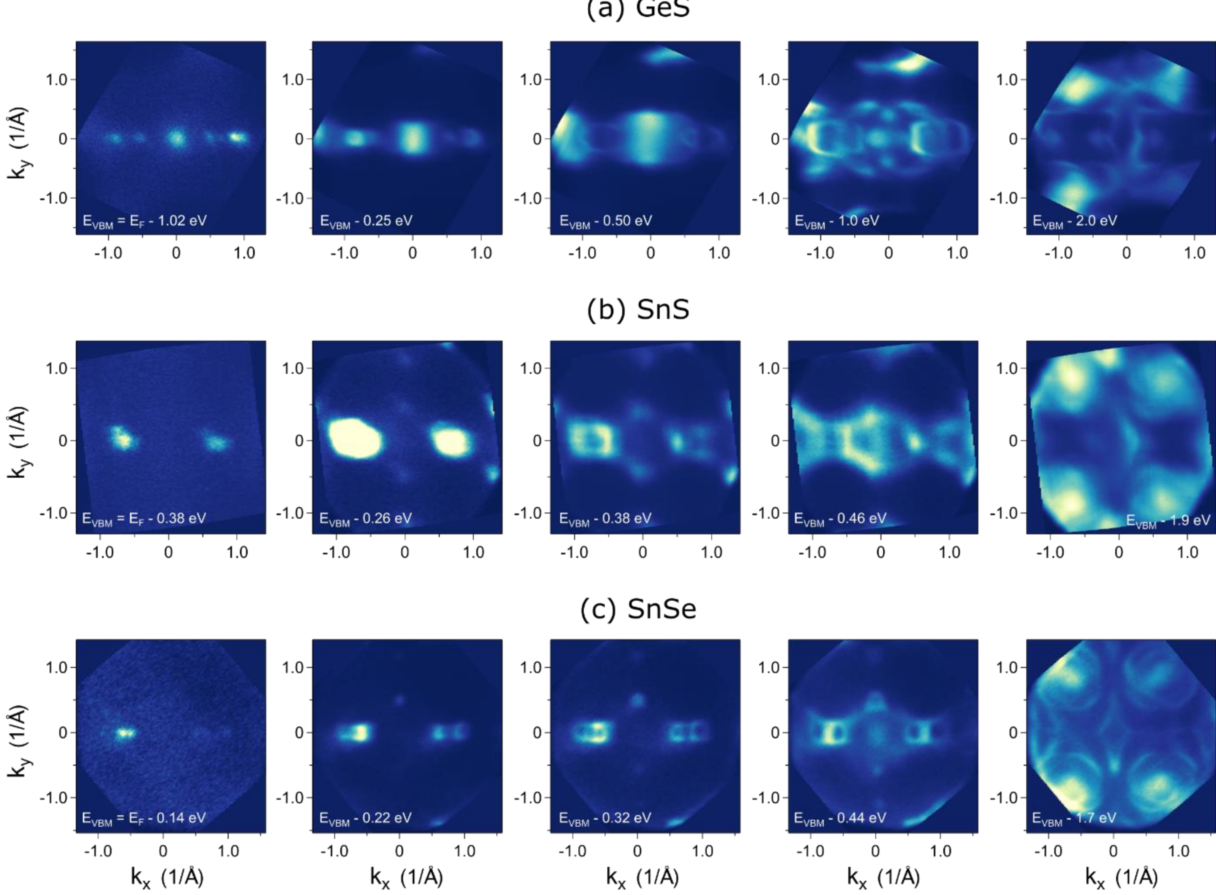

Figure S4. Constant energy contours acquired for a) GeS, b) SnS, and c) SnSe, at the energies for which characteristic features occur.

Table S2. Experimental (ARPES) and theoretical (HSE06 and mBJ-TB09) energies of the valence band valleys, with respect to the energy of the highest VBM, for GeS, SnS, and SnSe. All values are given in eV units.

BZ point	GeS			SnS			SnSe		
	ARPES	HSE06	mBJ	ARPES	HSE06	mBJ	ARPES	HSE06	mBJ
Λ_1	0	-0.19	-0.14	0	0	0	0	-0.05	-0.04
Λ_2	0	-0.10	-0.09	-0.05	-0.13	-0.13	0	0	0
Δ	≈ -0.5	-0.51	-0.45	-0.26	-0.20	-0.19	-0.22	-0.19	-0.14
Γ	0	0	0	-0.46	-0.66	-0.61	-0.44	-0.51	-0.45

WILEY-VCH

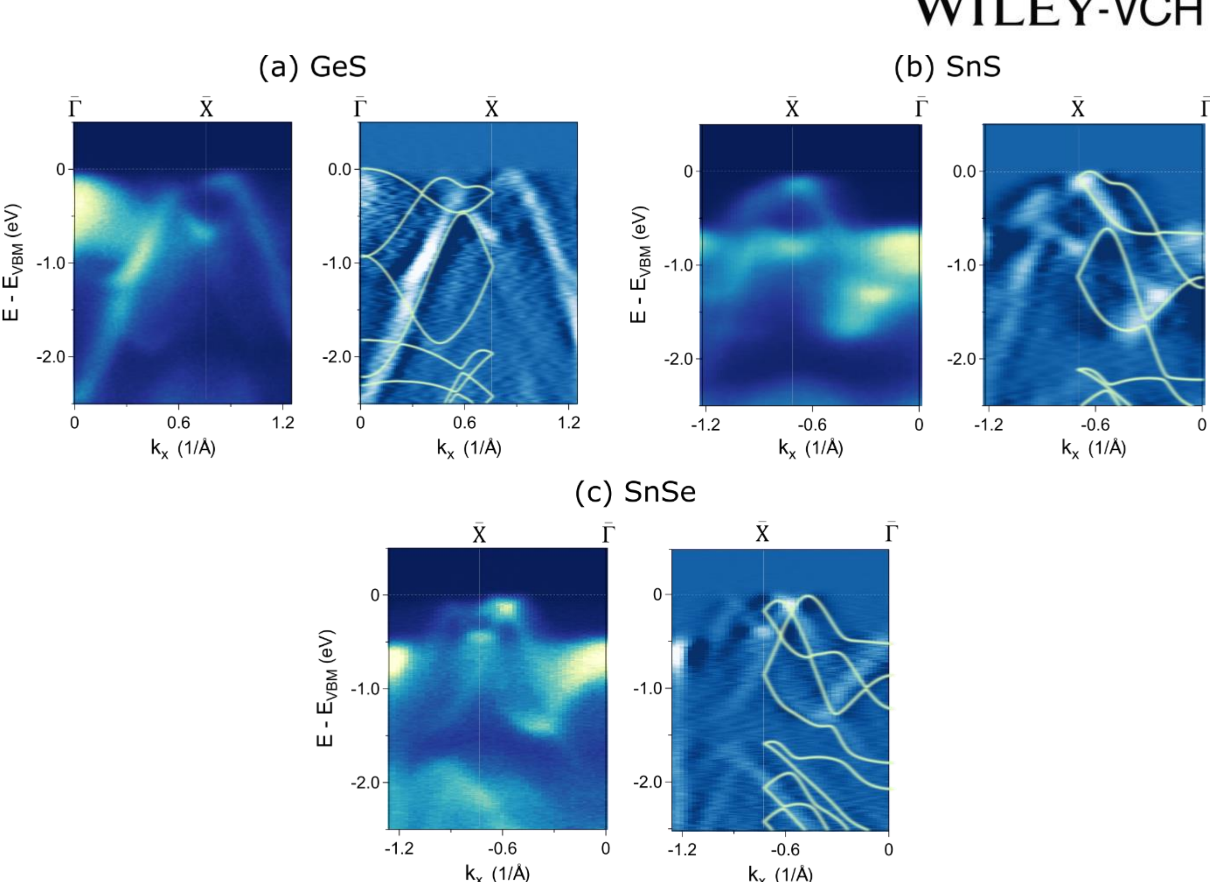

Figure S5. Close-ups of the photoemission maps (left side of each panel) and their second derivatives with superimposed calculated band structure (right side) in the Λ region in the k_x direction for GeS (a), SnS (b), and SnSe (c).

Table S3. Theoretical hole effective masses of GeS, SnS, and SnSe in the Λ_1, Λ_2, Δ, and Γ points of the BZ, along k_x and k_y directions, determined from band dispersions calculated with DFT. The values are given as fractions of the free electron mass m_0.

BZ point		GeS		SnS		SnSe	
		HSE06	mBJ	HSE06	mBJ	HSE06	mBJ
Λ_1	m_x	0.54	0.71	0.29	0.34	0.18	0.21
Λ_2	m_x	0.36	0.49	0.40	0.41	0.18	0.21
Δ	m_y	0.78	0.75	0.22	0.24	0.27	0.21
Γ	m_x	1.77	1.80	*n/p*	*n/p*	*n/p*	*n/p*
	m_y	1.40	1.27	5.37	5.24	1.99	2.30

n/p - non-parabolic band

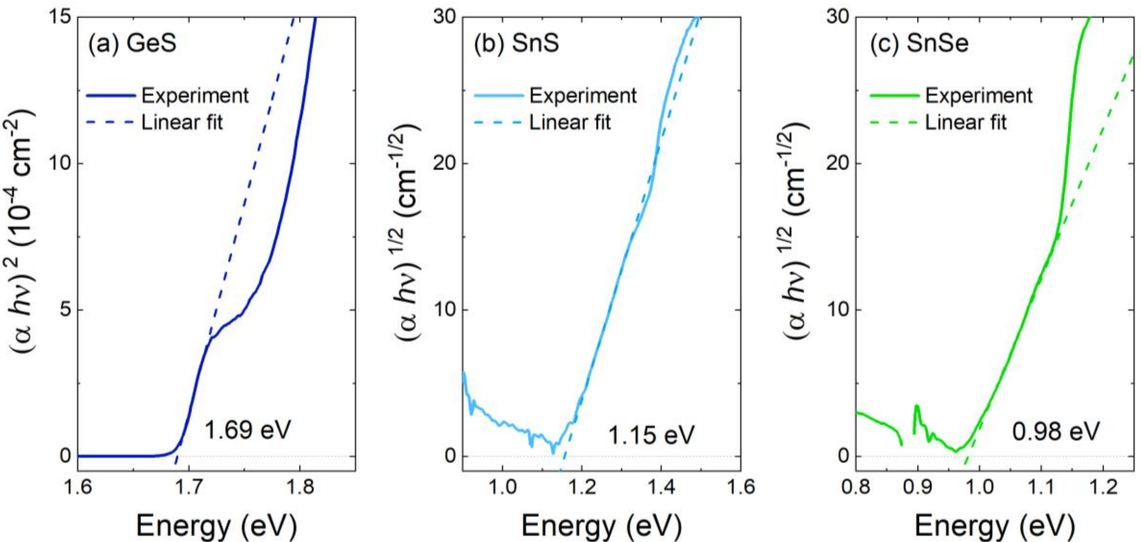

Figure S6. Tauc plots of the optical absorption coefficient spectra acquired for a) GeS, b) SnS, and c) SnSe, at the temperature of ≈80 K. From the linear fits to the experimental data energy gaps of each material have been evaluated. Direct character of the band gap was assumed for GeS, and indirect for tin chalcogenides.

CHAPTER 6

Influence of Native Defects on the Optical Properties of SnX_2 (X = S, Se) van der Waals Crystals

Agata K. Tołłoczko, Maciej Peter, Miłosz Rybak, Sandeep Gorantla, Alicja Bachmatiuk, Robert Kudrawiec

Journal of Physical Chemistry C, **128**, 39, 16640-16651 (2024)

Overview

Optical properties of tin dichalcogenides SnS_2 and $SnSe_2$ are studied by complementary methods of optical spectroscopy (PR, optical absorption, and PL). The Burstein-Moss effect was observed in the measurements, resulting from population of the bottom conduction band states by electrons from ionized donor defects. Additionally, for SnS_2, a strong defect-related photoluminescence emission was detected with an unusual lineshape, quenched at a certain energy. A model allowing to reproduce and explain the PL intensity spectral dependence is proposed.

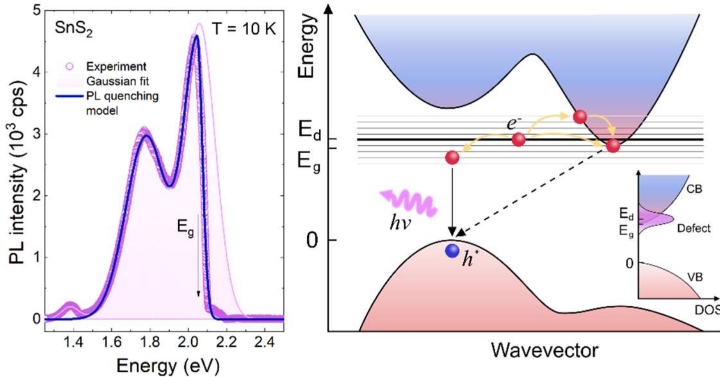

Fig. 6.1 Graphical abstract. Reprinted from Ref. [125] under CC-BY 4.0 license. Copyright 2024 A. K. Tołłoczko *et al.*

Author's contribution

Agata K. Tołłoczko (first author) and Maciej Peter (corresponding author) declare equal contribution to the work. AKT supervised the experiments (PR, optical absorption, PL, and Raman scattering) conducted by MP as his Master's Degree project and performed supplementary measurements to confirm the accuracy of the original results. MP processed and analyzed the acquired data, while AKT proposed the interpretation of the observed phenomena and a model describing the defect-related PL quenching.

Open Access
This article is licensed under CC-BY 4.0

pubs.acs.org/JPCC Article

Influence of Native Defects on the Optical Properties of SnX_2 (X = S and Se) van der Waals Crystals

Agata K. Tołłoczko,[‖] Maciej Peter,*[,‖] Miłosz Rybak, Sandeep Gorantla, Alicja Bachmatiuk, and Robert Kudrawiec

Cite This: https://doi.org/10.1021/acs.jpcc.4c03005

Read Online

ACCESS | Metrics & More | Article Recommendations | Supporting Information

ABSTRACT: SnX_2 crystals (X = S and Se) are van der Waals semiconductors with great potential for applications as photocatalysts and thermoelectric materials as well as in two-dimensional optoelectronics. According to density functional theory calculations, they exhibit indirect band gaps in the near-infrared ($SnSe_2$) or visible (SnS_2) spectral range. The materials characterize with the Fermi level positioned close to the conduction band (CB), as a consequence of low formation energy of native donor defects. The population of the bottom CB states by electrons leads to the Burstein−Moss (B−M) effect—an effective blue shift of the optical absorption edge. In our work, we exploit modulated reflectance (insensitive to the B−M shift) to determine the energy of the lowest direct band gap and verify the character of the measured absorption edge. Additionally, for SnS_2, a strong defect-related photoluminescence emission was detected, with an unusual line shape, quenched at certain energy. We postulate that the reason for such behavior is the proximity of the CB valley to the defect level, acting as a trap for electrons in the reciprocal space. A model allowing one to reproduce the PL intensity spectral dependence is proposed, providing information about the fundamental indirect band gap energy. In general, the obtained results reveal strong influence of the structural defects on the optical properties of SnX_2 crystals, which can be exploited to improve their performance in various applications.

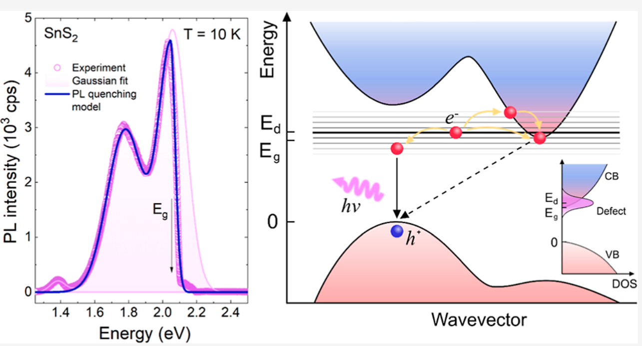

INTRODUCTION

Van der Waals (vdW) crystals have been known and studied for over 60 years; however, recently, they were rediscovered and perceived from an entirely different perspective, thanks to the development of the technology of single layer isolation.[1,2] Their two-dimensional (2D) character can be now investigated by different experimental methods and exploited in a variety of applications. Among vdW crystals, a family of tin dichalcogenides (SnX_2, where X is S or Se) attracts interest due to exceptional versality. To begin with, the materials are compounds of earth-abundant elements of low toxicity, which is extremely important for large-scale commercial applications. Owing to their semiconducting character, they can be exploited in optoelectronics (photodetection and solar cells),[3−6] but they also possess potential as thermoelectrics,[7−9] saturable absorbers for mode-locked lasers,[10−14] unexpectedly efficient photocatalysts,[15−20] and even adsorbers for water purification or gas sensing.[20−23] What is more, they are perfect candidates for integration with other vdW crystals, as they share the composition with other stoichiometric phases of tin chalcogenides (SnX and Sn_2X_3)[3,24−26] and the crystal structure with transition metal dichalcogenides (TMDs, such as MoX_2 and WX_2),[16,27−30] providing great possibilities for heterostructures engineering. The performance of SnX_2 in any of these applications is governed by their fundamental properties, which need to be thoroughly investigated and understood.

SnX_2 layers characterize with hexagonal atomic arrangement of a CdI_2-type structure, with Sn in an octahedral coordination, belonging to the space group $P\bar{3}m1$ (no. 164).[31,32] The structure is schematically illustrated in Figure 1a, along with the first Brillouin zone (BZ) of the reciprocal lattice (Figure 1b) and its two-dimensional projection onto the central plane (Figure 1c), with labeled high-symmetry points. This most stable polytype is referred to as 2H (using Ramsdell notation[33] common for CdI_2-like crystals), unfortunately often confused with the 2H phase of TMDs, in which the metal atom has trigonal prismatic coordination.[34] Using the notation typical for TMDs, the $P\bar{3}m1$ SnX_2 structure is labeled 1T. The difference between the two systems was clearly explained by

Received: May 7, 2024
Revised: August 2, 2024
Accepted: September 3, 2024

Downloaded via WROCLAW UNIV OF SCIENCE AND TECHLGY on September 26, 2024 at 11:11:19 (UTC).
See https://pubs.acs.org/sharingguidelines for options on how to legitimately share published articles.

© XXXX The Authors. Published by American Chemical Society

https://doi.org/10.1021/acs.jpcc.4c03005
J. Phys. Chem. C XXXX, XXX, XXX−XXX

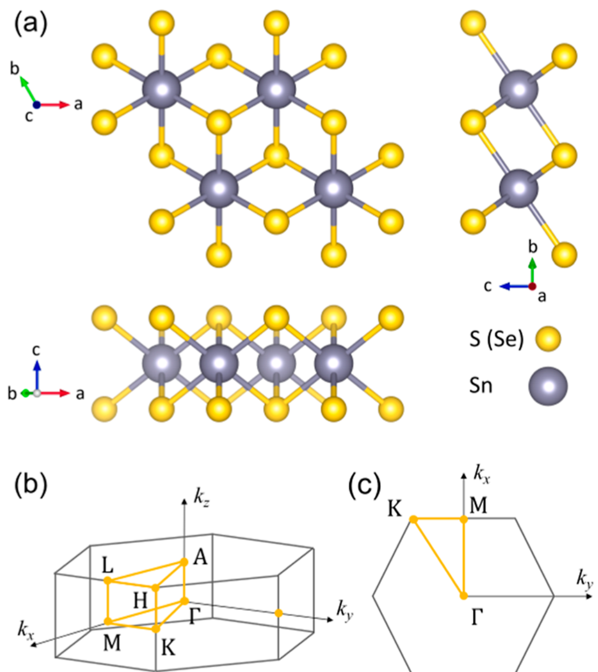

Figure 1. (a) Schematic illustration of the atomic structure of SnX_2 crystals, including top view on the layer plane and side views along the main crystallographic axes, created with VESTA software.[44] (b) Graphical representation of the first BZ of the reciprocal lattice and (c) its two-dimensional projection on the central plane of the 3D unit cell.

Gonzalez and Oleynik.[35] To date, the investigation of dielectric function and optical properties, supported by density functional theory (DFT) calculations, revealed the semiconducting character of SnX_2, with indirect band gaps of ~2.1 eV (SnS_2) and ~1.0 eV ($SnSe_2$), at room temperature.[35−39] When combined, the materials cover the broad spectral range of the electromagnetic spectrum, from NIR to UV. They are intrinsically n-type materials due to the presence of defect states at energies close to the conduction band (CB) (mainly chalcogen vacancies and interstitial tin).[7,15,31,40,41] It has also been reported for SnS_2 that structural defects at the crystal surface may improve the photocatalysis efficiency and act as adsorptive sites for metallic and organic cationic pollutants.[20] The defects also induce the Burstein−Moss (B−M) effect,[42,43] observed as an effective blue shift of the optical band gap due to the population of the electronic states at the bottom of the CB. The presence of the B−M effect was directly confirmed for pristine $SnSe_2$ by Lochocki et al.,[31] who observed the CB valley in the angle-resolved photoemission spectroscopy (ARPES) measurements. The effect may lead to misinterpretation of the experimental results, especially obtained by optical methods, and, as we believe, is the primary reason for major discrepancies in the literature regarding the character and energy of the fundamental band gap, which we discuss in detail further in the text.

Herein, we present a comprehensive study of the optical properties of SnX_2 crystals performed by means of complementary methods of optical spectroscopy: optical absorption, modulated reflectance (photoreflectance, PR), and photoluminescence (PL) as a function of temperature. We compare different approaches for the analysis of the optical absorption spectra, considering nonparabolic valence band (VB) dispersion. Using PR, for both materials, we identify the observed absorption edge as direct, despite the theoretically predicted indirect fundamental band gap. The observed phenomenon can be attributed to the Burstein−Moss effect, enhanced by low probability of the optical transitions resulting from the selection rules. The theoretical findings are supported by the lack of photoluminescence emission originating from interband optical transitions, although for SnS_2, strong defect-related emission was detected. In the acquired spectra, a peculiar quenching of the PL intensity at certain energy was observed, which could be the evidence of the proximity of a CB valley. We introduce a model allowing determination of the indirect band gap energy from the edge of the quenched defect-related emission. The obtained energies are reasonable, although they need to be further verified by a different, established method, in order to confirm their accuracy, as well as the applicability of the proposed model.

■ METHODS

Samples and Structural Characterization. In this study, SnS_2 and $SnSe_2$ bulk crystals grown by the chemical vapor transport method and acquired from SixCarbon company were investigated.

For structural characterization by means of scanning electron microscopy (SEM)/transmission electron microscopy (TEM), mechanically exfoliated flakes were transferred onto Cu TEM grids coated with a holey carbon support film. To eliminate any potential surface contamination, the TEM grids carrying the flakes were subjected to low-energy Ar/O plasma cleaning for 5−10 s before commencing the experiment. The investigation was performed under ultrahigh-vacuum conditions at room temperature using the state-of-the-art Thermo Fisher Scientific TITAN 60−300 G2 cube microscope, equipped with a super-X 4 detectors X-ray spectrometer, operating at an accelerating voltage of 300 kV. Experimental techniques included high-resolution TEM imaging, selected area electron diffraction, high-angle annular dark-field STEM (HAADF-STEM) imaging, and energy-dispersive X-ray spectroscopy (EDS) for comprehensive analysis. For HAADF-STEM imaging, specific parameters including a beam convergence semiangle of 21.4 mrad, a probe beam current of 40 pA, and detector collection angles ranging from 79.5 to 200 mrad were applied.

Experimental Methods. PR was measured using the lock-in technique (with the Stanford Research Systems SR830 phase-sensitive nanovoltmeter) to extract weak signals from the background. For the experiment, crystals of lateral dimensions of ~3 mm were selected. The samples were illuminated with white light from a quartz tungsten halogen (QTH) lamp. The reflected signal was dispersed by a 550 nm focal length grating monochromator and detected by a Si photodiode. For the modulation of the built-in electric field by photogeneration, a continuous wave (CW) laser diode of wavelength 405 nm (SnS_2) or 532 nm ($SnSe_2$) was used, mechanically chopped at a frequency of 280 Hz. The power of both lasers was set to 150 mW. The beam was not additionally focused on the sample surface, and the spot size was ~1.5 mm, which is comparable to the diameter of the white light beam.

For the optical absorption study, ~ 10 μm-thick flakes were prepared, and the signal was collected from a circular region of the sample of 0.5 mm diameter. The spectra were acquired based on the transmission measurements. As a white light source, a QTH lamp was used. The experiment was carried out in a so-called dark configuration, in which the sample is

https://doi.org/10.1021/acs.jpcc.4c03005
J. Phys. Chem. C XXXX, XXX, XXX−XXX

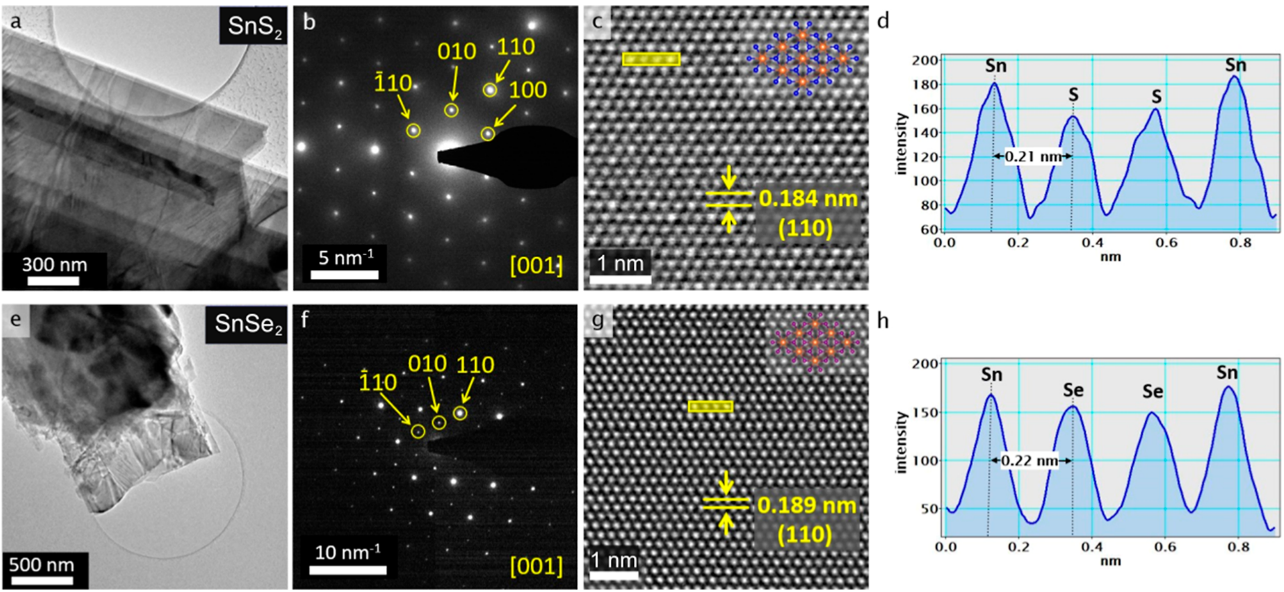

Figure 2. SEM/TEM characterization of SnS_2 (a−d) and $SnSe_2$ (e−h) samples. (a,e) TEM images of the examined flakes and (b,f) corresponding electron diffraction pattern indexed with the [001] zone axis trigonal crystal structure. (c,g) High-resolution HAADF-STEM images of the flakes along the [001] projection with an overlaid simulated crystal structure. In the top right corners of panels c and g, simulated crystal structures are overlaid, with orange and blue or purple spots corresponding to Sn and S or Se atoms, respectively. (d,h) Intensity profiles across Sn and S atomic columns from the boxed regions in panels c and g.

illuminated with monochromatic light of wavelength selected using a grating monochromator. For signal detection, Si (SnS_2) or InGaAs ($SnSe_2$) photodetectors and a lock-in amplifier were used as in the case of PR measurements.

The photoluminescence emission and Raman scattering spectroscopy were performed with a custom optical setup allowing measurements in the microscale. An incident laser beam of 532 nm (Raman) or 405 nm (PL) wavelength and output power adjusted from 0.1 to 500 μW was focused on the sample surface by a magnifying objective lens (50×, NA = 0.55), yielding a spot size of 20 μm, also used for emitted or scattered light collection. The signal was directed into a 550 nm focal length grating monochromator coupled with a liquid nitrogen-cooled CCD array detector camera.

For all optical experiments, the samples were mounted on a cold finger inside a cryostat connected with a closed-cycle helium cryocooler, allowing to cool the samples from room temperature to 10 K. The temperature was monitored and stabilized using a Lakeshore model 325 controller.

Computational Methods. The DFT calculations have been performed in the Vienna Ab Initio Simulation Package.[70] The electron−ion interaction was modeled using a projector-augmented-wave technique.[71] In the case of Sn atom, the 4d[10] states were included in a valence shell. The Perdew−Burke−Ernzerhof (PBE)[72] exchange−correlation (XC) functional was employed. A plane-wave basis cutoff of 500 eV and a 12 × 12 × 8 Monkhorst−Pack[73] k-point grid for BZ integrations were set. These values assured the convergence of the lattice constants, and the electronic gaps were within the precision of 0.001 Å and 0.001 eV, respectively. A Gaussian smearing of 0.02 eV was used for integration in the reciprocal space. The semiempirical Grimme's correction with Becke-Johnson damping (D3-BJ)[74] was employed to properly describe the weak vdW forces. The spin−orbit interaction (SO) was taken into account. We employ the modified Becke−Johnson (mBJ-TB09) exchange potential[75] and Heyd−Scuseria−Ernzerhof (HSE06) hybrid functional[76] for band structure calculations, on top of the optimized geometry obtained within the PBE + D3-BJ + SO approach. The comparison of the two methods has shown that the use of mBJ-TB09 potential allows improvement of the band gaps of the investigated materials with a relatively low computational cost.

RESULTS AND DISCUSSION

Structural Characterization. SnS_2 and $SnSe_2$ samples investigated in this work were initially characterized by TEM to experimentally confirm their structural quality. A summary of the obtained results is presented in Figure 2. Panels a−d illustrate the structural properties of SnS_2, and panels e−h illustrate the structural properties of $SnSe_2$. Figure 2a,e shows the TEM images of the edge regions of the respective samples after being transferred to a holey carbon support film-coated TEM grid. Figure 2b,f shows the corresponding electron diffraction patterns acquired for each flake, which was indexed in good agreement with the [001] zone axis theoretical diffraction pattern of the trigonal crystal structure. Figure 2c,g shows the high-resolution high-angle annular dark-field scanning TEM (HAADF-STEM) images from which the spacings between the atomic planes of 0.184 nm for SnS_2 and 0.189 nm for $SnSe_2$ could be extracted. In the top right corner of each panel, the simulated visualization of the crystal structure projected along the [001] direction is overlaid on the TEM image, remaining in good alignment with the observed atomic arrangement. To more precisely determine the distance between Sn and chalcogen atomic columns, intensity profiles of the yellow-boxed regions were extracted and are plotted in Figure 2d,h. The experimentally observed interatomic spacings of 0.21 nm for SnS_2 and 0.22 nm for $SnSe_2$ are in good agreement with the values calculated from the reference crystal structure (0.212 and 0.221 nm, respectively). The energy-dispersive X-ray spectrometry (EDS) maps of SnS_2 and $SnSe_2$, demonstrating the homogeneous distribution of Sn and S or Se

atoms, are provided in Figure S1 of the Supporting Information, together with the corresponding EDS spectra. In Figure S2 of the Supporting Information, additional optical microscope images of the measured samples are shown.

Raman scattering was measured for both crystals, at a temperature of 20 K and using a 532 nm, 200 μW CW laser diode for excitation. The results of the experiment are presented in Figure 3. For both materials, optical phonon

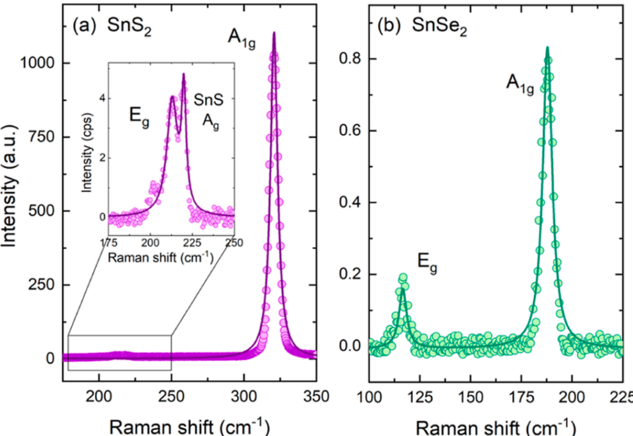

Figure 3. Raman scattering spectra of SnS_2 (a) and $SnSe_2$ (b), acquired at a temperature of 20 K, and excitation with 532 nm, 200 μW CW laser. The Lorentzian line shape was fitted to the observed phonon modes, identified as E_g and A_{1g} vibrations characteristic for the $\bar{3}m$ point group. For SnS_2, an additional line was observed (inset of panel a), which could be attributed to the A_g mode of the orthorhombic monochalcogenide phase, belonging to point group *mmm*.

modes characteristic to the point group $\bar{3}m$ were observed, i.e., total symmetric out-of-plane stretching A_{1g}, and weak centrosymmetric in-plane stretching E_g, at the frequencies summarized in Table S1. The Raman shifts at which the signal attributed to certain vibrations appears are in line with previous reports.[45,46] In the case of SnS_2, close to the E_g mode, another weak line was detected, at a frequency of 219 cm^{-1} (see the inset of Figure 3a), which may originate from the A_g mode of the orthorhombic SnS (point group *mmm*) or nonstoichiometric SnS_{2-x} phase. For $SnSe_2$, no such effect was observed; however, the detected intensity of the scattered light was significantly lower compared to SnS_2, and such a subtle feature could be lost due to noise.

The obtained results confirm the overall good quality and trigonal crystal structure of the investigated SnS_2 and $SnSe_2$ samples. The potential presence of the chalcogen-poor phases can be considered an intrinsic feature of the materials, resulting from the low formation energy of chalcogen vacancy native defects.

Optical Properties. Studies of the optical properties of SnS_2 and $SnSe_2$ reach back to the 1960s and involve mostly optical absorption characterization. Throughout the years, researchers studied the SnX_2 materials with different techniques; however, some major discrepancies can be found in the literature, regarding both the character and the energy of the fundamental band gap. First experimental report of optical absorption of SnS_2 was published by Greenaway and Nitsche,[47] in which the authors determine the indirect allowed optical band gap at an energy of 2.21 eV (corresponding to room temperature, such as all the following values, unless stated otherwise). Later, Domingo et al.[36] reported an indirect forbidden band gap of SnS_2 at 2.07 eV and observed a secondary direct forbidden absorption edge at 2.88 eV. In the same work, the indirect forbidden band gap and direct forbidden optical transition of $SnSe_2$ were found at 0.97 and 1.62 eV, respectively. Similar values (0.98 and 1.63 eV) were obtained by Manou et al.,[37] however assuming the allowed character of both optical transitions. Lee et al.[48] observed the indirect allowed band gaps of SnS_2 and $SnSe_2$ at 2.22 and 1.09 eV, respectively. Slightly lower values of 2.06 eV for SnS_2 and 1.02 eV for $SnSe_2$ were obtained by Julien et al.,[39] interpreted as indirect forbidden transitions. George and Joseph[38], along with the fundamental indirect absorption edge of SnS_2 at 2.12 eV reported another one at 2.31 eV. Some more recent studies performed by Burton et al.[41,49] and Whittles et al.[50] regarding the optical properties of SnS_2 reveal the indirect band gap at 2.25 eV and direct absorption edge at 2.38 eV. The authors acknowledge the discrepancy between their results and previous reports, however support the findings by the combined X-ray photoemission spectroscopy and inverse photoemission spectroscopy (IPES) characterization, revealing a band gap of 2.28 eV, in agreement with their optical measurements. Despite poorer resolution of the acquired data, the older reports seem more reliable as more attention was paid to the proper analysis of the absorption spectra. It is often neglected that according to the parabolic band model, in the Tauc plot for indirect transitions ($(\alpha h\nu)^{1/2}$ vs $h\nu$), two linear regions should be visible, corresponding to processes involving phonon absorption and emission, and only then, an accurate energy of the optical transition can be determined.[51] Unfortunately, the absorption edge with phonon absorption is often very weak or completely inactive if the phonon energy exceeds the thermal energy k_BT corresponding to the temperature at which the experiment is carried. Then, the analysis is limited to the phonon emission-related edge only. For relatively low phonon frequencies, the difference is most likely within the experimental error range; however, the potential influence on the final result should always be considered and, if possible, corrected by the optical phonon energy. Furthermore, in none of the aforementioned works, the possibility of the Burstein−Moss effect occurrence is considered, which could explain the discrepancies in the literature. When the Fermi level is positioned close to or inside the CB of a material, some CB states are occupied, and the optical band gap is effectively blue-shifted. Both optical absorption and IPES techniques are sensitive to such a shift, as they probe only the unoccupied electronic states. For $SnSe_2$, a direct evidence of the B−M effect presence is the study of Lochocki et al.[31] The authors were able to detect the signal originating from a CB valley by means of ARPES, which only reveals occupied states. The work is also the most reliable report of the fundamental indirect band gap of $SnSe_2$ of 0.90 eV.

In our study, we performed an in-depth investigation of the nature of the optical absorption edge of SnX_2 crystals by means of temperature-dependent PR and optical absorption. Being sensitive exclusively to direct optical transitions, PR spectroscopy provides the possibility to verify the character of the absorption edge.[52−55] The obtained results are summarized in Figure 4. In the PR spectra acquired at a temperature of 20 K, for both SnS_2 (Figure 4a) and $SnSe_2$ (Figure 4e), a broad feature was detected, being evidence of the presence of direct optical transitions in this spectral region. The evolution of the

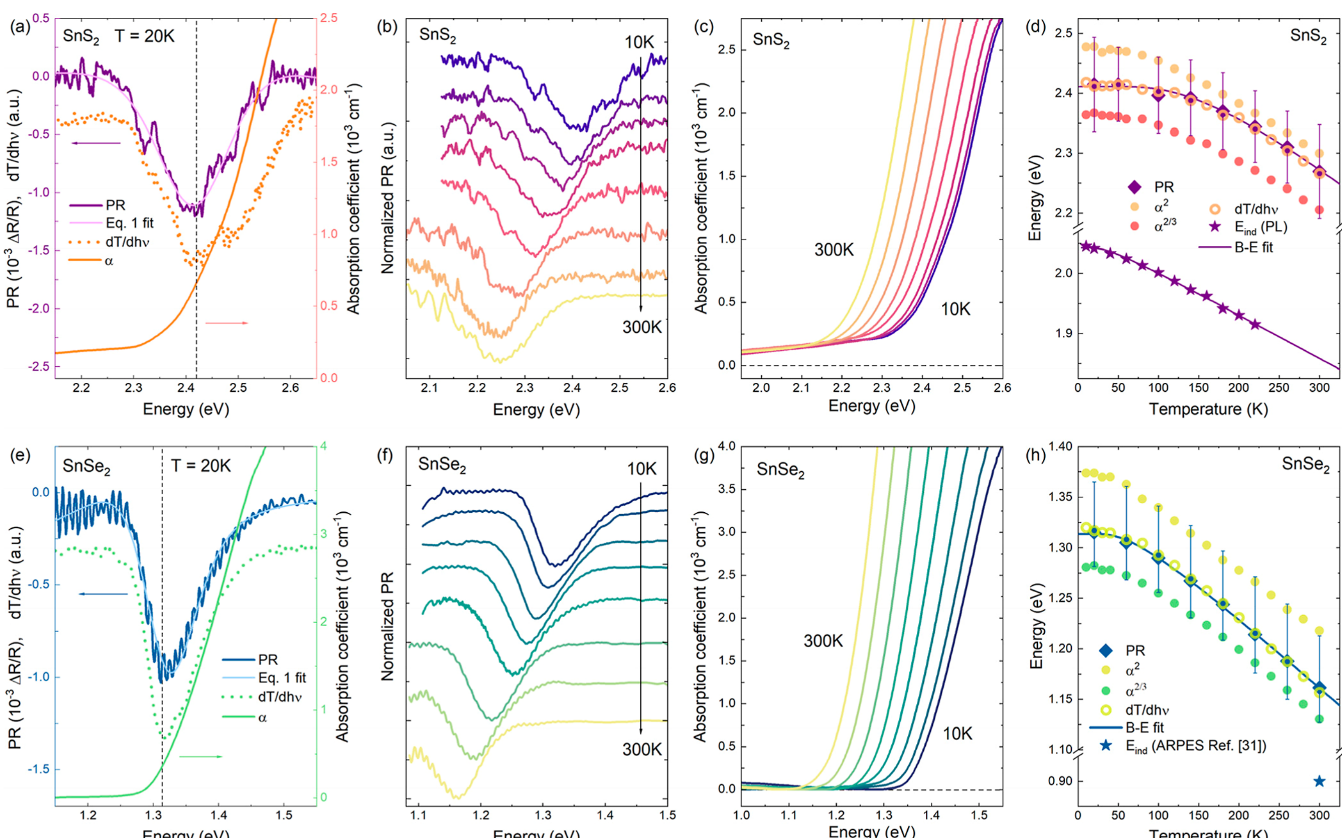

Figure 4. Results of PR and optical absorption measurements of SnS_2 (a−d) and $SnSe_2$ (e−h). A comparison of PR (with single resonance fitting of eq 1), absorption coefficient, and transmission first derivative spectra acquired at 20 K (a,e). Temperature evolution of PR (b,f) and absorption coefficient (c,g) spectra. Temperature dependence of the optical transition energies determined using different analysis methods (d,h). The individual plots correspond to the following approaches for direct transitions: PR resonance energy (diamond symbols, the error bars represent the resonance broadening), extrapolation of Tauc plot for direct allowed and forbidden transitions (full circles), and transmission first derivative maximum (open circles). The star symbols correspond to the fundamental indirect band gap, determined with the PL quenching model (eq 3) for SnS_2, or reported by Lochocki et al.[31] for $SnSe_2$. The solid lines are fits of the Bose−Einstein formula (eq 2) to the experimental data.

PR spectra with increasing temperature (Figure 4b,f) reveals an expected red shift of the observed feature energy. Although periodic laser excitation was used as the modulating factor, the distribution of the measured signal suggests a stronger contribution from the modulation of the sample temperature induced by laser radiation, rather than from the modulation of the built-in electric field by electron−hole pairs generation.

Therefore, for the analysis, we use the first derivative of the Lorentzian line shape, proper for thermoreflectance, instead of the third derivative established by Aspnes for photo- and electroreflectance.[56] It is worth noting that both procedures provide similar results. The fitting function is given by

$$\frac{\Delta R}{R}(h\nu) = Re\Big(\sum_j C_j e^{i\varphi_j}(h\nu - E_j + i\Gamma_j)^{-2}\Big) \quad (1)$$

where $h\nu$ is the photon energy, C_j is the j-th resonance amplitude, φ_j is the phase, E_j is the transition energy, and Γ_j is the broadening.

Regarding the unusual shape of the spectra, it is unclear whether the signal originates from a single optical transition with significant broadening or is a superposition of several PR resonances. Since the latter is more likely, we made an attempt to analyze the data assuming three (SnS_2) or two ($SnSe_2$) resonances; however, the arbitrary choice of the initial parameters turn out to strongly influence the final result, with multiple combinations leading to convergence of the fitting procedure, especially at higher temperatures. Therefore, for further analysis, only a single-resonance approach is applied, although we do not exclude the possible contribution of more than one optical transition. From the fitting, the energies corresponding to the temperature of 20 K were 2.42 and 1.31 eV for SnS_2 and $SnSe_2$, respectively (also listed in Table 1). The full temperature dependence of the determined energies is plotted in Figure 4d,h, together with the resonance broadening represented by error bars. Bose−Einstein formula was fitted to the temperature-dependence plot, given by

Table 1. Energies of the Fundamental Indirect and Lowest Direct Band Gap of SnS_2 and $SnSe_2$, Determined Theoretically by DFT Calculations (Using the mBJ-TB09 Exchange Potential and the HSE06 Hybrid Functional, Corresponding to a Temperature of 0 K) and Experimentally at 20 and 300 K

		DFT (0 K)			experiment	
		E_g^{ind}	E_g^{dir}		E_g^{ind}	E_g^{dir}
SnS_2	mBJ	2.11	2.60	20 K	2.05[a]	2.41[b]
	HSE	2.23	2.68	300 K		2.27[b]
$SnSe_2$	mBJ	1.09	1.45	20 K		1.31[b]
	HSE	1.17	1.48	300 K	0.90[c]	1.16[b]

[a]PL quenching model (eq 3). [b]PR spectra. [c]Lochocki et al.[31]

$$E(T) = E(0) - \frac{2a_B}{\exp\left(\frac{\theta_B}{T}\right) - 1} \quad (2)$$

where $E(0)$ is the energy at a temperature of 0 K, a_B is the strength of the electron−phonon interaction, and θ_B is the average phonon temperature. The values of the parameters are summarized in Table S2 of the Supporting Information.

Proceeding to the results of optical absorption measurements, the 20 K absorption coefficient spectra are superimposed over the PR data in Figure 4a,e. Since optical absorption is sensitive to both direct and indirect optical transitions, we expect to be able to observe the fundamental indirect band gap predicted theoretically for both SnS_2 and $SnSe_2$. Surprisingly, it can be seen in the figure that the sharpest rise of the absorption coincides with the energy of the PR resonance, suggesting direct character of the absorption edge. Similar behavior was previously observed for other vdW semiconductors, GeSe,[52,57] exhibiting optical properties dominated by direct transitions due to small energy distance between the fundamental indirect band gap and the lowest direct transition. In the case of SnX_2, an analogous explanation is not applicable, considering the significantly larger predicted distance between the two transitions. Even though DFT may fail to accurately evaluate the absolute energies of optical transitions, the relative distance between them is usually more reliable. In the measurements, no signal was detected in the energy range where the indirect absorption edge was expected. The possible causes of this phenomenon will be discussed further in the text, but first, we focus on the experimentally observed direct absorption edge. For the analysis of the absorption spectra, we use two alternative methods and compare the results in a discussion regarding their accuracy and suitability for the investigated materials.

Tauc Plot Method. The most common approach to analyze the absorption coefficient spectra is by using the Tauc plot,[58] allowing to determine the optical transition energy from the linear extrapolation of $(\alpha h\nu)^\gamma$ vs $h\nu$ plot, where γ is a parameter dependent on the transition type. The Tauc plot method is based on the assumption of a parabolic band dispersion. Although widely used, it provides good results for materials with simple band structure, when the absorption edge originates from a single, well-defined optical transition between parabolic valleys, but may fail for more complex structures. In a first approximation, we assume direct allowed character of the absorption edge and set $\gamma = 2$. The results of the fitting are presented in Figure S3a,c of the Supporting Information. For both SnS_2 and $SnSe_2$, the plot strongly diverges from the expected linear character, and only the high-energy regions of the spectra could be extrapolated. Such an approach may not be reliable, as even for materials with parabolic bands, the condition is best fulfilled only close to the valley top, and hence the absorption coefficient often follows the model at a relatively narrow energy range. As can be seen from Figure 4d,h, in which the temperature dependence of the extracted energies is plotted (yellow solid circles), there is a significant discrepancy between the values determined from the PR and absorption spectra. Therefore, as a second step, a possibility of direct forbidden character of the absorption edge should be considered by using the Tauc plot with $\gamma = 2/3$ (Figure S3b,d). In this case, the linear regions of the analyzed spectra were considerably more distinct and well defined, allowing more precise extrapolation, but most importantly positioned closer to the absorption edge. The energies of 2.36 and 1.33 eV were obtained for SnS_2 and $SnSe_2$, respectively, corresponding to the temperature of 10 K. The temperature evolution is presented in Figure 4d,h (red and green solid circles). In this case, the energies are red-shifted with respect to PR. Assuming that the Tauc method is correct for the investigated materials, the obtained results may suggest that the transition character is neither allowed nor entirely forbidden. Perhaps, adjusting the value of γ between 2/3 and 2 could result in satisfactory agreement, but the approach becomes empirical, losing the physical background of the Tauc method. The observed behavior can be explained by taking into account factors that may weaken the selection rules, such as broken crystal symmetry near structural defects or, relevant at higher temperatures, the electron−phonon interaction. It is also worth noting that the energies determined from both $(\alpha h\nu)^2$ and $(\alpha h\nu)^{2/3}$ plots fit perfectly within the boundaries of the PR resonance broadening, which may be another evidence of the contribution of multiple optical transitions with different oscillator strengths. At last, we do not consider the case of $\gamma = 1/2$ or $1/3$, i.e., indirect allowed or forbidden nature of the optical transition, since the direct character of the absorption edge is implied by the spectral coincidence with PR resonance.

A modification of the Tauc method was proposed by Cody et al.[59] for amorphic or disordered semiconductors, in which the transition energy is determined from the linear approximation of $(\alpha/h\nu)^\gamma$ plot. We applied the method to the acquired absorption spectra, assuming $\gamma = 2$ and $\gamma = 2/3$, although neither the linearity of the plot nor the agreement with PR resonance energies was improved compared to the Tauc plots. In fact, the determined values differ by less than 10 meV, which is below the experimental uncertainty. Also, no Urbach tail[60] was observed in the lnα vs $h\nu$ plots.

Transmittance Derivative Method. The second approach used for the optical absorption spectral analysis was the transmittance derivative method. While not as common as Tauc plot, it has a physical interpretation, and there are reports of its application for similar materials.[61] Analogous procedure is also well established in spectroscopic ellipsometry.[62,63] Absorption coefficient is an optical constant strictly related with the reflection coefficient, as it originates, respectively, from the imaginary and real part of the dielectric function of a material. Hence, the reflectance and transmittance (from which the absorption coefficient is extracted) spectra carry similar information about the dielectric function singularities observed as optical transitions in the experiment. The dielectric function is generally composed of broad regions with superimposed rather weak but sharp features at the energies of the van Hove critical points. Therefore, it is often more convenient to analyze the derivatives of the spectra, in which rapid changes are enhanced over a locally monotonous background. In the case of reflectance, a much more efficient way to observe these changes is by using a modulated variant of the method, allowing us to directly measure the differential spectrum (which can be understood as a partial derivative with respect to the modulated parameter, such as the built-in electric field or sample temperature in the case of PR) and detect even very weak signals. A modulated transmittance experiment can also be carried out but is considerably more challenging due to rapidly varying character of the absorption function at the band gap energy. Instead, a numerical derivative of the acquired transmittance spectrum $dT/dh\nu$ can be calculated. We applied the procedure to our data and compared the results with the

PR spectra, as presented in Figure 4a,e (dashed lines). For both samples, the agreement is outstanding, as the transmittance derivative follows exactly the PR resonance. For SnS_2, three distinguishable features can be observed. For $SnSe_2$, a broad asymmetrical peak with a tail at the high-energy side suggests contribution from at least two effects. With increasing temperature, the spectra become more uniform and the characteristic features can no longer be resolved (see Figure S3c,f of the Supporting Information), as happens with the PR results, most likely due to increasing thermal broadening. The temperature evolution of the energy at the $dT/dh\nu$ maximum was analyzed, as shown in Figure 4d,h (yellow open circles). The agreement between energies determined from PR and transmittance derivative is considerably improved compared to the Tauc method, suggesting that the approach may be more suitable for materials with complex electronic structure, as it is not restricted by any assumptions regarding band dispersion.

Electronic Band Structure. For the interpretation of the experimental results, the electronic band structure needs to be discussed. In Figure 5a,c, the band dispersion of SnS_2 and $SnSe_2$ is illustrated, obtained from DFT calculations employing mBJ-TB09 exchange potential (see the Methods section for details). As previously reported, for both materials, the fundamental band gap is indirect between the valence band maximum (VBM) close to the Γ point in the Γ−*K* path and the CB minimum (CBM) in the *L* point (marked with dashed arrows in Figure 5a,c), accompanied by a direct band gap in the Γ point (solid arrows). The energies for both materials are summarized in Table 1. From a comparison of the direct band gaps with the energies determined from 20 K PR spectra, it can be seen that the theoretical values are overestimated, but considering the experimental error, the agreement is acceptable. The absolute energies, often strongly influenced by the choice of the computational method,[52,64,65] are not as relevant for the interpretation of the experimental results as the electronic band dispersion. Nevertheless, the calculations with the use of the HSE06 hybrid functional were additionally performed, presented in Figure S5 of the Supporting Information. The method is generally known to accurately reproduce the band structure,[65] although in the case of SnX_2 crystals, the resulting band gaps were even higher than the values obtained from the mBJ calculations. Regardless of the choice of the computational method, it can be seen that the structure has a multivalley character and extremely flat VBs around the Γ point of the BZ. The lowest CB states form a characteristic *split-off* band, separated from the rest of the CB by ∼0.7 eV and composed of a mixture of chalcogen *p* orbitals with Sn *s* orbitals, as illustrated in Figure S4 of the Supporting Information. The upper CB is composed mainly of Sn *p* orbitals, with minor contribution from chalcogen *s* and *p* states, while the VB consists solely of chalcogen *p* orbitals. The structure is quite unusual, considering the optical activity. In high-symmetry points, bands are flat, and there are practically no type M_0 van Hove critical points[51,66] (in a 3D structure, VB maxima aligned with CB minima), indicating that the optical properties of the material are dominated by band-nesting transitions, occurring between parallel bands rather than between valley tops.

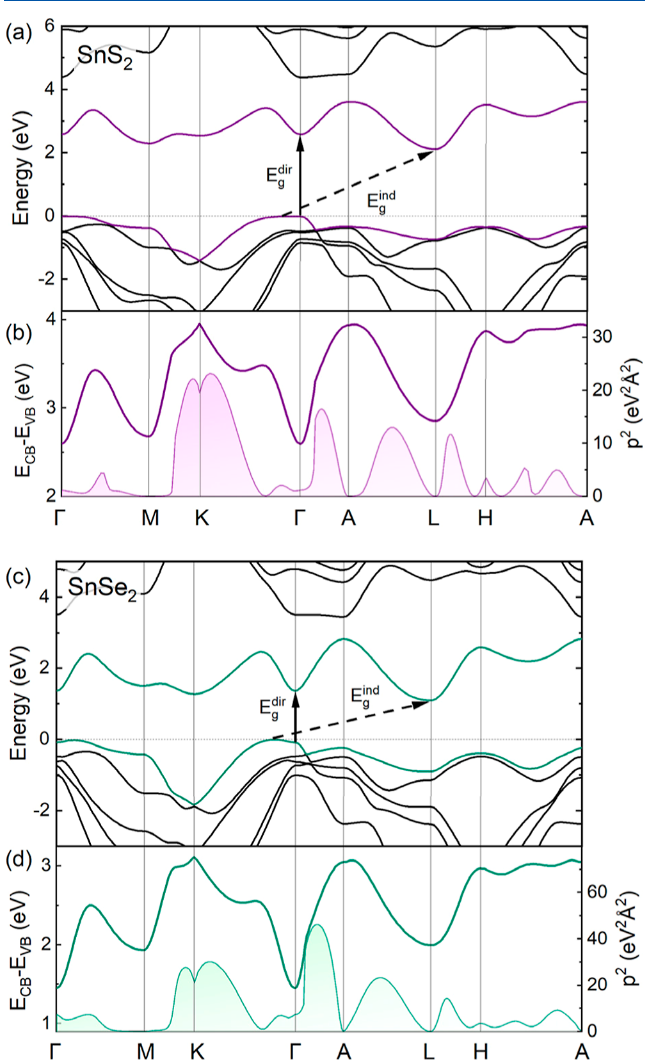

Figure 5. Electronic band dispersion of SnS_2 (a) and $SnSe_2$ (c) calculated with the mBJ-TB09 exchange potential. The interband distance (dark lines, left axis) and squared matrix element (shaded areas, right axis) between the highest VB and lowest CB (b,d).

To estimate the probability of the possible direct transitions across the BZ, the squared matrix element ρ^2 between the highest VB and lowest CB (the split-off band) was calculated and is plotted in Figure 5b,d as shaded areas. It reveals even more unexpected quality of the electronic structure, which is generally a low matrix element, vanishing in most of the high-symmetry points, implying low probability of the optical transitions. The matrix element increases away from high-symmetry points, confirming the potentially band-nesting character of the transitions allowed by the selection rules. In the Γ point, the matrix element is very low and increases rapidly away from the BZ center. The extremely flat band and matrix element distribution around the Γ point seem to explain our experimental observations. The unusual broadening and the shape of the PR resonance can be attributed to the contribution of multiple states around the Γ point, with different oscillator strengths. Low but nonzero values of ρ^2 suggest *quasi-forbidden* character of the optically active transitions, which was observed in the optical absorption spectra. For comparison, the matrix element between the highest VB and second lowest CB, above the split-off band, was found to reach considerably higher values.

Indirect Band Gap and Role of Defect States. According to DFT calculations, SnX_2 crystals are indirect band gap semiconductors, with the fundamental gap significantly narrower than the lowest direct one (with a

https://doi.org/10.1021/acs.jpcc.4c03005
J. Phys. Chem. C XXXX, XXX, XXX−XXX

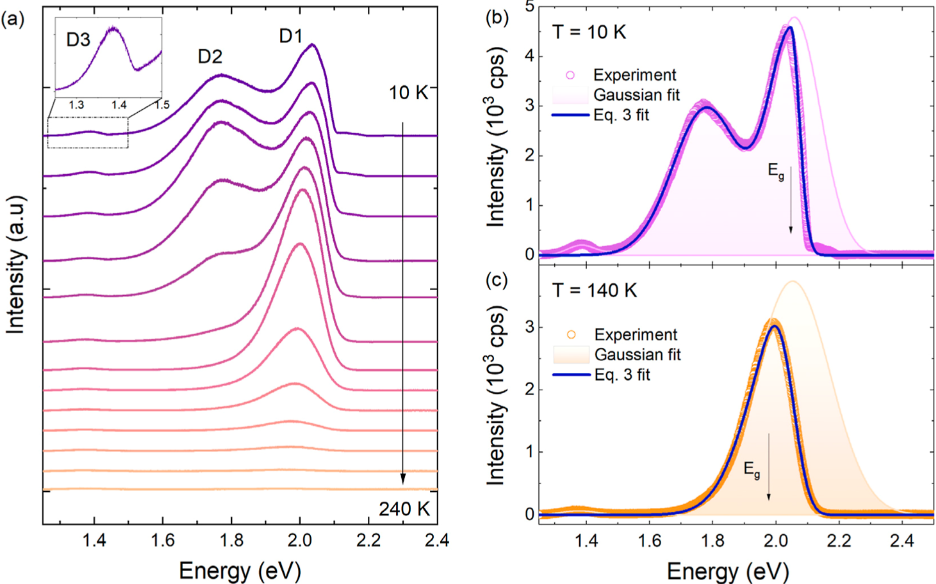

Figure 6. Temperature evolution of the defect-related photoluminescence emission spectra of SnS_2 (a). Results of fitting of the Gaussian line shape (shaded areas) and the model of the PL quenching given by eq 3 (dark blue solid lines) to the spectra acquired at 10 K (b) and 140 K (c). The spectra were acquired with the use of 405 nm, 200 μW CW laser.

difference of 500 meV for SnS_2 and 250 meV for $SnSe_2$). It is highly unlikely that the inaccuracy of the DFT procedures is such drastic. A technique typically allowing determination of the indirect band gap energy is the optical absorption. Surprisingly, in our experiments, we were not able to observe any feature that could be attributed to such a transition, although there are reports where a weak signal at reasonable energy was detected.[36−38] The reason the indirect band gap is not properly visible in the optical absorption may be the aforementioned Burstein−Moss effect, enhanced by a low transition matrix element. According to multiple reports,[7,31,39,41,50] both SnS_2 and $SnSe_2$ are intrinsically n-type semiconductors due to the presence of donor levels close to the CB edge. For $SnSe_2$, the evidence of the Fermi level positioned inside the CB is the study published by Lochocki et al.,[31] in which the authors were able to detect signal originating from the CB in ARPES measurements. From the experiment, the authors determine the Fermi level position 0.25 eV above the CBM and the band gap of 0.90 eV (at room temperature). They also confirm the theoretically predicted position of the CBM at the *L* point. To the best of our knowledge, there are no reports of analogous experiments carried for SnS_2. In an attempt to estimate an accurate energy of the indirect band gap, we discovered a different phenomenon allowing us to do so, involving photoluminescence emission measurements.

The PL method is often used as a preliminary verification of the band gap character, as the emission is typically absent for indirect optical transitions. Nevertheless, even then, low-intensity phonon-assisted PL can sometimes be detected or defect-related PL emission can occur, independently of the band gap character. The latter was observed for SnS_2, as presented in Figure 6. The nature of the emission was identified by excitation power-dependent measurements, shown in Figure S6, eliminating the possibility of interband character of the emission. In a double-logarithmic scale, the slope of the PL intensity vs excitation power plot of ∼0.5 indicates the defect-related process.[67] As can be seen in Figure 6a, the 10 K PL spectrum is composed of three features, labeled D1, D2, and D3. With increasing temperature, the intensity of peak D2 weakens as a result of energy transfer into peak D1. Further heating leads to quenching of the remaining PL signal. Based on the defect formation energy diagrams published by Liu et al.,[40] the observed emission lines can be assigned as follows: D1 corresponds to interstitial Sn, with theoretical energy inside the CB, leading to very easy ionization, D2 can be attributed to S vacancy, and D3 to interstitial S. The actual origin of the PL lines needs to be verified by a different experimental technique, such as deep level transient spectroscopy.[68,69] Further analysis of the acquired PL spectra revealed that throughout the whole temperature range, the shape of the D1 line is unusual. In Figure 6b,c, functions composed of three and two Gaussian lines were fitted to the spectra acquired at 10 and 120 K, respectively, but only to the data below the maximum of the D1 feature. Analogous analysis of all the spectra is presented in Figure S7 of the Supporting Information. The results of the fitting are plotted as shaded areas, and the extracted energies of lines D1, D2, and D3 are 2.06 1.78, and 1.38 eV, respectively. At the low energy side, the spectrum can be perfectly approximated by a Gaussian line shape, while at the high energy side, the emission is damped at a certain wavelength. The asymmetric shape of the emission line can be explained by the presence of a CB valley close to the defect energy. One possible mechanism of the observed phenomenon could be reabsorption of the emitted radiation at the indirect band gap, although in such a scenario, the indirect absorption edge should also be visible directly in the absorption experiment. Therefore, some other process must be responsible for PL quenching. We propose the following model, schematically illustrated in Figure S8 of the Supporting Information and explained in more detail in the figure caption. The density of states of the defect levels partly overlaps with the density of states from the L valley of the CB. Below the CBM, the electrons bound to defects can recombine radiatively with holes in the VB, most likely close to the Γ point, since in the wavevector space, their wave function is delocalized, and the

momentum is preserved in this process. At the energies above CBM, in a range where the density of states from defect levels and CB overlap, the electrons from the defect states more likely thermalize to the L valley of the CB, becoming localized in the wavevector space at different *k*-points than the VBM and can no longer efficiently contribute to the radiative processes. The effect is observed in the PL spectra as rapid damping of the emission intensity. We attempt to determine the indirect band gap using the following model

$$I_{PL}(h\nu) = G(h\nu, E_d)e^{-DOS_{CB}(h\nu, E_g)} \quad (3)$$

where I_{PL} is the PL emission intensity, E_g is the fundamental indirect band gap, and $G(h\nu, E_d)$ is a Gaussian function centered at the defect energy E_d (or a sum of two Gaussians, if needed). DOS_{CB} is the CB density of states, given by

$$DOS_{CB}(h\nu) = \begin{cases} 0 & h\nu < E_g \\ C(h\nu - E_g)^{1/2} & h\nu \geq E_g \end{cases} \quad (4)$$

with *C* being a constant. Additional technical details regarding the model and the fitting procedure are included in the Supporting Information, where we also consider a modification allowing simulation of a more empirical DOS_{CB} function shape, with an exponential tail below E_g. Based on these considerations, we conclude that the model (in either form) is more reliable at low temperatures. The fitting of eq 3 to the PL spectra allowed the emission shape to be reproduced with surprisingly good accuracy, as shown in Figure 6b,c with dark blue solid lines, and estimate the indirect band gap throughout the temperature range for which the PL signal was detected. The temperature dependence of the indirect band gap is plotted in Figure 4d with star symbols and extrapolated up to room temperature using the B−E formula (eq 2). Although the proposed model seems to describe well the observed phenomenon, its applicability and the accuracy of the determined band gap need to be verified by a better established method. Nevertheless, it is worth noting that the extracted band gap energy of 2.05 eV corresponding to 20 K is in good agreement with the value of 2.11 eV predicted by DFT calculations. What is more, the redshift of the indirect band gap with increasing temperature is comparable to the direct optical transition observed in PR or optical absorption. In previous reports, the indirect band gap of SnS_2 was observed in the optical absorption spectra at energies between 2.06 and 2.22 eV; however, these values correspond to room temperature. Our result yielding 2.05 eV was determined at 20 K; therefore, to compare results the value needs to be corrected by a thermal band gap narrowing of at least 100 meV. Such discrepancy is not unexpected and can be accounted for by the Burstein−Moss effect. With its presence, the observed indirect absorption edge is shifted toward higher energies, but the electronic band gap, defined as the distance between VB and CB, remains unchanged. We believe that our model applied to the acquired defect-related PL spectra allowed us to estimate the fundamental indirect band gap of SnS_2 of 2.05 ± 0.05 eV.

■ CONCLUSIONS

In this work, we exploited complementary methods of optical spectroscopy (modulated reflectance, optical absorption, and photoluminescence emission) to examine the fundamental properties of SnS_2 and $SnSe_2$ vdW crystals and elucidate discrepancies present in the literature. An additional aspect of the study was the comparison of different approaches to the analysis of the experimental results and discussion of their applicability for the case of the SnX_2 crystals but also their general limitations, which are often neglected.

The absorption edge observed in the experiment was identified as direct based on the spectral coincidence with the PR resonance, despite the theoretically predicted indirect character of the fundamental band gap. The energies of the direct optical transitions were 2.41 eV for SnS_2 and 1.31 eV for $SnSe_2$ at a temperature of 20 K. According to DFT calculations of the electronic band structure, the lowest direct transition occurs in the Γ point of the BZ. The distribution of the squared matrix element in this region suggests possible contribution of multiple states and low transition probability, explaining the significant broadening and unusual shape of the measured PR resonance. Another characteristic feature of the electronic band structure is an extremely flat VB dispersion, which is the reason why the analysis of the optical absorption spectra with the Tauc plot method (based on the assumption of parabolic band shape) did not give satisfactory results. Considerably better agreement with PR spectra was achieved in an alternative approach, involving the transmittance first derivate, which is grounded in common origin of the absorption and reflection coefficients from the dielectric function.

The lack of signal originating from the indirect band gap can be attributed to the Burstein−Moss effect. For both SnS_2 and $SnSe_2$, intrinsic n-type character was observed in multiple reports, being a consequence of the presence of donor defects localized close to the bottom of the CB, acting as a reservoir of the electrons populating the lowest states. For $SnSe_2$, the effect was directly observed in ARPES measurements by Lochocki et al.[31] For SnS_2, an evidence of its presence could be the peculiar damping of the defect-related photoemission at certain energy, observed in our experiment. With the proposed model allowing reproducing the spectral dependence of the PL intensity, we determined the fundamental indirect band gap of SnS_2 of 2.05 eV, at a temperature of 20 K. The value is reasonable but needs further verification. Since the model is based on simple assumption of the relative position of defect levels and band extrema, we believe that it should be applicable to any system fulfilling the conditions for which similar phenomenon can be observed.

The obtained results reveal a strong influence of the structural defects on the optical properties of SnX_2 crystals. By varying the defect concentration, the optical band gap can be adjusted to obtain an optimal value for certain applications. Defect concentration can also affect the efficiency of photocatalytic processes, sensitive to surface reactive sites, and thermoelectric conversion, by decreasing the lattice thermal conductivity. We report participation of the defect states in the radiative recombination processes, which greatly contribute to the general understanding of the SnX_2 crystal properties and point to possible directions for further investigation.

■ ASSOCIATED CONTENT

Supporting Information

The Supporting Information is available free of charge at https://pubs.acs.org/doi/10.1021/acs.jpcc.4c03005.

EDS maps of SnS_2 and $SnSe_2$ flakes, optical microscope images of the samples, Tauc plots of the absorption

coefficient and transmittance first derivate spectra, parameters of the Bose−Einstein fits to the temperature dependence of the direct optical transition energies, orbital composition of the electronic bands, comparison of two methods of the electronic band structure calculations (mBJ-TB09 vs. HSE06), excitation power dependence of the PL spectra of SnS_2, and details on the PL quenching model with a graphical illustration (PDF)

■ AUTHOR INFORMATION

Corresponding Author

Maciej Peter − *Department of Semiconductor Materials Engineering, Wrocław University of Science and Technology, 50-370 Wrocław, Poland;* orcid.org/0009-0005-9886-4898; Email: maciej.peter@pwr.edu.pl

Authors

Agata K. Tołłoczko − *Department of Semiconductor Materials Engineering, Wrocław University of Science and Technology, 50-370 Wrocław, Poland*

Miłosz Rybak − *Department of Semiconductor Materials Engineering, Wrocław University of Science and Technology, 50-370 Wrocław, Poland*

Sandeep Gorantla − *Łukasiewicz Research Network—PORT Polish Center for Technology Development, Wrocław 54-066, Poland*

Alicja Bachmatiuk − *Łukasiewicz Research Network—PORT Polish Center for Technology Development, Wrocław 54-066, Poland*

Robert Kudrawiec − *Department of Semiconductor Materials Engineering, Wrocław University of Science and Technology, 50-370 Wrocław, Poland; Łukasiewicz Research Network—PORT Polish Center for Technology Development, Wrocław 54-066, Poland;* orcid.org/0000-0003-2593-9172

Complete contact information is available at:
https://pubs.acs.org/10.1021/acs.jpcc.4c03005

Author Contributions

[‖]Agata K. Tołłoczko and Maciej Peter contributed equally to this work.

Notes

The authors declare no competing financial interest.

■ ACKNOWLEDGMENTS

This work was supported by the National Science Centre (NCN) Poland OPUS 20 no. 2020/39/B/ST3/02704. The computational studies were carried out with the use of WCSS and PLGrid Infrastructure.

■ REFERENCES

(1) Novoselov, K. S.; Mishchenko, A.; Carvalho, A.; Castro Neto, A. H. 2D Materials and van Der Waals Heterostructures. *Science* **2016**, *353* (6298), aac9439.

(2) Novoselov, K. S.; Geim, A. K.; Morozov, S. V.; Jiang, D.; Zhang, Y.; Dubonos, S. V.; Grigorieva, I. V.; Firsov, A. A. Electric Field Effect in Atomically Thin Carbon Films. *Science* **2004**, *306* (5696), 666−669.

(3) Zhong, Y.; Zhang, L.; Chen, W.; Zhu, H. Macro van Der Waals P-n Heterojunction Based on SnSe and SnSe2. *Nanotechnology* **2020**, *31* (38), 385203.

(4) Fan, C.; Li, Y.; Lu, F.; Deng, H.-X.; Wei, Z.; Li, J. Wavelength Dependent UV-Vis Photodetectors from SnS2 Flakes. *RSC Adv.* **2016**, *6* (1), 422−427.

(5) Cui, X.; Xu, W.; Xie, Z.; Wang, Y. High-Performance Dye-Sensitized Solar Cells Based on Ag-Doped SnS2 Counter Electrodes. *J. Mater. Chem. A* **2016**, *4* (5), 1908−1914.

(6) Gao, W.; Zheng, Z.; Li, Y.; Zhao, Y.; Xu, L.; Deng, H.; Li, J. High Performance Tin Diselenide Photodetectors Dependent on Thickness: A Vertical Graphene Sandwiched Device and Interfacial Mechanism. *Nanoscale* **2019**, *11* (28), 13309−13317.

(7) Pham, A.-T.; Vu, T. H.; Cheng, C.; Trinh, T. L.; Lee, J.-E.; Ryu, H.; Hwang, C.; Mo, S.-K.; Kim, J.; Zhao, L.; et al. High-Quality SnSe2 Single Crystals: Electronic and Thermoelectric Properties. *ACS Appl. Energy Mater.* **2020**, *3* (11), 10787−10792.

(8) Liu, M.; Zhang, J.; Xu, J.; Hu, B.; Liu, B.; Sun, K.; Yang, Y.; Wang, J.; Du, B. Phase Structure, Phase Transition and Thermoelectric Properties of Pristine and Br Doped SnSe2. *J. Solid State Chem.* **2020**, *289*, 121468.

(9) Zhan, S.; Zheng, L.; Xiao, Y.; Zhao, L.-D. Phonon and Carrier Transport Properties in Low-Cost and Environmentally Friendly SnS2: A Promising Thermoelectric Material. *Chem. Mater.* **2020**, *32* (24), 10348−10356.

(10) Li, G.; Wu, C.; Zhang, S.; Su, J.; Li, T. Passively Q-Switched Er:YAG Laser at 1645 Nm with SnS2 as a Novel Saturable Absorber. *Optik* **2019**, *183*, 163−167.

(11) Wang, R.; Zhang, L.; Sun, T.; Wang, H. Preparation and Characteristics of SnS2 Saturable Absorber and Its Application in Passively Q-Switched Nd:YAG/Cr4+:YAG Laser. *Optik* **2020**, *212*, 164712.

(12) Yang, H. R.; Liu, X. M. Nonlinear Optical Response and Applications of Tin Disulfide in the Near- and Mid-Infrared. *Appl. Phys. Lett.* **2017**, *110* (17), 171106.

(13) Feng, T.; Zhang, D.; Li, X.; Abdul, Q.; Shi, Z.; Lu, J.; Guo, P.; Zhang, Y.; Liu, J.; Wang, Q. J. SnS2 Nanosheets for Er-Doped Fiber Lasers. *ACS Appl. Nano Mater.* **2020**, *3* (1), 674−681.

(14) Li, G.; Feng, Y.; Li, L.; Du, W.; Liu, H.; Sun, X.; Zhao, X.; Ma, Y.; Jia, Y.; Chen, F. Broadband Nonlinear Optical Response and Sub-Picosecond Carrier Dynamics in Graphene-$SnSe_2$ van Der Waals Heterostructures. *Opt. Express* **2024**, *32* (2), 2867−2883.

(15) Li, L.; Chai, Z.; Jin, W.; Sun, H.; He, J.; Wu, G.; Xia, W. Sulfur Vacancy in SnS2 Nanoflake Adjusted by Precursor and Improved Photocatalytic Performance. *J. Alloys Compd.* **2023**, *932*, 167658.

(16) Jena, A.; Pichaimuthu, K.; Leniec, G.; Kaczmarek, S. M.; Chang, H.; Su, C.; Hu, S.-F.; Liu, R.-S. Defect Mediated Improvements in the Photoelectrochemical Activity of MoS2/SnS2 Ultrathin Sheets on Si Photocathode for Hydrogen Evolution. *ACS Appl. Mater. Interfaces* **2022**, *14* (35), 39896−39906.

(17) Zhao, Y.; Sun, D.; Hu, K.; Zhao, W.; Huang, F. Surface Defect Engineering of SnS2 Nanocrystals for Enhanced Photocatalytic Reduction of Cr (VI) under Visible Light. *Inorg. Chem. Commun.* **2020**, *114*, 107849.

(18) D'Olimpio, G.; Farias, D.; Kuo, C.-N.; Ottaviano, L.; Lue, C. S.; Boukhvalov, D. W.; Politano, A. Tin Diselenide (SnSe2) Van Der Waals Semiconductor: Surface Chemical Reactivity, Ambient Stability, Chemical and Optical Sensors. *Materials* **2022**, *15* (3), 1154.

(19) Guo, S.-Q.; Yang, B.; Hu, Z.; Zhen, M.; Gu, B.; Shen, B. Uncovering Mechanism of Photocatalytic Performance Enhancement Induced by Multivariate Defects on SnS2. *Nano Res.* **2023**, *16* (2), 2102−2110.

(20) Mondal, S.; Das, S.; Gautam, U. K. Defect-Rich, Negatively-Charged SnS2 Nanosheets for Efficient Photocatalytic Cr(VI) Reduction and Organic Dye Adsorption in Water. *J. Colloid Interface Sci.* **2021**, *603*, 110−119.

(21) Wang, S.; Yang, B.; Liu, Y. Synthesis of a Hierarchical SnS2 Nanostructure for Efficient Adsorption of Rhodamine B Dye. *J. Colloid Interface Sci.* **2017**, *507*, 225−233.

(22) Cheng, W.-Y.; Fuh, H.-R.; Chang, C.-R. First-Principles Study for Gas Sensing of Defective SnSe2Monolayers. *Appl. Sci.* **2020**, *10* (5), 1623.

(23) Yan, W.-J.; Chen, D.-Y.; Fuh, H.-R.; Li, Y.-L.; Zhang, D.; Liu, H.; Wu, G.; Zhang, L.; Ren, X.; Cho, J.; et al. Photo-Enhanced Gas

Sensing of SnS2 with Nanoscale Defects. *RSC Adv.* **2019**, *9* (2), 626−635.

(24) Li, Y.; Duan, J.; Berencén, Y.; Hübner, R.; Tsai, H.-S.; Kuo, C.-N.; Lue, C. S.; Helm, M.; Zhou, S.; Prucnal, S. Formation of a Vertical SnSe/$SnSe_2$ p-n Heterojunction by NH_3 Plasma-Induced Phase Transformation. *Nanoscale Adv.* **2023**, *5* (2), 443−449.

(25) Sánchez-Juárez, A.; Tiburcio-Silver, A.; Ortiz, A. Fabrication of SnS2/SnS Heterojunction Thin Film Diodes by Plasma-Enhanced Chemical Vapor Deposition. *Thin Solid Films* **2005**, *480*, 452−456.

(26) Tian, Z.; Zhao, M.; Xue, X.; Xia, W.; Guo, C.; Guo, Y.; Feng, Y.; Xue, J. Lateral Heterostructures Formed by Thermally Converting N-Type SnSe2 to p-Type SnSe. *ACS Appl. Mater. Interfaces* **2018**, *10* (15), 12831−12838.

(27) Aretouli, K. E.; Tsoutsou, D.; Tsipas, P.; Marquez-Velasco, J.; Aminalragia Giamini, S.; Kelaidis, N.; Psycharis, V.; Dimoulas, A. Epitaxial 2D SnSe2/2D WSe2 van Der Waals Heterostructures. *ACS Appl. Mater. Interfaces* **2016**, *8* (35), 23222−23229.

(28) Murali, K.; Dandu, M.; Das, S.; Majumdar, K. Gate-Tunable WSe2/SnSe2 Backward Diode with Ultrahigh-Reverse Rectification Ratio. *ACS Appl. Mater. Interfaces* **2018**, *10* (6), 5657−5664.

(29) Zribi, J.; Khalil, L.; Zheng, B.; Avila, J.; Pierucci, D.; Brulé, T.; Chaste, J.; Lhuillier, E.; Asensio, M. C.; Pan, A.; et al. Strong Interlayer Hybridization in the Aligned SnS2/WSe2 Hetero-Bilayer Structure. *npj 2D Mater. Appl.* **2019**, *3* (1), 27.

(30) Sun, Y.; Hu, R.; An, C.; Ma, X.; Zhang, J.; Liu, J. Visible to Near-Infrared Photodetector Based on SnSe2/WSe2 Heterojunction with Potential Application in Artificial Visual Neuron. *Nanotechnology* **2021**, *32* (47), 475206.

(31) Lochocki, E. B.; Vishwanath, S.; Liu, X.; Dobrowolska, M.; Furdyna, J.; Xing, H. G.; Shen, K. M. Electronic Structure of SnSe2 Films Grown by Molecular Beam Epitaxy. *Appl. Phys. Lett.* **2019**, *114* (9), 091602.

(32) Pałosz, B.; Salje, E. Lattice Parameters and Spontaneous Strain in AX2 Polytypes: CdI2, PbI2 SnS2 and SnSe2. *J. Appl. Crystallogr.* **1989**, *22* (6), 622−623.

(33) Ramsdell, L. S. Studies on Silicon Carbide. *Am. Mineral.* **1947**, No. 32, 64−82.

(34) Wilson, J. A.; Yoffe, A. D. The Transition Metal Dichalcogenides Discussion and Interpretation of the Observed Optical, Electrical and Structural Properties. *Adv. Phys.* **1969**, *18* (73), 193−335.

(35) Gonzalez, J. M.; Oleynik, I. I. Layer-Dependent Properties of ${\mathbf{SnS}}_{2}$ and ${\mathbf{SnSe}}_{2}$ Two-Dimensional Materials. *Phys. Rev. B* **2016**, *94* (12), 125443.

(36) Domingo, G.; Itoga, R. S.; Kannewurf, C. R. Fundamental Optical Absorption in Sn${\mathrm{S}}_{2}$ and Sn${\mathrm{Se}}_{2. *Phys. Rev.* **1966**, *143* (2), 536−541.

(37) Manou, P.; Kalomiros, J. A.; Anagnostopoulos, A. N.; Kambas, K. Optical Properties of SnSe2 Single Crystals. *Mater. Res. Bull.* **1996**, *31* (11), 1407−1415.

(38) George, J.; Joseph, K. S. Absorption Edge Measurements in Tin Disulphide Thin Films. *J. Phys. Appl. Phys.* **1982**, *15* (6), 1109−1116.

(39) Julien, C.; Eddrief, M.; Samaras, I.; Balkanski, M. Optical and Electrical Characterizations of SnSe, SnS2 and SnSe2 Single Crystals. *Mater. Sci. Eng., B* **1992**, *15* (1), 70−72.

(40) Liu, W.; Liu, M.; Wang, X.; Shen, T.; Chang, G.; Lei, M.; Deng, H.; Wei, Z.; Wei, Z. Thickness-Dependent Ultrafast Photonics of SnS2 Nanolayers for Optimizing Fiber Lasers. *ACS Appl. Nano Mater.* **2019**, *2* (5), 2697−2705.

(41) Burton, L. A.; Colombara, D.; Abellon, R. D.; Grozema, F. C.; Peter, L. M.; Savenije, T. J.; Dennler, G.; Walsh, A. Synthesis, Characterization, and Electronic Structure of Single-Crystal SnS, Sn2S3, and SnS2. *Chem. Mater.* **2013**, *25* (24), 4908−4916.

(42) Burstein, E. Anomalous Optical Absorption Limit in InSb. *Phys. Rev.* **1954**, *93* (3), 632−633.

(43) Moss, T. S. The Interpretation of the Properties of Indium Antimonide. *Proc. Phys. Soc. B* **1954**, *67* (10), 775−782.

(44) Momma, K.; Izumi, F. VESTA 3 for Three-Dimensional Visualization of Crystal, Volumetric and Morphology Data. *J. Appl. Crystallogr.* **2011**, *44* (6), 1272−1276.

(45) Smith, A. J.; Meek, P. E.; Liang, W. Y. Raman Scattering Studies of SnS2 and SnSe2. *J. Phys. C Solid State Phys.* **1977**, *10* (8), 1321−1323.

(46) Bhatt, S. V.; Deshpande, M. P.; Sathe, V.; Chaki, S. H. Effect of Pressure and Temperature on Raman Scattering and an Anharmonicity Study of Tin Dichalcogenide Single Crystals. *Solid State Commun.* **2015**, *201*, 54−58.

(47) Greenaway, D. L.; Nitsche, R. Preparation and Optical Properties of Group IV−VI2 Chalcogenides Having the CdI2 Structure. *J. Phys. Chem. Solids* **1965**, *26* (9), 1445−1458.

(48) Lee, P. A.; Said, G.; Davis, R.; Lim, T. H. On the Optical Properties of Some Layer Compounds. *J. Phys. Chem. Solids* **1969**, *30* (12), 2719−2729.

(49) Burton, L. A.; Whittles, T. J.; Hesp, D.; Linhart, W. M.; Skelton, J. M.; Hou, B.; Webster, R. F.; O'Dowd, G.; Reece, C.; Cherns, D.; et al. Electronic and Optical Properties of Single Crystal SnS2: An Earth-Abundant Disulfide Photocatalyst. *J. Mater. Chem. A* **2016**, *4* (4), 1312−1318.

(50) Whittles, T. J.; Burton, L. A.; Skelton, J. M.; Walsh, A.; Veal, T. D.; Dhanak, V. R. Band Alignments, Valence Bands, and Core Levels in the Tin Sulfides SnS, SnS2, and Sn2S3: Experiment and Theory. *Chem. Mater.* **2016**, *28* (11), 3718−3726.

(51) Yu, P. Y.; Cardona, M.. In *Optical Properties I. In Fundamentals of Semiconductors: Physics and Materials Properties*; Yu, P. Y., Cardona, M., Eds.; Springer: Berlin, Heidelberg, 2010; pp 243−344..

(52) Tołłoczko, A.; Zelewski, S. J.; Błaszczak, M.; Woźniak, T.; Siudzińska, A.; Bachmatiuk, A.; Scharoch, P.; Kudrawiec, R. Optical Properties of Orthorhombic Germanium Selenide: An Anisotropic Layered Semiconductor Promising for Optoelectronic Applications. *J. Mater. Chem. C* **2021**, *9* (41), 14838−14847.

(53) Kopaczek, J.; Polak, M. P.; Scharoch, P.; Wu, K.; Chen, B.; Tongay, S.; Kudrawiec, R. Direct Optical Transitions at K- and H-Point of Brillouin Zone in Bulk MoS2, MoSe2, WS2, and WSe2. *J. Appl. Phys.* **2016**, *119* (23), 235705.

(54) Zelewski, S. J.; Kudrawiec, R. Photoacoustic and Modulated Reflectance Studies of Indirect and Direct Band Gap in van Der Waals Crystals. *Sci. Rep.* **2017**, *7* (1), 15365.

(55) Kopaczek, J.; Zelewski, S. J.; Polak, M. P.; Gawlik, A.; Chiappe, D.; Schulze, A.; Caymax, M.; Kudrawiec, R. Direct and Indirect Optical Transitions in Bulk and Atomically Thin MoS2 Studied by Photoreflectance and Photoacoustic Spectroscopy. *J. Appl. Phys.* **2019**, *125* (13), 135701.

(56) Aspnes, D. E. Third-Derivative Modulation Spectroscopy with Low-Field Electroreflectance. *Surf. Sci.* **1973**, *37*, 418−442.

(57) Murgatroyd, P. A. E.; Smiles, M. J.; Savory, C. N.; Shalvey, T. P.; Swallow, J. E. N.; Fleck, N.; Robertson, C. M.; Jäckel, F.; Alaria, J.; Major, J. D.; et al. GeSe: Optical Spectroscopy and Theoretical Study of a van Der Waals Solar Absorber. *Chem. Mater.* **2020**, *32*, 3245−3253.

(58) Tauc, J. Optical Properties and Electronic Structure of Amorphous Ge and Si. *Mater. Res. Bull.* **1968**, *3* (1), 37−46.

(59) Cody, G. D.; Brooks, B. G.; Abeles, B. Optical Absorption above the Optical Gap of Amorphous Silicon Hydride. *Sol. Energy Mater.* **1982**, *8* (1−3), 231−240.

(60) Urbach, F. The Long-Wavelength Edge of Photographic Sensitivity and of the Electronic Absorption of Solids. *Phys. Rev.* **1953**, *92* (5), 1324.

(61) Hsueh, H.-C.; Li, J.-X.; Ho, C.-H. Polarization Photoelectric Conversion in Layered GeS. *Adv. Opt. Mater.* **2018**, *6* (4), 1701194.

(62) Viña, L.; Logothetidis, S.; Cardona, M. Temperature Dependence of the Dielectric Function of Germanium. *Phys. Rev. B* **1984**, *30* (4), 1979−1991.

(63) Nguyen, H. T.; Le, V. L.; Nguyen, T. M. H.; Kim, T. J.; Nguyen, X. A.; Kim, B.; Kim, K.; Lee, W.; Cho, S.; Kim, Y. D. Temperature Dependence of the Dielectric Function and Critical Points of α-SnS from 27 to 350 K. *Sci. Rep.* **2020**, *10* (1), 18396.

(64) Oliva, R.; Woźniak, T.; Dybala, F.; Tołłoczko, A.; Kopaczek, J.; Scharoch, P.; Kudrawiec, R. Valley Polarization Investigation of GeS under High Pressure. *Phys. Rev. B* **2020**, *101* (23), 235205.
(65) Tołłoczko, A. K.; Zelewski, S. J.; Ziembicki, J.; Olszowska, N.; Rosmus, M.; Woźniak, T.; Tongay, S.; Kudrawiec, R. Photoemission Study of the Thermoelectric Group IV-VI van Der Waals Crystals (GeS, SnS, and SnSe). *Adv. Opt. Mater.* **2023**, *12*, 2302049.
(66) Van Hove, L. The Occurrence of Singularities in the Elastic Frequency Distribution of a Crystal. *Phys. Rev.* **1953**, *89* (6), 1189−1193.
(67) Schmidt, T.; Lischka, K.; Zulehner, W. Excitation-Power Dependence of the near-Band-Edge Photoluminescence of Semiconductors. *Phys. Rev. B* **1992**, *45* (16), 8989−8994.
(68) Gelczuk, Ł.; Kopaczek, J.; Scharoch, P.; Komorowska, K.; Blei, M.; Tongay, S.; Kudrawiec, R. Probing Defects in MoS2 Van Der Waals Crystal through Deep-Level Transient Spectroscopy. *Phys. Status Solid RRL* **2020**, *14* (12), 2000381.
(69) Kim, J. Y.; Gelczuk, Ł.; Polak, M. P.; Hlushchenko, D.; Morgan, D.; Kudrawiec, R.; Szlufarska, I. Experimental and Theoretical Studies of Native Deep-Level Defects in Transition Metal Dichalcogenides. *npj 2D Mater. Appl.* **2022**, *6* (1), 75.
(70) Kresse, G.; Furthmüller, J. Efficient Iterative Schemes for Ab Initio Total-Energy Calculations Using a Plane-Wave Basis Set. *Phys. Rev. B* **1996**, *54* (16), 11169−11186.
(71) Holzwarth, N. A. W.; Tackett, A. R.; Matthews, G. E. A Projector Augmented Wave (PAW) Code for Electronic Structure Calculations, Part I: *Atompaw* for Generating Atom-Centered Functions. *Comput. Phys. Commun.* **2001**, *135* (3), 329−347.
(72) Paier, J.; Hirschl, R.; Marsman, M.; Kresse, G. The Perdew−Burke−Ernzerhof Exchange-Correlation Functional Applied to the G2−1 Test Set Using a Plane-Wave Basis Set. *J. Chem. Phys.* **2005**, *122* (23), 234102.
(73) Monkhorst, H. J.; Pack, J. D. Special Points for Brillouin-Zone Integrations. *Phys. Rev. B* **1976**, *13* (12), 5188−5192.
(74) Grimme, S.; Antony, J.; Ehrlich, S.; Krieg, H. A Consistent and Accurate Ab Initio Parametrization of Density Functional Dispersion Correction (DFT-D) for the 94 Elements H-Pu. *J. Chem. Phys.* **2010**, *132* (15), 154104.
(75) Tran, F.; Blaha, P. Accurate Band Gaps of Semiconductors and Insulators with a Semilocal Exchange-Correlation Potential. *Phys. Rev. Lett.* **2009**, *102* (22), 226401.
(76) Krukau, A. V.; Vydrov, O. A.; Izmaylov, A. F.; Scuseria, G. E. Influence of the Exchange Screening Parameter on the Performance of Screened Hybrid Functionals. *J. Chem. Phys.* **2006**, *125* (22), 224106.

Supporting Information

Influence of Native Defects on the Optical Properties of SnX_2 ($X = S, Se$) van der Waals Crystals

Agata K. Tołłoczko,[a] Maciej Peter,[a] Miłosz Rybak,[a] Sandeep Gorantla,[b] Alicja Bachmatiuk,[b] Robert Kudrawiec[a,b]*

[1] Department of Semiconductor Materials Engineering,
Wrocław University of Science and Technology,
Wybrzeże Wyspiańskiego 27, 50-370 Wrocław, Poland

[2] Łukasiewicz Research Network – PORT Polish Center for Technology Development,
Stabłowicka 147, Wrocław, Poland

*Corresponding author.

E-mail address: maciej.peter@pwr.edu.pl

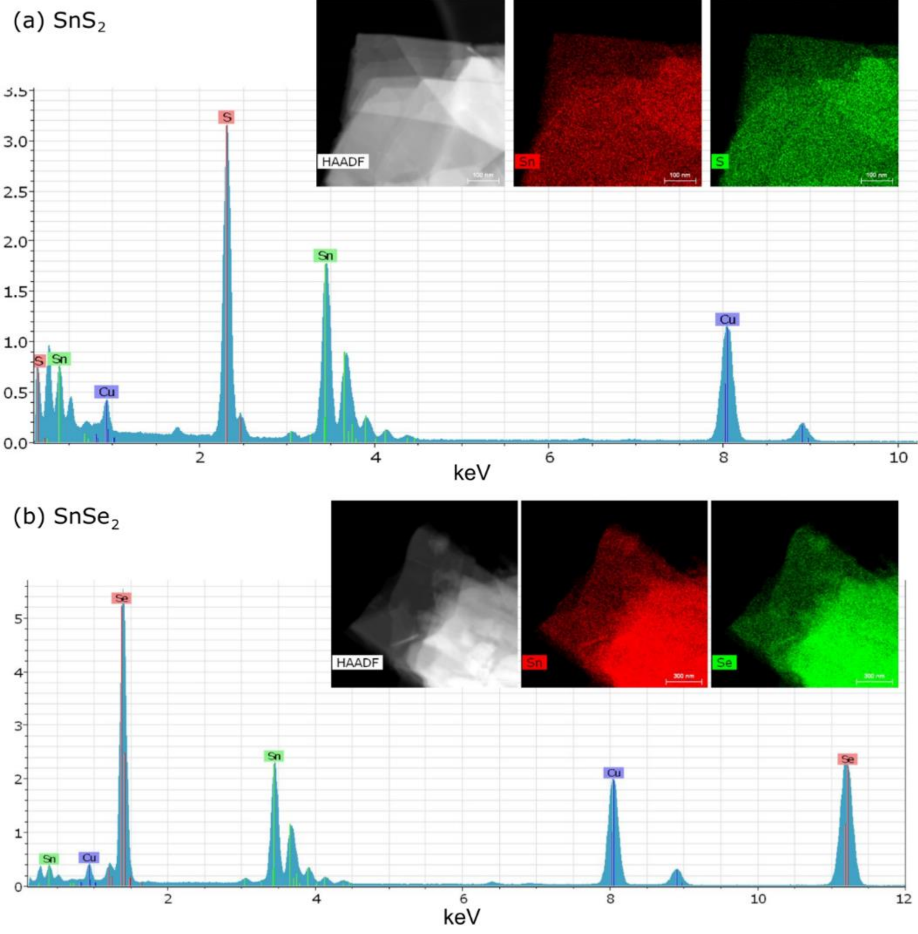

Fig. S1. EDS spectra acquired for SnS_2 (a) and $SnSe_2$ (b), corresponding to the EDS maps from Fig. 2 of the main text and presented here in top-right corner of each panel. Lines attributed to Sn, S or Se, and Cu were identified, with the latter originating from Cu TEM grid on which the samples were placed for the measurement.

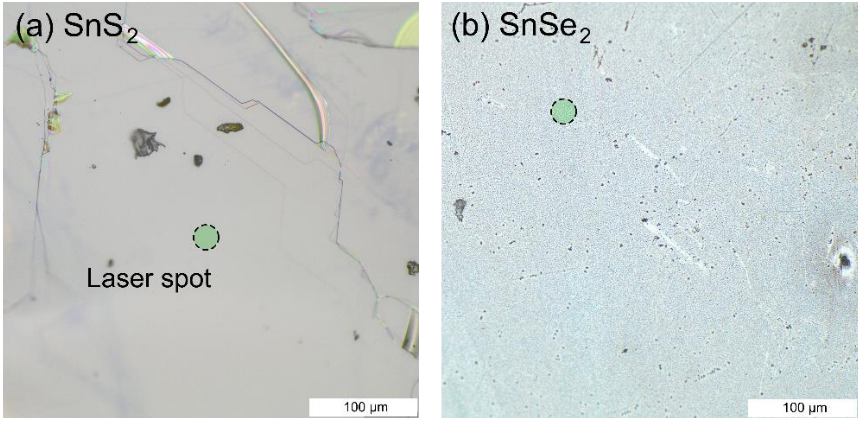

Fig. S2. Microscope images of the surface of SnS_2 (a) and $SnSe_2$ (b) samples. The size of the laser spot used for the Raman scattering and PL measurements is illustrated by green circles. For the experiment regions of the samples without any visible structural impurities were selected, such as these marked in the images (although not precisely these).

Table S1. Frequencies of the phonon modes observed in Raman scattering measurements.

Mode	Frequency (cm^{-1})	
	SnS_2	$SnSe_2$
E_g	213.4	116.5
A_{1g}	320.9	187.9

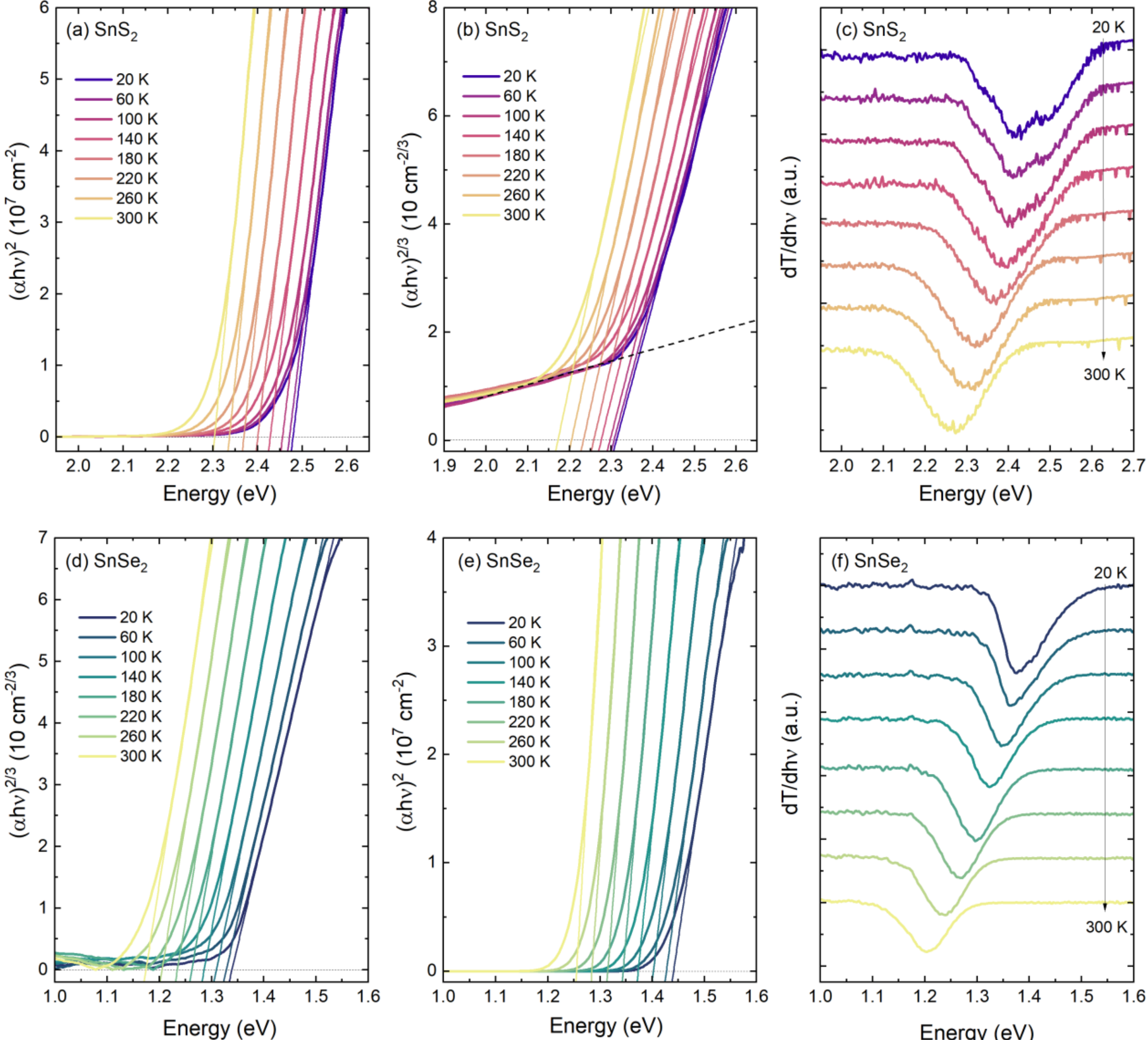

Fig. S3. Illustration of different methods of determination of the direct transition energies for SnS_2 (a-c) and $SnSe_2$ (d-f), in the temperature range from 20 to 300 K. Tauc plots for direct allowed (a,d) and direct forbidden (b,e) absorption edge, with linear extrapolations of the analyzed regions. In panel (b), due to presence of a background signal, the transition energy was extracted from the intersection of the linear fit of the $(\alpha h\nu)^{2/3}$ plot with extrapolation of the background. First derivatives of the transmittance spectra (c,f).

Table S2. Parameters of the Bose-Einstein fits to the temperature dependence of the direct optical transitions energies determined from PR spectra and $(\alpha h\nu)^{2/3}$ Tauc plots, for SnS_2 and $SnSe_2$.

Method	Parameter	SnS_2	$SnSe_2$
PR	$E(0)$ (eV)	2.41	1.30
	a_B (eV)	0.276	0.107
	θ_B (K)	481	267
$(\alpha h\nu)^{2/3}$	$E(0)$ (eV)	2.36	1.28
	a_B (eV)	0.120	0.063
	θ_B (K)	280	186

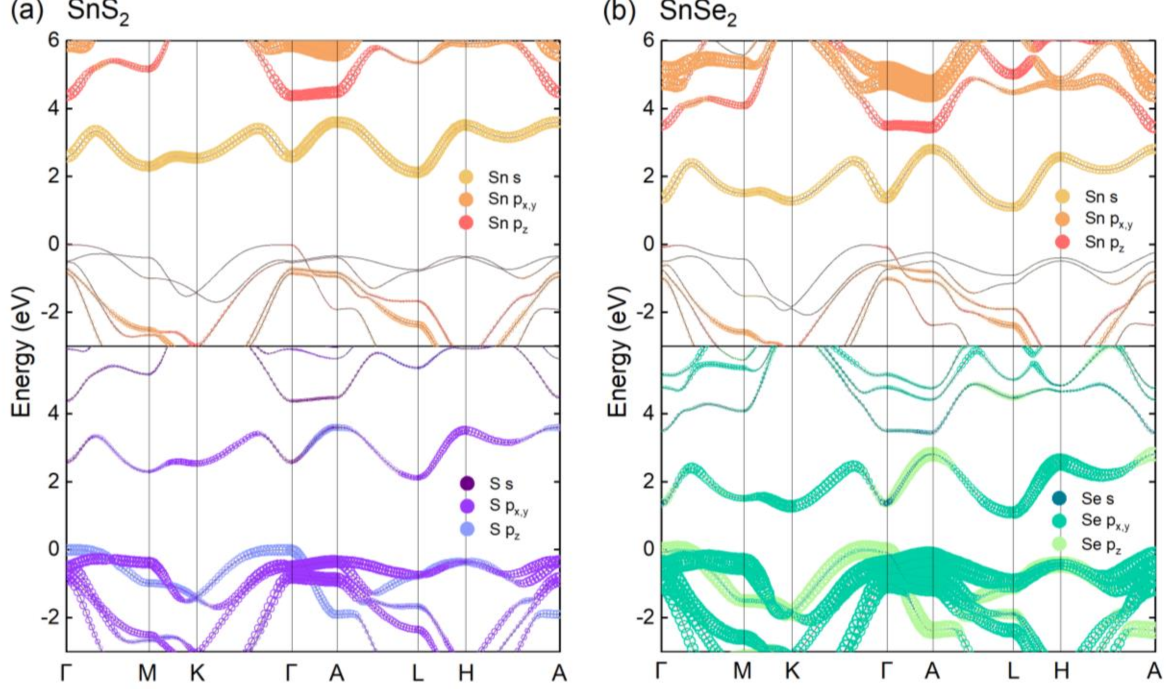

Fig. S4. Orbital composition of the electronic bands of SnS_2 (a) and $SnSe_2$ (b). Top and bottom panels illustrate the contribution of Sn and X orbitals, respectively.

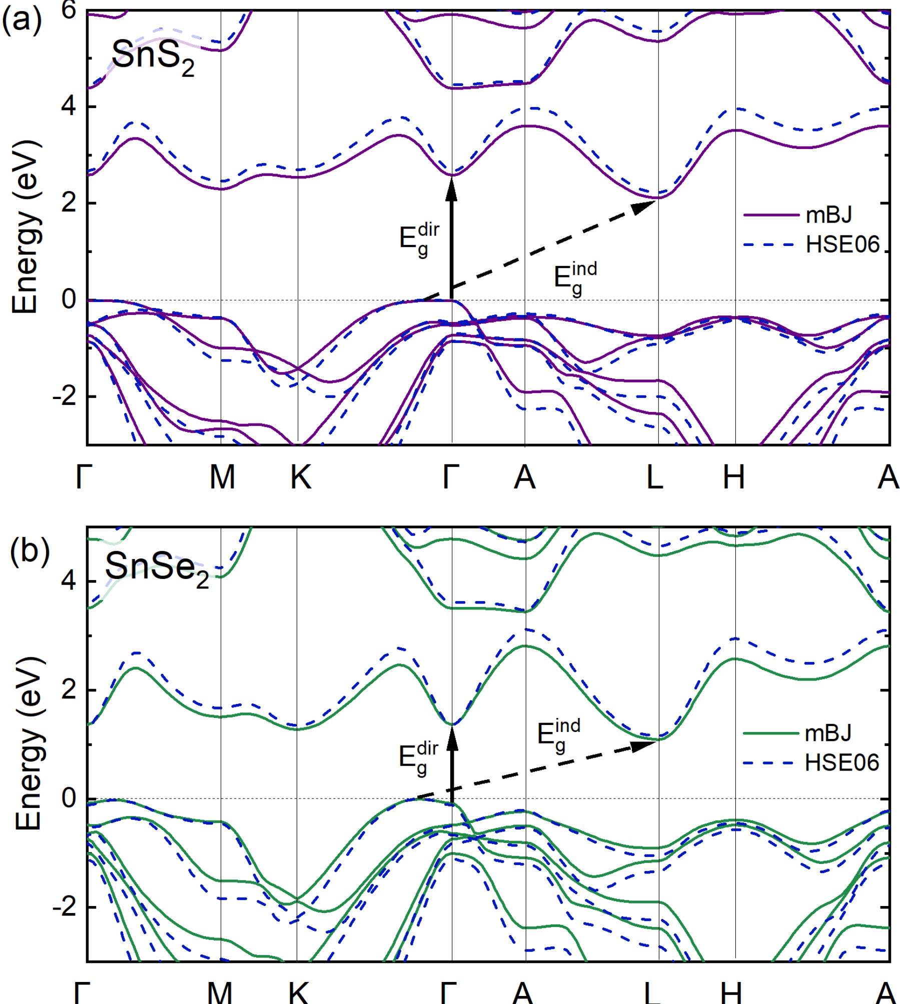

Fig. S5. The electronic band structure of SnS_2 (a) and $SnSe_2$ (b) calculated with mBJ-TB09 exchange potential (solid lines) and HSE06 hybrid functional (dashed lines).

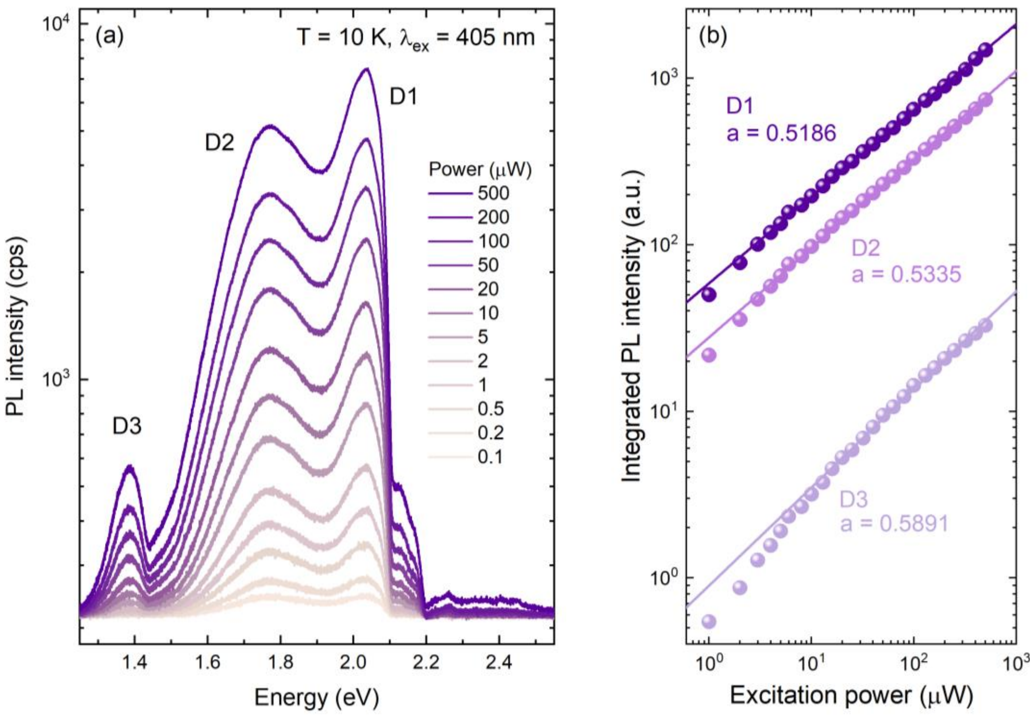

Fig. S6. Photoluminescence emission spectra of SnS_2 acquired with excitation power from 0.1 to 500 μW (a). Excitation power dependence of integrated PL intensity in log-log scale, with linear fits (b). The slopes of the fitted lines < 1 indicate defect-related nature of the emission.

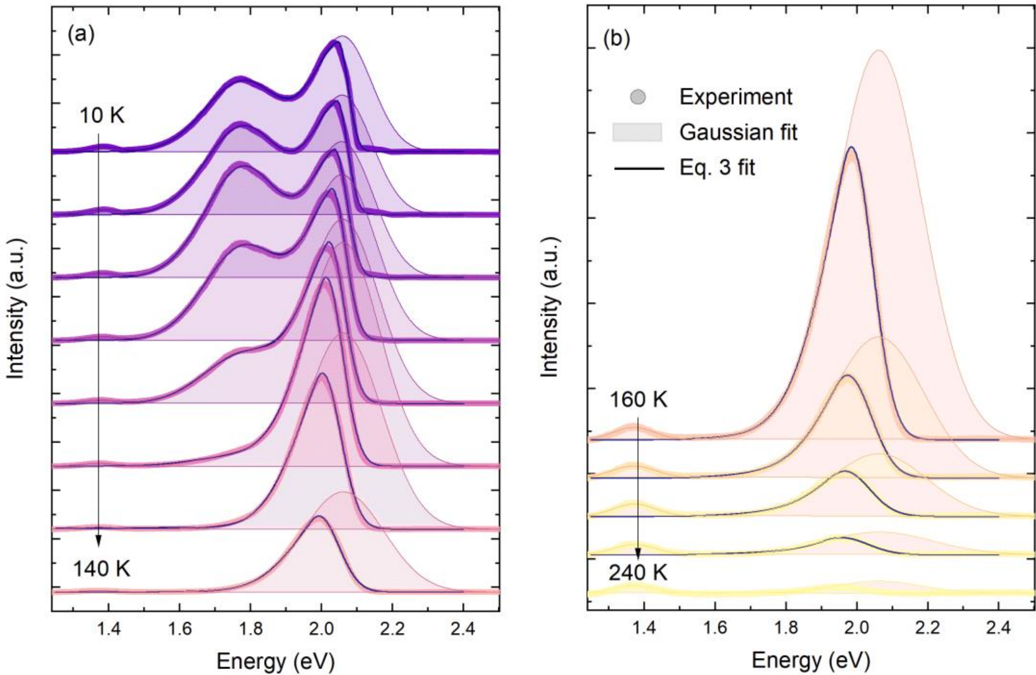

Fig. S7. The temperature evolution of the defect-related photoluminescence emission measured for SnS2. Results of the fitting of three (10 – 120 K) or two (140 - 240 K) Gaussian line-shape and the PL quenching model (Eq. 3) to the experimental data are superimposed over the spectra.

The PL quenching model

The spectral dependence of the defect-related photoluminescence intensity quenched by a mechanism illustrated in Fig. S8 is given by

$$I_{PL}(h\nu) = G(h\nu, E_d)\, e^{-DOS_{CB}(h\nu, E_g)} \qquad \text{Eq. S1}$$

where $G(h\nu, E_d)$ is a Gaussian function centered at defect energy E_d. $DOS_{CB}(h\nu, E_g)$ is the conduction band density of states, given by

$$DOS_{CB}(h\nu) = \begin{cases} 0 & h\nu < E_g \\ C\left(h\nu - E_g\right)^{1/2} & h\nu \geq E_g \end{cases} \qquad \text{Eq. S2}$$

where C is a constant, and $E_g = E_{CBM} - E_{VBM}$ is the fundamental band gap. The above formula is the simples approximation of the actual DOS, derived from the assumption of the parabolic shape of the conduction band close to its minimum. This form was used for the analysis presented in the main text, however we also consider a modification of the model by intr Eq. S3 an exponential tail of the density of states below E_g, described by Eq. S4.

$$DOS_{CB}(h\nu) = \begin{cases} f_1(h\nu) = Ae^{B\left(h\nu - (E_g + \delta)\right)} & h\nu < E_g + \delta \\ f_2(h\nu) = C\left(h\nu - E_g\right)^{1/2} & h\nu \geq E_g + \delta \end{cases}$$

where A, B, and C are constants, and δ is a small energy shift introduced to obtain smoother and more natural shape of the function at the junction of the two regions. To preserve the function from overparametrization, A = 1 was set (since a mutual dependence exists between constants A and C), and the remaining parameters where chosen so that continuity conditions are fulfilled at $h\nu = E_g + \delta$, i.e.

$$\begin{cases} f_1\left(E_g + \delta\right) = f_2\left(E_g + \delta\right) \\ \dfrac{df_1\left(E_g + \delta\right)}{dh\nu} = \dfrac{df_2\left(E_g + \delta\right)}{dh\nu} \end{cases} \qquad \text{Eq. S4}$$

By solving the system of equations, we obtain $B = \frac{C^2}{2}$, and $\delta = \frac{1}{C^2}$. Hence, in a final form DOS_{CB} is given by

$$DOS_{CB}(h\nu) = \begin{cases} e^{\frac{C^2}{2}\left(h\nu - \left(E_g + \frac{1}{C^2}\right)\right)} & h\nu < E_g + \dfrac{1}{C^2} \\ C\left(h\nu - E_g\right)^{1/2} & h\nu \geq E_g + \dfrac{1}{C^2} \end{cases} \qquad \text{Eq. S5}$$

To visualize the difference between Eq. S2 and Eq. S5, the functions are plotted in Fig. S9a, assuming $E_g = 2.0$ eV, and C = 10.

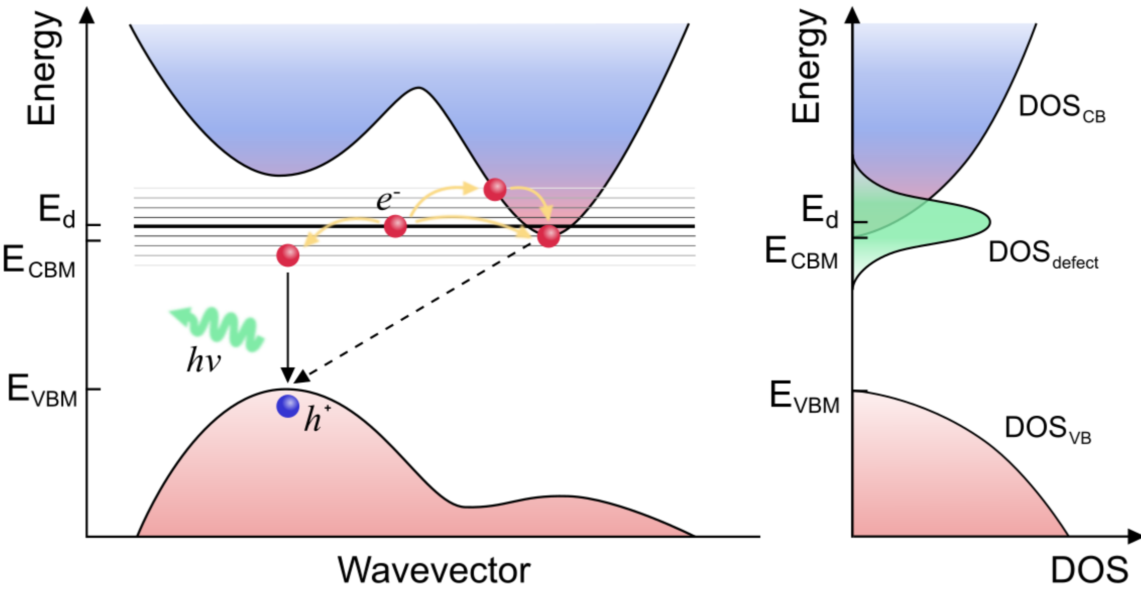

Fig. S8. Graphical illustration of the mechanism of the experimentally observed photoluminescence quenching. The presented band dispersion, electronic levels arrangement, and density of states distribution are only used for visualization of a concept, and do not correspond to an actual material. Valence and conduction band are shown as red and blue shaded areas, respectively. The residual red color at the bottom of the CB represent states occupied by the electrons originating from ionized donors (the Burstein-Moss effect). The black line at the energy E_d corresponds to a defect state, and the thin grey lines represent the state broadening. After excitation from the valence band, the electron (red ball) can populate the defect state and then be scattered (yellow arrows) between vibrational levels within the state broadening, either energetically lower or higher. At energies below CBM, the electron can recombine radiatively (solid arrow) with a hole (blue ball) in the valence band. In the process the momentum is preserved, as the wavefunction of the electron localized on a defect in the real space is delocalized in the reciprocal space. At the energy of CBM and above, the electron is more likely to occupy states in the conduction band, localized in the wavevector space. The electrons from the CB valley also can recombine with holes from VB, although due to difference in k-point, the transition is indirect and therefore non-radiative (dashed arrow). In the experiment the mechanism is observed as quenching of the defect-related PL emission above the energy of CBM.

The accuracy of the fitting to the experimental data was comparably good for either form of DOS_{CB}, however the resulting E_g values differed, as presented in Fig. S9b (star symbols). For DOS_{CB} given by Eq. S2, the acquired values are lower, and the temperature dependence is stronger, resulting in larger redshift of the transition energy, compared to Eq. S5. The discrepancy is most severe at high temperatures, suggesting the model at the current form is best applicable close to 0 K, providing similar values regardless of the presence of the exponential tail, but need some adjustments at higher temperatures.

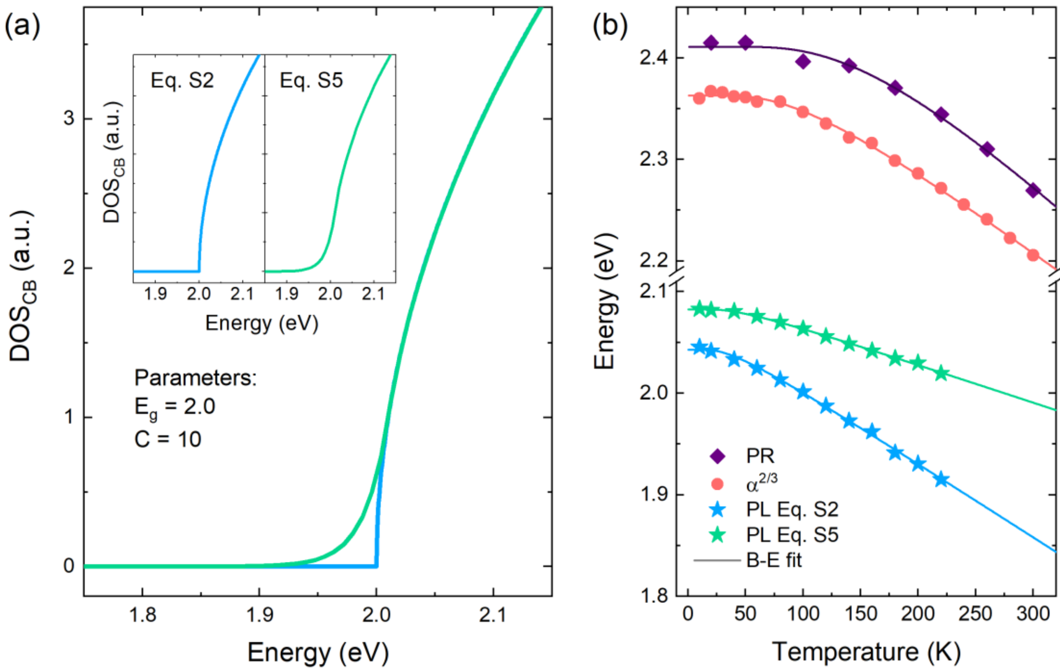

Fig. S9. Plots of the conduction band density of states (DOS_{CB}) given by Eq. S2 and Eq. S5 (a), and the temperature dependence of the optical transitions energies determined by different methods: photoreflectance (purple diamond symbols), $(\alpha h\nu)^{2/3}$ Tauc plot (red circles), and PL quenching model with DOS_{CB} given by Eq. S2 (green star symbols) and Eq. S5 (blue star symbols) (b).

Chapter 7

Conclusions

In this work, group IV mono- and dichalcogenides – materials belonging to a family of van der Waals crystals – were characterized exploiting various methods of optical and photoemission spectroscopy, supported by *ab initio* calculations. The experiments were performed to investigate the fundamental optical and electronic properties of the materials, as well as observe some unexpected phenomena and assess possibilities of exploiting them in specific applications.

Optical study of MX crystals (GeS, GeSe, SnS, and SnSe) allowed to determine the energy and character of the fundamental band gaps, resolving discrepancies present in the literature, and revealed strong in-plane anisotropy related to the electronic orbital composition of the electronic bands (especially different components of metal and chalcogen *p* states), dictating the selection rules. For GeSe, optical absorption spectra were dominated by direct optical transitions, despite the indirect character of the fundamental band gap (predicted by DFT calculations and confirmed by lack of photoluminescence emission), being a consequence of small energy distance between involved valleys in the electronic band structure. In the case of SnS and SnSe, indirect absorption edge was detected in polarization-resolved experiments, which allowed to reduce the intensity of the lowest direct transition active for light polarized along the *x* crystallographic direction. For GeS, the position of the valence band maximum observed in ARPES measurements inclined the direct character of the fundamental band gap. The slightly different optical behavior of the four representatives of MX family results from the relative position of valence and conduction band valleys varying depending on the chemical composition, as illustrated in Fig. 1.6. For GeS, the valley in the Γ point plays the role of VBM, while for GeSe valence band in this region of the BZ is pushed towards higher binding energies and VBM is located close to the X point. The effect is even stronger for SnS and SnSe, also featuring VBM close to the X point. Both Ge chalcogenides are characterized with CBM in the Γ point, while for SnX crystals, a valley in the Γ-X path is energetically the lowest.

The optical characterization of SnS_2 and $SnSe_2$ crystals revealed a similar effect of domination of the optical absorption spectra by direct optical transitions despite indirect fundamental band gap, however, the explanation of the phenomenon is quite different. The energy distance between the indirect and direct band gap is in this case considerable, and the fundamental absorption edge could not be detected due to the Burstein-Moss effect and very low probability of the transitions involving lowest CB states (within the *split-off*) band, indicated by vanishing matrix element in-plane components.

Further investigation and analysis of the obtained results lead to determination of possible applications of MX and MX_2 crystals Among various optoelectronic applications, most promising is polarization-sensitive photodetection, for which MXs are perfect candidates due to intrinsic linear dichroism of the optical response. Such technology is exploited for detection of light polarization changes after traveling through a birefringent medium, including various solids and liquid crystals,

but also biological systems such as protein solutions. The state-of-the-art polarization detectors are complex devices composed of multiple optical elements, therefore materials with intrinsic polarization sensitivity are extremally desired. Another potential application of MXs (especially tin compounds) is the thermoelectric conversion, more and more important in the era of growing energy demand. Low thermal conductivity combined with multivalley character of the electronic band structure lead to high thermoelectric figure of merit, for SnSe shown to exceed the value of typical Pb-based materials exploited in this branch of technology. In the case of MX_2 crystals, the most distinctive feature is the high concentration of native defects active as intrinsic dopants. The property can be utilized in various technologies, with photocatalysis and gas sensing attracting the most attention, where surface defects act as reactive and adsorptive sites.

Application opportunities can be further broadened by combining MX and MX_2 crystals with each other and with different van der Waals semiconductors to form heterostructures. Especially the intrinsic *p*-type and *n*-type character of MX and MX_2 materials, respectively, can be exploited in the design of *p*-*n* heterojunctions. For heterostructures and electrical contacts engineering determination of parameters such as work function, ionization potential, and electron affinity is crucial, as it allows to simulate band alignment with other materials and predict Ohmic or Schottky character of contacts with different metals. In this thesis, such characterization was performed by means of photoemission spectroscopy.

The study contributes to the general understanding of the fundamental properties of MX and MX_2 and phenomena involving interaction with light. The obtained results point toward the most promising future applications, which are polarization-sensitive optoelectronics and thermoelectric conversion.

Bibliography

(1) Novoselov, K. S.; Geim, A. K.; Morozov, S. V.; Jiang, D.; Zhang, Y.; Dubonos, S. V.; Grigorieva, I. V.; Firsov, A. A. Electric Field Effect in Atomically Thin Carbon Films. *Science* **2004**, *306* (5696), 666–669. https://doi.org/10.1126/science.1102896.

(2) Moore, G. E. Progress in Digital Integrated Electronics; IEEE, 1975; pp 11–13.

(3) Karl Rupp. Microprocessor Trend Data – Processed by Our World in Data, 2022. https://ourworldindata.org/grapher/transistors-per-microprocessor.

(4) Novoselov, K. S.; Mishchenko, A.; Carvalho, A.; Neto, A. H. C. 2D Materials and van Der Waals Heterostructures. *Science* **2016**, *353* (6298), aac9439. https://doi.org/10.1126/science.aac9439.

(5) Manzeli, S.; Ovchinnikov, D.; Pasquier, D.; Yazyev, O. V.; Kis, A. 2D Transition Metal Dichalcogenides. *Nat. Rev. Mater.* **2017**, *2* (8), 1–15. https://doi.org/10.1038/natrevmats.2017.33.

(6) Hsueh, H.-C.; Li, J.-X.; Ho, C.-H. Polarization Photoelectric Conversion in Layered GeS. *Adv. Opt. Mater.* **2018**, *6* (4), 1701194. https://doi.org/10.1002/adom.201701194.

(7) Liu, C.; Zheng, T.; Shu, K.; Shu, S.; Lan, Z.; Yang, M.; Zheng, Z.; Huo, N.; Gao, W.; Li, J. Polarization-Sensitive Self-Powered Schottky Photodetector with High Photovoltaic Performance Induced by Geometry-Asymmetric Contacts. *ACS Appl. Mater. Interfaces* **2024**, *16* (11), 13914–13926. https://doi.org/10.1021/acsami.3c16047.

(8) Tołłoczko, A.; Zelewski, S. J.; Błaszczak, M.; Woźniak, T.; Siudzińska, A.; Bachmatiuk, A.; Scharoch, P.; Kudrawiec, R. Optical Properties of Orthorhombic Germanium Selenide: An Anisotropic Layered Semiconductor Promising for Optoelectronic Applications. *J. Mater. Chem. C* **2021**, *9* (41), 14838–14847. https://doi.org/10.1039/D1TC04280G.

(9) Taylor, E. W.; Cramer, W. Birefringence of Protein Solutions and Biological Systems. *Biophys. J.* **1963**, *3* (2), 143–154.

(10) Khandelwal, A.; Mani, K.; Karigerasi, M. H.; Lahiri, I. Phosphorene – The Two-Dimensional Black Phosphorous: Properties, Synthesis and Applications. *Mater. Sci. Eng. B* **2017**, *221*, 17–34. https://doi.org/10.1016/j.mseb.2017.03.011.

(11) Gomes, L. C.; Carvalho, A. Phosphorene Analogues: Isoelectronic Two-Dimensional Group-IV Monochalcogenides with Orthorhombic Structure. *Phys. Rev. B* **2015**, *92* (8), 085406. https://doi.org/10.1103/PhysRevB.92.085406.

(12) Das, S.; Pandey, D.; Thomas, J.; Roy, T. The Role of Graphene and Other 2D Materials in Solar Photovoltaics. *Adv. Mater.* **2019**, *31* (1), 1802722. https://doi.org/10.1002/adma.201802722.

(13) Molaei, M. J. Light-Emitting Diodes Based on Van Der Waals Heterostructures: A Review. *Iran. J. Mater. Sci. Eng.* **2023**, *20* (2), 1–24. https://doi.org/10.22068/ijmse.3019.

(14) Kim, S.; Kim, M.; Kim, H. Self-Powered Photodetectors Based on Two-Dimensional van Der Waals Semiconductors. *Nano Energy* **2024**, *127*, 109725. https://doi.org/10.1016/j.nanoen.2024.109725.

(15) Wang, F.; Zhang, T.; Xie, R.; Liu, A.; Dai, F.; Chen, Y.; Xu, T.; Wang, H.; Wang, Z.; Liao, L.; Wang, J.; Zhou, P.; Hu, W. Next-Generation Photodetectors beyond Van Der Waals Junctions. *Adv. Mater.* **2024**, *36* (3), 2301197. https://doi.org/10.1002/adma.202301197.

(16) Aftab, S.; Hegazy, H. H.; Iqbal, M. Z.; Rim, Y. S. Emerging Trends in van Der Waals 2D TMD Heterojunction Bipolar Transistors. *J. Mater. Chem. C* **2023**, *11* (5), 1648–1667. https://doi.org/10.1039/D2TC04108A.

(17) Xia, F.; Wang, H.; Xiao, D.; Dubey, M.; Ramasubramaniam, A. Two-Dimensional Material Nanophotonics. *Nat. Photonics* **2014**, *8* (12), 899–907. https://doi.org/10.1038/nphoton.2014.271.

(18) Autere, A.; Jussila, H.; Dai, Y.; Wang, Y.; Lipsanen, H.; Sun, Z. Nonlinear Optics with 2D Layered Materials. *Adv. Mater.* **2018**, *30* (24), 1705963. https://doi.org/10.1002/adma.201705963.

(19) Yang, H. R.; Liu, X. M. Nonlinear Optical Response and Applications of Tin Disulfide in the Near- and Mid-Infrared. *Appl. Phys. Lett.* **2017**, *110* (17), 171106. https://doi.org/10.1063/1.4982624.

(20) Panday, S. R.; Fregoso, B. M. Strong Second Harmonic Generation in Two-Dimensional Ferroelectric IV-Monochalcogenides. *J. Phys. Condens. Matter* **2017**, *29* (43), 43LT01. https://doi.org/10.1088/1361-648X/aa8bfc.

(21) Moqbel, R.; Chang, Y.-R.; Li, Z.-Y.; Kung, S.-H.; Cheng, H.-Y.; Lee, C.-C.; Nagashio, K.; Lin, K.-H. Wavelength Dependence of Polarization-Resolved Second Harmonic Generation from Ferroelectric SnS Few Layers. *2D Mater.* **2022**, *10* (1), 015022. https://doi.org/10.1088/2053-1583/acab74.

(22) Zhao, L.-D.; Lo, S.-H.; Zhang, Y.; Sun, H.; Tan, G.; Uher, C.; Wolverton, C.; Dravid, V. P.; Kanatzidis, M. G. Ultralow Thermal Conductivity and High Thermoelectric Figure of Merit in SnSe Crystals. *Nature* **2014**, *508* (7496), 373–377. https://doi.org/10.1038/nature13184.

(23) Ding, G.; Gao, G.; Yao, K. High-Efficient Thermoelectric Materials: The Case of Orthorhombic IV-VI Compounds. *Sci. Rep.* **2015**, *5* (1), 9567. https://doi.org/10.1038/srep09567.

(24) Kaur, K.; Khandy, S. A.; Dhiman, S.; Sharopov, U. B.; Singh, J. Computational Prediction of Thermoelectric Properties of 2D Materials. *Electron. Struct.* **2022**, *4* (2), 023001. https://doi.org/10.1088/2516-1075/ac635b.

(25) Li, D.; Gong, Y.; Chen, Y.; Lin, J.; Khan, Q.; Zhang, Y.; Li, Y.; Zhang, H.; Xie, H. Recent Progress of Two-Dimensional Thermoelectric Materials. *Nano-Micro Lett.* **2020**, *12* (1), 36. https://doi.org/10.1007/s40820-020-0374-x.

(26) Samanta, M.; Ghosh, T.; Chandra, S.; Biswas, K. Layered Materials with 2D Connectivity for Thermoelectric Energy Conversion. *J. Mater. Chem. A* **2020**, *8* (25), 12226–12261. https://doi.org/10.1039/D0TA00240B.

(27) Gan, X.; Lei, D.; Wong, K.-Y. Two-Dimensional Layered Nanomaterials for Visible-Light-Driven Photocatalytic Water Splitting. *Mater. Today Energy* **2018**, *10*, 352–367. https://doi.org/10.1016/j.mtener.2018.10.015.

(28) Guo, S.-Q.; Yang, B.; Hu, Z.; Zhen, M.; Gu, B.; Shen, B. Uncovering Mechanism of Photocatalytic Performance Enhancement Induced by Multivariate Defects on SnS2. *Nano Res.* **2023**, *16* (2), 2102–2110. https://doi.org/10.1007/s12274-022-4926-x.

(29) Li, X.; Zuo, X.; Jiang, X.; Li, D.; Cui, B.; Liu, D. Enhanced Photocatalysis for Water Splitting in Layered Tin Chalcogenides with High Carrier Mobility. *Phys. Chem. Chem. Phys.* **2019**, *21* (14), 7559–7566. https://doi.org/10.1039/C9CP00088G.

(30) Fei, R.; Li, W.; Li, J.; Yang, L. Giant Piezoelectricity of Monolayer Group IV Monochalcogenides: SnSe, SnS, GeSe, and GeS. *Appl. Phys. Lett.* **2015**, *107* (17), 173104. https://doi.org/10.1063/1.4934750.

(31) A. Nikitina, A.; V. Lavrentev, F.; Yu. Yurova, V.; Yu. Piarnits, D.; O. Volkova, O.; V. Skorb, E.; G. Shchukin, D. Layered Nanomaterials for Renewable Energy Generation and Storage. *Mater. Adv.* **2024**, *5* (2), 394–408. https://doi.org/10.1039/D3MA00924F.

(32) Zhang, Y.; Zheng, Y.; Rui, K.; Hng, H. H.; Hippalgaonkar, K.; Xu, J.; Sun, W.; Zhu, J.; Yan, Q.; Huang, W. 2D Black Phosphorus for Energy Storage and Thermoelectric Applications. *Small* **2017**, *13* (28), 1700661. https://doi.org/10.1002/smll.201700661.

(33) He, Y.; Shen, X.; Zhang, Y. Layered 2D Materials in Batteries. *ACS Appl. Nano Mater.* **2024**. https://doi.org/10.1021/acsanm.3c06242.

(34) Zhang, C.; Huang, J.; Zhai, K.; Akhtari, K.; Shen, Z.; Ao, L.; Li, Z.; Qin, F.; Chang, Y.; Zhou, L.; Tang, M.; Dai, X.; Qiu, C.; Zhang, Y.; Wang, L.; Liu, Z.; Tian, Y.; Bahramy, M. S.; Yuan, H. Valence-Skipping and Quasi-Two-Dimensionality of Superconductivity in a van Der Waals Insulator. *Nat. Commun.* **2022**, *13* (1), 6938. https://doi.org/10.1038/s41467-022-34726-3.

(35) Cao, Y.; Fatemi, V.; Fang, S.; Watanabe, K.; Taniguchi, T.; Kaxiras, E.; Jarillo-Herrero, P. Unconventional Superconductivity in Magic-Angle Graphene Superlattices. *Nature* **2018**, *556* (7699), 43–50. https://doi.org/10.1038/nature26160.

(36) Oh, M.; Nuckolls, K. P.; Wong, D.; Lee, R. L.; Liu, X.; Watanabe, K.; Taniguchi, T.; Yazdani, A. Evidence for Unconventional Superconductivity in Twisted Bilayer Graphene. *Nature* **2021**, *600* (7888), 240–245. https://doi.org/10.1038/s41586-021-04121-x.

(37) Hu, C.; Gordon, K. N.; Liu, P.; Liu, J.; Zhou, X.; Hao, P.; Narayan, D.; Emmanouilidou, E.; Sun, H.; Liu, Y.; Brawer, H.; Ramirez, A. P.; Ding, L.; Cao, H.; Liu, Q.; Dessau, D.; Ni, N. A van Der Waals Antiferromagnetic Topological Insulator with Weak Interlayer Magnetic Coupling. *Nat. Commun.* **2020**, *11* (1), 97. https://doi.org/10.1038/s41467-019-13814-x.

(38) Lahoud, E.; Maniv, E.; Petrushevsky, M. S.; Naamneh, M.; Ribak, A.; Wiedmann, S.; Petaccia, L.; Salman, Z.; Chashka, K. B.; Dagan, Y.; Kanigel, A. Evolution of the Fermi Surface of a Doped Topological Insulator with Carrier Concentration. *Phys. Rev. B* **2013**, *88* (19), 195107. https://doi.org/10.1103/PhysRevB.88.195107.

(39) Geim, A. K.; Novoselov, K. S. The Rise of Graphene. *Nat. Mater.* **2007**, *6* (3), 183–191. https://doi.org/10.1038/nmat1849.

(40) Bolotin, K. I.; Sikes, K. J.; Jiang, Z.; Klima, M.; Fudenberg, G.; Hone, J.; Kim, P.; Stormer, H. L. Ultrahigh Electron Mobility in Suspended Graphene. *Solid State Commun.* **2008**, *146* (9), 351–355. https://doi.org/10.1016/j.ssc.2008.02.024.

(41) Chen, J.-H.; Jang, C.; Xiao, S.; Ishigami, M.; Fuhrer, M. S. Intrinsic and Extrinsic Performance Limits of Graphene Devices on SiO_2. *Nat. Nanotechnol.* **2008**, *3* (4), 206–209. https://doi.org/10.1038/nnano.2008.58.

(42) Chapter 5 - Bandstructure and Related Properties. In *Semiconductors and Semimetals*; Jain, S. C., Willander, M., Eds.; Silicon-Germanium Strained Layers and Heterostructures; Elsevier, 2003; Vol. 74, pp 91–145. https://doi.org/10.1016/S0080-8784(03)80018-2.

(43) Castro Neto, A. H.; Guinea, F.; Peres, N. M. R.; Novoselov, K. S.; Geim, A. K. The Electronic Properties of Graphene. *Rev. Mod. Phys.* **2009**, *81* (1), 109–162. https://doi.org/10.1103/RevModPhys.81.109.

(44) Kuc, A. Low-Dimensional Transition-Metal Dichalcogenides.

(45) Splendiani, A.; Sun, L.; Zhang, Y.; Li, T.; Kim, J.; Chim, C.-Y.; Galli, G.; Wang, F. Emerging Photoluminescence in Monolayer MoS2. *Nano Lett.* **2010**, *10* (4), 1271–1275. https://doi.org/10.1021/nl903868w.

(46) Chhowalla, M.; Shin, H. S.; Eda, G.; Li, L.-J.; Loh, K. P.; Zhang, H. The Chemistry of Two-Dimensional Layered Transition Metal Dichalcogenide Nanosheets. *Nat. Chem.* **2013**, *5* (4), 263–275. https://doi.org/10.1038/nchem.1589.

(47) Park, S.; Mutz, N.; Schultz, T.; Blumstengel, S.; Han, A.; Aljarb, A.; Li, L.-J.; List-Kratochvil, E. J. W.; Amsalem, P.; Koch, N. Direct Determination of Monolayer MoS2 and WSe2 Exciton Binding Energies on Insulating and Metallic Substrates. *2D Mater.* **2018**, *5* (2), 025003. https://doi.org/10.1088/2053-1583/aaa4ca.

(48) Mak, K. F.; He, K.; Shan, J.; Heinz, T. F. Control of Valley Polarization in Monolayer MoS2 by Optical Helicity. *Nat. Nanotechnol.* **2012**, *7* (8), 494–498. https://doi.org/10.1038/nnano.2012.96.

(49) Zeng, H.; Dai, J.; Yao, W.; Xiao, D.; Cui, X. Valley Polarization in MoS2 Monolayers by Optical Pumping. *Nat. Nanotechnol.* **2012**, *7* (8), 490–493. https://doi.org/10.1038/nnano.2012.95.

(50) Xu, X.; Yao, W.; Xiao, D.; Heinz, T. F. Spin and Pseudospins in Layered Transition Metal Dichalcogenides. *Nat. Phys.* **2014**, *10* (5), 343–350. https://doi.org/10.1038/nphys2942.

(51) Radisavljevic, B.; Radenovic, A.; Brivio, J.; Giacometti, V.; Kis, A. Single-Layer MoS2 Transistors. *Nat. Nanotechnol.* **2011**, *6* (3), 147–150. https://doi.org/10.1038/nnano.2010.279.

(52) Castellanos-Gomez, A. Black Phosphorus: Narrow Gap, Wide Applications. *J. Phys. Chem. Lett.* **2015**, *6* (21), 4280–4291. https://doi.org/10.1021/acs.jpclett.5b01686.

(53) Wei, Q.; Peng, X. Superior Mechanical Flexibility of Phosphorene and Few-Layer Black Phosphorus. *Appl. Phys. Lett.* **2014**, *104* (25), 251915. https://doi.org/10.1063/1.4885215.

(54) Ling, X.; Wang, H.; Huang, S.; Xia, F.; Dresselhaus, M. S. The Renaissance of Black Phosphorus. *Proc. Natl. Acad. Sci.* **2015**, *112* (15), 4523–4530. https://doi.org/10.1073/pnas.1416581112.

(55) Qiao, J.; Kong, X.; Hu, Z.-X.; Yang, F.; Ji, W. High-Mobility Transport Anisotropy and Linear Dichroism in Few-Layer Black Phosphorus. *Nat. Commun.* **2014**, *5*, 4475. https://doi.org/10.1038/ncomms5475.

(56) Wu, S.; Chen, Y.; Wang, X.; Jiao, H.; Zhao, Q.; Huang, X.; Tai, X.; Zhou, Y.; Chen, H.; Wang, X.; Huang, S.; Yan, H.; Lin, T.; Shen, H.; Hu, W.; Meng, X.; Chu, J.; Wang, J. Ultra-Sensitive Polarization-Resolved Black Phosphorus Homojunction Photodetector Defined by Ferroelectric Domains. *Nat. Commun.* **2022**, *13* (1), 3198. https://doi.org/10.1038/s41467-022-30951-y.

(57) Yuan, H.; Liu, X.; Afshinmanesh, F.; Li, W.; Xu, G.; Sun, J.; Lian, B.; Curto, A. G.; Ye, G.; Hikita, Y.; Shen, Z.; Zhang, S.-C.; Chen, X.; Brongersma, M.; Hwang, H. Y.; Cui, Y. Polarization-Sensitive Broadband Photodetector Using a Black Phosphorus Vertical p–n Junction. *Nat. Nanotechnol.* **2015**, *10* (8), 707–713. https://doi.org/10.1038/nnano.2015.112.

(58) Liang, L.; Wang, J.; Lin, W.; Sumpter, B. G.; Meunier, V.; Pan, M. Electronic Bandgap and Edge Reconstruction in Phosphorene Materials. *Nano Lett.* **2014**, *14* (11), 6400–6406. https://doi.org/10.1021/nl502892t.

(59) Morita, A. Semiconducting Black Phosphorus. *Appl. Phys. A* **1986**, *39* (4), 227–242. https://doi.org/10.1007/BF00617267.

(60) Warschauer, D. Electrical and Optical Properties of Crystalline Black Phosphorus. *J. Appl. Phys.* **1963**, *34* (7), 1853–1860. https://doi.org/10.1063/1.1729699.

(61) Akahama, Y.; Endo, S.; Narita, S. Electrical Properties of Black Phosphorus Single Crystals. *J. Phys. Soc. Jpn.* **1983**, *52* (6), 2148–2155. https://doi.org/10.1143/JPSJ.52.2148.

(62) He, D.; Wang, Y.; Huang, Y.; Shi, Y.; Wang, X.; Duan, X. High-Performance Black Phosphorus Field-Effect Transistors with Long-Term Air Stability. *Nano Lett.* **2019**, *19* (1), 331–337. https://doi.org/10.1021/acs.nanolett.8b03940.

(63) Li, L.; Yu, Y.; Ye, G. J.; Ge, Q.; Ou, X.; Wu, H.; Feng, D.; Chen, X. H.; Zhang, Y. Black Phosphorus Field-Effect Transistors. *Nat. Nanotechnol.* **2014**, *9* (5), 372–377. https://doi.org/10.1038/nnano.2014.35.

(64) Kulish, V. V.; Malyi, O. I.; Persson, C.; Wu, P. Adsorption of Metal Adatoms on Single-Layer Phosphorene. *Phys. Chem. Chem. Phys.* **2014**, *17* (2), 992–1000. https://doi.org/10.1039/C4CP03890H.

(65) Wang, H. Bridging the Gap - Rediscovering Black Phosphorus As an Anisotropic Layered Material for Electronics and Optoelectronics. *ECS Meet. Abstr.* **2015**, *MA2015-02* (33), 1212. https://doi.org/10.1149/MA2015-02/33/1212.

(66) Li, Q.; Zhou, Q.; Shi, L.; Chen, Q.; Wang, J. Recent Advances in Oxidation and Degradation Mechanisms of Ultrathin 2D Materials under Ambient Conditions and Their Passivation Strategies. *J. Mater. Chem. A* **2019**, *7* (9), 4291–4312. https://doi.org/10.1039/C8TA10306B.

(67) Kim, M.; Kim, H.; Park, S.; Kim, J. S.; Choi, H. J.; Im, S.; Lee, H.; Kim, T.; Yi, Y. Intrinsic Correlation between Electronic Structure and Degradation: From Few-Layer to Bulk Black Phosphorus. *Angew. Chem. Int. Ed.* **2019**, *58* (12), 3754–3758. https://doi.org/10.1002/anie.201811743.

(68) Island, J. O.; Steele, G. A.; Zant, H. S. J. van der; Castellanos-Gomez, A. Environmental Instability of Few-Layer Black Phosphorus. *2D Mater.* **2015**, *2* (1), 011002. https://doi.org/10.1088/2053-1583/2/1/011002.

(69) Arora, H.; Fekri, Z.; Vekariya, Y. N.; Chava, P.; Watanabe, K.; Taniguchi, T.; Helm, M.; Erbe, A. Fully Encapsulated and Stable Black Phosphorus Field-Effect Transistors. *Adv. Mater. Technol.* **2023**, *8* (2), 2200546. https://doi.org/10.1002/admt.202200546.

(70) Mohsseni Ahangar, R.; Farmanzadeh, D. Effects of Hexagonal Boron Nitride Encapsulation on the Electronic Properties of Cu, Li, and O-Doped Black Phosphorus Monolayer. *Phys. B Condens. Matter* **2023**, *660*, 414880. https://doi.org/10.1016/j.physb.2023.414880.

(71) Birowska, M.; Urban, J.; Baranowski, M.; Maude, D. K.; Plochocka, P.; Szwacki, N. G. The Impact of Hexagonal Boron Nitride Encapsulation on the Structural and Vibrational Properties of Few Layer Black Phosphorus. *Nanotechnology* **2019**, *30* (19), 195201. https://doi.org/10.1088/1361-6528/ab0332.

(72) Guo, Y.; Zhou, S.; Bai, Y.; Zhao, J. Oxidation Resistance of Monolayer Group-IV Monochalcogenides. *ACS Appl. Mater. Interfaces* **2017**, *9* (13), 12013–12020. https://doi.org/10.1021/acsami.6b16786.

(73) May, A. F.; Yan, J.; McGuire, M. A. A Practical Guide for Crystal Growth of van Der Waals Layered Materials. *J. Appl. Phys.* **2020**, *128* (5), 051101. https://doi.org/10.1063/5.0015971.

(74) Cai, M.; Thorpe, D.; Adamson, D.; Schniepp, H. Methods of Graphite Exfoliation. *J Mater Chem* **2012**, *22*, 24992–25002. https://doi.org/10.1039/C2JM34517J.

(75) Li, Y.; Kuang, G.; Jiao, Z.; Yao, L.; Duan, R. Recent Progress on the Mechanical Exfoliation of 2D Transition Metal Dichalcogenides. *Mater. Res. Express* **2022**, *9* (12), 122001. https://doi.org/10.1088/2053-1591/aca6c6.

(76) Huo, C.; Yan, Z.; Song, X.; Zeng, H. 2D Materials via Liquid Exfoliation: A Review on Fabrication and Applications. *Sci. Bull.* **2015**, *60* (23), 1994–2008. https://doi.org/10.1007/s11434-015-0936-3.

(77) Pacuski, W.; Grzeszczyk, M.; Nogajewski, K.; Bogucki, A.; Oreszczuk, K.; Kucharek, J.; Połczyńska, K. E.; Seredyński, B.; Rodek, A.; Bożek, R.; Taniguchi, T.; Watanabe, K.; Kret, S.; Sadowski, J.; Kazimierczuk, T.; Potemski, M.; Kossacki, P. Narrow Excitonic Lines and Large-Scale Homogeneity of Transition-Metal Dichalcogenide Monolayers Grown by Molecular Beam Epitaxy on Hexagonal Boron Nitride. *Nano Lett.* **2020**, *20* (5), 3058–3066. https://doi.org/10.1021/acs.nanolett.9b04998.

(78) Aras, F. G.; Yilmaz, A.; Tasdelen, H. G.; Ozden, A.; Ay, F.; Perkgoz, N. K.; Yeltik, A. A Review on Recent Advances of Chemical Vapor Deposition Technique for Monolayer Transition Metal Dichalcogenides (MX2: Mo, W; S, Se, Te). *Mater. Sci. Semicond. Process.* **2022**, *148*, 106829. https://doi.org/10.1016/j.mssp.2022.106829.

(79) Wang, J.; Li, T.; Wang, Q.; Wang, W.; Shi, R.; Wang, N.; Amini, A.; Cheng, C. Controlled Growth of Atomically Thin Transition Metal Dichalcogenides via Chemical Vapor Deposition Method. *Mater. Today Adv.* **2020**, *8*, 100098. https://doi.org/10.1016/j.mtadv.2020.100098.

(80) H. Hill, E. Layered 2D Material Heterostructures – a Colloidal Perspective. *J. Mater. Chem. C* **2024**, *12* (30), 11285–11318. https://doi.org/10.1039/D4TC01102C.

(81) Vaughn, D. D.; Patel, R. J.; Hickner, M. A.; Schaak, R. E. Single-Crystal Colloidal Nanosheets of GeS and GeSe. *J. Am. Chem. Soc.* **2010**, *132* (43), 15170–15172. https://doi.org/10.1021/ja107520b.

(82) Zhong, Y.; Zhang, L.; Chen, W.; Zhu, H. Macro van Der Waals P-n Heterojunction Based on SnSe and SnSe2. *Nanotechnology* **2020**, *31* (38), 385203. https://doi.org/10.1088/1361-6528/ab9a77.

(83) Aretouli, K. E.; Tsoutsou, D.; Tsipas, P.; Marquez-Velasco, J.; Aminalragia Giamini, S.; Kelaidis, N.; Psycharis, V.; Dimoulas, A. Epitaxial 2D SnSe2/ 2D WSe2 van Der Waals Heterostructures. *ACS Appl. Mater. Interfaces* **2016**, *8* (35), 23222–23229. https://doi.org/10.1021/acsami.6b02933.

(84) Dean, C. R.; Wang, L.; Maher, P.; Forsythe, C.; Ghahari, F.; Gao, Y.; Katoch, J.; Ishigami, M.; Moon, P.; Koshino, M.; Taniguchi, T.; Watanabe, K.; Shepard, K. L.; Hone, J.; Kim, P. Hofstadter's Butterfly and the Fractal Quantum Hall Effect in Moiré Superlattices. *Nature* **2013**, *497* (7451), 598–602. https://doi.org/10.1038/nature12186.

(85) Devakul, T.; Crépel, V.; Zhang, Y.; Fu, L. Magic in Twisted Transition Metal Dichalcogenide Bilayers. *Nat. Commun.* **2021**, *12* (1), 6730. https://doi.org/10.1038/s41467-021-27042-9.

(86) Tran, K.; Moody, G.; Wu, F.; Lu, X.; Choi, J.; Kim, K.; Rai, A.; Sanchez, D. A.; Quan, J.; Singh, A.; Embley, J.; Zepeda, A.; Campbell, M.; Autry, T.; Taniguchi, T.; Watanabe, K.; Lu, N.; Banerjee, S. K.; Silverman, K. L.; Kim,

S.; Tutuc, E.; Yang, L.; MacDonald, A. H.; Li, X. Evidence for Moiré Excitons in van Der Waals Heterostructures. *Nature* **2019**, *567*(7746), 71–75. https://doi.org/10.1038/s41586-019-0975-z.

(87) Tołłoczko, A. K.; Zelewski, S. J.; Ziembicki, J.; Olszowska, N.; Rosmus, M.; Woźniak, T.; Tongay, S.; Kudrawiec, R. Photoemission Study of the Thermoelectric Group IV-VI van Der Waals Crystals (GeS, SnS, and SnSe). *Adv. Opt. Mater.* **2024**, *12*(6), 2302049. https://doi.org/10.1002/adom.202302049.

(88) Wiedemeier, H.; Georg von Schnering, H. Refinement of the Structures of GeS, GeSe, SnS and SnSe. *Z. Krist.* **1978**, *148*. https://doi.org/10.1524/zkri.1978.148.3-4.295.

(89) Chen, Z.; Hwang, W.; Cho, M.; Hoang, A. T.; Kim, M.; Kim, D.; Kim, D. H.; Kim, Y. D.; Kim, H. J.; Ahn, J.-H.; Soon, A.; Choi, H.-J. In-Plane Optical and Electrical Anisotropy in Low-Symmetry Layered GeS Microribbons. *NPG Asia Mater.* **2022**, *14*(1), 1–11. https://doi.org/10.1038/s41427-022-00390-8.

(90) Le, V. L.; Cuong, D. D.; Nguyen, H. T.; Nguyen, X. A.; Kim, B.; Kim, K.; Lee, W.; Hong, S. C.; Kim, T. J.; Kim, Y. D. Anisotropic Behavior of Excitons in Single-Crystal α-SnS. *AIP Adv.* **2020**, *10* (10), 105003. https://doi.org/10.1063/5.0021690.

(91) Tan, D.; Lim, H. E.; Wang, F.; Mohamed, N. B.; Mouri, S.; Zhang, W.; Miyauchi, Y.; Ohfuchi, M.; Matsuda, K. Anisotropic Optical and Electronic Properties of Two-Dimensional Layered Germanium Sulfide. *Nano Res.* **2017**, *10*(2), 546–555. https://doi.org/10.1007/s12274-016-1312-6.

(92) Dasgupta, A.; Gao, J.; Yang, X. Anisotropic Third-Harmonic Generation in Layered Germanium Selenide. *Laser Photonics Rev.* **2020**, *14*(6), 1900416. https://doi.org/10.1002/lpor.201900416.

(93) Guo, R.; Wang, X.; Kuang, Y.; Huang, B. First-Principles Study of Anisotropic Thermoelectric Transport Properties of IV-VI Semiconductor Compounds SnSe and SnS. *Phys. Rev. B* **2015**, *92* (11), 115202. https://doi.org/10.1103/PhysRevB.92.115202.

(94) Li, A.; Hu, C.; He, B.; Yao, M.; Fu, C.; Wang, Y.; Zhao, X.; Felser, C.; Zhu, T. Demonstration of Valley Anisotropy Utilized to Enhance the Thermoelectric Power Factor. *Nat. Commun.* **2021**, *12* (1), 5408. https://doi.org/10.1038/s41467-021-25722-0.

(95) Liu, J.; Pantelides, S. T. Anisotropic Thermal Expansion of Group-IV Monochalcogenide Monolayers. *Appl. Phys. Express* **2018**, *11*(10), 101301. https://doi.org/10.7567/APEX.11.101301.

(96) Qin, G.; Qin, Z.; Fang, W.-Z.; Zhang, L.-C.; Yue, S.-Y.; Yan, Q.-B.; Hu, M.; Su, G. Diverse Anisotropy of Phonon Transport in Two-Dimensional Group IV–VI Compounds: A Comparative Study. *Nanoscale* **2016**, *8* (21), 11306–11319. https://doi.org/10.1039/C6NR01349J.

(97) Lebedev, A. I. Ferroelectricity and Piezoelectricity in Monolayers and Nanoplatelets of SnS. *J. Appl. Phys.* **2018**, *124*(16), 164302. https://doi.org/10.1063/1.5035419.

(98) Zhu, M.; Zhong, M.; Guo, X.; Wang, Y.; Chen, Z.; Huang, H.; He, J.; Su, C.; Loh, K. P. Efficient and Anisotropic Second Harmonic Generation in Few-Layer SnS Film. *Adv. Opt. Mater.* **2021**, *9* (22), 2101200. https://doi.org/10.1002/adom.202101200.

(99) Siddique, S.; Gong, Y.; Abbas, G.; Yaqoob, M. M.; Li, S.; Zulkifal, S.; Zhang, Q.; Hou, Y.; Chen, G.; Tang, G. Realizing High Thermoelectric Performance in P-Type SnSe Crystals via Convergence of Multiple Electronic Valence Bands. *ACS Appl. Mater. Interfaces* **2022**, *14*(3), 4091–4099. https://doi.org/10.1021/acsami.1c20549.

(100) Wang, C. W.; Xia, Y. Y. Y.; Tian, Z.; Jiang, J.; Li, B. H.; Cui, S. T.; Yang, H. F.; Liang, A. J.; Zhan, X. Y.; Hong, G. H.; Liu, S.; Chen, C.; Wang, M. X.; Yang, L. X.; Liu, Z.; Mi, Q. X.; Li, G.; Xue, J. M.; Liu, Z. K.; Chen, Y. L. Photoemission Study of the Electronic Structure of Valence Band Convergent SnSe. *Phys. Rev. B* **2017**, *96*(16), 165118. https://doi.org/10.1103/PhysRevB.96.165118.

(101) Murgatroyd, P. A. E.; Smiles, M. J.; Savory, C. N.; Shalvey, T. P.; Swallow, J. E. N.; Fleck, N.; Robertson, C. M.; Jäckel, F.; Alaria, J.; Major, J. D.; Scanlon, D. O.; Veal, T. D. GeSe: Optical Spectroscopy and Theoretical Study of a van Der Waals Solar Absorber. *Chem. Mater.* **2020**. https://doi.org/10.1021/acs.chemmater.0c00453.

(102) Tołłoczko, A. K.; Ziembicki, J.; Grodzicki, M.; Serafińczuk, J.; Tongay, S. A.; Erdi, M.; Olszowska, N.; Rosmus, M.; Kudrawiec, R. Linear Dichroism of the Optical Properties of SnS and SnSe van Der Waals Crystals. arXiv September 25, 2024. https://doi.org/10.48550/arXiv.2409.17412.

(103) Jones, L. A. H.; Linhart, W. M.; Fleck, N.; Swallow, J. E. N.; Murgatroyd, P. A. E.; Shiel, H.; Featherstone, T. J.; Smiles, M. J.; Thakur, P. K.; Lee, T.-L.; Hardwick, L. J.; Alaria, J.; Jäckel, F.; Kudrawiec, R.; Burton, L. A.; Walsh, A.; Skelton, J. M.; Veal, T. D.; Dhanak, V. R. Sn $5{s}^{2}$ Lone Pairs and the Electronic Structure of Tin Sulphides: A Photoreflectance, High-Energy Photoemission, and Theoretical Investigation. *Phys. Rev. Mater.* **2020**, *4* (7), 074602. https://doi.org/10.1103/PhysRevMaterials.4.074602.

(104) Smiles, M. J.; Skelton, J. M.; Shiel, H.; Jones, L. A. H.; Swallow, J. E. N.; Edwards, H. J.; Murgatroyd, P. A. E.; Featherstone, T. J.; Thakur, P. K.; Lee, T.-L.; Dhanak, V. R.; Veal, T. D. Ge 4s2 Lone Pairs and Band Alignments in GeS and GeSe for Photovoltaics. *J. Mater. Chem. A* **2021**, *9* (39), 22440–22452. https://doi.org/10.1039/D1TA05955F.

(105) Whittles, T. J.; Burton, L. A.; Skelton, J. M.; Walsh, A.; Veal, T. D.; Dhanak, V. R. Band Alignments, Valence Bands, and Core Levels in the Tin Sulfides SnS, SnS2, and Sn2S3: Experiment and Theory. *Chem. Mater.* **2016**, *28* (11), 3718–3726. https://doi.org/10.1021/acs.chemmater.6b00397.

(106) Grodzicki, M.; Tołłoczko, A. K.; Majchrzak, D.; Hommel, D.; Kudrawiec, R. Band Alignments of GeS and GeSe Materials. *Crystals* **2022**, *12* (10), 1492. https://doi.org/10.3390/cryst12101492.

(107) Suzuki, I.; Kawanishi, S.; Tanaka, K.; Omata, T.; Tanaka, S. Contribution of the Sn 5s State to the SnS Valence Band: Direct Observation via ARPES Measurements. *Electron. Struct.* **2022**, *4* (2), 025004. https://doi.org/10.1088/2516-1075/ac6ea8.

(108) Walsh, A.; Payne, D. J.; Egdell, R. G.; Watson, G. W. Stereochemistry of Post-Transition Metal Oxides: Revision of the Classical Lone Pair Model. *Chem. Soc. Rev.* **2011**, *40* (9), 4455–4463. https://doi.org/10.1039/C1CS15098G.

(109) Chang, C.; Tan, G.; He, J.; Kanatzidis, M. G.; Zhao, L.-D. The Thermoelectric Properties of SnSe Continue to Surprise: Extraordinary Electron and Phonon Transport. *Chem. Mater.* **2018**, *30* (21), 7355–7367. https://doi.org/10.1021/acs.chemmater.8b03732.

(110) Rakshit, M.; Jana, D.; Banerjee, D. General Strategies to Improve Thermoelectric Performance with an Emphasis on Tin and Germanium Chalcogenides as Thermoelectric Materials. *J. Mater. Chem. A* **2022**, *10* (13), 6872–6926. https://doi.org/10.1039/D1TA10421G.

(111) Biswas, K.; He, J.; Blum, I. D.; Wu, C.-I.; Hogan, T. P.; Seidman, D. N.; Dravid, V. P.; Kanatzidis, M. G. High-Performance Bulk Thermoelectrics with All-Scale Hierarchical Architectures. *Nature* **2012**, *489* (7416), 414–418. https://doi.org/10.1038/nature11439.

(112) Fan, C.; Li, Y.; Lu, F.; Deng, H.-X.; Wei, Z.; Li, J. Wavelength Dependent UV-Vis Photodetectors from SnS2 Flakes. *RSC Adv.* **2015**, *6* (1), 422–427. https://doi.org/10.1039/C5RA24905H.

(113) Li, L.; Chai, Z.; Jin, W.; Sun, H.; He, J.; Wu, G.; Xia, W. Sulfur Vacancy in SnS2 Nanoflake Adjusted by Precursor and Improved Photocatalytic Performance. *J. Alloys Compd.* **2023**, *932*, 167658. https://doi.org/10.1016/j.jallcom.2022.167658.

(114) Cui, X.; Xu, W.; Xie, Z.; Wang, Y. High-Performance Dye-Sensitized Solar Cells Based on Ag-Doped SnS2 Counter Electrodes. *J. Mater. Chem. A* **2016**, *4* (5), 1908–1914. https://doi.org/10.1039/C5TA10234K.

(115) Gao, W.; Zheng, Z.; Li, Y.; Zhao, Y.; Xu, L.; Deng, H.; Li, J. High Performance Tin Diselenide Photodetectors Dependent on Thickness: A Vertical Graphene Sandwiched Device and Interfacial Mechanism. *Nanoscale* **2019**, *11* (28), 13309–13317. https://doi.org/10.1039/C9NR01966A.

(116) Pham, A.-T.; Vu, T. H.; Cheng, C.; Trinh, T. L.; Lee, J.-E.; Ryu, H.; Hwang, C.; Mo, S.-K.; Kim, J.; Zhao, L.; Duong, A.-T.; Cho, S. High-Quality SnSe2 Single Crystals: Electronic and Thermoelectric Properties. *ACS Appl. Energy Mater.* **2020**, *3* (11), 10787–10792. https://doi.org/10.1021/acsaem.0c01846.

(117) Li, G.; Wu, C.; Zhang, S.; Su, J.; Li, T. Passively Q-Switched Er:YAG Laser at 1645 Nm with SnS2 as a Novel Saturable Absorber. *Optik* **2019**, *183*, 163–167. https://doi.org/10.1016/j.ijleo.2019.02.132.

(118) Wang, R.; Zhang, L.; Sun, T.; Wang, H. Preparation and Characteristics of SnS2 Saturable Absorber and Its Application in Passively Q-Switched Nd:YAG/Cr4+:YAG Laser. *Optik* **2020**, *212*, 164712. https://doi.org/10.1016/j.ijleo.2020.164712.

(119) D'Olimpio, G.; Farias, D.; Kuo, C.-N.; Ottaviano, L.; Lue, C. S.; Boukhvalov, D. W.; Politano, A. Tin Diselenide (SnSe2) Van Der Waals Semiconductor: Surface Chemical Reactivity, Ambient Stability, Chemical and Optical Sensors. *Materials* **2022**, *15* (3), 1154. https://doi.org/10.3390/ma15031154.

(120) Mondal, S.; Das, S.; Gautam, U. K. Defect-Rich, Negatively-Charged SnS2 Nanosheets for Efficient Photocatalytic Cr(VI) Reduction and Organic Dye Adsorption in Water. *J. Colloid Interface Sci.* **2021**, *603*, 110–119. https://doi.org/10.1016/j.jcis.2021.06.092.

(121) Yan, W.-J.; Chen, D.-Y.; Fuh, H.-R.; Li, Y.-L.; Zhang, D.; Liu, H.; Wu, G.; Zhang, L.; Ren, X.; Cho, J.; Choi, M.; Chun, B. S.; Coileáin, C. Ó.; Xu, H.-J.; Wang, Z.; Jiang, Z.; Chang, C.-R.; Wu, H.-C. Photo-Enhanced Gas Sensing of SnS2 with Nanoscale Defects. *RSC Adv.* **2019**, *9* (2), 626–635. https://doi.org/10.1039/C8RA08857H.

(122) Pałosz, B.; Salje, E. Lattice Parameters and Spontaneous Strain in AX2 Polytypes: CdI2, PbI2 SnS2 and SnSe2. *J. Appl. Crystallogr.* **1989**, *22* (6), 622–623. https://doi.org/10.1107/S0021889889006916.

(123) Gonzalez, J. M.; Oleynik, I. I. Layer-Dependent Properties of ${\mathbf{SnS}}_{2}$ and ${\mathbf{SnSe}}_{2}$ Two-Dimensional Materials. *Phys. Rev. B* **2016**, *94* (12), 125443. https://doi.org/10.1103/PhysRevB.94.125443.

(124) Ramsdell, L. S. Studies on Silicon Carbide. *Am. Mineral.* **1947**, No. 32, 64.

(125) Tołłoczko, A. K.; Peter, M.; Rybak, M.; Gorantla, S.; Bachmatiuk, A.; Kudrawiec, R. Influence of Native Defects on the Optical Properties of SnX2 (X = S and Se) van Der Waals Crystals. *J. Phys. Chem. C* **2024**, *128* (39), 16640–16651. https://doi.org/10.1021/acs.jpcc.4c03005.

(126) Liu, W.; Liu, M.; Wang, X.; Shen, T.; Chang, G.; Lei, M.; Deng, H.; Wei, Z.; Wei, Z. Thickness-Dependent Ultrafast Photonics of SnS2 Nanolayers for Optimizing Fiber Lasers. *ACS Appl. Nano Mater.* **2019**, *2* (5), 2697–2705. https://doi.org/10.1021/acsanm.9b00190.

(127) Lochocki, E. B.; Vishwanath, S.; Liu, X.; Dobrowolska, M.; Furdyna, J.; Xing, H. G.; Shen, K. M. Electronic Structure of SnSe2 Films Grown by Molecular Beam Epitaxy. *Appl. Phys. Lett.* **2019**, *114* (9), 091602. https://doi.org/10.1063/1.5084147.

(128) Cheng, W.-Y.; Fuh, H.-R.; Chang, C.-R. First-Principles Study for Gas Sensing of Defective SnSe2 Monolayers. *Appl. Sci.* **2020**, *10* (5), 1623. https://doi.org/10.3390/app10051623.

(129) Jena, A.; Pichaimuthu, K.; Leniec, G.; Kaczmarek, S. M.; Chang, H.; Su, C.; Hu, S.-F.; Liu, R.-S. Defect Mediated Improvements in the Photoelectrochemical Activity of MoS2/SnS2 Ultrathin Sheets on Si Photocathode for Hydrogen Evolution. *ACS Appl. Mater. Interfaces* **2022**, *14* (35), 39896–39906. https://doi.org/10.1021/acsami.2c06797.

(130) Wang, S.; Yang, B.; Liu, Y. Synthesis of a Hierarchical SnS2 Nanostructure for Efficient Adsorption of Rhodamine B Dye. *J. Colloid Interface Sci.* **2017**, *507*, 225–233. https://doi.org/10.1016/j.jcis.2017.07.053.

(131) Yu, P. Y.; Cardona, M. Optical Properties I. In *Fundamentals of Semiconductors: Physics and Materials Properties*; Yu, P. Y., Cardona, M., Eds.; Springer: Berlin, Heidelberg, 2010; pp 243–344. https://doi.org/10.1007/978-3-642-00710-1_6.

(132) Tauc, J. Optical Properties and Electronic Structure of Amorphous Ge and Si. *Mater. Res. Bull.* **1968**, *3* (1), 37–46. https://doi.org/10.1016/0025-5408(68)90023-8.

(133) Viña, L.; Logothetidis, S.; Cardona, M. Temperature Dependence of the Dielectric Function of Germanium. *Phys. Rev. B* **1984**, *30* (4), 1979–1991. https://doi.org/10.1103/PhysRevB.30.1979.

(134) Nguyen, H. T.; Le, V. L.; Nguyen, T. M. H.; Kim, T. J.; Nguyen, X. A.; Kim, B.; Kim, K.; Lee, W.; Cho, S.; Kim, Y. D. Temperature Dependence of the Dielectric Function and Critical Points of α-SnS from 27 to 350 K. *Sci. Rep.* **2020**, *10* (1), 18396. https://doi.org/10.1038/s41598-020-75383-0.

(135) Seraphin, B. O.; Bottka, N. Field Effect of the Reflectance in Silicon. *Phys. Rev. Lett.* **1965**, *15* (3), 104–107. https://doi.org/10.1103/PhysRevLett.15.104.

(136) Seraphin, B. O.; Bottka, N. Band-Structure Analysis from Electro-Reflectance Studies. *Phys. Rev.* **1966**, *145* (2), 628–636. https://doi.org/10.1103/PhysRev.145.628.

(137) Jezierski, K.; Markiewicz, P.; Misiewicz, J.; Panek, M.; Ściana, B.; Korbutowicz, R.; Tłaczała, M. Application of Kramers-Krönig Analysis to the Photoreflectance Spectra of Heavily Doped GaAs/SI-GaAs Structures. *J. Appl. Phys.* **1995**, *77* (8), 4139–4141. https://doi.org/10.1063/1.359503.

(138) Aspnes, D. E. Third-Derivative Modulation Spectroscopy with Low-Field Electroreflectance. *Surf. Sci.* **1973**, *37*, 418–442. https://doi.org/10.1016/0039-6028(73)90337-3.

(139) Schmidt, T.; Lischka, K.; Zulehner, W. Excitation-Power Dependence of the near-Band-Edge Photoluminescence of Semiconductors. *Phys. Rev. B* **1992**, *45* (16), 8989–8994. https://doi.org/10.1103/PhysRevB.45.8989.